Amphiphilic Polypeptides and Silk-based Hybrid Biomaterials: Synthesis and Stimuli-Responsive Self-Assembly for Biomedical Applications

Thesis Submitted to AcSIR
For the Award of the Degree of

DOCTOR OF PHILOSOPHY
In
Chemical Sciences

By

Bhawana Pandey
Registration Number: 10CC13J26023

Under the guidance of
Dr. Ashootosh. V. Ambade (Supervisor)
Dr. Sayam Sen Gupta (Co-Supervisor)

CSIR-National Chemical Laboratory
Pune-411008, India

राष्ट्रीय रासायनिक प्रयोगशाला
(वैज्ञानिक तथा औद्योगिक अनुसंधान परिषद)
डॉ. होमी भाभा रोड, पुणे - 411 008. भारत
NATIONAL CHEMICAL LABORATORY
(Council of Scientific & Industrial Research)
Dr. Homi Bhabha Road, Pune - 411008. India

CERTIFICATE

This is to certify that the work incorporated in this Ph.D. thesis entitled **"Amphiphilic Polypeptides and Silk-based Hybrid Biomaterials: Synthesis and Stimuli-Responsive Self-Assembly for Biomedical Applications"** submitted by **Ms. Bhawana Pandey** to **Academy of Scientific and Innovative Research (AcSIR)** in fulfillment of the requirements for the award of the Degree of Doctor of Philosophy, embodies original research work under my supervision. We further certify that this work has not been submitted to any other University or Institution in part or full for the award of any degree or diploma. Research material obtained from other sources has been duly acknowledged in the thesis. Any text, illustration, table etc., used in the thesis from other sources, have been duly cited and acknowledged.

Bhawana Pandey
(Research Student)

Dr. Ashootosh V. Ambade
(Research Supervisor)

Dr. Sayam Sen Gupta
(Research Co-Supervisor)

Communications Channels ☎ +91 20 25902000 +91 20 25893300 +91 20 25893400 Fax +91 20 25902601 (Director) +91 20 25902660 (Admin.) +91 20 25902639 (Business Development) URL : www.ncl-india.org

DECLARATION

I hereby declare that the thesis entitled "**Amphiphilic Polypeptides and Silk-based Hybrid Biomaterials: Synthesis and Stimuli-Responsive Self-Assembly for Biomedical Applications"** submitted to **Academy of Scientific & Innovative Research (AcSIR)** for Award of the **Degree of Philosophy in Chemical Sciences**, has been carried out by me at CSIR-National Chemical Laboratory, Pune-411008, India, under the supervision of Dr. Ashootosh V. Ambade (CSIR-NCL) and Co-Supervision of Dr. Sayam Sen Gupta (IISER-Kolkata). The work is original and has not been submitted in part or full by me for any other degree or diploma to this or any other University.

Date: 11.06.2018 **Bhawana Pandey**

Polymer Science and Engineering Division
CSIR-National Chemical Laboratory,
Pune - 411008, India.

Dedicated to my Parents

Acknowledgement

It is my great pleasure to present my work in the form of this PhD thesis. It was a bumpy road, full of ups and downs, but never lonely. This thesis would not be completed without my expressing my gratitude towards my companions in this journey.

First and foremost, I feel an immense pleasure to express my deep gratitude to my Ph.D. supervisors ***Dr. Sayam Sen Gupta*** *and to* ***Dr. Ashootosh V. Ambade*** *for giving me the opportunity to pursue Ph.D. under their guidance. I am always very grateful to them for sharing their scientific knowledge and experience, constructive thoughts and wonderful suggestions. Their excellent mentorship, scientific insight, and professional integrity had a large influence in shaping my personality during this journey of Ph.D. and will have an everlasting imprint on my life. It was really a great pleasure for me to work with them which gave me lot of understatnding and research experience in the complicated area of polymer chemistry. I do sincerely acknowledge the freedom rendered by them in the laboratory for independent thinking, planning and execution of research. Without their encouragement and guidance, it would not have been possible for me to complete this thesis.*

I acknowledge my research collaborator: Prof. Arindam Chowdhury from IIT Bombay and his students Jaladhar Mahato, Dharmendar Sharma and Karishma for their insight and help with spectroscopic techniques. My special thanks go to Dr. Guruswamy Kumaraswamy for his advice, valuable suggestions, and fruitful discussion on various aspects of 3D materials. I acknowlege the help of his student Soumyajyoti Chatterjee for his help in my research project. I am very grateful to Dr. Anuya Nisal for her valuable support in handling the natural biopolymer (silk) and 3D biomaterials. Special thanks to Govind Bhosle from Dr. Moneesha Fernandes lab in NCL, who help me with biological studies in my last stage of PhD work. I would also like to thank my doctoral advisory committee Dr. D. Srinivas, Dr. Asha S.K, Dr. P.P Wadgaonkar and Dr. K. Krishanmoorthy for giving me fruitful comments and suggestions during my whole research activity at NCL.

My thesis would not have been complete with help from various people in NCL; I must thank Dr. B. L. V. Prasad, Dr. Rahul Banerjee, Dr. Kadhiravan Shanmuganathan, and their research groups for their help me to use their laboratory facilities. I sincerely acknowledge Dr. P. R. Rajamohanan for central NMR facility, Mrs. D. Dhoble and Mrs. P. Purohit for allowing me to use the J wing's instrument room anytime and Mr. R.S.

Gholap from CMC for providing the microscopic analysis facility. I need to express my thanks to the support and all the staff members of our division and especially Mr. Raheja (CEPD) for his valuable cooperation and help to process all the official work.

I would like to thank the Council of Scientific and Industrial Research (CSIR), New Delhi, for the research fellowship during my Ph.D. period. I am thankful to Director, CSIR-National Chemical Laboratory for extending all possible infrastructural facilities to complete my research work.

A description of this journey would not be complete without mentioning my wonderful lab mates. I am very fortunate to have seniors in my Lab Malvi, Mrityunjoy da, Debasis da, Anal da, Chaka, Sushma, Asif, and Munmun, Kundan, Santanu, Vinita, Debasree di, who provided me a great place to work and make the lab an enjoyable place. My special thanks to my senior Soumen, for training me in the art of synthesis and polymer chemistry. I would like to thank all my present labmates: Vinita, Praveen, Bittu, Sandipan (Sandy), Basudeb and my juniors: Anagh, Maria, Mayur, RKD, Bhawana (my student), Anu, Abhishek and my IISER Kolkata labmates: Krishna Veni, Jithin for being such wonderful collegue. I would specially like to acknowledge Nimisha and Basudeb and Naganath for helping me in my research projects. Also thankful to Dr. Basab Bijoyi Dhar (Basab da) for his help in various research activity. I will always cherish the fun time in our lab trips and new year parties. It was really great working in the D-wing of PAML building; I greatly acknowledge every one of present and past members and wish them great success.

I want to express my gratitude towards my university chemistry teacher Prof. R.T Pardasani, Prof. Mohini Arora, Prof. M.P Dhobal, Dr. Akhil Barjatya and Dr. Jitendra Sharma for motivating me towards this fascinating world of research. I am also very thankful to my university seniors: Ravi Sir, Anita di, Suman di, kavita di, yachita di, for their support which makes my life much easier in NCL. I ackowledge my seniors in IIT Bombay: Anita di (Nehra), Ritu di, Ritambhara di for helping me every way while working in IIT Bombay (especially the unforgettable surprise).

Life would not have so beautiful without my wonderful friends. I am very thankful to my classmates and friends who are always been there with me in NCL: Vinita, Priti, Ruchi (my previous roommate), Vijay, Amit, Manoj and Sandeep. I going to miss our group parties. Special thanks goes to my two friends Monalisa, Ragini and their family for their love, care, well-wishes and 'especially' for the home-made food. Special thanks to Saumya Di for her enormous support like an elder sister. I want to acknowledge my

(BSc.) friends Poonam, Apoorva, Yashika and NCL friends, Swechccha, Reshma, Pravin (my ex-roommate),Monika, Shubra, Nidhi, Yogita, Deepika, Chayanika, Atreyee, Prajitha, Moumita, Sithara, Vikas, Nagnath, Indrapal, Ulhas, Dharmesh, Arjun, Pranab, Sai Geetika, Ram, Prashant, Aniket, Shrikant for making my life enjoyable. Lastly, I want to express my heartfelt gratitude to my best friend for making my life 'Joy'ful.

There are no words to express my gratitude and immense love to my family, my parents "Suresh Chand Pandey" and "Vijay Laxmi Pandey" and my lovely younger sister "Akanksha Pandey"(she is my DON) and my ever-supportive elder brother "Bharat Bhushan Pandey" for their love, support and sacrifice. It is my mother and father's prayer, relentless hard work and constant struggle to overcome the odds of life, which has inspired me to pursue life with a great ambition. I want to acknowledge the blessing of my grandmother (late) and grandfather. I thank my sister in law (Apurva) and two cute twin nephew (Taksh) and niece (Tiya) for their love and support. Specially acknowledge to my cousin brother 'Mohit' and my uncle 'Mahendra Sharma' and my aunt 'Jyoti Sharma'. Finally, I thank the Almighty for giving me the opportunity and strength to take this wonderful journey called life.

……Bhawana

Table of Contents

Particulars	Page
List of figures	vii
List of schemes	xiv
List of tables	xv
General remarks	xvi
List of abbreviations	xviii
Abstract of the thesis	xx

Chapter 1: Introduction and Literature Survey				
1.1	Polypeptides in biology			1
1.2	Post translational modifications of proteins			2
	1.2.1	Glycosylation		3
		1.2.1.1	Biological roles-physical properties	4
		1.2.1.2	Biological roles of carbohydrates as recognition elements	5
	1.2.2	Phosphorylation		7
	1.2.3	Glycosylation plus phosphorylation		8
1.3	Carbohydrate binding proteins			8
	1.3.1	Poly-valency of glycoprotein		10
1.4	Synthetic functional polypeptides mimic the functions of natural proteins			11
	1.4.1	Synthesis of polypeptides		13
1.5	Self-assembly of amphiphilic polypeptides			14
	1.5.1	Importance of polypeptides self-assembly		14
	1.5.2	Mechanism of self-assembly of block-co-polypeptides		15
	1.5.3	Preparation of block-co-polypeptides vesicles		18
1.6	Nano-carriers for drug delivery			19
	1.6.1	Concept of targeted drug delivery		20
	1.6.2	Active targeting of tumor cells		21
1.7	Targeted drug delivery			22
	1.7.1	Smart polypeptides-based nanomaterials for drug delivery		24
		1.7.1.1	Redox-responsive systems	25
		1.7.1.2	pH-responsive systems	27
		1.7.1.3	Enzyme-responsive systems	28
		1.7.1.4	Multiple stimuli-responsive systems	29
1.8	Glycopolypeptide based nano-carriers			30
1.9	Summary of individual chapters			34
1.10	References			36

Chapter 2: Glycopolypeptide grafted Bioactive Polyionic Complex Vesicles (PICsomes) and their Specific Polyvalent Interactions			
2.1	Introduction		44
2.2	Experimental section		46
	2.2.1	General	46
	2.2.2	Synthesis of N^{ε}-trifluoroacetyl-L-lysine-N-carboxyanhydride	47
	2.2.3	Synthesis of mannose-N-carboxyanhydrides	47
	2.2.4	Synthesis of γ-benzyl-L-glutamate- N-carboxyanhydride	48
	2.2.5	Synthesis of alkyne functionalized mannose glycopolypeptide (Pr-AcGP_{20}) as a hydrophilic block	48
	2.2.6	Acetyl group deprotection of alkyne functionalized mannose glycopolypeptide (Pr-GP_{20})	48
	2.2.7	Synthesis of azido terminated Poly-L-lysine (N_3-PLL_{100}) as cationic block	49
	2.2.8	Deprotection of N_3-$PLL(TFA)_{100}$ polymer	49
	2.2.9	Synthesis of glycopolypeptide-b-poly-L-lysine (GP_{20}-PLL_{100}) cationic polymer	50
	2.2.10	Synthesis of PEG_{2k}-$PBLG_{100}$	50
	2.2.11	Deprotection of PEG_{2k}-$PBLG_{100}$ polymer	50
	2.2.12	Synthesis of rhodamine labeled PEG_{2k}-$PBLG_{100}$ polymer	51
	2.2.13	Synthesis of homo-anionic copolymer (Hx-PLG_{100})	51
	2.2.14	Self-assembly of charged block polypeptides	51
	2.2.15	Sample preparation for TEM, AFM, SEM and DLS analysis	52
	2.2.16	Preparation of FITC encapsulated GP-PICsomes	52
	2.2.17	Release studies	52
	2.2.18	Fluorescence imaging of GP-PICsomes	53
	2.2.19	Sample preparation for fluorescence imaging of GP-PICsomes	53
	2.2.20	Sample preparation for fluorescence imaging of GP-PICsomes aggregation and de-aggregation	54
2.3	Results and discussions		54
	2.3.1	Synthesis and characterization of cationic block copolymers	54
	2.3.2	Synthesis and characterization anionic block copolymers	58
	2.3.3	Self-assembly of charged block copolymers	59
	2.3.4	Stability and dye encapsulation studies of GP-PICsomes	62
	2.3.5	Visualization of individual GP-PICsomes	64
	2.3.6	Dynamics of GP-PICsomes and their interaction with Con A	66
2.4	Conclusions		71
2.5	References		72
Chapter 3: Amphiphilic Glycopolypeptide based Crosslinked Nanocarriers for Dual Stimuli-Responsive Drug Delivery			
3.1	Introduction		75
3.2	Experimental section		77
	3.2.1	General	77

	3.2.2	Synthesis of branched hydrophobic initiator		78
		3.2.2.1	Synthesis of tetraethylene glycol monotosylate	78
		3.2.2.2	Synthesis of azido-tetraethylene glycol	78
		3.2.2.3	Synthesis of azido-tetraethylene glycol diol	78
		3.2.2.4	Synthesis of azide-terminated branched polycaprolactone	79
		3.2.2.5	Synthesis of amine-terminated and acetyl protected branched polycaprolactone $(PCL_{50})_2$-NH_2	79
	3.2.3	Synthesis of N-carboxyanhydrides (NCA)		80
		3.2.3.1	Synthesis of galacto-N-carboxyanhydrides	80
		3.2.3.2	Synthesis of D,L-propargyl glycine N-carboxyanhydride	80
	3.2.4	Synthesis of cleavable disulfide crosslinker : Bis-(azidoethyl) disulfide (BADS)		81
		3.2.4.1	Synthesis of bis-(tosylate ethyl) disulfide	81
		3.2.4.2	Synthesis of cross-linker bis-(azidoethyl) disulfide	81
	3.2.5	Synthesis of block coglycopolypeptide $(PCL_{50})_2$-b-Pr-gly_6-b-$AcGP_{40}$ by ring opening polymerisation (ROP) of N-carboxyanhydrides		81
	3.2.6	Acetyl group deprotection of block copolymer [$(PCL_{50})_2$-b-Pr-gly_6-b-$AcGP_{40}$		82
	3.2.7	Determination of propargyl group in block copolymer [$(PCL_{50})_2$-b-Pr-gly_6-b-$AcGP_{40}$ via click chemistry		82
	3.2.8	Self-Assembly of deprotected $(PCL_{50})_2$-b-Pr-gly_6-b-GP_{40} copolymer in aqueous solution		83
		3.2.8.1	Preparation of uncrosslinked (UCL) micelles	83
		3.2.8.2	Preparation of interface cross-linked (ICL) micelles	83
		3.2.8.3	Determination of critical micelle concentration (CMC)	83
	3.2.9	Sample preparation for TEM, AFM and DLS analysis		84
	3.2.10	Circular dichroism measurements		84
	3.2.11	Doxorubicin encapsulation in UCL and ICL micelles		84
		3.2.11.1	Preparation of DOX-loaded UCL micelles	84
		3.2.11.2	Preparation of DOX-loaded ICL micelles	85
	3.2.12	*In vitro* drug release studies		85
		3.2.12.1	Glutathione-mediated drug release studies	85
		3.2.12.2	Enzyme mediated drug release studies	85
	3.2.13	*In vitro* cytotoxicity studies		86
	3.2.14	Cellular uptake study using epifluorescence microscopy		86
3.3	Results and Discussions			87
	3.3.1	Synthesis and characterization of amine-terminated branched polycaprolactone initiator $(PCL_{50})_2$-NH_2		87
	3.3.2	Synthesis and characterization of mikto-arm star copolymer:$(PCL_{50})_2$-b-Pr-gly_6-b-GP_{40}		89
	3.3.3	Estimation of alkyne groups in star block copolymer [$(PCL_{50})_2$-		92

		b-Pr-gly$_6$-b-GP$_{40}$	
	3.3.4	Self-assembly of mikto-arm star copolymer in aqueous medium	93
	3.3.5	Preparation of interface crosslinked (ICL) Micelles	96
	3.3.6	Dye encapsulation and CMC determination	98
	3.3.7	Stability studies of micelles	99
	3.3.8	Doxorubicin loading in UCL and ICL micelles	102
	3.3.9	*In vitro* drug release studies: redox and enzyme responsive release studies	103
	3.3.10	Cytotoxicity studies	107
	3.3.11	Cellular uptake studies	109
3.4	Conclusions		111
3.5	References		111
Chapter 4: pH-Responsive Self-Assembled Nanostructures from Amphiphilic Mannose-6-Phosphate Glycopolypeptides for Lysosomal Drug Delivery			
4.1	Introduction		114
4.2	Experimental section		116
	4.2.1	General	116
	4.2.2	Synthesis of acetal containing chloro terminated poly(propylene glycol) monobutyl ether of (PPO−Ace-Cl)	116
	4.2.3	Synthesis of acetal containing azide terminated poly(propylene glycol) monobutyl ether PPO−Ace-N_3	117
	4.2.4	Procedure for the synthesis of alkyne functionalized M6P-glycopolypeptides	117
	4.2.5	Synthesis of amphiphilic mannose-6-phosphate glycopolypeptide (15M6P-GP-ace-PPO) via Click reaction	118
	4.2.6	Deprotection procedure for 15M6P-GP-ace-PPO block copolymers	118
	4.2.7	Self-assembly of deprotected copolymers 15M6P-GP-ace-PPO in aqueous solution	119
	4.2.8	Sample preparation for TEM, AFM and DLS analysis	119
	4.2.9	Circular dichroism measurements	119
	4.2.10	Dye encapsulation studies and CMC determination	119
	4.2.11	pH-responsive studies	120
	4.2.12	*In vitro* cytotoxicity studies	120
	4.2.13	Cellular uptake studies using epifluorescence microscopy	121
4.3	Results and discussion		121
	4.3.1	Synthesis of acetal containing azide end functionalised poly (propylene glycol) monobutyl ether (PPO−Ace-N_3)	121
	4.3.2	Synthesis of alkyne functionalised M6P-Glycopolypeptides:	122
	4.3.3	Synthesis of mannose-6-phosphate glycopolypeptide (15M6P-GP-ace-PPO) via click reaction	123
	4.3.4	Self-assembly of amphiphilic mannose-6-phosphate glycopolypeptide (15M6P-GP-ace-PPO)	126
	4.3.5	Dye encapsulation studies	128

	4.3.6	pH-responsive studies		129
	4.3.7	*In vitro* cell cytotoxicity studies		131
	4.3.8	Cellular uptake studies		132
4.4	Conclusion			133
4.5	References			134
Chapter 5: Silk-Mesoporous Silica based Hybrid Macroporous Scaffolds using Ice-Templating Method: Mechanical, Release and Biological Studies				
5.1	Introduction			137
5.2	Experimental Section			139
	5.2.1	General		139
	5.2.2	Synthesis of spherical SBA-15 (Santa Barbara Amorphous-15 Particles)		140
	5.2.3	Encapsulation of small molecule and macromolecule in SBA-15 particles		140
		5.2.3.1	Encapsulation of calcein inside SBA-15 particles	140
		5.2.3.2	Encapsulation of macromolecules (FITC-BSA) inside SBA-15 particles	141
	5.2.4	Preparation of Silk-SBA-15 hybrid scaffolds (~75% Inorganic content)		141
	5.2.5	Preparation of scaffolds of different organic-inorganic content		141
		5.2.5.1	Preparation of hybrid scaffolds containing 75% inorganic content (SH-75) with different concentration of methanol	142
		5.2.5.2	Preparation of hybrid scaffolds containing 60% inorganic content (SH-60-1)	142
		5.2.5.3	Preparation of hybrid scaffolds containing 90% inorganic content (SH-90-1)	142
		5.2.5.4	Control scaffolds	143
	5.2.6	Scanning electron microscopy analysis		143
	5.2.7	Mechanical studies		143
	5.2.8	Fourier transform infrared spectroscopy analysis		143
	5.2.9	Procedure for estimation of porosity and water uptake capacity		143
		5.2.9.1	Porosity	143
		5.2.9.2	Water uptake capacity	144
	5.2.10	Loading and *in vitro* release behavior of small molecules and macromolecules		144
		5.2.10.1	Loading and *in vitro* release of small molecule (calcein)	144
		5.2.10.2	Loading and *in vitro* release of macromolecules (FITC-BSA)	145
	5.2.11	Enzymatic degradation		145
	5.2.12	*In vitro* cell viability studies: Live/Dead assay		146
	5.2.13	*In vitro* cell proliferation studies		146
		5.2.13.1	MTT assay	146

		5.2.13.2	DAPI staining assay	146
		5.2.13.3	*In vitro* cell morphology study by actin cytoskeleton staining	147
5.3	Results and Discussions			147
	5.3.1	Preparation of silk-mesoporous silica based hybrid scaffolds		147
	5.3.2	Morphology of silk-mesoporous silica based hybrid scaffolds		150
	5.3.3	Mechanical properties		153
	5.3.4	Analysis of secondary structure transition		156
	5.3.5	*In vitro* release studies of model molecules		156
		5.3.5.1	Release study for calcein	157
		5.3.5.2	Release study for FITC-BSA	158
	5.3.6	*In vitro* enzyme degradation studies		160
	5.3.7	*In vitro* cell viability and cell proliferation studies		161
5.4	Conclusions			163
5.5	References			164
Chapter 6: Summary and Future Directions				
6.1	Summary			166
6.2	Future directions			168
	6.2.1	Understanding biophysical phenomenon		168
	6.2.2	Glycopolypeptide-based smart biomaterials		169
6.3	References			172
Appendix				
Appendix A				174
Appendix B				185
Appendix C				191
Appendix D				195

List of Figures

Figure 1.1	Different levels of protein organisation	1
Figure 1.2	Most common types of post translational modifications of proteins	3
Figure 1.3	A symbolic representation of a glycocalyx chain attached to a cytoskeleton	4
Figure 1.4	Glycans as recognition elements of the cell	6
Figure 1.5	Cation-independent (CI) multifunctional transmembrane glycoprotein mannose-6-phosphate (M6P) receptor containing both glycosylated and phosphorylated groups	8
Figure 1.6	Schematic representation for the binding of influenza virus to the epithelial cells	10
Figure 1.7	Schematic representation of monovalent versus polyvalent binding of ligand to receptor	11
Figure 1.8	Expected application of synthetic functional polypeptides.	12
Figure 1.9	Synthesis of polypeptides by ring opening polymerization of *N*-carboxyanhydride	13
Figure 1.10	Schematic showing two pathways for synthesis of side-chain modified polypeptides	14
Figure 1.11	Synthetic polypeptide based soft-materials for various applications	15
Figure 1.12	Schematic mechanism of self-assembly of amphiphilic blocks copolymers	17
Figure 1.13	Schematic representation of vesicle formation	17
Figure 1.14	Schematic showing formation of polyionic complex (PIC) based nanostructures	19
Figure 1.15	Represents the active and passive tissue targeting through the ligand functionalized nanoparticles	21
Figure 1.16	Schematic representation of degradation of nanostructures in presence of stimuli with the release of encapsulates molecules	23
Figure 1.17	The range of stimuli-responsive synthetic polypeptides	25
Figure 1.18	Disulfide containing PEG-detachable polyionic complex (PIC) micellar systems	26
Figure 1.19	Incorporation of disulfide linkage via intramicellar shell crosslinking in cysteine-based polypeptide micelles	27
Figure 1.20	Represented the pH-responsive polypeptide based vesicular structure which rupture to release the encapsulated molecules	28
Figure 1.21	Multiple stimuli-responsive polypeptide based nanocarriers. (a) Novel glycopeptides grafted superparamagnetic Fe_3O_4 nanoparticle (b) Dual stimuli-responsive (pH and redox) interlayer crosslinked polypeptide micelles	29
Figure 1.22	Represented chemical structure produces the corresponding nano-structures imaged by TEM	31
Figure 1.23	Represented chemical structure produces the corresponding nano-structures imaged by TEM	32
Figure 1.24	Schematic illustration of bioactive amphiphilic glycopolypeptide-b-poly(propylene oxide) GP-PPO based	32

	polymersomes for dual dye encapsulation studies	
Figure 1.25	Schematic illustration of star polymer into different nanostructures obtained by tuning hydrophilic and hydrophobic polymer chain length	33
Figure 1.26	Represented chemical structure of glycopolypeptide based stimuli-responsive block polymers produce the corresponding nano-structures (a) pH-responsive Lac-PGA-b-PPhe block copolypeptides form micelles (b) Bioreducible PCL–SS–GPPs amphiphilic glycopolypeptide based micelles receptor mediated drug delivery and efficient MRI contrast property	34
Figure 2.1	Representation depicting the structures of hydrophilic-charged block copolymers and their self-assembly into glycopolypeptide-based PICsomes (GP-PICsomes) under aqueous environments. Possibly, some of the PEG_{2k} chains and glycopolypeptide moieties may be present in the outer layers and the inner layers, respectively. Although a high density of glycopolypeptides is present on the surface, only a few of them are blown up in the cartoon depiction for clarity	46
Figure 2.2	Size exclusion chromatogram of (a) Pr-$AcGP_{20}$ (b) N_3-$PLL(TFA)_{100}$ (c)PEG_{2k}-$PBLG_{100}$ and Hexyl-$PBLG_{100}$.	56
Figure 2.3	Characterisation of cationic block copolymer (a) FTIR spectra of the synthesized block copolymer GP_{20}-PLL_{100} (catiomer) after "click" reaction (black). (b) Aqueous GPC curves of the GP_{20}-PLL_{100} from reaction mixture overlaid with curves of parent polymers	56
Figure 2.4	^{1}H NMR spectrum of the synthesized GP_{20}-PLL_{100} (**4**) block copolymer (catiomer)	57
Figure 2.5	Circular dichroism spectra of parent polymers Pr-GP_{20}, N_3-PLL_{100} and block catiomer GP_{20}-PLL_{100} in 10 mM Phosphate buffer (pH 7.4)	57
Figure 2.6	^{1}HNMR spectrum of the synthesized PEG_{2k}-PLG_{100} (3c) block copolymer (aniomer)	59
Figure 2.7	GP-PICsomes formed via self-assembly upon addition of equimolar amounts of GP_{20}-PLL_{100} and PEG_{2k}-PLG_{100} (a) SEM image of GP-PICsomes (b) Size distribution of GP-PICsomes from SEM images (c) TEM image of GP-PICsomes (d) AFM image of the GP-PICsomes drop cast from aqueous solution on silicon wafer and corresponding height profile	61
Figure 2.8	Absorption and emission spectra of FITC dextran loaded GP-PICsomes	63
Figure 2.9	(a) Emission spectrum of FITC-Dextran in PBS released from the dialysis tube over a time period of 48 h (b) Plot of % of FITC-Dextran as a function of time	63
Figure 2.10	Fluorescence images of individual GP-PICsomes labeled with both FITC and RhB in solution (a-c) and spin cast on glass coverslips (d-f), collected through band pass filters for FITC (a, d) and RhB (b, e) emission (colored green and red, respectively), along with pseudo color images (c,f) obtained via quantitative superposition of intensity images acquired for the same area	64

	through two detection channels. The line-profiles (color coded) of single GP-PICsomes (identified in c and f) on the top (a-c) and bottom (d-f) depict the emission intensity in each detection channel and the normalized emission for the overlay images (c,f) in solution and under dry conditions	
Figure 2.11	Schematic depiction of multivalent association of GP-PICsomes mediated by mannose binding lectin (Con-A) which lead to aggregation, and disassembly of aggregates only in presence of excess free mannose (not galactose) in solution	66
Figure 2.12	(a) Dynamics of individual RhB labeled GP-PICsomes in the absence of any external hydrodynamic force. Top and bottom rows represent ten single-frame sequential snapshots for two representative GP-PICsomes in solution. Left and right panels represent corresponding maximum projection (MP) images[46] of same area (at 2× magnification) for trajectory duration of 40.5s and 13.5s. (b-d) Solution dynamics and eventual surface association of GP-PICsome aggregates of various sizes formed upon addition of Con-A, in absence (b) and presence (c-d) of weak hydrodynamic flow. Rightmost panels in (b-d) depict MP images over entire trajectories from which representative single-frame sequential snapshots are shown for each aggregate. (e) Variety of multiple scattered GP-PICsome aggregates attached on to glass surface with blowups (5×5 μm) depicting the presence of many GP-PICsomes within each aggregate. (f) Formation of very large extended aggregate clusters of GP-PICsomes upon incubation with Con-A for 30 min. Movie 6 provided in Figure A7 depicts clustering of aggregates in three dimensions	68
Figure 2.13	Dissociation/de-aggregation of an immobile RhB-GP-PICsome aggregate cluster upon addition of excess monomeric mannose solution. The first panel (0-4.5s) depicts the time-average image of the aggregate-cluster in absence of flow, while other panels are sequential single-frame snapshots under flow in absence (5-6s) and presence (>6s) of mannose (300 mM) containing buffer. (b) Sequential single-frame snapshots of an immobile GP-PICsome aggregate cluster (Aggregate-1) attached to glass surface under continuous flow of 300 mM galactose containing buffer. Single-frame snapshots of a larger aggregate cluster (Aggregate-2, right) incubated with 300 mM galactose for 5 min, under momentary buffer flow (suddenly turned on and off, as represented by arrowheads)	70
Figure 3.1	Schematic representation of the synthesized amphiphilic block coglycopolypeptides and their self-assembly into uncrosslinked (UCL) and interface crosslinked (ICL) nanostructures for targeted and controlled drug delivery	77
Figure 3.2	^{1}H NMR of amine terminated branched polycaprolactone initiator $(PCL_{50})_2$-NH_2	88
Figure 3.3	^{1}H NMR spectrum of protected mikto-arm star copolymer	91

	$(PCL_{50})_2$-b-Pr-gly_6-b-$AcGP_{40}$	
Figure 3.4	(a) GPC chromatograms of amine-terminated branched $(PCL_{50})_2$-NH_2) and protected star copolymer (P1) (b) CD spectrum of deprotected star copolymer (P2) in DI water	91
Figure 3.5	^{1}H NMR spectrum of polymer P1 after click reaction with benzyl azide	92
Figure 3.6	Transmission electron microscopic (TEM) image of UCL micelles (inset shows individual micelles) (b) Atomic force microscopic (AFM) image of UCL micelles	95
Figure 3.7	DLS size distribution of UCL and ICL micelles.	96
Figure 3.8	Images from (a) TEM (inset shows individual micelles) and (b) AFM analysis of ICL micelles	97
Figure 3.9	UV-Vis absorption spectra of free RBOE in water and RBOE encapsulated in UCL and ICL micelles	99
Figure 3.10	Plot of fluorescence intensity versus the logarithm of the polymer concentration (μM) in aqueous solution (a) Uncrosslinked (UCL) micelles (b) Interface crosslinked (ICL) micelles. Inset: Fluorescence emission spectra of RBOE in an aqueous solution of the polymer at different concentrations	99
Figure 3.11	Stability studies of UCL and ICL micelles: DLS size distribution curves (a) upon dilution by 10-fold volume of DMF and (b) below CMC	101
Figure 3.12	Changes in RBOE fluorescence intensity encapsulated in UCL and ICL micelles with time	101
Figure 3.13	(a) UV-Vis absorption spectra of free DOX and DOX encapsulated in UCL and ICL micelles (b) DLS measurement of DOX encapsulated UCL and ICL micelles (c) TEM image of DOX-loaded UCL micelles (d) TEM image of DOX-loaded ICL micelles	103
Figure 3.14	Release of DOX from ICL micelles (a) in presence of esterase and GSH (~2 μM GSH and ~10 mM GSH) (b) by applying dual stimuli (Case 1: Redox and Enzyme) (c) by applying dual stimuli (Case 2: Enzyme and Redox)	104
Figure 3.15	MTT assay data of (a) UCL and ICL micelles (b) DOX-loaded UCL and ICL micelles	109
Figure 3.16	Epifluorescence microscopic images of intracellular distribution of (a) DOX loaded UCL and (b) DOX loaded ICL micelles at different time intervals (2, 12, 24, 48h) (c) free DOX, in HepG2 cell. For each panel, the images from the left to right show staining of cell nuclei by DAPI (shown in blue), DOX fluorescence in the cells (shown in red), overlay of the two images. The scale bars are 10 μm in all the images	110
Figure 4.1	Schematic showing structures of amphiphilic pH-responsive mannose-6-phosphate containing block coglycopolypeptides (15M6P-GP-Ace-PPO) and their assembly into micelles for pH-triggered drug release inside lysosomes	116
Figure 4.2	(a) FTIR spectra of the synthesized 15M6P-GP-ace-PPO block copolymer after "click" reaction. (b) Overlay of GPC curves of	124

	individual parent blocks (PPO and15M6P-GP) and 15M6P-GP-ace-PPO block copolymer prepared after "click" reaction	
Figure 4.3	^{1}H NMR of protected 15M6P-GP-ace-PPO block copolymer represents corresponding peaks to protons of PPO block and M6P-GP block	125
Figure 4.4	Circular dichroism spectra of the synthesized 15M6P-GP-ace-PPO block copolymer in buffer (pH 7.4)	126
Figure 4.5	(a) TEM image of 15M6P-GP-ace-PPO micelles (scale: 100 nm) (b) size distribution of micelles from TEM image (c) DLS analysis of micelles from aqueous solution	127
Figure 4.6	(a) FE-SEM image of micelles in water (inset of (c) shows a FE-SEM of a single micelle) (b) AFM image of the micelles drop cast from aqueous solution on a silicon wafer (c) the corresponding height profile of micelles	128
Figure 4.7	UV-Vis absorption spectra of free RBOE in water and RBOE encapsulated in 15M6P-GP-ace-PPO micelles in water	128
Figure 4.8	(a) Plot of fluorescence intensity versus the logarithm of the polymer concentration (μM) in aqueous solution. (b) Fluorescence emission spectra of RBOE in an aqueous solution of the polymer at different concentrations	129
Figure 4.9	(a) pH-responsive dye release profile at two different pH (7.4 and 4.5) in specific time intervals (b) Hydrodynamic diameter of the degraded micelles obtained after acetal bond cleavage at pH 4.5 via DLS. (inset: TEM image of the degraded micelles after acetal bond cleavage shows aggregated disassembled structures)	130
Figure 4.10	MTT assay for 15M6P-GP-ace-PPO block polymer that assembled into micelles performed on MCF-7 cell line	131
Figure 4.11	Lysosome targeting with RBOE encapsulated M6P-GP-ace-PPO micelles: MCF-7 (a-d) cells were cultured for 4 h, respectively, with RBOE encapsulated M6P-GP micelles (200 μg/mL) in DMEM and then stained with LysoTracker Green (50 nM) for 30 min. The cells were probed by epi-fluorescence microscopy. Merging of the RBOE signal (shown in green) and that of LysoTracker Green (shown in green) revealed colocalization as indicated by the orange-yellow spots/areas (bars, 5 μm); cyan color arrow indicates punctate-like vesicles	132
Figure 4.12	Color intensity profile in MCF-7 cells representing the variation of color (both green and red) intensity with distance for a small sub-section of merged image. MCF-7 incubated with RBOE encapsulated M6P-GP-ace-PPO micelles show only orange yellowish spherical indicating co-localization of both dyes as is also observed object in the intensity profile	133
Figure 5.1	Preparation of macroporous silk hybrid scaffolds using "ice templating method" and physical crosslinking	138
Figure 5.2	(a) SEM image of SBA-15 particles (b) TEM images of synthesized SBA-15 particles showing formation of hierarchical mesoporous structure. (c) Nitrogen adsorption-desorption isotherm of SBA-15 particles	148
Figure 5.3	Morphological characteristics of SH-75-1 scaffold (a) Photograph of large sized SH-75-1 hybrid scaffold prepared	149

	using silk fibroin and micron size mesoporous SBA-15 particles using ice templating method (b) Scanning electron micrographs of hybrid SH-75-1 scaffold (c) SEM Image of SH-75-1 scaffold at high magnification (black arrow showing SBA-15 particles are embedding within the pore wall) (d) Pore size distribution of SH-75-1 scaffold	
Figure 5.4	TGA of SBA-15 particles (black line) as a control (b) TGA of SH-75-1 scaffold (red line) prepared using the micron sized SBA-15 particles and silk using ice templating method	150
Figure 5.5	(a) Photographs of prepared scaffolds (SH-75-1, SH-75-0, SF-100-1, SF-100-0) after lyophilisation and (b) Photographs of scaffolds (SH-75-1, SH-75-0, SF-100-1, SF-100-0) after addition of water (5 min)	151
Figure 5.6	SEM images of scaffolds (a) SH-60-1 scaffold (inset: magnified section showing pore wall of SH-60-1 scaffold) (b) SH-90-1 scaffolds (c) Pure silk scaffolds (SF-100-1) after lyophilisation.	152
Figure 5.7	Water absorption capacity of SH-75-1 scaffolds shows that equilibrium is attained after 24 h	153
Figure 5.8	(a) Effect of methanol on Young's modulus of SH-75 scaffolds (b) FTIR Spectra of SH-75 scaffolds (c) compression stress-strain curve of SH-75 scaffolds at different strain value viz. from 10 to 60 %	155
Figure 5.9	(a) Release profile of calcein (small molecule) from SH-75-1 scaffolds and bare SBA-15 particles (b) Release profile of FITC-BSA (macromolecule) from SH-75-1scaffolds and bare SBA-15 particles (c) Circular dichroism spectrum of FITC-BSA after and before release from SH-75-1scaffolds	159
Figure 5.10	(a) Degree of degradation of hybrid scaffolds in the presence of protease enzyme (b) SEM image of SH-75-1 scaffolds at 14^{th} day of enzyme degradation. (c) Photographs of SH-75-1 scaffolds degraded with time	161
Figure 5.11	(a) Cell proliferation assay (MTT assay) of L929 cells cultured on SH-75-1 scaffolds (b) Epifluorescence Microscopic Images of Live /Dead assay performed on SH-75-1 scaffolds at 7^{th} day. Scale bar is 50 µm	162
Figure 5.12	Epifluorescence Microscopic Images of cell proliferation assay of L929 cells cultured and stained with DAPI on SH-75-1 scaffolds. Scale bar is 50 µm	162
Figure 5.13	Epifluorescence images of L929 actin cytoskeleton stained by Alexa Fluor 488 Phalloidin at the end of 7^{th} day cell growth on SH-75-1 scaffold. Scale bar is 50 µm	163
Figure 6.1	Illustration of different biophysical phenomena at the subcellular level	169
Figure 6.2	Synthetic strategy proposed for glycopolypeptide based PIC structures for gene delivery in cancer treatment	170
Figure 6.3	Proposed scheme for sugar-responsive hydrophilic glycopolypeptide-boronic acid based self-assembled structures for insulin delivery in diabetic treatment	171
Figure 6.4	Fabrication of glycopolypeptide-borax based gels	172

Figure 6.5	Schematic illustration of enzyme/drug-loaded M6P-GP functionalized MSN nanocarrier synthesis	172

List of Schemes

Scheme 2.1	Synthesis of alkyne functionalized mannose glycopolypeptide (Pr-GP_{20}) as hydrophobic block	55
Scheme 2.2	Synthesis of azido terminated Poly-L-lysine (N_3-PLL_{100}) as cationic block	55
Scheme 2.3	Synthesis of glycopolypeptide-b-poly-*L*-lysine (GP_{20}-PLL_{100}) cationic polymer (4)	56
Scheme 2.4	Synthesis of PEG_{2k}-PLG_{100} anionic polymers by ROP of Bn-Glu-NCA using PEG_{2k}-NH_2 as the macroinitiator	58
Scheme 3.1	Synthesis of azide-terminated branched polycaprolactone $(PCL_{50})_2$-N_3	87
Scheme 3.2	Synthesis of amine-terminated branched polycaprolactone $(PCL_{50})_2$-NH_2	88
Scheme 3.3	Synthesis of galactose-N-carboxyanhydrides	90
Scheme 3.4	Synthesis of D,L- propargylglycine N-carboxyanhydride	90
Scheme 3.5	Synthesis of amphiphilic triblock glycopolypeptides $(PCL_{50})_2$-b-Pr-gly_6-b-GP_{40}	90
Scheme 3.6	Click reaction of triblock glycopolypeptide $(PCL_{50})_2$-b-Pr-gly_6-b-GP_{40} with benzyl azide to obtain P3	92
Scheme 3.7	Synthesis of cleavable disulphide crosslinker bis-(azidoethyl) disulfide (BADS)	95
Scheme 3.8	Schematic for the synthesis of interface crosslinked micelles via click chemistry	95
Scheme 3.9	Schematic representation of release of drugs from SCL micelles through single and dual stimuli	103
Scheme 4.1	Synthesis of acetal containing azide terminated poly (propylene glycol) monobutyl ether (PPO−Ace-N_3) as acid-cleavable hydrophobic block	122
Scheme 4.2	Synthesis of alkyne functionalized M6P-glycopolypeptides (Pr-15M6P-GP)	123
Scheme 4.3	Synthesis of amphiphilic 15M6P-GP-ace-PPO glycopolypeptide using click reaction	124

List of Tables

Table 1.1	Correlation of morphology to "packing parameter" and "hydrophilic weight fraction" of the amphiphile	18
Table 2.1	Synthesis of alkyne-AcGP, azide-PLL(TFA), PEG_{2k}-PBLG and their corresponding deprotected polymers	59
Table 3.1	Represents characteristics of blank and DOX-loaded UCL and ICL micelles	103
Table 5.1	Represents prepared SH-75-1 scaffolds with varying inorganic-organic content	153
Table 5.2	Represents properties of SH-75-1 hybrid scaffolds with varying methanol content	154
Table 5.3	Represents SH-75 silk-hybrid scaffolds with varying methanol content	155

Instrumentation

- ^{1}H NMR spectra were recorded on AV-200 MHz, AV-400 MHz, DRX-500 MHz,or JEOL ECX 400 MHz and Bruker Advance 500 MHz spectrometer using tetramethylsilane (TMS) as an internal standard. Chemical shifts have been expressed in ppm units downfield from TMS.
- ^{13}C NMR spectra were recorded on AV-50 MHz, AV-100 MHz, DRX-125 or JEOL ECX 100 MHz and Bruker Advance 125 MHz spectrometer.
- FT-IR spectra were recorded on IR 470 and Shimadzu Perkin Elmer (683 or 1310 spectrometers) FT-IR spectrum GX instrument. For solid IR, KBr pellets were prepared by mixing 3 mg of sample with 97 mg of KBr. Sodium chloride optics was used for liquid samples. Spectra are measured in cm^{-1}.
- Gel permeation chromatography (GPC) was performed on a VISKOTEK TDA 305-040 TRIPLE DETECTOR ARRAY viscometer (VISC), refractive index (RI), right angle light scattering (RALS), low angle light scattering (LALS) GPC/SEC MODULE. Separations were done by one guard column (TGAURD, ORG GUARD COL 10X4.6 MM) and three columns (T6000M, GENERAL MIXED ORG 300X7.8 MM) and, 0.05 M LiBr in DMF as the eluent at 60 °C by maintaining a constant flow rate of 1 mL min^{-1}. Samples for GPC analysis were prepared at a concentrations of 5 mg/mL. Instrument was calibrated using PMMA standards. Dispersity (Đ) values were calculated using OmniSEC software.
- UV-vis spectra were recorded on Cary-300 UV-vis spectrometer using 1 cm quartz cuvette at 25°C.
- Transmission electron microscopy (TEM) measurements were performed at 100 kV on an FEI Technai T20 instrument. Atomic Force Microscopy (AFM) measurement was performed on Asylum MFP-3D instrument. Image analysis was performed on a Nanoscope IV (Veeco) software. Scanning electron microscopy (SEM) was performed using a Quanta 200 3D scanning electron microscope (SEM).
- Hydrodynamic diameter of particles were measured by using 90 *Plus* Particle Size Analyzer (Brookhaven Instruments Corporation) at an angle of 90° equipped with a laser beam of 633 nm wavelength.

- Fluorescence spectroscopy measurements were carried out on fluorimeter QM40 from Photon Technology International, Inc.

Experimental Section

- All reactions were carried out under nitrogen or argon atmosphere with dry, freshly distilled solvents under anhydrous conditions unless otherwise specified. Yields refer to chromatographically and spectroscopically homogeneous materials unless otherwise stated.
- All evaporations were carried out under reduced pressure on Buchi rotary evaporator below 45 °C unless otherwise specified.
- Silica gel (60–120), (100-200), and (230-400) mesh were used for column chromatography.

.

List of Abbreviations

Abbreviation	Expansion
Ac	Acetyl
AcOH	Acetic acid
Ace	Acetal
Aq	Aqueous
Az	Azide
BSA	Bovine Serum Albumin
AFM	Atomic Force Microscopy
CEVE	Chloroethyl Vinyl Ether
CD	Circular Dichroism
CI-MPR	Cation-Independent Mannose-6-Phosphate Receptor
CMC	Critical Micelle Concentration
Con-A	Concanavalin-A
CuAAC	Copper-catalyzed Azide-Alkyne Cycloaddition
DCC	Dicyclohexyl Carbodiimide
DCM	Dichloromethane
DEPT	Distortionless Enhancement by Polarization Transfer
Dh	Hydrodynamic Diameter
DI	Deionised Water
Đ	Dispersity (D-stroke)
DLS	Dynamic Light Scattering
DMAP	N,N-Dimethylaminopyridine
DMF	N,N-Dimethylformamide
DMSO	Dimethyl Sulfoxide
DP	Degree of Polymerization
DPTS	4-(Dimethylamino)pyridinium 4-toluenesulfonate
DOX	Doxorubicin
EDTA	Ethylenediaminetetra acetic acid
EtOAc	Ethyl Acetate
eq	Equivalents
FITC	Flourescien Isothiocyanate
FT-IR	Fourier Transform-Infrared
GPC	Gel Permeation Chromatography
GP	Glycopolypeptide
g	Gram
h	Hour

Hz	Hertz
J	Coupling Constant
MeOH	Methanol
mg	Milligram
mL	Millilitre
mmol	Millimole
min	Minutes
4ÅMS	4Å Molecualar sieves
MWCO	Molecular Weight Cut Off
M6P	Mannose-6-Phosphate
MTT	(3-(4,5-Dimethylthiazol-2-yl)-2,5-Diphenyltetrazolium Bromide
M_n	Number Average Molecular Weight
M_w	Weight Average Molecular Weight
NMR	Nuclear Magnetic Resonance
PBS	Phosphate Buffer Saline
PCL	Poly(ε-caprolactone)
PEG	Polyethylene Glycol
PIC	Polyionic Complex
PLL	Poly-*L*-Lysine
PPO	Polypropylene Glycol
p-TSA	*para*-Toluene sulphonic acid
RBOE	Rhodamine B Octadecyl Ester
RITC	Rhodamine Isothiocyanate
RhB	Rhodamine B
ROP	Ring Opening Polymerisation
SEM	Scanning Electron Microscopy
SEC	Size Exclusion Chromatrography
TEG	Tetraethylene Glycol
TFA	Triflouro Acetic Acid
TEM	Transmission Electron Microscopy
THPTA	Tris(3-hydroxypropyltriazolylmethyl)amine
THF	Tetrahydrofuran
TIRF	Total Internal Reflection Fluorescence
TLC	Thin Layer Chromatography
UV-vis	Ultraviolet-visible
W_{philic}	Hydrophilic Weight Fraction

Abstract

Polypeptides are the constituents of proteins which perform various cellular functions such as catalyzing the metabolic reaction, structural building material, replication of DNA, response to stimuli, transporting molecules and many others. When these polypeptides are glycosylated, they are called the glycoproteins or glycopolypeptides. They have well defined secondary structures and are expected to be biocompatible as compared to other conventional biopolymers and are functionally close to naturally occurring proteoglycans. The ring opening polymerization of N-carboxyanhydride allows the synthesis of high molecular weight, end-functionalized, and structurally well defined functional polypeptides in an efficient way. By using this methodology, functional polypeptides mimicking the molecular composition of natural protein are synthesized. Besides glycosylated polypeptides, phospho-glycosylated polypeptides can also modulate biological interactions in cells and thus can be used for therapeutic applications. In addition to that, this methodology can be extended to synthesize amphiphilic functional polypeptides that can be self-assembled into soft nano-materials for possible use as carriers in targeted and controlled drug delivery. Therefore, access to these structurally defined functional polypeptides is essential to unravelling their function and subsequently using them for various biomedical applications. Silk fibroin represents an important class of biomaterial and has application in tissue engineering due to its versatile property such as excellent mechanical strength, tunable porosity, swelling property, biocompatibility, and biodegradability. They can be modified to hybrid 3D materials to enhance their activity towards drug delivery in combination with tissue engineering.

Chapter 1: Introduction

Introduction chapter includes a detailed literature report about the PTM's glycosylation and phosphorylation and their role in functional proteomics. It then provides an overview of the synthesis of novel functional polypeptides and their interaction with receptor proteins known as lectins (carbohydrate-binding proteins). This chapter also briefly discusses different aspects of polypeptide self-assembly for several biomedical applications. Further, the importance of stimuli-responsive polymers for drug delivery application is highlighted, and examples of various stimuli-responsive functional polypeptides are given.

Chapter 2: Glycopolypeptide-Grafted Bioactive Polyionic Complex Vesicles (PICsomes) and Their Specific Polyvalent Interactions

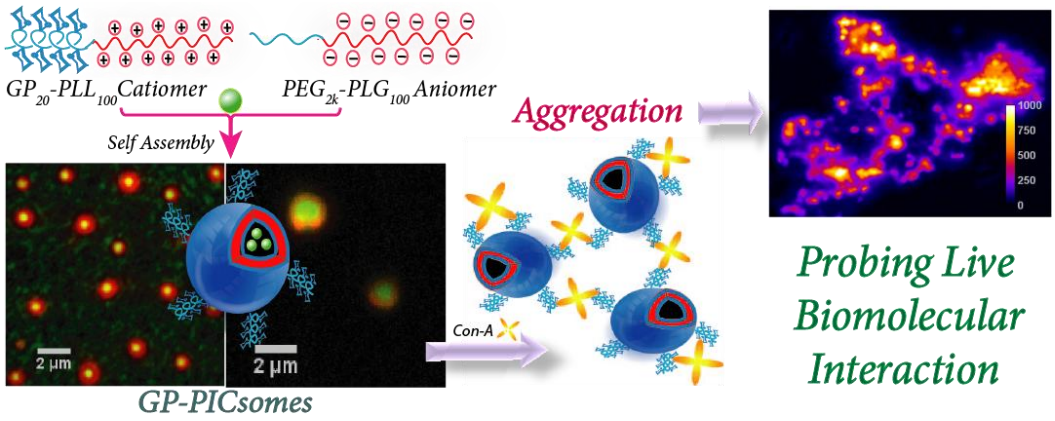

Figure 1: Schematic showing structures of hydrophilic-charged block copolymers and their self-assembly into glycopolypeptide-based PICsomes (GP-PICsomes) in aqueous environment and their specific polyvalent interaction with lectins.

This chapter discusses the development of understanding of specific biomolecular interaction processes through the glycopolypeptide-based supramolecular soft structures such as polymersomes, which were formed by the self-assembly of hydrophilic charged block copolymers. The new class of polymersomes, i.e. polyionic complex vesicles (PICsomes) with glycopolypeptides present on the outer surface were prepared. Oppositely charged hydrophilic block copolymers of glycopolypeptide$_{20}$-b-poly-L-lysine$_{100}$ and PEG$_{2k}$-b-poly-L-glutamate$_{100}$ were synthesized using a combination of ring-opening polymerization of N-carboxyanhydrides and "click" chemistry. The catiomer and aniomer are self-assembled under physiological conditions to form glycopolypeptide-conjugated PICsomes (GP-PICsomes) of micrometer dimensions. Electron and atomic force microscopy were performed on the PICsomes to check the hollow morphology of the PICsomes. As GP-PICsomes are relatively larger (~micrometers) in size, therefore, the hollowness of the supramolecular structure was further investigated by fluorescence microscopy of single GP-PICsomes, both in solution and under dry conditions, using spatially distributed fluorescent probes. Moreover, multivalent interactions between PICsomes mediated by a carbohydrate-binding protein were understood by imaging the real-time dynamics of single PICsomes in solution phase by the help of TIRF microscopy. The immediate association and eventual aggregation of several GP-PICsomes were observed in the presence of Con-A which led to the formation of large insoluble aggregate

clusters. This result revealed that after self-assembly carbohydrate moieties are protruded on the outer surface, which retained their biochemical activity. Furthermore, it was very challenging to study the disaggregation process of aggregated GP-PICsomes clusters in the presence of excess mannose; it was just the opposite in the presence of excess galactose. With the help of these studies, the specificity and bioactivity of self-assembled GP-PICsomes regarding lectin-mediated polyvalent interactions was elucidated.

Chapter 3: Amphiphilic Glycopolypeptide-based Interface Crosslinked Nanostructures for Dual Stimuli-Responsive Drug Delivery

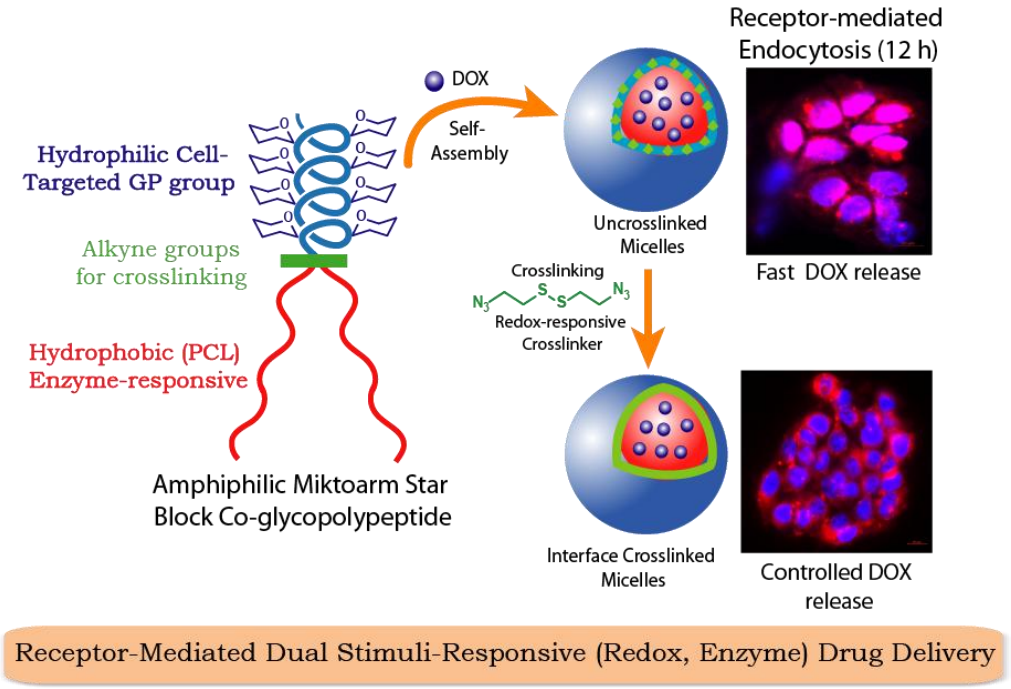

Figure 2: Schematic representations of structures of amphiphilic block coglycopolypeptides and their self-assembly into uncrosslinked (UCL) and interface crosslinked (ICL) nanostructures for the stimuli-responsive and targeted drug delivery.

This chapter deals with the synthesis and self-assembly of miktoarm star block coglycopolypeptides into dual stimuli-responsive (redox and enzyme) crosslinked micellar structures, which exhibit both specific cell-targeting ability and controlled drug release property. Micelle-based nanocarriers have been extensively used for drug delivery applications but are disintegrated in the bloodstream due to significant dilution (Critical Micelle Concentration) and thus reduce therapeutic efficacy and cause undesired side effects. Crosslinking of micelles is an effective approach to solve this problem. An amphiphilic biocompatible miktoarm star copolymer [$(PCL_{50})_2$-*b*-Pr-gly_6-*b*-GP_{40}] which

comprises two hydrophobic poly(ε-caprolactone) blocks, a short poly(propargylglycine) middle block and the hydrophilic glycopolypeptide block were designed and synthesized. Poly(ε-caprolactone) was chosen as the degradable enzyme-responsive block. The star copolymer was initially self-assembled into uncrosslinked (UCL) micellar structures. Further, free alkyne group of the middle poly(propargyl glycine) block (interface) was reacted with azide-containing redox-responsive crosslinker (bis-(azidoethyl) disulfide) using "click chemistry" to form interface crosslinked (ICL) micelles. Stability of ICL micelles compared to UCL micelles was studied by dilution assay. Furthermore, synergistic effect of both the stimuli (redox and enzyme) on the drug release behaviour of ICL micelles was investigated by using DOX as a model anticancer drug. Further, biological studies have been done to check the cytotoxicity of ICL micelles and stimuli mediated DOX release was evaluated in living cells to evaluate the efficacy of ICL micelles as a stable nanocarrier for controlled and targeted drug delivery.

Chapter 4: pH-Responsive Self-Assembled Nanostructures from Amphiphilic Mannose 6-phosphate Glycopolypeptides (M6P-GP's) for Lysosome Targeted Drug Delivery

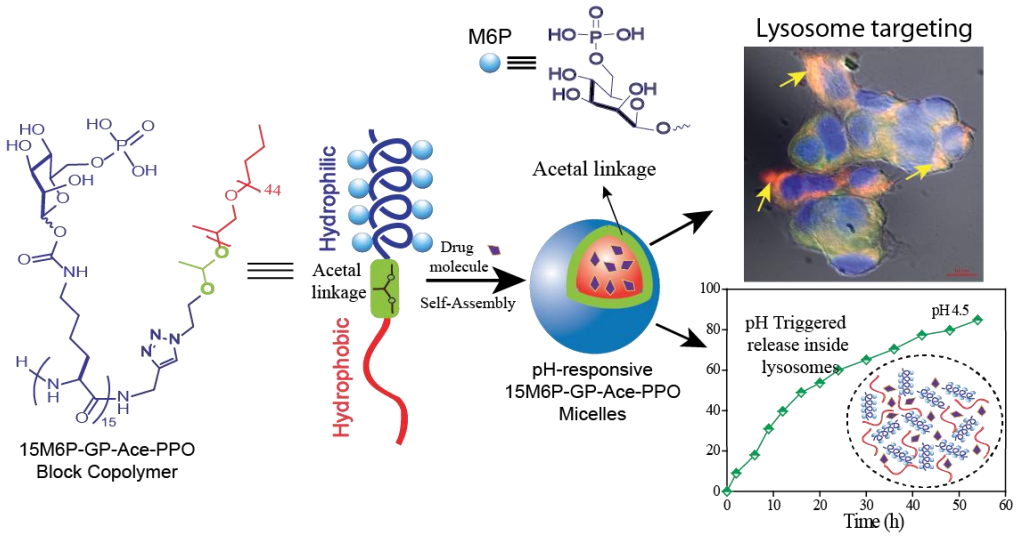

Figure 3: Schematic showing structures of amphiphilic pH-responsive mannose-6-phosphate containing block coglycopolypeptides (15M6P-GP-Ace-PPO) and their assembly into micelles for pH-triggered drug release inside lysosomes.

This chapter describes the preparation of the M6P-labeled nanocarriers by self-assembly of amphiphilic pH-responsive M6P-containing glycopolypeptide. The ability of cation-independent mannose-6-phosphate receptor (CIMPR) to deliver cargo specifically to the

lysosome can thus be selectively exploited using M6P-labeled nanocarriers to carry the cytotoxic drugs specifically inside lysosomes for destroying cancer cells. Since the lysosomes have low pH, the incorporation of the pH-responsive group in M6P-labeled nanocarriers would enhance the controlled release of the encapsulated drug inside the lysosome. Therefore, amphiphilic M6P-glycopolypeptide (15M6P-acetal-PPO) with the pH-responsive group was synthesized by click reaction of alkyne-containing M6P-glycopolypeptide and the azide-functionalized acetal containing PPO (PPO−Ace-N_3) as a hydrophobic block. M6P-labeled nanocarriers with pH-responsive groups were prepared by self-assembly of the $M6P_{15}$-acetal-PPO amphiphilic block copolymer and were characterized by DLS, TEM, AFM, fluorescence spectroscopy techniques and dye release studies. Further, cellular studies were performed with the M6P-labeled nanocarriers to check their cytotoxicity and uptake towards lysosomes of mammalian cells. It was demonstrated that trafficking of M6P-labeled nanocarriers inside the lysosomes likely occurs with the CI-MPR receptor pathway.

Chapter 5: Silk-Mesoporous Silica-based Hybrid Scaffolds using Ice-Templating Method: Mechanical, Release and Biological Studies

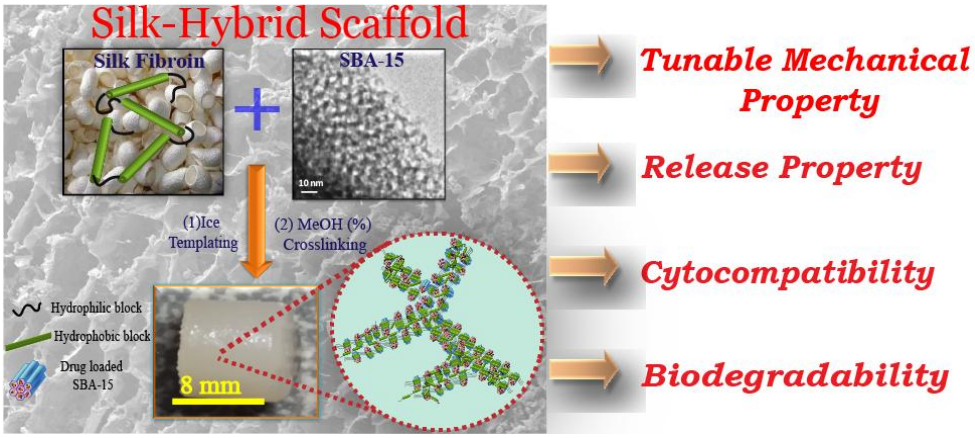

Figure 4: Schematic representation of fabrication of macroporous silk-mesoporous silica based hybrid scaffolds using "ice templating method" and physical crosslinking.

Considering the advantage of natural biopolymer "silk fibroin" and mesoporous silica particles (SBA-15), a macroporous 3D silk-hybrid scaffold as a biomaterial was fabricated to enhance the drug-eluting property along with the tissue regeneration and repair process. The fabrication of self-standing silk hybrid 3D scaffolds was done by embedding high percentage (~75%) of submicrometer-sized mesoporous silica particles (SBA-15) within the silk matrix using ice templating method and physical crosslinking. By varying

methanol concentration as a means to cross-link, the mechanical strength of hybrid scaffolds was observed in the soft tissue range (37 ± 0.6 kPa to 181 ± 5.9 kPa), which is due to the formation of β-sheet in the silk matrix and was studied by infrared spectroscopy. Further, drug release property of the hybrid scaffolds was investigated by two model molecules (FITC-BSA as macromolecule and calcein as a small molecule) which are encapsulated in the hybrid scaffolds *via* mesoporous silica particles. Hybrid scaffolds obtained by the physical mixing of silk fibroin as organic and mesoporous silica particles as an inorganic component are biocompatible and biodegradable. Finally, the cell proliferation and cytotoxicity studies were performed on the hybrid scaffolds which indicate that these scaffolds are suitable candidates for tissue engineering applications.

Chapter 6: Summary and Future Directions

Presents an overall summary of the work and describes the major findings of the studies. Future directions based on the work reported in the thesis are also discussed.

CHAPTER 1

Introduction and Literature Survey

1.1 Polypeptides in Biology

Polypeptides play an important role in the biological system as they are the constituents of proteins, which perform various cellular functions such as catalyzing the metabolic reaction, structural building material, replication of DNA, response to stimuli, transporting molecules and many others .[1,2] Polypeptides are linear chains of poly-(amino acid)s in which amino acids are covalently linked through peptide (amide) bonds. The Polypeptide chains can undergo specific hydrogen bonding between the primary sequences of amino acids and finally get folded into highly regular sub-structure such as α-helix and β-sheet (Figure 1.1).[3] These sub-structures are again folded into the specific three-dimensional framework, controlled by various non-covalent interactions such as hydrophobic interaction, hydrogen bonding, ionic interactions and van der Waals forces. These folded three-dimensional structures are the native state of the protein.[4] These 3D units can further assemble into large structures by non-covalent interaction and serve as specific catalytic and binding sites for several biological processes.[4,5] The sequence of amino acids is important to determine the final structure of proteins, but beside this, the final activity of the fully developed protein is based on the 3D structure of the protein.

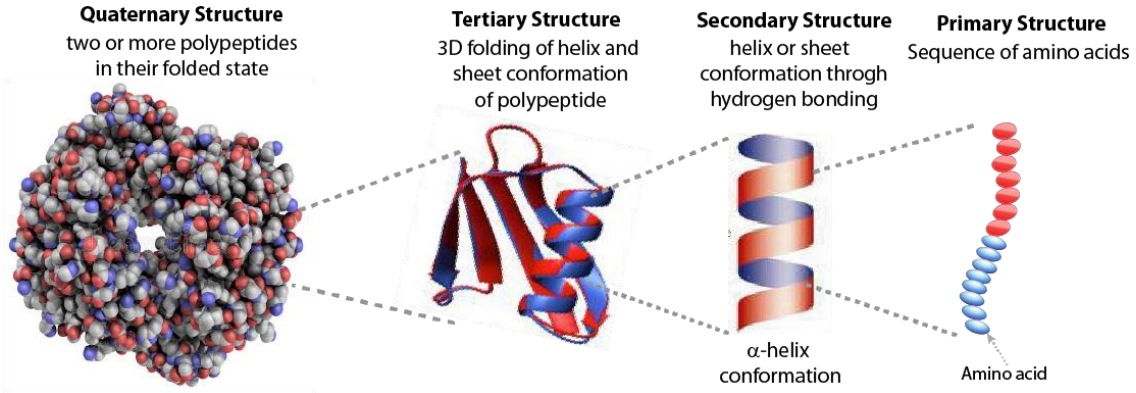

Figure 1.1 Different levels of protein organization.

In biological systems, the DNA contains the information of the amino acid sequence in protein for every genotype, and it acts as a repository of all the information for the synthesis of proteins. This synthesized protein determines the characteristic of all the forms of living organisms and participates in several biological functions in the organism. Proteins synthesis takes place in ribosomes, where mRNA transforms the information encoded in DNA into a polypeptide chain.[6] After the protein synthesis, a part of protein gets chemically modified by a process known as post-translational modification (PTM) process, which alters the chemical and physical properties (activity, stability, folding) and

most importantly the function of proteins. PTM's can occur at the side chain of amino acids as well as at the C- or N- terminal of protein's.[7] PTM helps in expanding the chemical repertoire of the 20 standard amino acids by either incorporating a new one functional moiety or by modifying an existing functional group.

1.2 Post-Translational Modifications of Proteins (PTMs)

PTMs are a type of biochemical reaction mechanism in which a particular amino acid residue in a protein is covalently modified by the internal biological enzymes.[8,9]As the evolution of any living species proceeds, the gene sequences or genomics are continuously modified, which are not convenient for basic organism development. In addition there is always a continuous war against disease and disintegration. It also affects the entire set of proteins (proteome) which is expressed by a genome, cell, tissue, or organism at a certain time. However, PTMs helps to overcome this genetic imprisonment and allows the protein properties to be changed 'spontaneously', in response to the requirements on a developmental or physiological time scale. From the biological aspect, this proteome diversification is mostly caused by PTM's and is more extensively observed in the eukaryotes as compared to the prokaryotes. Therefore, genomes of higher eukaryotes are committed to only 5% of these enzymes which are responsible for post-translational modifications.[9] The PTM's process can be categorised into two broad areas. One is the enzyme-catalyzed covalent attachment of the functional group to the side chain residue of the protein, and the second one is the enzymatic cleavage of peptide backbones in proteins.[7] During the protein translation process in ribosomes, the side residues of amino acids incorporated in proteins are precisely limited because of the presence of only 22 proteogenic amino acids. Nonetheless, the post-translational modification process enlarges the overall chemical pool of 22 natural amino acids by incorporating new functional groups such as carbohydrates, phosphates, methyl, acetate, and many others.[7] At present, more than 200 different types of PTMs have been discovered including glycosylation phosphorylation, acetylation, amidation, methylation and many other (Figure 1.2).[10] Out of which two of them are most common and abundant, i.e. glycosylation and phosphorylation. In the next subsection, I will discuss why these two types of PTMs are more important in functional proteomics.

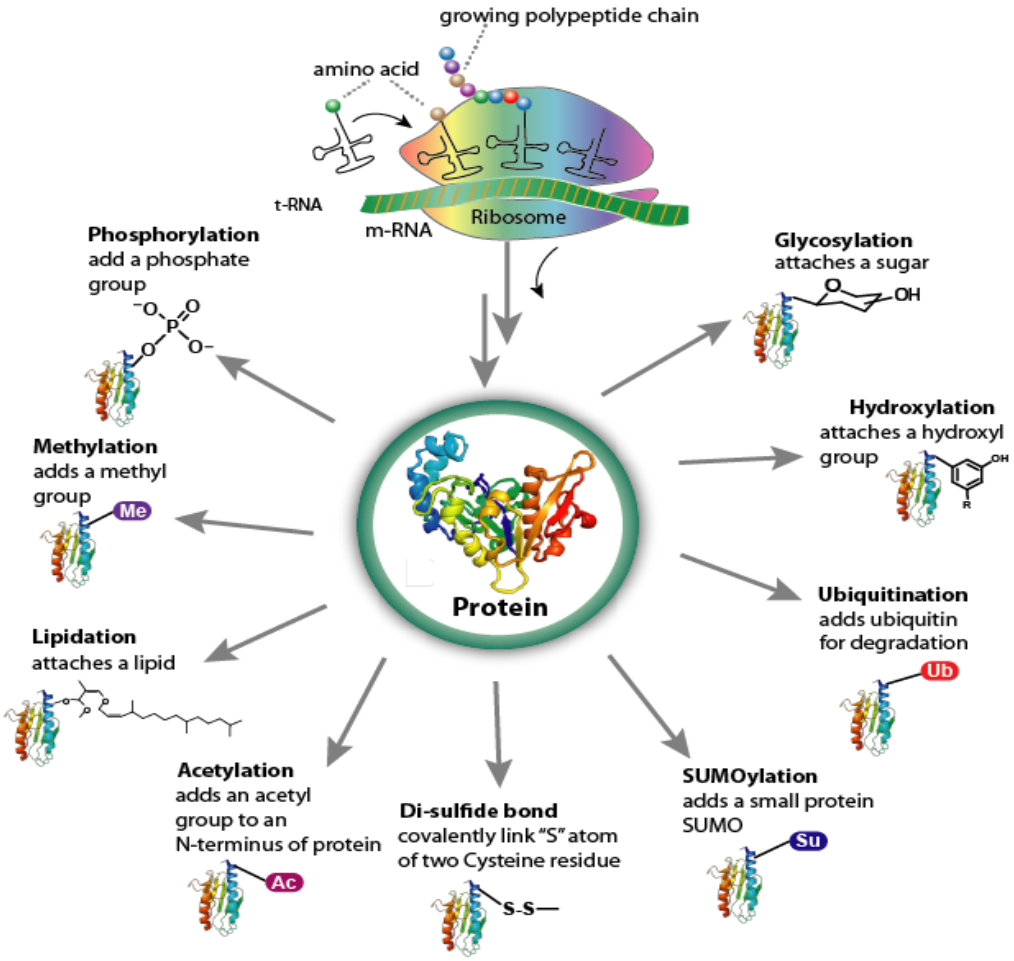

Figure 1.2: Most common types of post-translational modifications (PTM's) of proteins.

1.2.1 Glycosylation

The process of selective attachment of saccharides to the specific parts of proteins, lipids and other organic residues called glycosylation and the products formed are known as glycans.[11-13] Glycosylation is one of the most ubiquitous type of PTM's and approximately 50% of human proteins are expected to be glycosylated. Glycosylation of protein can be divided into four major classes depending on the type of linkage between the carbohydrates and amino acids. They are *O*-linked glycosylation, *N*-linked glycosylation, attachment of glycophosphatidylinositol (GPI) anchor and *C*-mannosylation.[11] In the *O*-glycosylation, a carbohydrate is attached to the hydroxyl group (OH) of threonine or serine amino acids of a modified protein chain. In *N*-glycosylation, the carbohydrate moiety is attached to carboxamido nitrogen (N) of Asn residues, particularly in the tri-peptide sequence Asn-X-Ser/Thr. Intracellularly these two glycosylation processes occur in two distinct regions namely, the Golgi apparatus and endoplasmic reticulum (ER) which produce *O*-linked glycans and *N*-linked glycans, respectively. The glycosylation process in which protein is attached to lipid anchor via

glycan chain is known as GPI anchor attachment. However, there are only a few examples of *C*-mannosylation, as the essential carbon nucleophiles on amino acid side chains are difficult to create.

1.2.1.1 Biological Roles-Physical Properties

Carbohydrates are the unique and diverse biomolecules created by nature together with proteins and nucleic acids. For decades, carbohydrates were simply known as the powerhouse of cell that supplied energy to the body to undergo many biochemical processes. However, many discoveries have been made and theories have been proposed to understand the nature and function of carbohydrates in different fields.[14] Glycobiology is one of the inspired applications of carbohydrate chemistry which is primarily the study of the biology of saccharides (sugar chains or glycans), their structure and biosynthesis, and that are widely distributed in nature.[15-17]

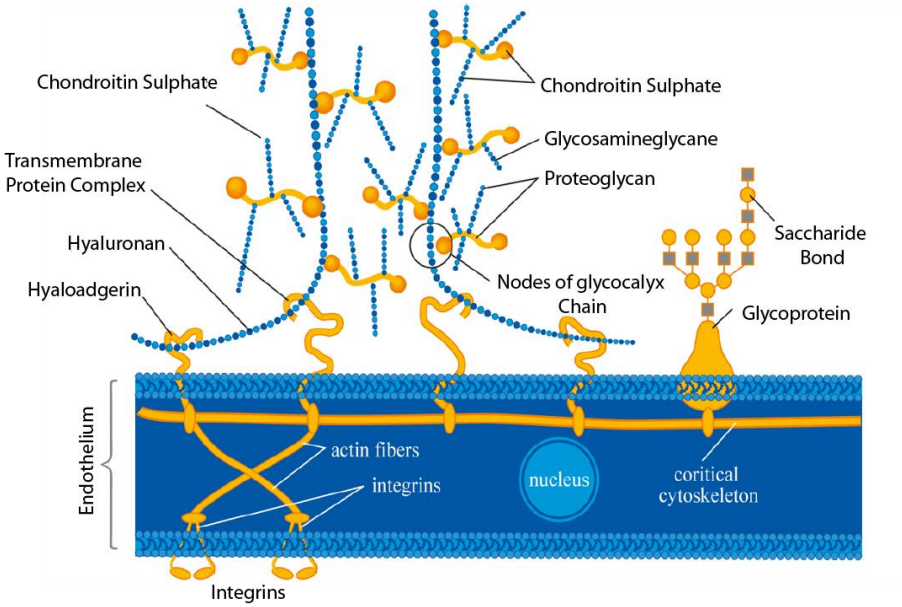

Figure 1.3: A symbolic representation of a glycocalyx chain attached to a cytoskeleton.

A carbohydrate provides benign physical properties to the glycoproteins required for their various important bioactivities *in vivo*. The glycans facilitate proper folding and the stabilization of the conformation of the glycoprotein. Another important function of carbohydrates is to form extracellular polymeric matrix known as 'glycocalyx'[13]. It involves the carbohydrate to covalently bind to lipids and proteins present on the cell surface, and additional glycoproteins and polysaccharides which are non-covalently attached to them (Figure 1.3).[18-20] Glycocalyx is a coat type structure which covers the cell and acts as a first layer of defence against the pathogen. It also plays a major role in

the resistance property of bacteria as it allows bacteria to adhere which create a bio-film that is resistant to various drugs. This property sometimes makes it difficult to counter the bacterial infection. In human body also, the glycocalyx performs important functions of protecting the cells inside the wall of the blood vessels which allows them to withstand the strong flow of liquid across their wall surfaces. It is also present in the apical part of microvilli within the digestive tract, especially in the small intestine, where it provides an additional surface for absorbing nutrients and enzymes secreted by the absorptive cells and helps in the final steps of digestion of proteins and sugars.

Various organs such as the stomach, small intestine, and airways in the lungs need mucus secretion for proper functioning. The mucus is generally secreted by the epithelial cell linings of the body cavity of the organ and mostly consists of the glycoprotein. In the stomach, this mucus served as a protective coating of the cells against the harsh acidic condition needed for the digestion of food. The mucins, when attached to a sugar, will gain reasonable water-holding capacity which makes them resistant to proteolytic digestive enzymes. In the lungs, it acts as a protective mask to trap bacteria and keeps our lungs clean and healthy. Glycoproteins also protect the skin surface by forming a tough barrier through mutual attachment. For example, cadherins is a type of glycoprotein which acts as a glue to hold skin cells together.

Other organisms, such as plants, bacteria, insects, and fish also contain glycoproteins. It can possess a diverse range of chemical structures depending upon which they can show certain characteristic properties. For example, in certain mammals, glycoproteins are known to function as “anti-freeze” protein due to their unique ability to reduce the freezing point of aqueous solutions in a non-colligative manner.[21] This inhibits ice recrystallization to induce dynamic ice and hence may have various applications in cell/tissue/organ cryo-storage, as well as can serve as texture enhancers, frozen food preservatives and cryosurgery.

1.2.1.2 Biological Roles of Carbohydrates as Recognition Elements

On the cellular surface, the glycans are present in the form of glycolipids, oligosaccharides, glycoproteins, polysaccharides and other glycoconjugates. They are the key candidate in performing various important biological recognition processes, such as cell adhesion, cell-cell interaction, intracellular trafficking, immune response, development, pathogen interaction, cancer progression, host- and blood group, etc (Figure

1.4).[14,22] They add another dimension to the proteome complexity by encoding the specific molecular recognition for regulation of protein activity. Therefore, it is not surprising that they act as 'signature,' which defines that what organism a cell belongs to (host or intruder).

For example, the presence of specific glycoprotein on RBC's helps the body to identify its own blood and tells not to attack it. Here the structure of oligosaccharides in glycoproteins and glycolipids are the main determinant of human ABO blood group system and determines which one among them antigenic, more immunogenic than other blood groups systems and plays a crucial role in the transfusion medicine. For the O type blood group, a trisaccharide as H antigen is referred. On the other hand, for the blood group A, a tetrasaccharide with an additional *N*-acetyl-D-galactosamine residue at the C-3 of galactose ring of H antigen is present. A tetrasaccharide with an additional D-galactose residue at the C-3 of galactose ring of H antigen is responsible for the blood group B.

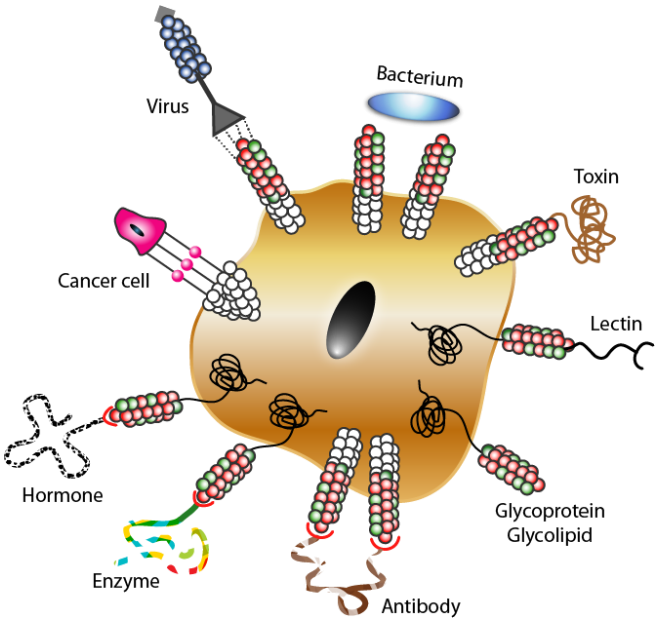

Figure 1.4: Glycans as recognition elements of the cell.

The glycoproteins on the cellular surface are involved in cell signalling process and transmit the information between the cells (signal transduction).[23-28] It has been also recognized that certain N-linked glycoprotein plays a demanding role in hormone signal transduction.[29] Furthermore, the cell surface oligosaccharides present in the host cells can act as receptors for the microbes such as bacteria, virus which use these for adhesion and invasion of the cell.[30] For example, the sialic acid present in host cell surface functions as a receptor to attach the surface of hemagglutinin, present in influenza virus. Further, the

human immunodeficiency virus (HIV) enters the target cells by the sequential interaction (binding) of the glycoprotein GP120 to the CD4 receptors present on the immune cells.[31] This binding induces a series of conformational changes in the structure of glycoprotein GP120 which leads to the fusion of the virus with the host cell membrane.[31]

Specific types of glycoproteins are often highly expressed on the surface of tumors as compared to healthy cells. Such cell-surface carbohydrate markers are the basis for the discovery of new carbohydrate-based vaccines and carbohydrate-based nanocarriers to target several diseases. The most prominent example of a glycosylation sequence which serves as a signal for protein targeting is the mannose-6-phosphate (M6P) sequence on the lysosomal enzymes.[32] The M6P sequence initiates the sequence of sorting of several lysosomal enzymes and helps them to deliver specifically to the lysosomes. Similarly, M6P receptors are highly expressed in an early stage of breast and prostate cancer cells. Also, the glycosylated sequence bears a targeting function, i.e., asialoagalacto-(GlcNAc terminated) and asialo-(Gal terminated) glycoproteins are present on liver hepatocytes and macrophages, respectively.[33] Furthermore, glycosylation influences neuronal function such as neurite outgrowth and their morphology, which helps in modulating physiological events like memory, learning, storage, and transfer.[34] The complexity of glycans also plays the directorial role in neuronal development during embryogenesis.[35]

1.2.2 Phosphorylation

Another ubiquitous form of PTM of protein is phosphorylation, in which an amino acid residue of protein is phosphorylated by the addition of a covalently bound phosphate group. The phosphates play a significant role in biological processes of many organisms, e.g. as a chemical component of plasma membrane (phospholipids), nucleotides (ATP), nucleic acids (DNA and RNA), etc. The reverse of phosphorylation i.e., dephosphorylation is also a crucial process for the spatiotemporal regulation of proteins involved in almost every cellular process.[36] The PTM involves addition or removal of a di-anionic phosphate group somewhere on a protein, which might change its physicochemical properties, dynamics, kinetics, and stability.[37] It regulates the functioning of numerous proteins involved in growth, metabolism, division, differentiation, signal transduction, motility, muscle contraction, organelle trafficking, learning and memory immunity, membrane transport and so on in living organism.[37-42] Subsequently, it also regulates the nature and strength of protein-protein interactions, thereby regulating protein binding and coordinating different pathways.[43,44]

1.2.3 Glycosylation plus Phosphorylation

We have already discussed the enormous amount of biological role played by glycosylation and phosphorylation individually. These two PTMs are the individual candidates for almost every biological process. However, there are some enticing cellular processes, which require the participation of both the PTM's in a concerted manner. For example, cation-independent (CI) mannose-6-phosphate receptor (CI-MPR), which is multifunctional transmembrane glycoprotein and contains both carbohydrate and phosphate groups that are involved in delivery of lysosomal hydrolases from intracellular secretory proteins in the mammalian cells (Figure 1.5). [32]

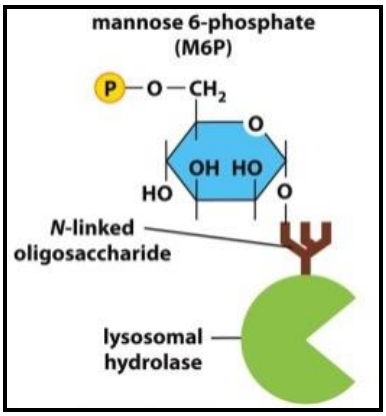

Figure 1.5: Cation-independent (CI) multifunctional transmembrane glycoprotein mannose-6-phosphate (M6P) receptor containing both glycosylated and phosphorylated groups.

1.3 Carbohydrate Binding Proteins

Initial steps in the carbohydrate-mediated cellular processes on cell surface involve several binding events between saccharides and receptors on the surface of other cells and are expected to be highly specific. Carbohydrate-binding proteins (receptors) helps in cell signalling process by binding to extra or intracellular glycans present in different biological molecules such as enzymes, hormones, cytokines, neurotransmitters, cell adhesion molecules, growth factors, etc.[30] These specific types of carbohydrate binding proteins known as lectins are present in all types of organisms and play a key role in extracellular recognition.[45-46] Due to their structural diversities, lectins have been categorised as S-type, I-type, F-type, C-type, P-type etc.[45-47] Galectins are S-type lectin majorly expressed in leucocytes, mostly in activated T-cells, T-regs (regulatory T-cells), macrophages and DCs (dendritic cells).[48-50] They regulate key immunological processes such as apoptosis, cytokine production, intracellular differentiation, and tolerance. This family of proteins display binding specificity for β-galactoside sugars, such as *N*-acetyl-

lactosamine. The I-type lectin Siglecs (Sialic acid-binding immunoglobulin-type lectins) are found on immune cell surface that binds sialic acid.[51,52] F-type lectins specifically bind to the fucose as the key group which undergoes various alterations in several cancer and inflammation.[30,53,54] An example of C-type lectin is asialoglycoprotein receptors (ASGPR) which are highly expressed on the surface of hepatocytic cells (liver cells) which helps to remove the target glycoproteins from circulation.[55,56] The ASGPR overexpression is also perceived in various human carcinoma cell lines such as liver cancer.[57,58] Another important member that belongs to this category is mannose-binding lectin (MBL) which is presents on the surface of pathogenic microorganisms such as bacteria, protozoa, fungi, and viruses.[59] In humans, the mannose-binding receptor MRC2 (mannose receptor C-type 2) is also overexpressed on dendritic cells, macrophages and breast cancer cells (MCF-7/MDA-MB-231).[60,61] In P-type lectin family, there are two important members; one is cation-dependent mannose 6-phosphate receptor (CD-MPR), and the other is insulin-like growth factor II/cation independent mannose 6-phosphate receptor (IGF-II/CI-MPR). They are differentiated from all other type of lectins due to their ability to recognize phosphorylated mannose residues.[32] They play a key role in transporting newly synthesized various lysosomal enzymes carrying mannose-6-phosphate (M6P) signals to lysosomes. The CI-MPR receptors are over-expressed in the initial stages of several cancers such as prostate and breast cancer.

Therefore, lectins plays an important role in several biological functions which include extracellular molecular binding, molecular chaperones during glycoprotein synthesis, intracellular journey of glycoconjugates, self/non-self recognition, endocytosis mediation, cell-cell interactions and trafficking of cell-cell interactions, regulation of cell growth, anti-inflammatory action, urate transport actions and scavenging of cellular waste, etc. They are also helpful in regulation of immune system by involving other biological molecules in trafficking process within the immune system, their enhancements and suppression and finally help in preventing autoimmunity. A key for regulating these important cellular processes lies in the variety of carbohydrate units present on the cell surface together with a large number of copies. The most important concept is the polyvalent nature of carbohydrates.

1.3.1 Polyvalency of Carbohydrates in Biology

All the biological processes involved in proper functioning of cell are basically guided by the specific recognition property of glycoprotein with a variety of corresponding ligands

present on the cell surface cooperative with the number of copies (polyvalent) of such units present. Polyvalent nature of carbohydrates can be defined as the ratio of binding affinity of each ligand in the multimer to monomer.[36] This perspective of multiple interactions with unique collective properties opens up a new door in the field of therapeutic drug delivery and the development of clinical research in biology.

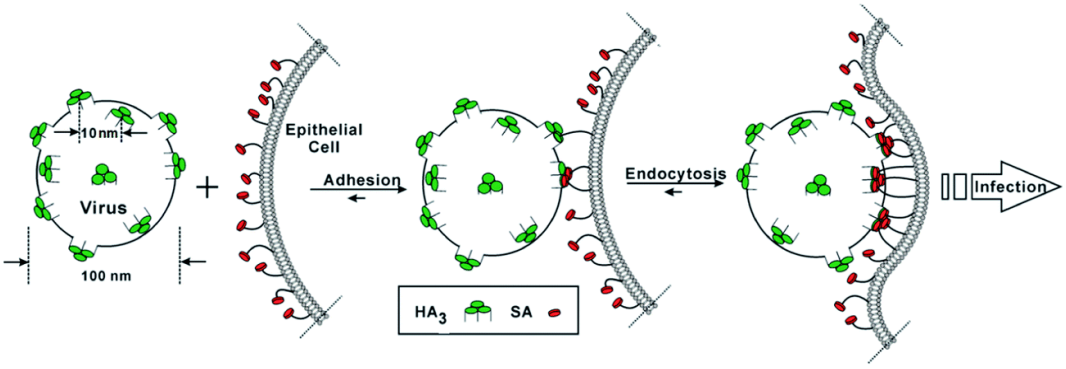

Figure 1.6: Schematic representation for the binding of influenza virus to the epithelial cells (this figure is adapted from publication 54).

Numerous examples of polyvalent interactions are present in biology. One distinguishing example is the infection of an influenza virus to the bronchial epithelial cells (Figure 1.6).[30] At first, the influenza virus attaches by the polyvalent interactions between hemagglutinin (HA, a type of lectin present on the surface of the influenza virus) and multiple moieties of the carbohydrate sialic acid (N-acetylneuraminic acid) that are heavily locate on the surface of epithelial cells. In the early steps of carbohydrate-mediated cellular processes, binding events occur between carbohydrates and specific receptors present on the surface of different cells. However, in the solution phase studies, it is shown that carbohydrate-protein binding interactions are very weak (in the mM range) because different carbohydrate ligand exhibits similar affinities for the same protein receptor. Thus, the origin of the specificity of carbohydrate-protein interaction that mediates specific cellular processes in spite of very weak affinity was ambiguous. This has been partially explained by the phenomenon of polyvalency. Carbohydrate-protein binding events usually involve several simultaneous interactions between carbohydrates that are clustered on cell surfaces and protein receptors that contain multiple carbohydrate binding sites. This is called “Glyco cluster effect” where the binding epitopes displayed on a large platform can saturate the multiple receptors hanging on the receptor and enhance their binding avidities (the synergistic bond strength between multiple ligands and multiple receptors) many folds through what is called the “Polyvalency” (Figure 1.7)[62-67].

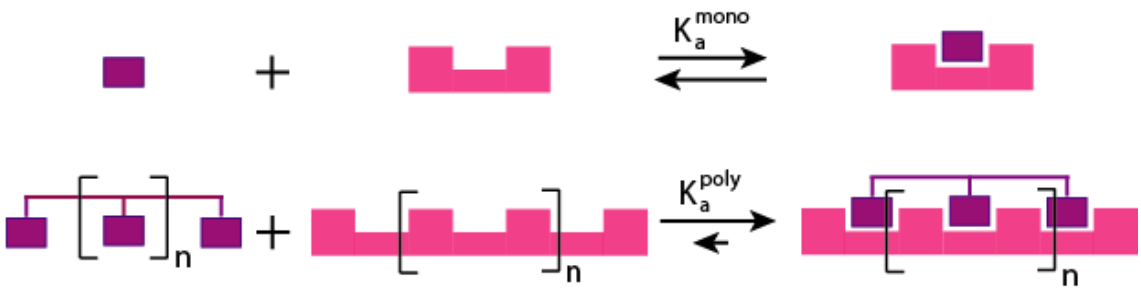

Figure 1.7: Schematic representation of monovalent versus polyvalent binding of ligand to receptor.

1.4 Synthetic Functional Polypeptides Mimic the Functions of Natural Proteins

To understand the functions of a natural protein (glycoproteins) and consequently use them for specific biomedical application, it is necessary to create a route to synthesize structurally defined functional polypeptides (polymers with pendant functional group moieties on a polypeptide backbone). Synthetic functional polypeptides can mimic the molecular composition of natural protein and are expected to mimic their function also (Figure 1.8). As all protein-mediated biological processes depend on specific biomolecular interactions between protein-protein and protein-ligand, by investigating these interactions which are linked with different diseases, a way is generated to understand the molecular mechanisms underlying several diseases and other cellular phenomena. These studies help us for the development of novel therapeutic strategies in the clinical research area.

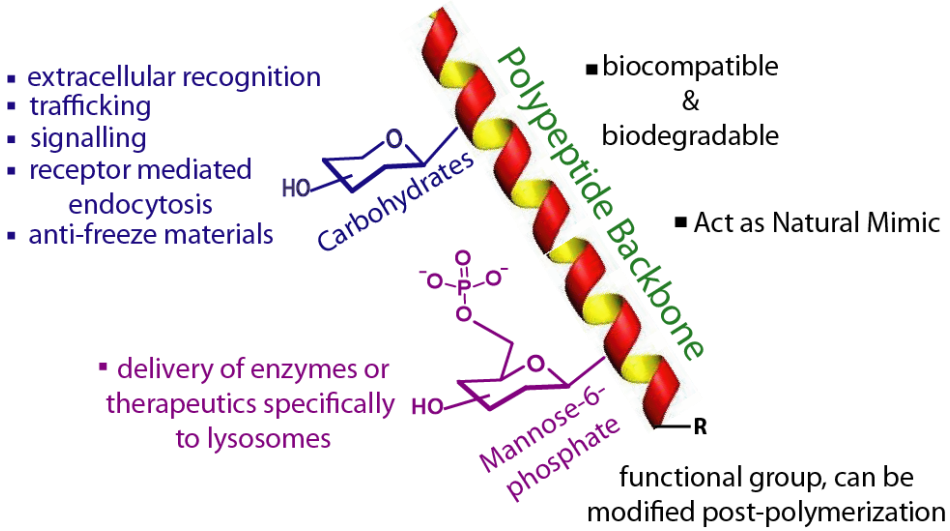

Figure 1.8: Expected application of synthetic functional polypeptides.

The biological molecules which are present on the binding sites of natural proteins and involved in a disease associated protein-protein or protein-ligand interaction are the promising candidates for therapeutic applications.[68,69] These mimetic molecules can be

produced either through chemical peptide synthesis or using recombinant protein synthesis. An important advantage of synthetic peptide involves the formation of an identical replica of specific protein fragments with diverse chemical modifications. These modifications also help to regulate the proteolytic sustainability of the molecules which enhance their use as potential drug delivery vehicles.

Pathogenesis of several diseases involves specific protein-ligand and protein-protein interaction in their earlier stages. Therefore, modified synthetic polypeptides which have the ability to mimic the characteristic protein-binding site and act as potent inhibitors of the interactions can be a promising strategy for therapeutic applications. As synthetic polypeptide-based materials are inherently biodegradable and biocompatible, they are attractive due to their great potential in biomedical and pharmaceutical applications such as drug delivery vehicles and tissue engineering. Moreover, synthetic polypeptides have the ability to form stable secondary structures, such as α-helix and β-sheet like natural protein, which helps them to undergo unique self-assembly processes. Therefore, there is a huge scope for synthetic chemist to generate a library of synthetic functional polypeptides that are structurally as well as functionally similar to natural proteins. These synthetic functional polypeptides could also help us to make soft-biomaterials with unique biological properties through self-assembly process.

1.4.1 Synthesis of Polypeptides

Since many years considerable effort has been made to imitate the structural and functional properties of proteins in synthetic systems. Nonetheless, the preparation of polypeptides by conventional solid phase synthesis is very assiduous, and purification steps are very tedious. The synthesis of high molecular weight polypeptides (> 100 repeating units) with controlled size distribution was also not permissible using this methodology. The ring opening polymerization (ROP) of N-carboxyanhydride (NCA) of amino acids is an economical and highly feasible process for the preparation of long chain polypeptides, especially in comparison to solid-phase peptide synthesis (Figure 1.9).[70] A large scale and rapid production of high molecular weight polypeptides with good yield is the main advantage of this polymerisation. During this chemical process, unnatural modified amino acid and D-enantiomer NCAs can also be polymerized, which allows to introduce exceptional diversity in polypeptide functionality. Beside all advantages, this process also has some shortcomings like the inability to accurately control chain length which results in broad chain length distributions in polypeptides. Moreover, it exhibits

poor control of residue sequence in copolymerizations. All these drawbacks make the synthetic polypeptides as heterogeneous materials, contrary to natural proteins which are obtained as pure molecules. However, recent achievement of living and controlled polymerizations of NCAs allows the synthesis of polypeptides with well-defined chain lengths and of block co-polypeptides with controlled compositions and controlled sequences of respective polypeptide domains.[70] This will allow polypeptide based materials to be more sophisticated mimics of proteins.

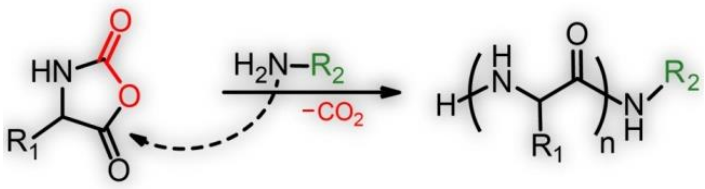

Figure 1.9: Synthesis of polypeptides by ring opening polymerization of *N*-carboxyanhydride.

Current studies are more interested in modification of chemical functionality present on the polypeptide side-chain and led to the synthesis of side-chain modified synthetic polypeptides. Side-chain modifications in the polypeptide affect both functional and conformational properties. In literature, there are two fundamental routes defined for preparation of side-chain modified polypeptides: (1) First route is the direct polymerisation of functionalized NCA monomer, (2) second route is the post-polymerization modification of polypeptide side chain, where various desired functional groups are chemically conjugated to reactive polypeptide side-chains (Figure 1.10).[71]

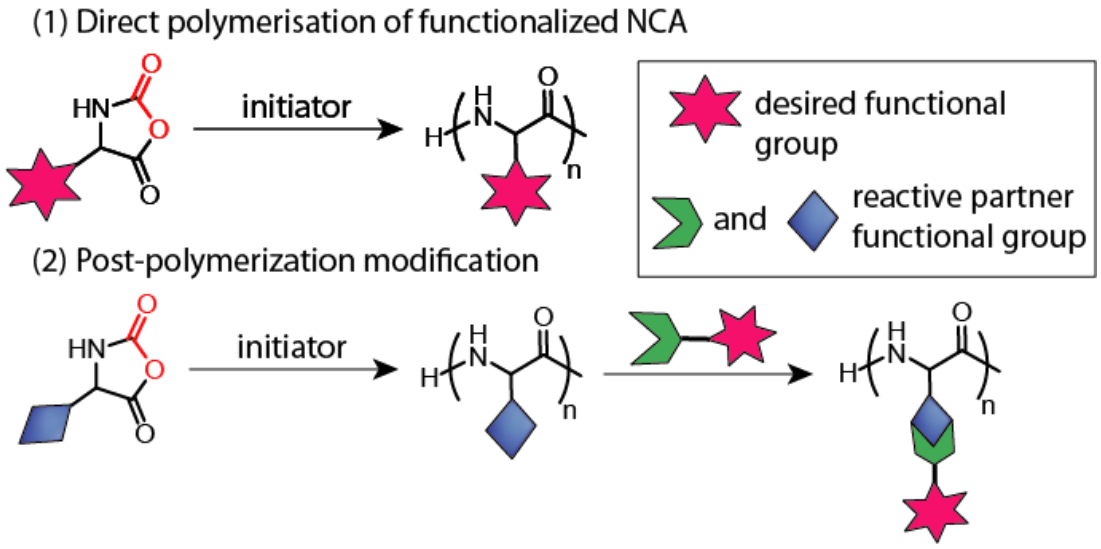

Figure 1.10: Schematic showing two pathways for synthesis of side-chain modified polypeptides.

1.5 Self-Assembly of Amphiphilic Polypeptides

1.5.1 Importance of Polypeptides Self-assembly

Self-assembly represents the spontaneous arrangement of disordered molecules into well-organized structures. Self-assembly of protein in a biological system is unique, and these self-assembled structures possess specific biological function.[72-75] Hence, understanding the self-assembly of the polypeptide is crucial to the current strive of nano-biotechnology because it assists the understanding of the aggregation behaviour of complex polypeptides and that could be extended to protein systems. Moreover, the understanding of supramolecular self-assembly of simple block co-polypeptides permits the formation of hierarchically self-assembled structures that are unique in nature.[76,77] The advantageous parameters of polypeptide block copolymers such as biocompatibility, biodegradability and their self-assembly into various supramolecular aggregates allows them to undergo important bio-medical applications, such as drug delivery and tissue engineering (Figure 1.11).[78]

Conformational transition in several proteins occurs in response to environmental stimuli, generally known as switching mechanism. By understanding such type of induction in protein conformation, this can further be employed in the synthetic polypeptides to control their properties, and resultant materials can be potentially used in the field of stimuli-responsive drug delivery, bio-sensing, tissue engineering, and so-called smart biomaterials. Further, the synthetic polypeptide can be made to behave as stimuli-responsive materials by introducing the diversity in their constituent amino acids. Like natural protein, synthetic polypeptides exist in stable secondary structures, such as α-helix and β-sheet. Therefore, the secondary conformation of polypeptides can be tuned under a specific condition which leads to the formation of well-defined self-assembled structures. Moreover, their scope would be increased if the non-natural amino acids or other small organic moieties are incorporated in them.

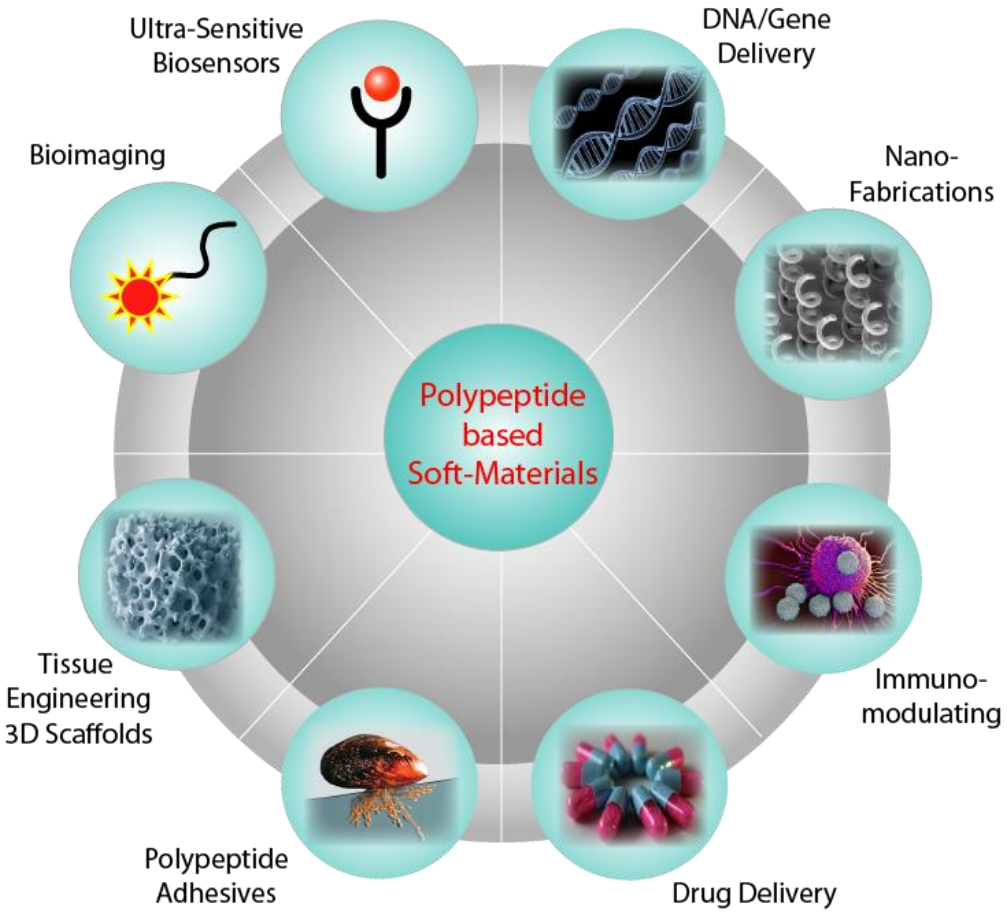

Figure 1.11: Synthetic polypeptide based soft-materials for various applications.

1.5.2 Mechanism of Self-Assembly of Block-Copolypeptides

Amphiphilic block co-polypeptides have the tendency to self-assemble into well-defined nanostructures such as vesicles, micelles, cylinders, or nanofibers in aqueous phase.[80-82] The equilibrium morphology, size and final structure of the self-assembled aggregates is primarily determined by the chemical structure (nature) of the polymer, the relative block length, and concentration of polymer, or depending on environmental factors, such as the temperature, pH, solvent used, and ionic strength.[83-88] The different morphologies achieved are especially an outcome of the inherent molecular curvature and how this affects the overall packing of the copolymer chains in the particular structure. The interfacial curvature basically depends on the relative length of hydrophilic and hydrophobic blocks and nature of hydrophobic block and increases with the hydrophilic weight fraction. Due to this, self-assembly is directed by the balance between entropic freedom of the hydrophilic chains at corona and shielding of the hydrophobic core from the aqueous solution. Therefore, as the hydrophilic weight fraction increases, it helps the assemblies to be more stable without close packing which lowers the overall free energy of the system with increased entropic freedom/mobility of coronal chains through

increased curvature. The morphology obtained after self-assembly of small molecular weight polymer can be understood from dimensionless packing parameter (ρ), (Figure 1.12).[89]

$$\rho = V/a_0.l$$

where V is volume fraction of hydrophobic chain, a_0 is interfacial area and l is the length of hydrophobic chain. If the packing parameter is less than unity ($\rho < 1/3$), it gives spherical micelles, non-spherical micelles, if it is between $1/3 < \rho < 1/2$ gives cylindrical micelles and for $1/2 < \rho < 1$ gives vesicles (Figure 1.12). If ρ is approximately 1 then it mostly gives bicontinuous plane, if ρ is above unity it gives inverted structures (Figure 1.13). This concept can be used to predict of morphologies of amphiphilic block-copolymers. However, the hydrophilic weight fraction ($W_{philic} = f$) is better suited to predict the expected morphology for polymeric amphiphiles.[90-93] It is defined as:

W_{philic} = Mol. wt of hydrophilic block / Mol. wt of block copolymer

It has been proposed that block copolymers, with a hydrophilic fraction (f) > 50% mostly formed micelles while for (f) = (35±10) % mostly vesicles or "polymersomes" and for (f) <25% inverse structure is formed. All these factors finally depend on thermodynamic and kinetic parameters and finally the chemical nature of block copolymer which yields different structures, which might be perfectly fitted with the hydrophilic fraction (f).[94,95]

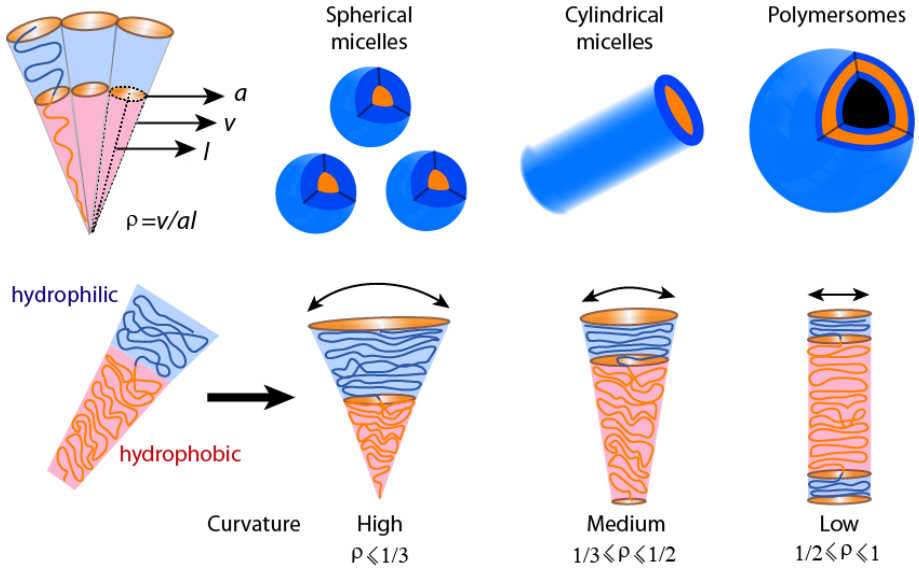

Figure 1.12: Schematic mechanism of self-assembly of amphiphilic block copolymers.

Among various morphologies formed through block copolymer self-assembly, the mechanism of formation of vesicles/polymersomes is better understood (Figure 1.13). It

involves formation via two-step process in which first step is the formation of bilayer structure and in the second step it closes to form a vesicle.[83,96]

Morphology	Packing Parameter (ρ)	W_{philic}
Sphere (Micelles)	1/3	>50%
Cylinder (Worm-like Micelles)	1/2	≈50%
Bilayer (Polymersomes)	1	≤50%

Table 1.1: Correlation of morphology to "packing parameter" and "hydrophilic weight fraction" of the amphiphile.

Initially the amphiphile forms bilayer sheet-like micelles due to the unfavourable interfacial energy of the hydrophobic-hydrophilic interface. Further, if sheet-like aggregates are sufficiently large enough to make interfacial energy predominant, the sheet-like micelles will enclose to form vesicles. Basically, the formation of bilayers is associated with the decrease in entropy due to reduced degrees of freedom of the polymer chains. In polypeptides, the secondary conformations are associated with formational entropy as well as different internal degrees of freedom. For example, α-helical polypeptides have very low internal degrees of freedom in comparison to its random conformation. Due to these factors, a polypeptide with different secondary conformations influences their self-assembly process to form various nanostructures.[97]

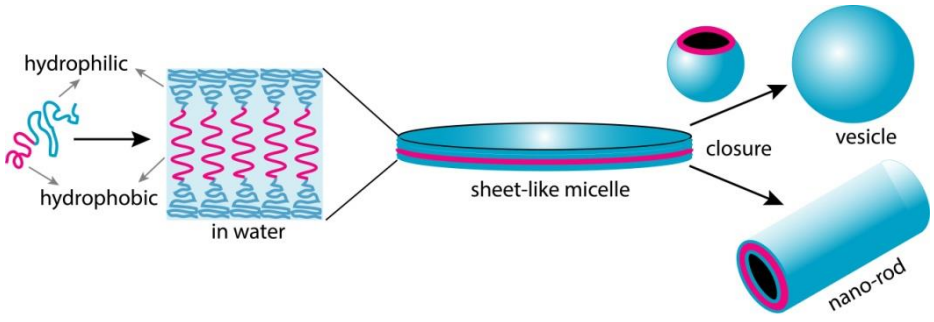

Figure 1.13: Schematic representation of vesicle formation.

1.5.3 Preparation of Block-Co-polypeptides Vesicles

Most common techniques used for the preparation of vesicles are solvent displacement,[98] nano-precipitation method [99] and film rehydration method.[100] Till now, the most common

method used for the preparation of vesicles is the solvent displacement or nano-precipitation method. Initially, the amphiphilic block copolymer is dissolved in an appropriate organic solvent in which both the blocks are perfectly soluble and it is followed by addition of the second solvent (usually water) which solubilises only one block. Usually, this process leads to the formation of aggregated structures when the organic solvent is replaced with the second solvent. Finally, upon the removal of the organic solvent by dialysis self-assembled structures are obtained. Although, this is the suitable method for the formation of self-assembled structures, it still has certain disadvantages like time-consuming removal of organic solvent and is not favourable for the encapsulation of biological molecules such as proteins.

To overcome these limitations, the use of polyion complexes (PICs) can afford a better solution as they are formed in aqueous media without the use of organic solvents, and the preparation process is quite simple. Kataoka et al. were the first to develop a methodology for the formation of PIC structures. They prepared vesicles in aqueous medium from a pair of oppositely charged block or homopolymers namely, PEG-poly(aspartic acid) and PEG-poly([5-aminopentyl]-aspartamide) by virtue of an electrostatic interaction.[101] The preparation of the PICsomes only requires mixing of two oppositely charged block co-polypeptides in an aqueous solution. In addition to vesicles, micellar structures can also be formed by using this technique depending upon the nature and length of block copolymers. (Figure 1.14).[102-108] This method offers a simplified approach to prepare vesicles, but it cannot be considered as general method owing to the limitations of the chemical properties of the polymers. In chapter 2, I will discuss more about this technique of self-assembly.

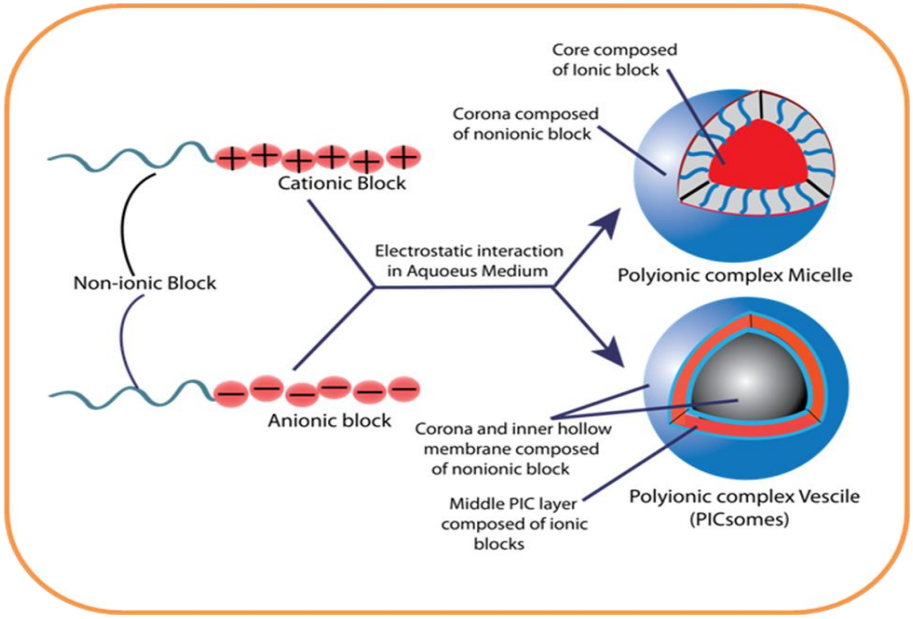

Figure 1.14: Schematic showing formation of polyionic complex (PIC) based nanostructures.

1.6 Nano-Carriers for Drug Delivery

A family of diseases, commonly known as cancer involves abnormal cell growth with the potential to invade or spread in the other parts of the body.[109] With the high mortality rate, it represents one of the major health problems in the world. According to reports in 2012, cancer causes 8.2 million or 14.6% of human deaths globally. There are different forms of cancer; the most common are breast cancer, lung cancer, prostate cancer, cervical cancer, colorectal cancer, etc. The possible treatments for cancer are radiation therapy, chemotherapy, and targeted therapy and finally surgery. Among them, chemotherapy is one of the major treatments. Although various chemotherapeutic agents (anticancer drugs) are used to boost the survival rate of patients their adverse side effects such as leukaemia and cardio-toxicity make them limited for use. This happens due to the lack of specificity of these anti-cancer drugs. Hence, there is a necessity to use these drugs in a different form such as by encapsulating them in nano-vehicles. These nanocarriers not only target tumour cells for the specific delivery of the drug to the tumour site but can also perform for a longer period without affecting normal cells. More simply, nanocarriers render several advantages over free drug-delivery in cancer cells: (a) prevent the drug molecules from other interactions with the biological system (b) protect the drug from premature degradation (c) improve absorption of the drugs into the selected tissue (for example, solid tumour) and d) control the pharmacokinetics or drug tissue distribution profile. EPR-

mediated drug delivery using nanocarriers is currently seen as an effective route to bring drugs to and into tumours.[110]

Nowadays the use of both synthetic and naturally occurring block polymers is highly explored for the drug delivery application. Nano-material comprises of polymeric self-assemblies, polymer conjugates, lipid-based nano-carriers such as liposomes, micelles, dendrimers, carbon nanotubes, and gold nanoparticles including nanoshell and cages are used in a variety of applications in drug delivery, imaging, photothermal ablation of tumours, radiation sensitizers, detection of apoptosis and lymph node mapping .[110,111]

1.6.1 The Concept of Targeted Drug Delivery

As tumour cells grow quickly, they stimulate the production of blood vessels, known as "cancer angiogenesis".[112] The newly formed blood vessels are abnormal in nature and architecture. Due to this, endothelial lining of tumour vessels are much leakier as compared to normal vessels. It leads to abnormal molecular and fluid transport dynamics, especially for macromolecular drugs. Due to this effect, molecules of certain sizes (typically liposome, nanoparticle, and macromolecular drugs) leave the vascular bed and accumulate inside the interstitial space (tumour tissue) much more as compared to normal tissues. Such spontaneous accumulation or "passive" targeting is known as enhanced permeability and retention (EPR) effect (Figure 1.15).[113] It is shown that drug loaded nanocarriers within the range of ~100 nm in diameter can easily leak out of the blood vessels and accumulated in tumour tissues by EPR effect,[114] whereas low molecular weight pharmaceutical agents (free drug) are not able to preserve themselves in tumours for a longer period due to their ability to return to the blood circulation via diffusion process.[115-117] The first clinical trial example of passive targeting using nanocarriers comes in mid of the 1980s, and the first nanoparticle-based product on liposome-protein-polymer conjugation was marketed in the 1990s.[110] Although passive targeting is important for chemotherapy it still suffers from some limitations. Lack of control may induce several problems like multiple drug resistance (MDR), a situation where cells become resistant towards one or multiple drugs which causes failure of chemotherapy.[118,119]

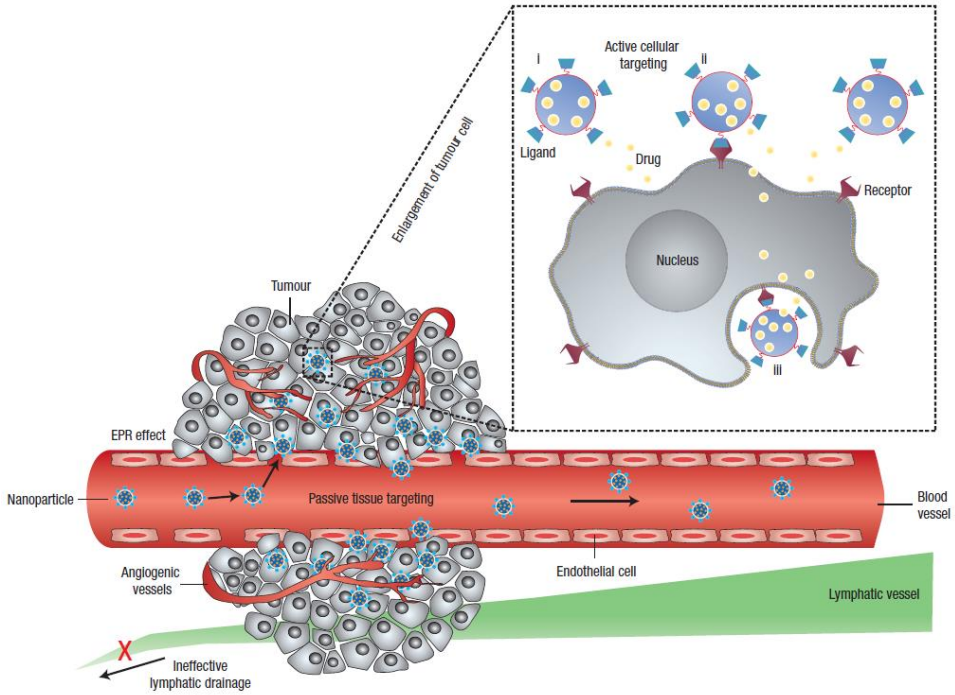

Figure 1.15: Represents the active and passive tissue targeting through the ligand functionalized nanoparticles. (Adapted with permission from ref. 110. Copyright 2007 Nature Nanotechnology).

1.6.2 Active Targeting of Tumour Cells

An important way to overcome the aforementioned limitations is to design a nanocarrier which not only identifies the specific cancer cell but also undergoes internalization before the delivery of drug inside the cell. According to prior discussion, nearly all type of tumours have overexpressed cancer-specific antigen/receptor on their cell surfaces. Hence, a more practical approach would be the specific targeting of these receptors with the ligands (binding groups) located on the surface of nanocarriers. Numerous factors are responsible for attaining effective and targeted drug delivery. Among them, the unique factor is the interactions occurring between the targeting ligand and receptor which are very specific with respect to high binding affinities and avidities. Due to their high specific area over volume ratio in the nanoparticle, it is possible to achieve high ligand density on the surface for targeting purposes. For example, for the efficient delivery of liposome to B-cell receptors by using the anti CD19 monoclonal antibody (mAb), the density of the receptors on the cell surfaces should be ~10^4-10^5 copies per cell. A similar case of breast cancer model requires ErbB2 receptor density of 10^5 per cell for the better therapeutic efficiency.[120] High binding affinity can be achieved through polyvalency of carbohydrates as has been discussed in the 1.3.1 section already. Owing to the property of

polyvalency, the use of carbohydrate containing nano-carrier based drug delivery system has been extensively explored. [116,120,121]

Understanding the nature and behaviour of functional nanoparticles capable of specific biomolecular targeting remains an attractive challenge in nano-biotechnology as there are further implications in clinical trials. Although much advancement has been discussed in the fabrication of carbohydrates-based nano-carriers, still many important aspects remain unclear that need to be addressed fully. These aspects are: how the biomolecular interaction can be probed using carbohydrate as ligand system, how much specificity can be achieved by virtue of carbohydrate residue, probing the co-localization of hydrophilic and hydrophobic molecules in the nanocarriers, and most important is the controlled drug delivery from nanocarriers along with the targeted drug delivery and so on so forth. However, the controlled drug delivery from stimuli-responsive nanocarriers and nanomaterials is extensively discussed in further sections. All these studies about glycopolypeptide based nanocarriers will help such systems to evolve from study level to clinical trials. In my further chapters, I will try to address some of the points mentioned above.

1.7 Stimuli-Responsive Nanomaterials

Challenges present in the field of nanomedicine demand sensitive and efficient approaches, which boost the responses for biomedical applications.[122,123] In this direction, there is a need to develop sensitive nanomaterials, which responds to the biological environments by varying their chemical and physical properties. These materials can efficiently help to detect early sign or a slight change in the disease affected area and hence can serve in the early diagnosis of the complex diseases like cancer and degenerative diseases.[122] These sensitive materials are basically known as stimuli-responsive materials or smart materials, which responds to variety of stimuli such aschemical (pH, redox, ion),[124] biological (small metabolites and large biomolecules such as enzymes),[125] and physical (temperature, mechanical force, and electric/magnetic fields).[126] By controlling the rate of an applied stimulus, they can be used for various types of application such as controlled/triggered/targeted drug delivery,[127] tissue engineering/ cell culture,[128] biosensors,[129] chemo-mechanical actuators[130-132] and environmental remediation.[133]

To develop stimuli-responsive nanomaterials, multifunctional polymers are heavily explored for various applications like controlled release nano-materials/biomaterials,[134-137] self-healing materials,[138,139] shape memory materials[140,141] and catalysis.[142,143] As discussed in the previous section, nanotechnology or nanoscience provides ways for treatment of various diseases by presenting novel nanosystems like vesicles, micelles, dendrimers, liposomes, among others to transport many biologically active agents like drugs, proteins, and DNA. Their efficiency towards controlled delivery can be improved by converting them into stimuli-responsive (multifunctional) or smart nanomaterials. A response from the smart nanocarriers allows their enhanced localisation in the appropriate biological region and controlled release of cargo at the desired location. The important feature of this type of materials is their reversible nature - the property of polymer to rebound to its initial state when the counter trigger is applied. Upon applying stimuli, these nanosystems respond by the change in polymer architecture, conformation of polymer and their solution properties, which can also vary their macroscopic behaviour and finally disrupt the assembly (Figure 1.16).[145,146] The biological system has the inherent property of regeneration, self-healing and can reproduce in organised although complicated manner. This unique property of the biological system is due to the presence of natural polymers like nucleic acid and protein/polypeptides. Natural biopolymers possess specific stimuli-responsive constituents which undergo abrupt and strong conformational changes at some critical condition. They also show stability against a broad range of external stimuli inside the biological system.[147, 148] By understanding the behaviour of natural stimuli-responsive polymers, several synthetic smart polymers can be designed to mimic their adaptive behaviour.

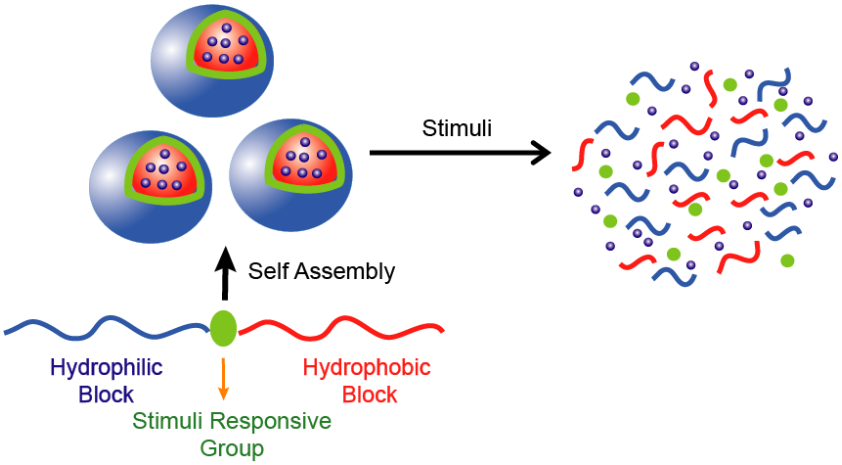

Figure 1.16 Schematic representation of degradation of nanostructures in presence of stimuli with the release of encapsulate molecules.

1.7.1 Smart Polypeptides-based Nanomaterials for Drug Delivery

Stimuli-responsive drug delivery is one of the developing areas in the field of smart nanomaterials for the controlled and triggered drug delivery. As discussed in the previous section that polypeptides are important building blocks for designing variety of biomaterials because of their biocompatibility, biodegradability and ability tomimic natural proteins.[140-150] Over past decades, a lot of research has been done on the advancement of synthetic polypeptides in the biomedical field and for this purpose stimuli-responsive well-defined synthetic polypeptides (''smart'' polypeptides) along with the incorporation of different functionalities have been extensively explored.[151-156] Responsive polypeptides tend to undergo conformational changes and phase transition followed by variations in the chemical and physical properties of the polypeptides in response to an external stimulus such as the environment (i.e. temperature, pH), biologically relevant species (i.e. biomolecules), irradiation with light or exposure to a magnetic field (Figure 1.17).[155,156] In response to physiologically relevant stimuli, conformational changes occur in the polypeptide chain in the self-assembled nanostructures, which lead to disruption of secondary interaction (hydrogen bonding, hydrophobic effects and electrostatic interactions), therefore they have many advantages over other systems in gene and drug delivery applications.[157-160] Another type of response can change the polymer structure either by bond breaking or bond forming in the main chain or in the pendant chain by crosslinking reaction, acid-base reaction, or redox reactions among others.[144,160]

It is well known that cancerous cells have different internal environment as compared to normal cells towards various factors like pH, redox, and others.[157-164] Large amount of research has been already done on the application of these polymer nanoassemblies as drug delivery vehicles for cancer diagnostics and therapy. During cancer therapy (chemotherapy), the loaded anticancer drugs do not differentiate between normal cells and affected cells leading to the death of normal cells. As discussed in section 1.6.1 that nanocarriers preferentially accumulate in and target the tumour cells by Enhanced Permeability and Retention (EPR) effect[113] rather than the healthy tissues. To reach the targeted area, these polymer assemblies should be stable under circulation and should release the drugs in a controlled and targeted manner. To achieve this, polypeptide-based assemblies should have both stimuli-responsive and targeted groups. As the targeted carbohydrate groups are already discussed in above section, here main focus is on the

polypeptide containing stimuli-responsive component. In the following sections, all types of polypeptide-based stimuli-responsive systems that are helpful in formation of smart nanocarriers are briefly discussed.

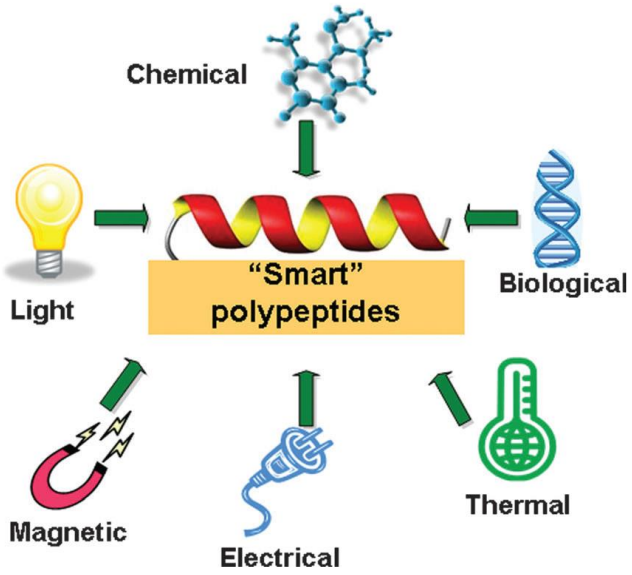

Figure 1.17: The range of stimuli-responsive synthetic polypeptides (Adapted with permission from ref. 156. Copyright 2013 Royal Society of Chemistry).

1.7.1.1 Redox Responsive Systems

The design and synthesis of redox (reduction-oxidation) responsive polypeptides is usually done by incorporating disulfide linkages in the main chain, at the side chain, or in the cross-linker during self-assembly.[165] The disulfide linkage can be readily and rapidly cleaved in a reductive environment mostly in the presence of the most abundant intracellular reducing molecule namely, glutathione (GSH, c-glutamylcysteinyl-glycine).[166] GSH concentration is substantially higher in intracellular environment (1-10 mM) in cancerous cells as compared to extracellular environment (2 µM in plasma) which leads to selective intracellular release.[163] Also, GSH is overexpressed in some of the cancer cells like lung cancer cells because of which its level is 6-7 fold higher in tumour cells as compared to that in normal cells. The high stability under extracellular physiological conditions and their selective disulfide cleavage make these redox-responsive polypeptides promising candidates for the development of sophisticated delivery systems for DNA, siRNA, antisense oligonucleotide (as ODN), proteins, anti-cancer drugs.[163,167]

One example is the incorporation of the disulphide bond in a polypeptide chain developed by Kataoka and co-workers. They prepared PEG-detachable micellar systems using PEG

bearing disulfide linkage as a macroinitiator in NCA polymerisation and form novel redox-sensitive PEG-SS-poly[N-(2-aminoethyl)-2-aminoethyl]-α,β-aspartamide] and PEG-SS-poly(α,β-aspartic acid) polypeptides (Figure 1.18).[168]

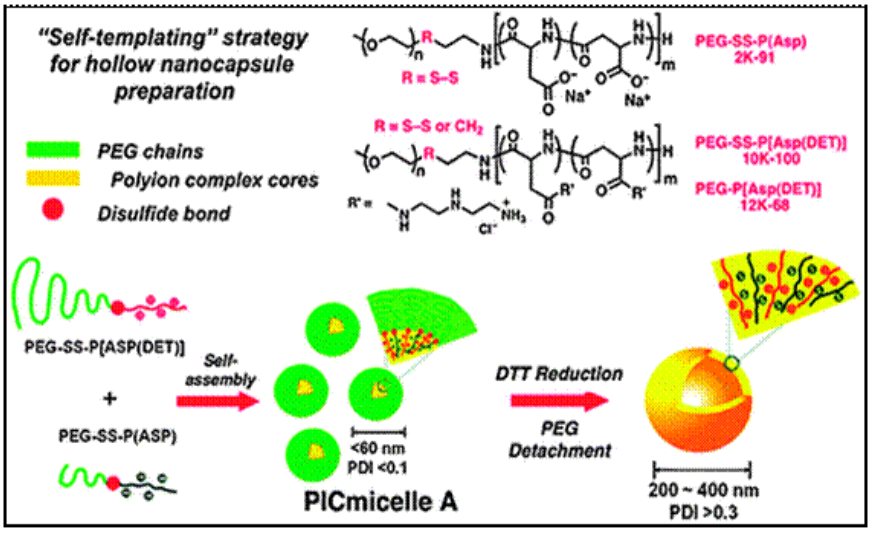

Figure 1.18: Disulfide containing PEG-detachable polyionic complex (PIC) micellar systems (Adapted with permission from ref. 168. Copyright 2009 American Chemical Society).

Another example is the incorporation of the disulfide bond in self-assembled polypeptide structures via self-crosslinking in cysteine polypeptides by oxidation of thiol groups in the air or by using thiol based crosslinker (Figure 1.19)[169] since crosslinking in the nanostructures such as micelles could enhance their stability in the *in vivo* intracellular environment. Crosslinking can be introduced in the hydrophilic, hydrophobic or interfacial region in the micellar system. Pioneering work has been done by Wooley and co-workers and also by Armes and co-workers in the field of crosslinking in the micellar assemblies to address their stability issue. They also showed that crosslinking provides another advantage by incorporating different stimuli-responsive groups in the micellar system for the controlled delivery of drugs.[170]

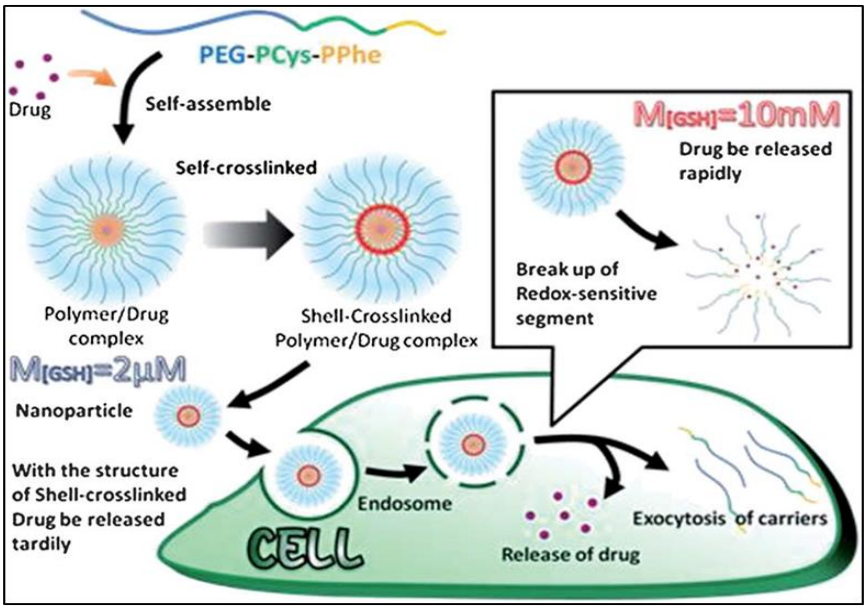

Figure 1.19: Incorporation of disulfide linkage via intramicellar shell crosslinking in cysteine-based polypeptide micelles (Adapted with permission from ref. 169a. Copyright 2012 Royal Society of Chemistry).

1.7.1.2 pH-Responsive Systems

The extracellular pH in tumoral tissues is acidic (~5.7) and is lower than normal physiological pH (7.4) of the human body.[157,171,172] Also, the pH of intracellular compartments such as the endosomes and lysosomes (pH 4.5–6.5) is also much acidic than the extracellular environment (pH 7.4).[172] Hence, the synthesis of pH-responsive polypeptides is important for drug delivery systems, where they can be exploited to trigger the release of a drug from nanocarriers in response to lower pH.[173] In response to the pH of the surrounding environment, amine or carboxylic acid groups in the side chain of polypeptides undergo protonation and deprotonation process. These processes lead to reversible transitions in polypeptide conformation and also change their self-assembly behaviour, and further affect the solubility and aggregation. Therefore, polyelectrolytes such as poly(lysine)[174] and poly(glutamic acid)[175] have been extensively used as the building block for the preparation of pH-sensitive polypeptides -based nanocarriers, which show the pH-driven solubility in response to pH around their pKa. Another option for preparing pH-responsive block co-polypeptide is by introducing acid labile groups in the polymer backbone.[176]

Deming and co-workers first reported a pH-responsive vesicle by using poly(N_{ε}-2-[2-(2-methoxyethoxy) ethoxy] acetyl-L-lysine)$_{160}$-b-poly(L-leucine$_{0.3}$-co-L-lysine$_{0.7}$)$_{40}$ ($KP_{160}(L_{0.3}/K_{0.7})_{40}$) (Figure 1.20).[177] The formation of pH-responsive vesicles with a

hydrophobic $P(L_{0.3}/K_{0.7})_{40}$ layer and hydrophilic KP_{160} inner and outer shells was demonstrated in the presence of Fura-2 dye at pH 10.6. When the pH was reduced by the addition of acid the vesicle membranes were disrupted rapidly, resulting in the release of the encapsulated Fura-2 dye. Other pH-responsive polypeptide-based materials are reported using block copolypeptide composed of glutamic acid, leucine, lysine, arginine, histidine and phenylalanine.[178]

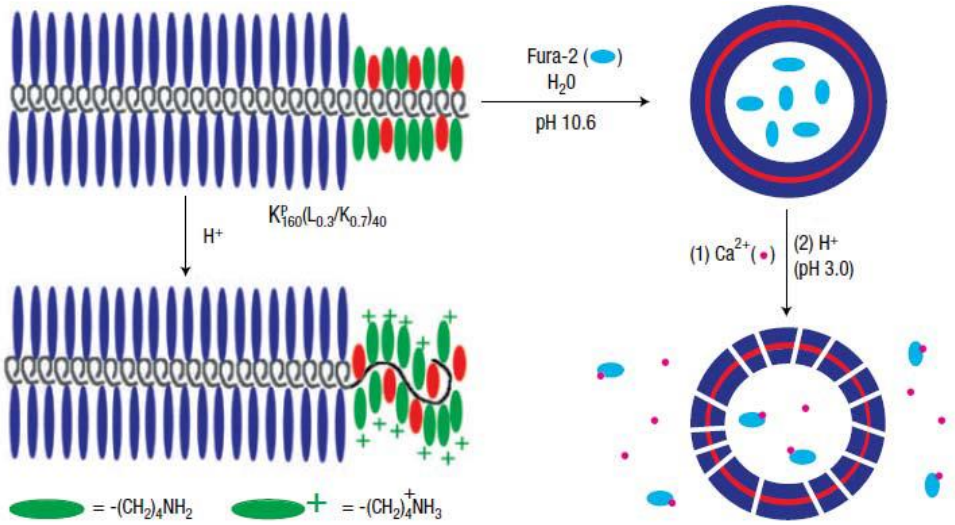

Fig. 1.20: Represented the pH-responsive polypeptide based vesicular structure which rupture to release the encapsulated molecules (Adapted with permission from ref. 177. Copyright 2004 Nature Materials).

1.7.1.3 Enzyme-Responsive Systems

Enzymes play an important role in various biological and metabolic processes inside the cell. The main advantage behind the use of enzyme as a trigger for the stimuli-responsive polypeptides is that most of the enzymes catalyze several chemical reactions under moderate conditions (low temperature, neutral pH, and buffered aqueous solutions), where many conventional chemical reactions fail. Trigger for the enzyme-responsiveness can be (1) dysregulated enzymes in the diseased tissue (*e.g.*, overexpressed MMPs in most tumor tissue) (2) reversible or irreversible changes in chemical structures and functional properties of polymeric nanomaterials in response to specific enzymes. Nano-assemblies from block copolymer can be rendered enzyme responsive by incorporating enzyme-responsive linkers of moieties in the main chain or in the pendant groups which are recognized by a specific enzyme (biocatalyst). This recognized site is further cleaved during the enzymatic reaction, and nanomaterial is programmed to release the cargo with spatial and temporal control.[179] Recently, Wooley and co-workers reported enzyme-

responsive polypeptide-based hydrogelator, methoxy poly(ethylene glycol)-block-poly(L-alanine-coglycine- co-L-isoleucine) (mPEG-b-P(A-G-I)), synthesized by statistical terpolymerization of α-amino acid N-carboxyanhydride (NCA) monomers of L-alanine, glycine and L-isoleucine. This termonomer mixture was selected for statistical incorporation of matrix metalloproteinase (MMP) MMP-2 and 9-active G-IAG cleavage sites.[180]

1.7.1.4. Multiple Stimuli-Responsive Systems

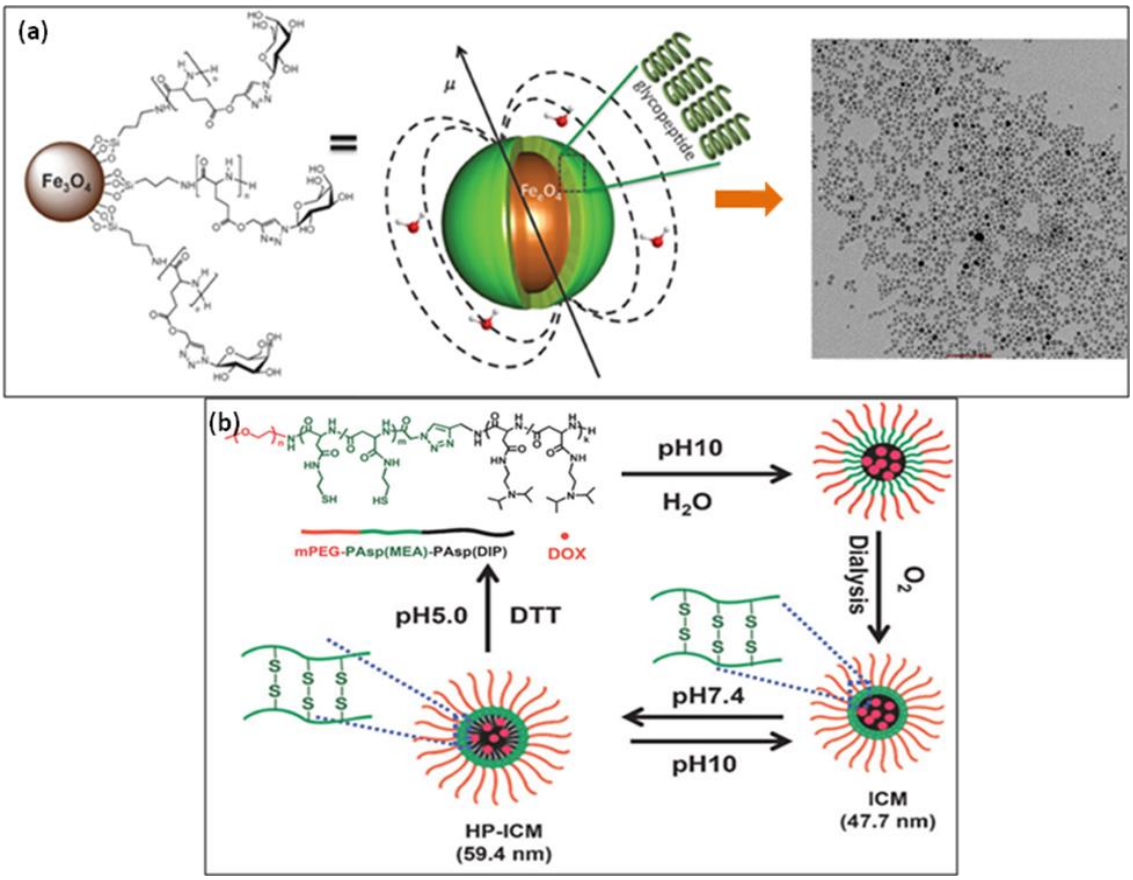

Figure 1.21: Multiple stimuli-responsive polypeptide based nanocarriers. (a) Novel glycopeptides grafted superparamagnetic Fe_3O_4 nanoparticle (Adapted with permission from ref.183 © 2013 WILEY-VCH Verlag GmbH & Co. KGaA, Weinheim) (b) Dual stimuli-responsive (pH and redox) interlayer crosslinked polypeptide micelles (Adapted with permission from ref. 182 © 2011 WILEY-VCH Verlag GmbH & Co. KGaA, Weinheim).

In the quest to bring advancement in stimuli-responsive drug delivery systems, there is a need to prepare the smart nanomaterial which can respond to a combination of two or more signals simultaneously. It will not only increase the efficacy of drug therapies but also support the diagnosis of diseases by monitoring various physiological changes at a

time. The dual stimuli-responsive systems are best suited for theranostic (combination of diagnostic and therapy) application, where one functionality can provide early site diagnosis of disease while other is responsible for treatment. Thus, the availability of various physical, chemical, and biological stimuli is necessary for multiple responsive systems.[136,181] For example, a redox and pH-sensitive interlayer crosslinked polypeptidic micelles showed a triggered disassembly and a burst release of doxorubicin in the reductant-rich and acidic environment, resulting in an *in vivo* improvement of the therapeutic efficacy of the loaded drug (Fig. 1.21b).[182] Recently, novel glycopeptides grafted superparamagnetic Fe_3O_4 nanoparticles have been synthesized (Fig. 1.21a).[183] The grafted particles have high sugar density, which shows the bioactivity whereas T1-weighted MRI property shows its magnetic responsivity.

1.8. Glycopolypeptide based Nano-Carriers

As previously described, carbohydrates are important in several biological processes like cell to cell signalling, cell adhesion and proliferation hence they can be suitable candidates for the drug delivery process as ligand moiety on the surface of nanocarriers. For the purpose of designing such polymer-based targeted drug delivery carriers, there is a need to understand the specific recognition property and control of cell physiology by carbohydrates. This requires polyvalent carbohydrates so that they mimic natural glyco-conjugates such as glyco-proteins and glyco-lipids.[184-186] For this, there is necessity to synthesize carbohydrate containing macromolecules which has polyvalent nature. However, synthesis of carbohydrate containing macromolecules such as glyco-dendrimers or complex glycoconjugates is time consuming and involves multi-step synthesis. Beside this, the synthesis of amphiphilic glycopolypeptides by ring opening polymerisation of amino acid NCAs are more favourable because they are synthesized from their corresponding monomers by one-step polymerization. They also exhibit secondary conformation and due to this they can be self assembled into precise nano-structure by simple procedures. Since the self-assembly occurs in the presence of therapeutic molecules, they can be encapsulated inside the assemblies and then finally delivered at the targeted/specific location.

Heise and co-workers demonstrated amphiphilic post-glycosylated polypeptides poly(γ-benzyl-*l*-glutamate)-*b*-poly(galactosylated propargylglycine) for the preparation of biologically active polymersomes (Figure 1.22).[187] These amphiphilic glycopolypeptides

are synthesized by functionalization of poly(γ-benzyl-*l*-glutamate)-*b*-poly(propargylglycine) block copolymer with azido glycans by using click chemistry. However, it should be noted that there are several limitations involved with this post polymerization glycosylation as described earlier.

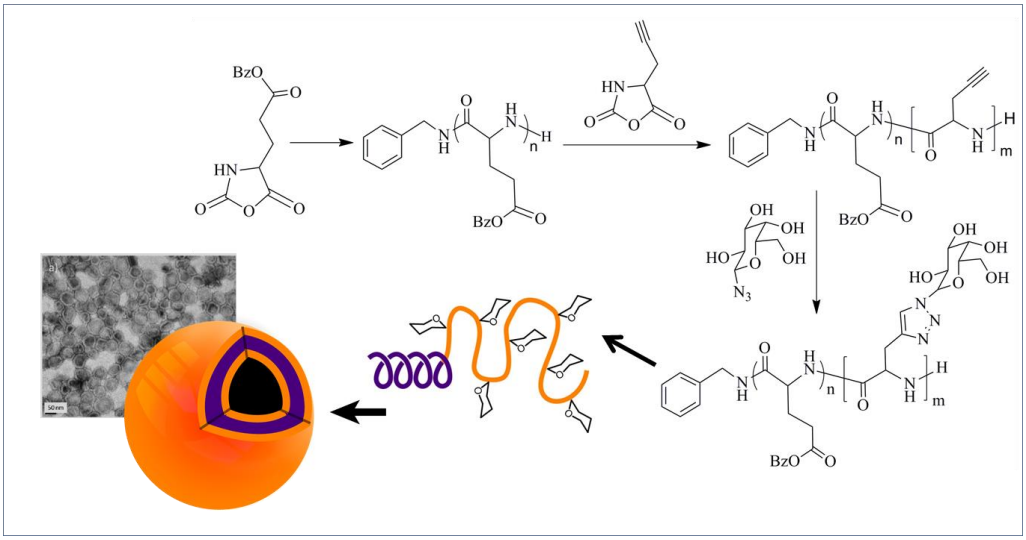

Figure 1.22: Represented chemical structure produces the corresponding nano-structures imaged by TEM (Adapted with permission from ref. 187. Copyright 2012 American Chemical Society).

The research group of Dr. Sayam Sen Gupta at NCL demonstrated the preparation of self-assembled nanostructures with a range of 1D to 3D topologies afforded by amphiphilic dendron–glycopolypeptide conjugates (Figure 1.23).[188] The synthesis of block copolymer involves conjugation of azide end functionalized glycopolypeptide block with alkyne-terminated hydrophobic wedge-like dendron block using click chemistry. The resultant block copolymers selectively afford various glycosylated morphologies such as nano-rods and micelles in aqueous solution, organogel in DMSO simply by varying the molecular parameters of both the blocks. The availability of surface carbohydrate groups on these nanostructures was also demonstrated by lectin binding interaction.

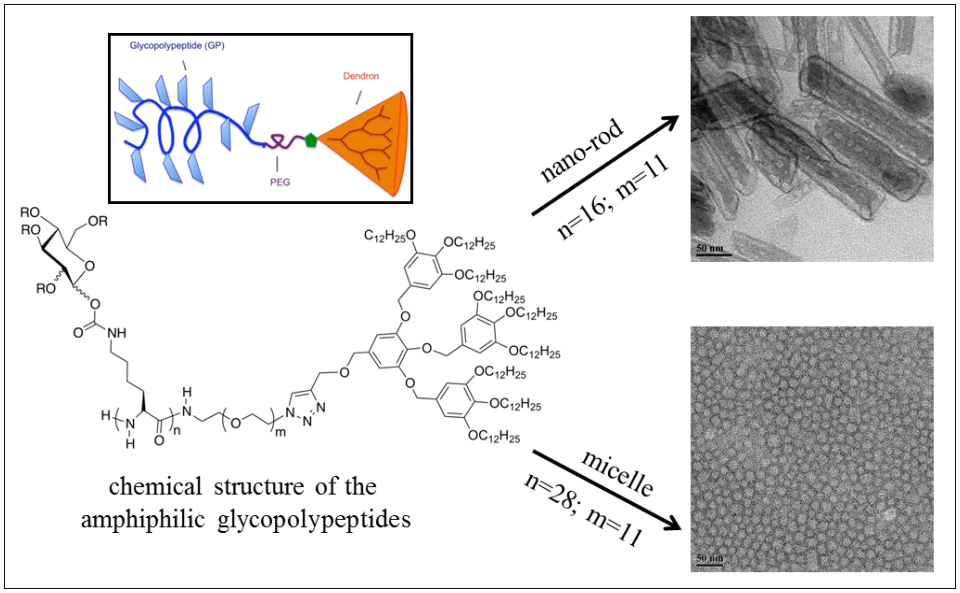

Figure 1.23: Represented chemical structure produces the corresponding nano-structures imaged by TEM (Adapted with permission from ref. 188. Copyright 2012 American Chemical Society).

Das et al. demonstrated the formation of glycopolypeptide-based polymersomes from the self assembly of amphiphilic glycopolypeptide-b-poly(propylene oxide) (GP-PPO) block copolymer (Figure 1.24). They showed that presence of an ordered helical glycopolypeptide segment is required for their self-assembly into spherical nanoscale (~50 nm) polymersomes. Spectrally resolved fluorescence microscopic techniques were used to visualize individual polymersomes and effectively probe the co-localization of dyes and energy-transfer behaviour. The availability of surface galactose groups on these polymersomes was also demonstrated by lectin binding interaction, which reveals the bioactivity.[189]

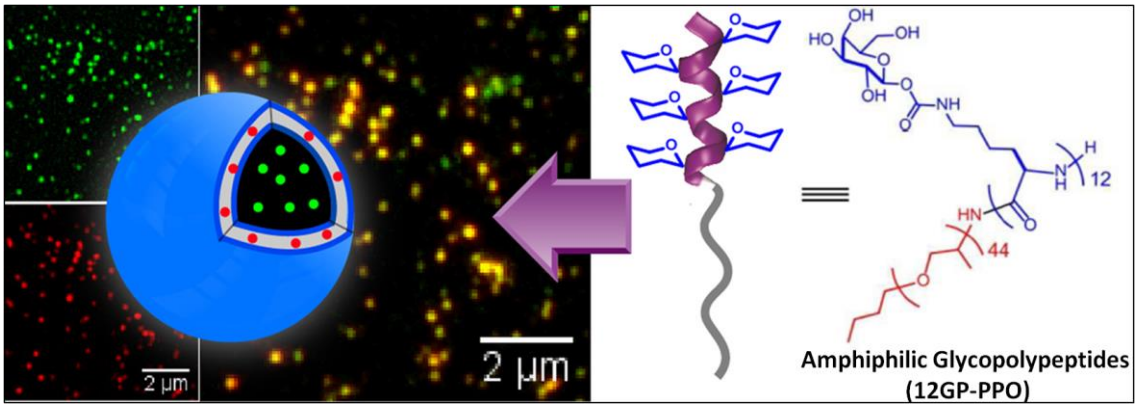

Figure 1.24: Schematic illustration of bioactive amphiphilic glycopolypeptide-b-poly(propylene oxide) GP-PPO based polymersomes for dual dye encapsulation studies (Adapted with permission from ref. 189. Copyright 2015 American Chemical Society).

Pati et al. demonstrated the preparation of AB_2 type glycopolypeptide-poly(ε-caprolactone) based star block copolymer with tunable nanocarriers morphology such as micelles, rods and vesicles were obtained by varying copolymer chain length in aqueous solution (Figure 1.25).[190] They showed that formation of nanocarriers was attributed to the dynamics between hydrophilic−hydrophobic ratio, helical nature of GP block, and crystalline nature of PCL. Carbohydrate specific cellular uptake of vesicles and nanorods was observed independent of solution morphology making them potentially useful for receptor-mediated drug delivery.

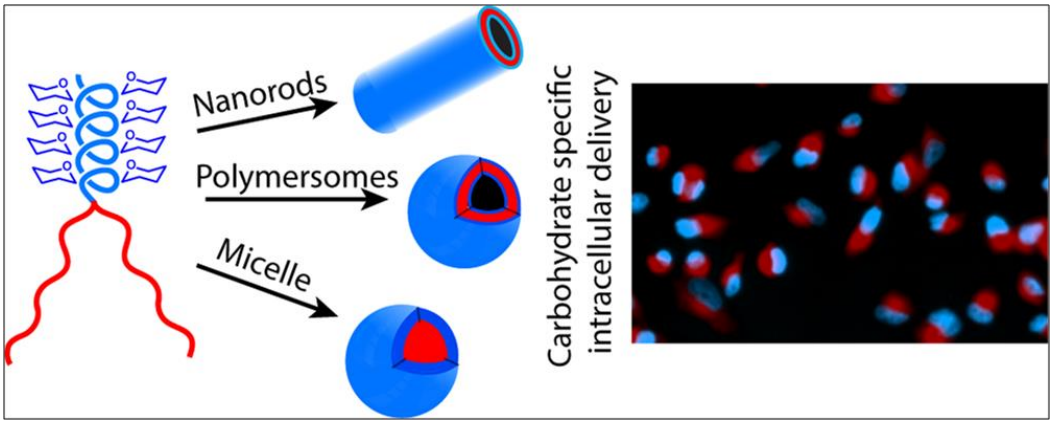

Figure 1.25: Schematic illustration of glycopolypeptide based star polymer into different nanostructures obtained by tuning hydrophilic and hydrophobic polymer chain length (Adapted with permission from ref. 190. Copyright 2016 American Chemical Society).

As there are major challenges present in the field of therapeutic research such as controlled and targeted drug delivery to the disease affected area it demands the development of nanocarriers which show the site-specific targeting along with the controlled release of drugs and without any adverse effect on normal cells. For intracellular targeted drug delivery, glycopolypeptides-based nanocarriers play an important role as discussed in previous section. For controlled delivery of therapeutics, a stimuli-responsive polymer plays an essential role and is also described in section 1.7. Few literature reports are available wherein effect of glycopolypeptide as both the targeting groups and stimuli-responsive groups for controlled drug delivery are described in the individual nanocarriers. For example, Jan and co-workers developed the synthesis and self-assembly pH-responsive of lactobionolactone-conjugated poly(L-glutamic acid)-b-poly(L-phenylalanine) amphiphilic block copolypeptides (Lac-PGA-b-PPhe). The amphiphilic glycopolypeptides self-assembled into bioactive galactose-coated micelles that encapsulate anticancer drug (DOX) and effectively release it under pH-sensitive condition. The saccharide-conjugated micelles were found to effectively bind to the

tumour cells via the asialoglycoprotein receptor-mediated (ASGPR) recognition and subsequently showed higher cellular uptake towards HepG2 liver cancer cells (Figure 1.26a).[191] Further, Jiang and co-workers demonstrated the synthesis and self-assembly of reduction sensitive amphiphilic poly(ε-caprolactone)-b-glycopolypeptides (PCL–SS–GPPs) as a diblock copolypeptides. The disulphide containing self-assembled galactose and lactose decorated micelles loaded with DOX and SPIO showed controlled drug delivery and efficient MRI contrast behaviour (Figure 1.26b).[192]

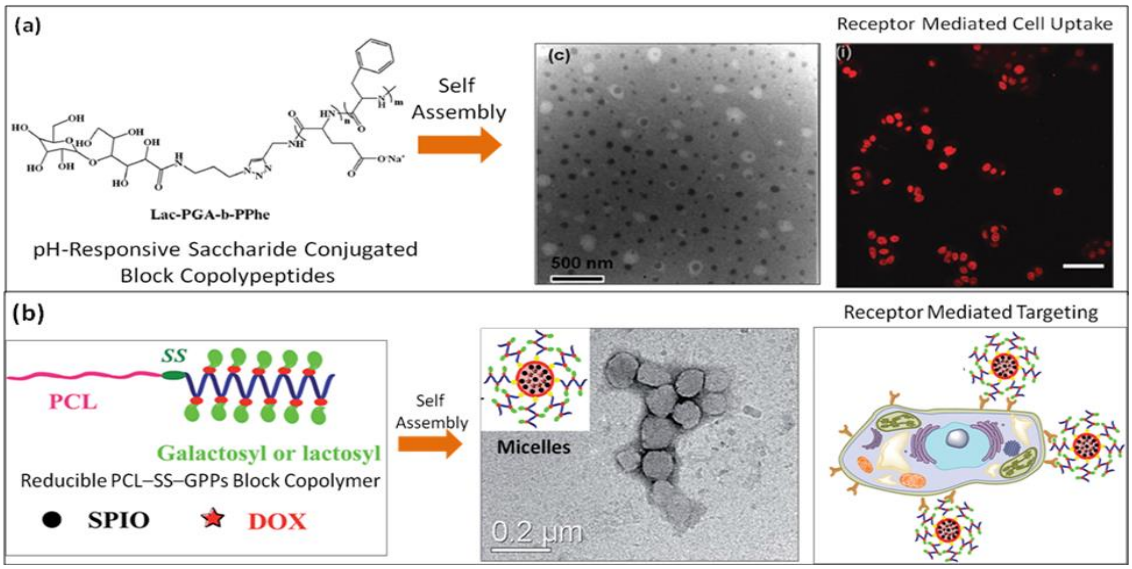

Figure 1.26: Represented chemical structure of glycopolypeptide based stimuli-responsive block polymers produce the corresponding nano-structures. (a) pH-responsive Lac-PGA-b-PPhe block copolypeptides form micelles (Adapted with permission from ref. 191. Copyright 2015, Royal Society of Chemistry). (b) Bioreducible PCL–SS–GPPs amphiphilic glycopolypeptide based micelles receptor mediated drug delivery and efficient MRI contrast property (this figure is adapted from the reference 192).

1.9 Summary of Individual Chapters

The literature survey reveals that polypeptides are the mimics of natural glycoproteins. They exhibit secondary structure and are biodegradable and biocompatible. In particular, amphiphilic glycopolypeptides can be self-assembled into various morphologies like micelles, vesicles, rods that are of great interest as targeted drug delivery vehicles and nanoreactors. Introduction of more than one stimuli-responsive group into the amphiphilic glycopolypeptide renders the resulting assemblies capable of programmed and controlled delivery of encapsulated cargo in combination with the targeted drug delivery. There is wide scope for design and development of novel stimuli-responsive glycopolypeptide architectures for exploration of solution morphologies as smart drug delivery systems. Considering the many opportunities for design and synthesis of glycopolypeptides-based self-assembly in solution

towards controlled and targeted drug delivery applications, in the present work I have focused on synthesis of amphiphilic smart glycopolypeptides and explored their self-assemblies for biomedical applications. For this, the thesis has been divided into four work chapters followed by conclusion chapter.

Chapter 2 discusses the formation of a new class of glycopolypeptide-based polymersomes (GP-PICsomes) in which glycopolypeptides are grafted onto the surface so that they can potentially interact with specific carbohydrate-binding proteins (lectins). The efficient synthesis of glycopolypeptide-based positively charged poly(amino acid)s and their self-assembly with PEG-conjugated negatively charged poly(amino acid)s in an aqueous media to generate bioactive glycopolypeptide PICsomes is demonstrated. The visualisation of individual micron-sized PICsomes was envisioned by effectively probing with co-localization of dyes through fluorescence microscopic techniques. Formation of micron-sized PICsomes permits for the visualization (using optical microscopy) of their interaction in the presence of specific lectins and aggregation/deaggregation dynamics in solution phase. Such measurements can demonstrate whether carbohydrate-decorated PICsomes retain their biological activity (and specificity) apart from probing the role of lectins in mediating inter-PICsome interactions. Using fluorescent GP-PICsomes, the real-time imaging of dynamic events induced by the binding of GP-PICsomes with a receptor (lectin), leading to the formation of various higher-order aggregates, which disassemble only in the presence of excess (monomeric) mannose, is shown demonstrating the biochemical specificity of pendant groups on the surface.

Chapter 3 discloses how targeting ability of glycopolypeptides based nanocarriers is combined with the stimuli-responsiveness to enhance their capability towards biological application. Glycopolypeptide based crosslinked micellar system incorporated with dual stimuli-responsive groups is developed for the controlled and targeted drug delivery towards tumor cells. Biocompatible miktoarm star ABC triblock copolymers comprising glycopolypeptide as the hydrophilic block, poly (e-caprolactone) as the hydrophobic block and short poly(glycine) block for further crosslinking are synthesized. The triblock copolymer is synthesized by ring-opening polymerization (ROP) of two consecutive NCA's by using hydrophobic PCL as primary amine macroinitiator. The amphiphilic triblock copolymers are self-assembled to form uncrosslinked (UCL) micelles with carbohydrates displayed on the surface. As the conventional micelle degrades in biological environment at a particular concentration (CMC) *in vivo*, the effective approach

to solve this problem is to stabilize micelle structures by cross-linking. The UCL micelles were crosslinked via the propargyl groups in the core shell interface region by redox-responsive crosslinker to form interface crosslinked (ICL) micelles. The synergistic stimuli-responsive release of drug from micelles is studied and their use as drug nanocarriers is shown by the intracellular release of loaded drugs (DOX) in liver cancer (HepG2) cells.

Chapter 4 discusses the delivery of drugs inside lysosomes by M6P-glycopolypeptide based nanocarriers for their effective use in cancer therapy. Lysosomal specific mannose-6-phosphate receptor (CIMPR) are overexpressed in the early stage of several cancers and because of this it can act as early marker for several cancers. Therefore, it can be selectively used to deliver therapeutics specifically to the lysosome. For this, end-functionalized polyvalent mannose-6-phosphate glycopolypeptides (M6P-GPs) by ROP of M6P-NCA is synthesized. Further, pH-responsive amphiphilic block-co-M6P-glycopolypeptides (15M6P-acetal-PPO) are prepared by click chemistry using the azide-terminated acetal containing poly(propylene oxide) (PPO) as a hydrophobic block. pH-responsive micellar morphologies are obtained from the self-assembly of the amphiphilic $M6P_{15}$-acetal-PPO block copolymer. Further, pH-responsive release studies are performed to show the stimuli-responsive release of dye. The as prepared synthetic M6P decorated micelles are found to display minimal toxicity to cells *in vitro* and show exceptional selectivity for trafficking into lysosomes in MCF-7 cell line. It is also demonstrated that trafficking of M6P-GPs in mammalian cells is likely associated with the CI-MPR receptor pathway.

In **Chapter 5,** macroporous silk-based hybrid 3D scaffolds are developed for soft tissue engineering application along with the drug delivery property. These scaffolds are prepared by embedding high percentage (~75%) of submicrometer-sized mesoporous silica particles (SBA-15) within the silk matrix using ice templating method and physical crosslinking in silk matrix. Further, we the release of drug from scaffolds is studied by incorporating the small molecule (Calcein) and macromolecules (FITC-BSA) via SBA-15 particles in hybrid scaffolds. The mechanical property of scaffolds is tuned by varying the percentage of crosslinking in silk hydrophobic region (β-sheet formation). It is shown that Young's modulus of the scaffolds lies in the distinct region of soft tissues. The morphological, mechanical and biological properties of these hybrid scaffolds are studied. Finally, the cell proliferation and cytotoxicity studies on the hybrid scaffolds indicate

these scaffolds to be suitable for tissue engineering applications. The details of this work are discussed in Chapter **5**.

Chapter 6 presents an overall summary of the work and describes the major findings of the studies. Future directions based on the work reported in the thesis are also discussed.

1.10 References

1. Petsko, G. A.; Ringe, D. *New Science Press*, **2004**.
2. Peters, T. Proteins: Structure and Function. David Whitford. Chichester, West Sussex, England: John Wiley & Sons Ltd., **2005**, ISBN 0-471-49894-7. *Clin. Chem.* **2005**, *51*, 2220–2221.
3. Protein Structure. In Introduction to Proteins; Chapman & Hall/CRC Mathematical & Computational Biology; *CRC Press*, **2010**, 67–208.
4. Richards, F. M. *Ann. Rev. Biophys. Bioeng.* **1977**, *6*, 151-176.
5. Chothia, C. *Ann. Rev. Biochem.* **1984**, *53*, 537-572.
6. Finishing the Euchromatic Sequence of the Human Genome. **2001**, 931-945.
7. Walsh, C. T. Posttranslational Modification of Proteins: Expanding Nature's Inventory; W. H. Freeman, **2006.**
8. Walsh, C. T.; Garneau-tsodikova, S.; Gatto, G. J. *Angew. Chem.* **2005**, 7342-7372.
9. Pratt, Donald Voet; Judith G. Voet; Charlotte W. Fundamentals of biochemistry: life at the molecular level (2. ed.). **2006**. Hoboken, NJ: Wiley.
10. Khoury, G. A.; Baliban, R. C.; Floudas, C. A. *Sci. Rep.* **2011**, *90*, 1-5.
11. Moremen, K. W.; Tiemeyer, M.; Nairn, A. V. *Nat. Rev. Mol. Cell. Biol.* **2012**, *13*, 448–462.
12. Lowe, J. B.; Marth, J. D. *Annu. Rev. Biochem.* **2003**, *72*, 643–691.
13. Alphonsus, C. S.; Rodseth, R. N. *Anaesthesia* **2014**, *69*, 777–784.
14. Yamazaki, N.; Kojima, S.; Bovin, N.V.; Andre, S.; Gabius, S.; Gabius, H.-J. *Adv. Drug Delivery Rev.* **2000**, *43*, 225–244.
15. Becker, D. J.; Lowe, J. B. *Glycobiology* **2003**, *13*, 41–53.
16. Gama, C. I.; Hsieh-Wilson, L. C. *Curr. Opin. Chem. Biol.* **2005**, *9*, 609–619.
17. a) Rampal, R.; Luther, K. B.; Haltiwanger, R. S. *Curr. Mol. Med.* **2007**, *7*, 427–445. b) Gabius, H. J.; Andre, S.; Kaltner, H.; Siebert, H. C. *Biochim. Biophys. Acta* **2002**, *1572*, 165–177.
18. Reitsma, S.; Slaaf, D. W.; Vink, H.; van Zandvoort, M. A. M. J.; oude Egbrink, M. G. A. *Pflugers Arch.* **2007**, *454*, 345–359.
19. Van den Berg, B. M.; Nieuwdorp, M.; Stroes, E. S. G.; Vink, H. *Pharmacol. Rep.* **2006**, *58*, 75–80.
20. Rudd, P. M.; Merry, A. H.; Wormald, M. R.; Dwek, R. A. *Curr. Opin. Struct. Biol.* **2002**, *12*, 578–586.
21. Yeh, Y.; Feeney, R. E. *Chem. Rev.* **1996**, *96*, 601–618.
22. Murrey, H. E.; Hsieh-Wilson, L.C.; *Chem. Rev.* **2008**, *108*, 1708–1731.
23. Yamaguchi, H. *Trends Glycosci. Glycotechnol.* **2002**, *14*, 139–151.
24. Rudd, P. M.; Merry, A. H.; Wormald, M. R.; Dwek, R. A. *Curr. Opin. Struct. Biol.* **2002**, *12*, 578–586.
25. Wells, L.; Vosseller, K.; Hart, G. W. *Science* **2001**, *291*, 2376–2378.

26. Kalovidouris, S. A.; Gama, C. I.; Lee, L. W.; Hsieh-Wilson, L. C. *J. Am. Chem. Soc.* **2005**, *127*, 1340–1341.
27. Murrey, H. E.; Gama, C. I.; Kalovidouris, S. A.; Luo, W. I.; Driggers, E. M.; Porton, B.; Hsieh-Wilson, L. C. *Proc. Natl. Acad. Sci. U.S.A.* **2006**, *103*, 21–26.
28. Sandi, C.; Rose, S. P. R.; Mileusnic, R.; Lancashire, C. *Neuroscience* **1995**, *69*, 1087–1093.
29. Fares, F. *Biochim. Biophys. Acta - Gen. Subj.* **2006**, *1760*, 560–567.
30. (a) Mammen, M.; Chio, S.-K. and Whitesides, G. M. *Angew. Chem. Int. Ed.* **1998**, *37*, 2754–2794 (b) Bhatia, S.; Dimde, M.; Haag, R. Multivalent Glycoconjugates as Vaccines and Potential Drug Candidates. *Med. Chem. Commun.* **2014**, *5*, 862–878.
31. Kwong, P. D.; Wyatt, R.; Robinson, J.; Sweet, R. W.; Sodroski, J.; Hendrickson, W. A. *Nature* **1998**, *393*, 648–659.
32. Ghosh, P.; Dahms, N. M.; Kornfeld, S. *Nat. Rev. Mol. Cell Biol.* **2003**, *4*, 202–212.
33. Stockert, R. J. *Physiol. Rev.* **1995**, *75*, 591–609.
34. Dodd, J.; Morton, S. B.; Karagogeos, D.; Yamamoto, M.; Jessell, T. M. *Neuron* **1988**, *1*, 105–116.
35. Haltiwanger, R. S.; Lowe, J. B. *Annu. Rev. Biochem.* **2004**, *73*, 491–537.
36. Cohen, P. *Nat. Cell. Biol.* **2002**, *4*, 127–130.
37. Nishi, H.; Hashimoto, K.; Panchenko, A. R. *Struct. Des.* **2011**, *19*, 1807–1815.
38. Cohen, P. *Eur J Blochem.* **1985**, *151*, 439-448.
39. Humphrey, S. J.; James, D. E.; Mann, M. *Trends Endocrinol. Metab.* **2015**, *26*, 676–687.
40. Levitan, I. B. *Annu. Rev. Physiol.* **1994**. *56*, 193-212.
41. Cohen, P. TIBS, **2000**, *4*, 596–601.
42. Cohen, P. **2001**, *268*, 5001-5010.
43. Johnson, L. N.; Lewis, R. J. *Chem. Rev.* **2001.** *101*, 2209-2242.
44. Ubersax, J. A.; Ferrell Jr, J. E. *Nat Rev Mol Cell Biol* **2007**, *8*, 530–541.
45. The Lectins. Properties, Functions, and Applications in Biology and Medicine, ed. I. E. Liener, N. Sharon and I. J. Goldstein, *Academic Press Inc.*, **1986**.
46. Kilpatrick, D. C. *Biochim. Biophys. Acta, Gen. Subj.* **2002**, *1572*, 187–197.
47. Simon Ting, S. R.; Chen, G.; Stenzel, M. H. *Polym. Chem.* **2010**, *1*, 1392–1412.
48. Liu, F.-T.; Rabinovich, G. A. *Nat Rev Cancer* **2005**, *5*, 29–41.
49. Elola, M. T.; Chiesa, M. E.; Alberti, A. F.; Mordoh, J.; Fink, N. E. *J. Biomed. Sci.* **2005**, *12*, 13–29.
50. Vasta, G. R. *Nat Rev Micro* **2009**, *7*, 424–438.
51. Crocker, P. R.; Paulson, J. C.; Varki, A. *Nat. Rev. Immunol.* **2007**, *7*, 255–266.
52. Wasik, B. R.; Barnard, K. N.; Parrish, C. R. *Trends Microbiol.* **2016**, *24*, 991–1001.
53. Vasta, G. R.; Ahmed, H.; Bianchet, M. A.; Fernández-Robledo, J. A.; Amzel, L. M. *Ann. N. Y. Acad. Sci.* **2012**, *1253*, E14–E26.
54. Bhatia, S.; Dimde, M.; Haag, R. *Med. Chem. Commun.* **2014**, *5*, 862–878.
55. Cummings, R. D.; McEver, R. P. C-type Lectins. In: Varki A, Cummings RD, Esko JD, et al., editors. Essentials of Glycobiology. 2nd edition. Cold Spring Harbor (NY): Cold Spring Harbor Laboratory Press; **2009**. Chapter 31.
56. Saunier, B.; Triyatni, M.; Ulianich, L.; Maruvada, P.; Yen, P.; Kohn, L. D. *J. Virol.* **2003**, *77*, 546–559.

57. Geuze, H. J.; Slot, J. W.; Strous, G. J. A. M.; Lodish, H. F.; Schwartz, A. L. *Cell* **1983**, *32*, 277–287.
58. Roggenbuck, D.; Mytilinaiou, M. G.; Lapin, S. V; Reinhold, D.; Conrad, K. *Auto-Immunity Highlights* **2012**, *3*, 119–125.
59. Neth, O.; Jack, D. L.; Dodds, A. W.; Holzel, H.; Klein, N. J.; Turner, M. W. *Infect. Immun.* **2000**, *68*, 688–693.
60. Figdor, C. G.; van Kooyk, Y.; Adema, G. J. *Nat Rev Immunol.* **2002**, *2*, 77–84.
61. McGreal, E. P.; Rosas, M.; Brown, G. D.; Zamze, S.; Wong, S. Y. C.; Gordon, S.; Martinez-Pomares, L.; Taylor, P. R. *Glycobiol.* **2006**, *16*, 422–430.
62. David, A.; Kopeckova, P.; Kopecek, J. and Rubinstein, A. *Pharm. Res.* **2002**, *19*, 1114–1122.
63. David, A.; Kopeckova, P.; Rubinstein, A. and J. Kopecek, *Bioconjugate Chem.* **2001**, *12*, 890–899.
64. Montet, X.; Funovics, M.; Montet-Abou, K.; Weissleder, R.; Josephson, L. *J. Med. Chem.* **2006**, *49*, 6087–6093.
65. Shamay, Y.; Paulin, D.; Ashkenasy, G. and David, A. *J. Med. Chem.* **2009**, *52*, 5906–5915.
66. Sliedregt, L. A. J. M. *et al. J. Med. Chem*. **1999**, *42*, 609–618.
67. Lee, R. T. and Lee, Y. C. *Glycoconjugate J.* **2000**, *17*, 543–551.
68. Gonzalez, M. W.; Kann, M. G. Chapter 4: Protein Interactions and Disease. *PLoS Comput. Biol.* **2012**, *8*, e1002819.
69. Thompson, Craig, B. *Science***, 1995,** *267*, 1456-1462.
70. Deming, T. J. *Adv. Polym. Sci.* **2013**, *262*, 1−38.
71. Deming, T. J. *Chem. Rev.* **2016**, *116*, 786–808.
72. Zhang, S. *Biotechnol. Adv.* **2002**, *20*, 321–339.
73. Greenwald, J.; Riek, R. *Structure* **2010**, *18*, 1244–1260.
74. Zhao, X.; Zhang, S. *Chem. Soc. Rev.* **2006**, *35*, 1105–1110.
75. Whitesides, G. M.; Boncheva, M. *Proc. Natl. Acad. Sci.* **2002**, *99*, 4769–4774.
76. Vriezema, D. M.; Aragones, M. C.; Elemans, J. A. A. W.; Cornelissen, J. J. L. M.; Rowan, A. E.; Nolte, R. J. M. *Chem. Rev.* **2005**, *105*, 1445-1490.
77. Baumeister, W.; Walz, J.; Zühl, F.; Seemüller, E. *Cell* **1998**, *92*, 367-380.
78. Tu, R. S.; Tirrell, M. *Adv. Drug Deliv. Rev.* **2004**, *56*, 1537–1563.
79. Shen, Y.; Fu, X.; Fu, W.; Li, Z. *Chem. Soc. Rev.* **2015,** *44 (3,)* 612– 622.
80. Carlsen, A.; Lecommandoux, S. *Curr. Opin. Colloid Interface Sci.* **2009**, *14*, 329–339.
81. Rodríguez-Hernández, J.; Chécot, F.; Gnanou, Y.; Lecommandoux, S. *Prog. Polym. Sci.* **2005**, *30*, 691–724.
82. Sarikaya, M.; Tamerler, C.; Schwartz, D. T.; Baneyx, F. *Annu. Rev. Mater. Res.* **2004**, *34*, 373–408.
83. Antonietti, M.; Forster, S. *Adv. Mater.* **2003**, *15*, 1323–1333.
84. Bates, F. S.; Fredrickson, G. H. *Phys. Today* **1999**, *52*, 32–38.
85. Cölfen, H. *Macromol. Rapid Commun.* **2001**, *22*, 219–252.
86. Forster, S.; Antonietti, M. *Adv. Mater*. **1998**, *10*, 195–217.
87. Forster, S.; Konrad, M. *J. Mater. Chem*. **2003**, *13*, 2671–2688.
88. Lim Soo, P.; Eisenberg, A. *J. Polym. Sci. Part B,* **2004**, *42*, 923-938.
89. Israelachvili. J. N. "Intermolecular and Surface Forces", 2nd edition. *Academic Press*, **1992**.

90. Evans, D. F.; Wennerstrom, H. *The Colloidal Domain, Second Ed.*; *Wiley-VCH*: *New York* **1999**.
91. Hadjichristidis, N.; Pispas, S.; Floudas, G. *Block Copolymers*: *Wiley*: *Hoboken NJ* **2003.**
92. Zhulina, E. B.; Adam, M.; LaRue, I.; Sheiko, S. S.; Rubinstein, M. *Macromolecules* **2005**, *38*, 5330–5351.
93. Discher, D. E.; Eisenberg, A. *Science* **2002**, *297*, 967–973.
94. Du, J. Z.; O'Reilly, R. K. *Soft Matter* **2009**, *5*, 3544–3561.
95. Blanazs, A.; Armes, S. P. and Ryan, A. J. *Macromol. Rapid Commun*. **2009**, *30*, 267–277.
96. Du J.; Chen, Y. *Macromolecules* **2004**, *37*, 5710-5716.
97. Tian, B.; Tao, X.; Ren, T.; Weng, Y.; Lin, X.; Zhang, Y.; Tang, X. *J. Mater. Chem.* **2012**, *22*, 17404–17414.
98. Soo, P. L. Eisenberg, A. *J. Polym. Sci., Part B: Polym. Phys.* **2004**, *42*, 923–938.
99. Sanson, C.; Schatz, C.; Le Meins, J.-F.; Soum, A.; Thévenot, J.; Garanger, E.; Lecommandoux, S. *J. Control. Release* **2010**, *147*, 428–435.
100. Yan, X.; Cui, Y.; Qi, W.; Su, Y.; Yang, Y.; He, Q.; Li, J. *Small* **2008**, *4*, 1687–1693.
101. Harada, A.; Kataoka, K. *Macromolecules* **1995**, *28*, 5294–5299.
102. Chuanoi, S.; Kishimura, A.; Dong, W.-F.; Anraku1, Y.; Yamasaki, Y.; Kataoka, K. *Polym. J.* **2014**, *46*, 130−135.
103. Koide, Y.; Kishimura, A.; Osada, K.; Jang, W.-D.; Yamasaki, Y.; Kataoka, K. *J. Am. Chem. Soc.* **2006,** *128*, 5988− 5989.
104. Dong, W.-F.; Kishimura, A.; Anraku, Y.; Chuanoi, S.; Kataoka, K. *J. Am. Chem. Soc.* **2009**, *131*, 3804−3805.
105. Anraku, Y.; Kishimura, A.; Oba, M.; Yamasaki, Y.; Kataoka, K. *J. Am. Chem. Soc.* **2010**,*132*, 1631−1636.
106. Anraku, Y.; Kishimura, A.; Yamasaki, Y.; Kataoka, K. *J. Am. Chem. Soc.* **2013**, *135*, 1423− 1429.
107. Kishimura, A.; Koide, A.; Osada, K.; Yamasaki, Y.; Kataoka, K. *Angew. Chem., Int. Ed.* **2007**, *46*, 6085−6088.
108. Oana, H.; Kishimura, A.; Yonehara, K.; Yamasaki, Y.; Washizu, M.; Kataoka, K. *Angew. Chem., Int. Ed.* **2009**, *48*, 4613−4616.
109. World Health Organization. Retrieved **2011**-01-05.
110. Peer, D.; Karp, J. M.; Hong, S.; Farokhzad, O. C.; Margalit, R.; Langer, R. *Nat Nano* **2007**, *2*, 751–760.
111. Stuart, M. A. C.; Huck, W. T. S.; Genzer, J.; Muller, M.; Ober, C.; Stamm, M.; Sukhorukov, G. B.; Szleifer, I.; Tsukruk, V. V.; Urban, M. *Nat. Mater.* **2010**, *9*, 101–113.
112. Nishida, N.; Yano, H.; Nishida, T.; Kamura, T.; Kojiro, M. Vasc. *Health Risk Manag.* **2006**, *2*, 213–219.
113. Matsumura, Y.; Maeda, H. *Cancer Res.* **1986**, *46*, 6387–6392.
114. Steeg, P. S. *Nature Med.* **2006**, *12*, 895–904.
115. Bertrand, N.; Wu, J.; Xu, X.; Kamaly, N.; Farokhzad, O. C. *Adv. Drug Deliv. Rev.* **2014**, *66*, 2–25.
116. Torchilin, V. P. *Nat. Rev. Drug Discov*. **2005**, *4*, 145–160.
117. Hobbs, S. K. *et al. Proc. Natl. Acad. Sci. USA* **1998**, *95*, 4607–4612.
118. Gottesman, M. M.; Fojo, T.; Bates, S. E. *Nat. Rev. Cancer* **2002**, *2*, 48–58.

119. Peer, D.; Margalit, R. *Cancer Lett.* **2006**, *237*, 180–187.
120. Menezes, D. E. L.; Pilarski, L. M.; Allen, T. M. *Cancer Res.* **1998**, *58*, 3320–3330.
121. Yu, B. O.; Tai, H. C.; Xue, W.; Lee, L. J.; Lee, R. J. *Mol. Membr. Biol.* **2010**, *27*, 286–298.
122. Alvarez-Lorenzo, C.; Concheiro, A. *Chem. Commun.* **2014**, *50*, 7743– 7765.
123. Cabane, E.; Zhang, X.; Langowska, K.; Palivan, C. G.; Meier, W. *Biointerphases* **2012**, *7*,1-27.
124. Gil, E. S.; Hudson, S. M. *Prog. Polym. Sci.* **2004**, *29*, 1173−1222.
125. Liechty, W. B; L.; Kryscio, D. R.; Slaughter, B. V.; Peppas, N. A. *Annu. Rev. Chem. Biomol. Eng.* **2010,** *1*,149–173.
126. Delcea, M.; Mohwald, H.; Skirtach, A. G. *Adv. Drug Delivery Rev.* **2011**, *63*, 730–747.
127. Bajpai, A.; Shukla, S. K.; Bhanu, S.; Kankane, S. *Prog. Polym. Sci.* **2008**, *33*, 1088–1118.
128. Khan, F.; Tanaka M. *Int. J Mol Sci*. **2017**, *19*, (17), 1-14.
129. Hu, J.; S. Liu. *Macromolecules* **2010**, *43*, 8315–8330.
130. Ma, M.; Guo, L. D.; Anderson, G.; Langer, R. *Science* **2013**, *339*, 186–189.
131. Zhao, Q.; Dunlop, J. W.; Qiu, X.; Huang, F.; Zhang, Z.; Heyda, J.; Dzubiella, J.; Antonietti, M.; Yuan, J. *Nat. Commun.* **2014**, *5*, 4293-4301.
132. Hu, Z.; Zhang X.; Li, Y. *Science* **1995**, *269*, 525-527.
133. Parasuraman, D.; Serpe, M. J. *ACS Appl. Mater. Interfaces*. **2011**, *3*, 2732–2737.
134. Colson, Y. L.; Grinstaff, M. W. *Adv. Mater.* **2012**, *24*, 3878–3886.
135. Kelley, E. G.; Albert, J. N. L.; Sullivan, M. O.; Epps III, T. H. *Chem. Soc. Rev.* **2013**, *42*,7057–7071.
136. Zhuang, J.; Gordon, M. R.; Ventura, J.; Li, L.; Thayumanavan, S. *Chem. Soc. Rev.* **2013**, *42*, 7421–7435.
137. Ganta, S.; Devalapally, H.; Shahiwala, A.; Amiji, M. *J. Control. Release* **2008**, *126*, 187–204.
138. Yang, Y.; Urban, M. W. *Chem. Soc. Rev.* **2013**, *42*, 7446–7467.
139. Habault, D.; Zhang, H.; Zhao, Y. *Chem. Soc. Rev.* **2013**, *42*, 7244–7256.
140. Liu, C.; Qin, H.; Mather, P. T. *J. Mater. Chem.* **2007**, *17*, 1543.
141. Grubbs, R. B.; Sun, Z. *Chem. Soc. Rev.* **2013**, *42*, 7436–7445.
142. Brust, M.; Schiffrin, D. J.; Bethell, D.; Kiely, C. J. *Adv. Mater.* **1995**, *7*, 795–797.
143. Zhang, J.; Zhang, M.; Tang, K.; Verpoort, F.; Sun, T. *Small* **2014**, *10*, 32–46.
144. Roy, D.; Cambre, J. N.; Sumerlin, B.S. *Prog Polym Sci.* **2010,** *35*, 278–301.
145. Wei, M.; Gao, Y.; Li, X.; Serpe, M. J. *Polym. Chem.* **2017**, *8*, 127– 143.
146. Galaev, I.Y.; Mattiasson, B. *Trends Biotechnol* **1999**, *17*, 335–340.
147. Kumar, A.; Srivastava, A.; Galaev, I.Y.; Mattiasson, B. *ProgPolym Sci.* **2007**, *32*, 1205–1237.
148. Deming, T. J. *Prog. Polym. Sci.* **2007**, *32*, 858-875.
149. Carlsen, A.; Lecommandoux, S.; *Curr. Opin. Colloid Interface Sci.* **2009**, *14*, 329-339.
150. Schlaad, H.; *Adv. Polym. Sci.* **2006**, *202*, 53-73.
151. Lavasanifar, A.; Samuel, J.; Kwon, G. S. *Adv. Drug Delivery Rev.* **2002**, *54*, 169-190.
152. Bae, Y.; Kataoka, K.; *Adv. Drug Delivery Rev.* **2009**, *61*, 768-784.
153. van Dongen, S. F. M.; de Hong, H. P. M.; Peters, R. J. R. W.; Nallani, M. R.; Nolte, J. M.; van Hest J. C. M.; *Chem. Rev.* **2009**, *109*, 6212-6274.
154. Li, C. *Adv. Drug Delivery Rev.* **2002**, *54*, 695-713.

155. He, C. L.; Zhuang, X. L.; Tang, Z. H.; Tian, H. Y.; Chen, X. S. *Adv. Healthcare Mater.* **2012**, *1*, 43-48.

156. Huang, J.; Heise, A. *Chem. Soc. Rev*. **2013**, *42*, 7373-7390.

157. Danhier, F.; Feron, O.; Preat, V.; *J. Controlled Release*. **2010**, *148*, 135-146.

158. Schmaljoham, D. *Adv. Drug Delivery Rev.* **2006**, *58*, 1655-1670.

159. Liu, R.; Fraylichh, M.; B Saunders, R. *Colloid Polym. Sci.* **2009**, *287*, 627-643.

160. Choi, Y. Y.; Joo, M. K.; Sohn, Y. S.; Jeong, B. *Soft Matter* **2008**, *4*, 2383-2387.

161. Schmaljohann, D. *Adv. Drug Deliv.* **2006**, *58*, 1655–1670.

162. Peppas, N. A.; Wood, K. M.; Blanchette, J. O. *Expert Opin. Biol. Ther.* **2004**, *4*, 881-887.

163. Saito, G.; Swanson, J. A.; Lee, K. D. *Adv. Drug Delivery Rev.* **2003**, *55*,199-215.

164. Meng, F.; Hennink, W. E.; Zhong, Z. *Biomaterials* **2009**, *30*, 2180-2198.

165. Raina, S.; Missiakas, D. *Annu. Rev. Microbiol*, **1997**, *51*, 179-202.

166. (a) Elias, S. J.; Arner, A. H. *Eur. J. Biochem.* **2000**, *267*, 6102-6109; (b) Townsend, D. M.; Tew, K. D.; Tapiero, H. *Biomed. Pharmacother.* **2003**, *57*, 145-155; (c) Go, Y. M.; Jones, D. P. *Biochim. Biophys. Acta*. **2008**, *1780*, 1273-1290.

167. Kim, T. I.; Kim, S. W. *React. Funct. Polym.* **2011**, 71, 344-349.

168. Dong, W.; Kishimura, A.; Anraku, Y.; Chuanoi, S.; Kataoka, K. *J. Am. Chem. Soc.* **2009** , 131 , 3804-3805.

169. (a) Zhang, X. Z. *Polym. Chem.* **2012**, *3*, 1084-1090 (b) Habraken, G. J.; Koning, C. E.; Heuts, J. P.; Heise, A. *Chem. Commun.* **2009**, *24*, 3612-3614.

170. (a) Read, E. S.; Armes, S. P. *Chem. Commun.*, **2007**, *29*, 3021–3035. (b) O'Reilly, R. K.; Hawker, C. J.; Wooley, K.L. *Chem. Soc. Rev.* **2006,** *35*, 1068—1083.

171. (a) Lee, E. S.; Gao Z.; Bae, Y. H. *J. Controlled Release*. **2008,** *132*, 164-170; (b) Ganta, S.; Devalapally, H.; Shahiwala A.; Amiji, M. *J. Controlled Release*. **2008,** *126*, 187-204.

172. Mellman, I.; Fuchs, R.; Helenius, A. *Annu. Rev. Biochem*. **1986**, *55*, 663-700.

173. Felber, A. E.; Dufresne, M. H.; Leroux, J. C. *Adv. Drug Delivery Rev.* **2012**, *64*, 979-992.

174. (a) Tian, H.; Chen, X.; Lin, H.; Deng, C.; Zhang, P.; Wei Y.; Jing, X. *Chem.–Eur. J*. **2006,** *12*, 4305-4312; (b) Huang, H. H.; Li, J. Y.; Liao, L. H.; Li, J. H.; Wu, L. X.; Dong, C. K.; Lai P. B.; Liu, D. J. *Eur. Polym. J.* **2012**, *48*, 696-704.

175. (a) Li, Y. Y.; S. Hua, H.; Xiao, W.; Wang, H. Y.; Luo, X. H.; Li, C.; Cheng, S. X.; Zhang X. Z.; Zhuo, R. X. J. *Mater. Chem.* **2011**, *21*, 3100-3106; (b) Wang, C.; Kang, Y.; Liu, T. K.; Li, Z. B.; Wang Z. Q.; Zhang, X. *Polym. Chem.* **2012,** *3*, 3056-3059.

176. Xiao, Y.; Hong, L. H.; Javadi, A.; Engle, J. W.; Xu, W. J.; Yang, Y. N.; Zhang, Y.; Barnhart, T. E.; Cai, W. B.; Gong, S. Q. *Biomaterials* **2012**, *33*, 3071-3082.

177. Bellomo, E. G.; Wyrsta, M. D.; Pakstis, L. D.; Pochan J.; Deming, T. J. *Nat. Mater.* **2004,** *3*, 244-248.

178. (a) Iatrou, H.; Frielinghaus, H.; Hanski, S.; Ferderigos, N.; Ruokolainen, J.; Ikkala, O.; Richter, D.; Mays, J.; Hadjichristidis, N. *Biomacromolecules* **2007**, *8*, 2173-2181. (b) Sun, J.; Chen, X. S.; Deng, C.; Yu, H. J; Xie Z. G.; Jing, X. B.; *Langmuir* **2007**, *23*, 8308-8315; (c) Sun, J.; Huang, Y. B.; Shi, Q.; Chen, X. S.; Jing, X. B. *Langmuir* **2009,** *25*, 13726-13729. (d) Gaspard, J.; Silas, J. A.; Shantz D. F.; Jan, J.; *Supramol. Chem.* **2010,** *22*, 178-185. (e) Kim, M. S.; Dayananda, K.; Choi, E. K.; Park, H. J.; Kim, J. S.; Lee, D. S. *Polymer* **2009,** *50*, 2252-2257.

179. Hu, Q.; Katti, P. S.; Gu, Z. *Nanoscale* **2014**, *6*, 12273– 12286.

180. Fan, J.; Li, R.; Wang, H.; He, X.; Nguyen, T. P.; Letteri, R. A.; Zou, J.; Wooley, K. L. *Org. Biomol. Chem.* **2017**, *15*, 5145-5154.

181. Guragain, S.; Bastakoti, B. P.; Malgras, V.; Nakashima, K.; Yamauchi, Y. *Chem. - Eur. J.* **2015**, *21*, 13164-13174.

182. Dai, J.; Lin, S.; Cheng, D.; Zou, S.; Shuai, X. *Angew. Chem. Int. Ed.* **2011,** *50*, 9404–9408.

183. Borase, T.; Ninjbadgar, T.; Kapetanakis, A.; Roche, S.; O'Connor, R.; Kerskens, C.; Heise A.; Brougham, D. F. *Angew. Chem. Int. Ed.* **2013**, *52*, 3164-3167.

184. Bertozzi, C. R.; Kiessling, L. L. *Science* **2001**, *291*, 2357−2364.

185. Kiessling, L. L.; Gestwicki, J. E.; Strong, L. E. *Curr. Opin. Chem. Biol*. **2000**, *4*, 696−703.

186. Roy, R. *Curr. Opin. Struct. Biol*. **1996**, *6*, 692−702.

187. Huang, J.; Bonduelle, C.; Thévenot, J.; Lecommandoux, S.; Heise, A. *J. Am. Chem. Soc*. **2012**, *134*, 119−122.

188. Pati, D.; Kalva, N.; Das, S.; Kumaraswamy, G.; Sen Gupta, S.; Ambade, A. V. *J. Am. Chem. Soc.* **2012**, *134*, 7796–7802.

189. Das, S.; Sharma, D. K.; Chakrabarty, S.; Chowdhury, A.; Sen Gupta, S. *Langmuir* **2015**, *31*, 3402−3412.

190. Pati, D.; Das, S.; Patil, N. G.; Parekh, N.; Anjum, D. H.; Dhaware, V.; Ambade, A. V.; Sen Gupta, S. *Biomacromolecules* **2016**, *17*, 466–475.

191. Wang, S.S.S.; How, S.C.; Chen, Y.D.; Tsai, Y.H.; Jan, J.-S. *J. Mater. Chem. B.* **2015,** *3*, 5220–5231.

192. Yang, H.-K.; Bao, J.-F.; Mo, L.; Yang, R.-M.; Xu, X.-D.; Tang, W.-J.; Lin, J.-T.; Zhang, L.-M.; Jiang, X.-Q. *RSC. Adv.* **2017,** *7*, 21093-21106.

CHAPTER 2

Glycopolypeptide grafted Bioactive Polyionic Complex Vesicles (PICsomes) and their Specific Polyvalent Interactions

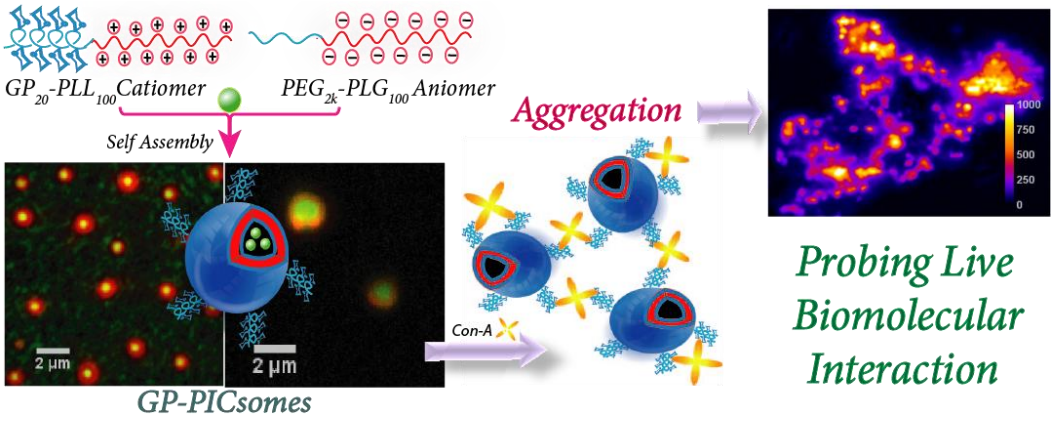

This chapter has adapted from the corresponding paper;

Bhawana Pandey, Jaladhar Mahato, Karishma Berta Cotta, Soumen Das, Dharmendra K. Sharma, Arindam Chowdhury and Sayam Sen Gupta*.*ACS Omega*, **2016**, *1* (4), pp 600–612. **DOI:** 10.1021/acsomega.6b00142

2.1 Introduction

Multivalent interactions of carbohydrates with their corresponding receptors are key to the high specificity of these important biomolecular events. In this context, a vast number of multivalent synthetic glycoconjugates have been prepared over the past decades, including dendritic scaffolds, linear polymers, micelles, and nanoparticles.[1-4] Among these, glycopolypeptides, where sugar units are attached to a polypeptide backbone with well-defined secondary structures, mimic the molecular composition of proteoglycans and thus represent suitable candidates for biological applications.[5-10] Construction of supramolecular nano/microstructures (such as micelles or vesicles) from glycopolypeptides are advantageous as they are better mimics of densely populated carbohydrates on the cell surface than the individual glycopolypeptides. Such self-assembled structures can then be used to understand carbohydrate-protein interaction, which would be more realistic mimics of living systems. Recently, several groups have reported synthetic amphiphilic glycopolypeptide-based block copolymers that undergo self-assembly to generate morphologically different micro/nano-structures.[11-15] By varying factors like molecular weight, chemical composition, functionality and architecture of the amphiphilic block copolymers, the self-assembly could be controlled to afford size-selection and a broad variety of morphologies.[16]

Typically, fabrication of polymersomes using conventional self-assembly of amphiphilic block copolymer is tedious and involves procedures like multiple dialysis, sonication and heating. These techniques, combined with the use of organic solvents, can cause damage to the loaded cargo (sensitive biomolecules such as proteins, enzyme or drugs) and may also induce toxicity in biological systems.[17,18] In addition, for the delivery of hydrophilic macromolecules, their poor solubility in non-aqueous medium and low penetration through the hydrophobic membrane in amphiphilic polymersomes limits their functionality as semipermeable containers.[19] To overcome these limitations, utilization of polyion complexes (PICs) can provide better solution because PIC formation can be carried out in aqueous media without the use of organic solvents and the preparation process is remarkably straightforward.[20,21] Oppositely charged hydrophilic block copolymers undergo self-assembly process *via* electrostatic interactions leading to the formation of PIC assemblies or vesicles, the morphology of which depend on the length and composition of ionic blocks as well as the length of aliphatic spacer side chains.[22-24] Although PIC vesicles (PICsomes) possess a hollow spherical structure similar to

polymersomes self-assembled from amphiphilic polymers, the PIC membrane sandwiched between outer and inner hydrophilic shell layers is semipermeable to hydrophilic solutes as opposed to hydrophobic shell layer of amphiphilic polymersomes. Kataoka and co-workers first demonstrated formation of PIC micellar nanostructures and subsequently, unilamellar polymersomes in aqueous media by the electrostatic self-assembly of oppositely charged double hydrophilic block copolymers (or charged homopolymers) composed of biocompatible poly(ethylene glycol) (PEG) and poly(amino acid)s.[25-30]

In the quest to expand the repertoire of glycopolypeptide based nano/micro-structures formed *via* self-assembly of homo and block amphiphilic glycopolypeptides, development of a new class of glycopolypeptide-based PICsomes were envisioned in which glycopolypeptides are present on the surface so that they can potentially interact with specific carbohydrate binding proteins (lectins). This chapter describes the efficient synthesis of glycopolypeptide-based positively charged poly(amino acid)s and their-self-assembly with PEG-based negatively charged poly(amino acid)s in aqueous medium to generate bioactive glycopolypeptide PICsomes (GP-PICsomes) (Figure 2.1). The micrometer dimensions of these GP-PICsomes with a high surface density of high molecular weight glycopolypeptides make them close mimics of the protein-bound carbohydrates found on cell surfaces. In this context, it is important to understand their surface bioactivity, which has typically been studied for smaller supramolecular soft structures using techniques such as surface plasmon resonance, calorimetric assays, and DLS analysis.[31-35] The formation of large PICsomes allow for visualization (using optical microscopy) of their interaction in presence of specific lectins, as well as aggregation/de-aggregation dynamics in solution. Such measurements can demonstrate whether carbohydrate-decorated PICsomes retain their biological activity as well as specificity apart from probing the role of lectins in mediating inter-PICsome interactions.

Recently, the lectin induced aggregation kinetics of dextran-coated colloidal silica (hard) particles have been investigated on PEGylated glass surface using confocal microscopy.[36] Although this provided insights into aggregation mechanisms of mixed synthetic biomaterials induced by specific biomolecular interactions, the polyvalent binding of lectins with glycoprotein mimics such as glycopolypeptides grafted on soft polymersomes and their resulting aggregation behaviour has not been studied. Using fluorescent GP-PICsomes, real time imaging of dynamic events induced by binding of GP-PICsomes with a receptor (lectin) leading to formation of various higher order aggregates, which

disassemble only in the presence of excess (monomeric) mannose was carried out to demonstrate biochemical specificity of surface pendant groups.

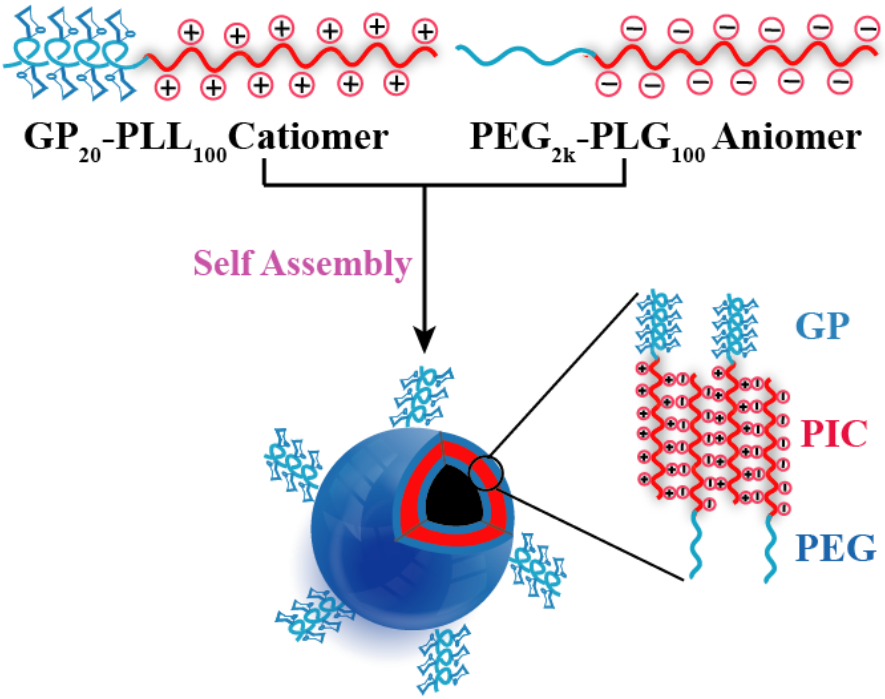

Figure 2.1: Representation depicting the structures of hydrophilic-charged block copolymers and their self-assembly into glycopolypeptide-based PICsomes (GP-PICsomes) under aqueous environment. Possibly, some of the PEG_{2k} chains and glycopolypeptide moieties may be present in the outer layers and the inner layers, respectively. Although a high density of glycopolypeptides is present on the surface, only a few of them are blown up in the cartoon depiction for clarity.

2.2 Experimental Section

2.2.1 *General*

Poly(ethylene glycol) monomethyl ether (PEG-OH, M_n = 2000 g/mol), Rhodamine B isothiocyanate (RITC) and FITC-Dextran (M_n=5000) were purchased from Sigma Aldrich. Glyco-N-carboxyanhydride was prepared by using our previously published methodology.[37] Ligand THPTA (tris(3-hydroxypropyltriazolylmethyl)amine) was synthesized by following the method of Finn and Coworkers.[38] Amine-terminated polyethylene glycol monomethyl ether (2000) was synthesized by following the method of Loos and coworkers.[39] All the other chemicals used were obtained from Merck, India.

GPC measurements of ionic block copolymers were performed in WATER ALLIANCE 2690 SEPERATION MODULE (RI DETECTOR 2410). Separations were achieved by three columns (G2000PW, G3000PW, G4000PW) using 10 mM phosphate buffer with 100 mM NaCl (pH 7.4) at a flow rate of 0.5 mL/min at room temperature. GPC samples were prepared at concentrations of 2.5 mg/mL.

*2.2.2 Synthesis of N$^{\varepsilon}$-trifluoroacetyl-L-lysine-N-carboxyanhydride (**2b**)*

To a solution of N$^{\varepsilon}$-trifluoroacetyl-*L*-lysine amino acid (500 mg, 1.9 mmol) in freshly distilled out tetrahydrofuran (10 mL) was added a solution of triphosgene (282 mg, 0.95 mmol) in anhydrous tetrahydrofuran (4 mL) under argon and the reaction mixture was heated to 50°-55°C. Subsequently α-pinene (0.4 mL, 2.85mmol) was added and the reaction mixture was allowed to stir for an additional 2 h. The reaction mixture was then cooled to room temperature and was then poured into dry hexane (400 mL) to afford a white precipitate. The white precipitate of NCA was filtered off by vacuum quickly and crystallized two more times by using ethyl acetate/petroleum ether mixtures. Finally the precipitate of N$^{\varepsilon}$-Trifluoroacetyl-*L*-lysine-N-carboxyanhydride was dried under vacuum and transferred into glove box. Final yield is 450 mg (90%).

^{1}H NMR (500.13 MHz, Acetone-d_6): δ (ppm): 1.48-1.68 (m, 4H), 1.86-1.98 (m, 2H), 3.35-3.39 (dd, 2H), 4.54-4.57 (t, 1H), 7.96 (s, amide 1H), 8.49 (s, amide 1H); ^{13}C NMR (125.76 MHz, Acetone-d_6): δ (ppm): 23.08, 32.25, 40.42, 58.59, 116.39, 118.67, 153.15, 157.84, 158.13, 172.27. FT-IR (cm^{-1}): 1858, 1785, 1775, 1265 $^{\nu}$co (unsymmetrical stretching).

2.2.3 Synthesis of mannose-N-carboxyanhydrides

To a solution of per-*O*-acetylated-D-mannose -*L*-lysine carbamate (500 mg, 0.96 mmol) in freshly distilled out tetrahydrofuran (10 mL) was added accordingly a solution of triphosgene (142 mg, 0.480 mmol) in anhydrous tetrahydrofuran (2 mL) under argon and the reaction mixture was heated to 50-55°C. α-pienene (0.228 mL, 1.44 mmol) was then added and the reaction mixture was allowed to stir for an additional 1 h. The reaction mixture was then cooled to room temperature and then poured into dry hexane (300 mL) to afford a white precipitate, which was filtered off quickly and crystallized two more times using a mixture of ethyl acetate and petroleum ether. Finally, the white precipitate of glyco-*N*-carboxyanhydride obtained was dried under vacuum and transferred to the glove box. Final yield: 425 mg, 80%.

^{1}H NMR (500.13 MHz, $CDCl_3$): δ (ppm): 1.35−1.88 (m, 6H), 1.99, 2.03, 2.07, 2.16 (s, 4H), 3.23 (q, 2H), 3.68 (t, 1H), 4.08 (m, 1H), 4.13 (dd, 1H), 4.23 (dd, 1H), 4.35 (dd, 1H), 5.20−5.35 (m, 3H), 5.94 (d, 1H), 6.72 (bs, 1H); ^{13}C NMR (125.76 MHz, $CDCl_3$): δ (ppm): 20.8, 20.9, 22.2, 29.3, 31.6, 40.7, 57.9, 62.7, 66.1, 68.9, 69.3, 70.5, 91.7, 152.3, 153.8, 170.0, 170.3, 170.4, 170.6, 171.2; FT-IR (dioxane) (cm^{-1}): 1785 and 1858 ^{v}co (unsymmetrical stretching).

*2.2.4 Synthesis of γ-benzyl-L-glutamate-N-carboxyanhydride (**3a**)*

To a solution of γ-Benzyl-*L*-glutamate amino acid (500 mg, 2.10 mmol) in freshly distilled out tetrahydrofuran (10 mL) was added a solution of triphosgene (312.5mg, 1.05 mmol) in anhydrous tetrahydrofuran (4 mL) under argon and the reaction mixture was heated to 50°-55°C. Then α-pinene (0.5 mL, 3.16 mmol) was added and the reaction mixture was allowed to stir for 2 h. The reaction mixture was then cooled to room temperature and there after poured into dry hexane (400 mL) to afford a white precipitate. The white precipitate of N-carboxyanhydrides was filtered off by vacuum quickly and crystallized two more times by using ethyl acetate/petroleum ether mixtures. Finally the precipitate of γ-Benzyl-*L*-glutamate- N-carboxyanhydride was dried under vacuum and transferred into glove box. Final yield is 425mg (85%).

^{1}H NMR (500.13 MHz, $CDCl_3$): δ (ppm): 2.33-2.58 (m, 2H), 2.85 (t, 2H), 4.66 (t, 1H), 5.40 (s, 2H), 7.25 (bs, 1H), 7.61-7.65 (m, 5H); ^{13}C NMR (125.76 MHz, $CDCl_3$): δ (ppm): 26.7, 29.5, 56.7, 67.0, 128.2-128.7, 135.2, 152.2, 169.9, 172.3. FT-IR (cm^{-1}): 2890, 1858, 1785, 1775, 1495, 1250, 1056.

*2.2.5 Synthesis of alkyne-functionalized mannose glycopolypeptide (Pr-AcGP_{20}) as a hydrophilic block (**1d**)*

To a solution of α-manno-O-lys NCA (100 mg/mL) in dry dioxane was added with a "proton sponge" 1,8-bis(dimethylamino)naphthalene (1.0 equiv with respect to monomer, 1 M) as an additive and freshly distilled propargyl amine (0.5 M) as the initiator inside the glove box. The progress of the polymerization was monitored by FT-IR spectroscopy. The reaction was generally completed within 16 h. Then the solvent from reaction mixture was removed under reduced pressure. The resulting residue was dissolved in dichloromethane, and the polymer precipitated out by addition of methanol was collected by centrifugation and dried to get white solid.^{1}H NMR (400 MHz, CDCl3): δ (ppm): 1.10−1.80 (m, 6H), 1.92−2.18 (m, 12H), 2.97−3.35 (m, 2H), 3.70−3.90 (amide H's), 3.95− 4.35 (m, 3H), 4.95−5.35 (m, 2H), 5.35−5.50 (m,1H), 5.50−5.75 (m, 1H), 5.70−6.25 (amide H's).

2.2.6 Acetyl group deprotection of alkyne-functionalized mannose glycopolypeptide (Pr-GP_{20})

To a solution of acetyl-protected block copolypeptides (Pr-AcGP_{20}) in tetrahydrofuran, hydrazine monohydrate (25 equiv) was added and the reaction was allowed to stir at room temperature for 12 h. Reactions were quenched by the addition of acetone and the solvent was completely removed under reduced pressure. The filtrate was dried under reduced pressure and redissolved in deionized water and then transferred into a dialysis tubing MWCO of 2 KDa. The compound was dialyzed against deionized water for 3 days, with water changes once every 2 h for the first day and then thrice per day. Then the dialyzed polymer was lyophilized to get white fluffy solid.

^{1}H NMR (400 MHz, D2O): δ (ppm): 1.35−2.12 (m, 6H), 2.28(s, 1H), 3.00−3.25 (m, 2H), 3.60−3.90 (m, 5H), 3.95−4.45 (m, 2H), 5.80−5.95 (m, 1H).

*2.2.7 Synthesis of azido terminated poly-L-lysine (N_3-PLL_{100}) as cationic block (**2c**)*

To a solution of N$^{\varepsilon}$-Trifluoroacetyl-*L*-lysine NCA (2b) in dry DMF (100 mg/mL) was added azido-PEG-amine (DMF solution 0.5M) as the initiator (M/I= 100) inside the glove box. The progress of the polymerization was monitored by FT-IR spectroscopy. The reaction generally was completed within 36 h. The resulting polymer was re-precipitated in deionised (DI) water for couple of times. The precipitated polymer was collected by centrifugation and washed with DI water. A white solid was obtained and dried under high vacuum at 50 $^{\circ}$C to yield N_3-PLL(TFA)$_{100}$ (2c) in almost 90% yield.

^{1}H NMR (400 MHz, DMSO-d_6): δ (ppm): 1.25-2.12 (br m, 6H), 3.00−3.25 (br m, 2H), 3.48-3.68 (m, for CH_2CH_2O unit in initiator 24H), 3.7-4.4 (br m, 1H). FT-IR (cm^{-1}): 2116, 1342, 1649, 1552, 1264, 1059, 1107.

*2.2.8 Deprotection of N_3-PLL(TFA)$_{100}$ polymer (**2d**)*

The removal of labile triflouroacetyl (TFA) protecting groups of lysine was achieved by dissolving the polymer (100 mg) in THF (4 mL) followed by drop wise addition of KOH solution (1.5 eq) and stirring for an additional 24 h at room temperature. After complete deprotection, the solvent was removed by rotary evaporator to afford a solid residue. The residue was re-dissolved in deionized water and transferred to dialysis tubing (3.5 kDa MWCO). The samples were dialyzed against 0.01 N HCl for one day and then with water for another day with several water changes. Dialyzed polymers were lyophilized to yield N_3-PLL_{100} (2d) as white solids in the form of hydrochloride salt.

^{1}H NMR (400 MHz, D_2O): δ (ppm): 1.35-1.9 (m, 6H), 2.95−3.2 (m, 2H), 3.48-3.68 (m, for CH_2CH_2O unit in initiator 24H), 4.3-4.7 (br m, 1H). FT-IR (cm^{-1}): 3328, 2938, 2116, 1726, 1649, 1552, 1324, 1264.

*2.2.9 Synthesis of glycopolypeptide-b-poly-L-lysine (GP_{20}-PLL_{100}) cationic polymer (**4**)*

Azide-functionalized deprotected poly-*L*-Lysine (2d) (0.8 equiv) was added to a solution of deprotected alkyne terminated glycopolypeptide (1d) in phosphate buffer (pH=7.4, 50 mM), and the resultant reaction mixture was degassed by three freeze-pump-thaw cycles. A premixed solution of $CuSO_4$ (0.25 eq) and ligand THPTA (1.25 eq) was added followed by addition of sodium ascorbate (2.5 eq) and the reaction was allowed to proceed for 24 h at room temperature. The progress of the reaction was monitored by FT-IR spectroscopy. After completion of the reaction (disappearance of azide stretch ≥95%), reaction mixture was directly transferred into a dialysis tube (12 kDa MWCO) and dialyzed against EDTA solution for 1 day with solution (water) change every 4h and, followed by dialysis against deionized water solution for another day. Finally, the reaction mixture was dialyzed against 0.01 N HCl for an additional 1 day. Dialyzed polymers were lyophilized to yield white fluffy solids in the form of hydrochloride salt.

^{1}H NMR (400 MHz, D_2O): δ (ppm): 1.29−1.96 (br m, 12H), 2.78-2.95 (br m, 2H), 3.0-3.3 (br m, 2H), 3.4-3.53 (m, 24H), 3.56−3.72 (br m, 5H), 3.75−3.95 (br m, 2H), 4.2−4.45 (br m, 1H), 5.72-5.79 (br m, 1H). FT-IR (cm^{-1}): 3328, 2950, 1752, 1650, 1552, 1250.

*2.2.10 Synthesis of PEG_{2k}-$PBLG_{100}$ (**3b**)*

To a solution of benzyl-*L*-glutamate NCA in dry DMF (3a) (100 mg/mL) was added PEG_{2k}-NH_2 (DMF solution, 0.5 M) as the initiator (M/I= 100) inside the glove box (The progress of the polymerization was monitored by FT-IR spectroscopy. The reaction was generally complete within 24 h. The resulting polymer was re-precipitated in deionised (DI) water several times, collected by centrifugation and washed with DI water. The white solid obtained was dried under high vacuum at 50 °C to afford PEG_{2k}-$PBLG_{100}$ (3b) in almost 90% yield.

^{1}H NMR (400 MHz, $CDCl_3$): δ (ppm): 1.5-2.6 br (m, 4H),3.39 (br m, 3H), 3.4-3.7 (m,180H for CH_2CH_2O unit in initiator), 3.93-4.2 (br m,1H), 4.9-5.3 (br m, 2H), 7.42 (s, 5H) FT-IR (cm^{-1}): 3328, 1652, 1548, 1342, 1167, 1107, 749, 697.

*2.2.11 Deprotection of PEG_{2k}-$PBLG_{100}$ polymer (**3c**)*

A solution of PEG_{2k}-$PBLG_{100}$ polymer (100 mg) in THF (4 mL) was placed in 50 mL round bottom flask and cooled to 4°C. To this, NaOH solution (0.5 mL, 2M; ~1.5 equiv per carboxylic group) was added drop wise at 4°C, which resulted in a turbid solution after few minutes. The solution was left under vigorous stirring for 16 h at room temperature . After complete deprotection, the solvent was removed on rotary evaporator.. The crude product obtained was re-dissolved in deionised water, transferred into a dialysis tubing (3.5 kDa MWCO) and then dialyzed against DI water for two days with water being changed six times. Dialyzed polymers were lyophilized to yield PEG_{2k}-PLG_{100} (white solid) as a sodium salt.

^{1}H–NMR (400 MHz, D_2O): δ (ppm): 1.80-2.40 (br m, 4H), 2.14-2.38 (m, 2H), 3.39 (br m, 3H), 3.4-3.7 (m, 180H for CH_2CH_2O unit in initiator), 4.26-4.31 (br m, 1H). FT-IR (cm^{-1}): 3440, 3228, 1649, 1544, 1407, 1342.

*2.2.12 Synthesis of rhodamine-labeled PEG_{2k}-$PbLG_{100}$ polymer (**3d**)*

Et_3N (16.9 µmol, 22 µL) and RITC (6.7 mg, 3eq) were added to a solution of PEG_{2k}-$PBLG_{100}$ polymer (100 mg, 4.16 µmol) in dry DMF (5 mL) and stirred for 48 h. The reaction mixture was then precipitated in methanol (at least 5 times) to remove excess RITC. Finally, labeled polymer was deprotected and purified by dialysis as stated above. Dialyzed polymers were lyophilized to yield rhodamine-labeled anionic polymer (RhB-PEG_{2k}-PLG_{100}) as pink solids.

^{1}H–NMR (400 MHz, D_2O): δ (ppm): 1.5-2.6 (br m, 4H), 3.39 (s, 3H), 3.4-3.7 (m,180H for CH_2CH_2O unit in initiator), 3.93-4.2 (br m, 1H), 4.9-5.3 (br m, 2H), 7.42,7.47 (m, H for rhodamine phenyl protons) FT-IR (cm^{-1}): 3440, 3228, 1648, 1530, 1407, 1342, 794.

2.2.13 Synthesis of homo-anionic copolymer (*Hx-PLG_{100})*

Homo-anionic copolymer (Hx-PLG_{100}) was synthesized by polymerizing benzyl-*L*-glutamate NCA with hexylamine as initiator in dry DMF. The deprotection of the benzyl group to yield Hx-PLG_{100} was carried out using the same protocol described for the deprotection of PEG_{2k}-$PBLG_{100}$ polymer.

^{1}H–NMR (400 MHz, D_2O): δ (ppm): 0.83 (t, 3H for initiator), 1.80-2.40 (m, 4H), 2.14-2.38 (m, 2H), 4.26-4.3 (br, 1H). FT-IR (cm^{-1}): 3440, 3228, 1648, 1542, 1407.

2.2.14 Self-assembly of charged block polypeptides

Cationic block copolymers (GP_{20}-PLL_{100}) at a concentration of 1.0 mg/mL and anionic block copolymers (PEG_{2k}-PLG_{100}) at a concentration of 0.73 mg/mL were individually

solubilized in 50 mM phosphate buffer (pH 7.4). The solutions were filtered through a 0.22 μm membrane filter to remove dust particles and any other insoluble portions. GP_{20}-PLL_{100} solutions were added in one portion to a solution of PEG_{2k}-PLG_{100} at RT in an equal charge ratio of $-COO^-$ and $-NH_3^+$ and mixed thoroughly using a vortex mixer for 2 min. The resulting polymer solution was incubated for 24 h at room temperature to generate the GP-PICsomes. RhB labeled PICs were formed from rhodamine-labeled block aniomer (RhB-PEG_{2k}-PLG_{100}) with block catiomer (GP_{20}-PLL_{100}) following a similar methodology.

2.2.15 Sample preparation for TEM, AFM, SEM and DLS analysis

The solution of the GP-PICsomes (10 μL) was spotted on carbon-coated 400 mesh copper grid, kept for 15-20 min, the excess solvent was removed by touching the edge of the grid with Whatman filter paper and then grid was negatively stained by 0.2 wt% uranyl acetate for 10 s. The grid was washed twice with deionized water to remove excess unbound uranyl acetate from the grid. Grids were dried in desiccators for 20 h and analysed by transmission electron microscopy. For AFM and SEM analysis GP-PICsomes solution was drop casted on silicon wafer and dried for 24 h. An aqueous solution of GP-PICsomes was filtered using 0.45 μm filter paper for DLS analysis.

2.2.16 Preparation of FITC encapsulated GP-PICsomes

The encapsulation of hydrophilic molecule FITC-Dextran into the GP-PICsomes was done by the co-assembly method. First, filtered solutions of PEG_{2k}-PLG_{100} (1.46 mg/mL) and GP_{20}-PLL_{100} (1 mg/mL) were prepared separately in 50 mM phosphate buffer. 500 μL of GP_{20}-PLL_{100} solution (1 mg/mL) was added to a 500 μL solution containing 0.75 mg FITC-Dextran (M_n=5000) and 0.73 mg of PEG_{2k}-PLG_{100} in phosphate buffer (50 mM, pH 7.4) and mixed thoroughly with a vortex mixer. The solution was incubated for 24 h at room temperature to encapsulate FITC-Dextran into GP-PICsomes. The mixture was then placed into a dialysis membrane (50 kDa MWCO) and dialyzed against phosphate buffer (10 mM) at 4 °C for 24 h while changing buffer at a 4 h interval. Within 24 h all un-encapsulated FITC-Dextran was excluded from the dialysis membrane. After the removal of free FITC-Dextran, the mixture was dialyzed against deionized water for 24 h.

2.2.17 Release studies

Immediately after removal of excess FITC-Dextran, the dye loaded GP-PICsomes solution was transferred into a fresh dialysis tube and then immersed into 30 mL of

phosphate buffer solution (10 mM) and stirred at room temperature for 2 days. At predefined time points, aliquots (1 mL) were removed from the buffer solution outside the dialysis membrane, which was replaced with an equal volume of fresh buffer. Concentration of FITC-Dextran in the aliquots was estimated by fluorescence spectroscopy. Finally, release of FITC-Dextran from the GP-PICsomes was reported as a percentage of the total amount released from the dialysis tubes.

2.2.18 Fluorescence imaging of GP-PICsomes

An epifluorescence/total internal reflection fluorescence (TIRF) microscopy setup built on an inverted microscope (Nikon Eclipse TE2000-U) was used for imaging GP-PICsomes and study the process of aggregation and de-aggregation. Details on the home-built setup is provided elsewhere.[12] In brief, a 488 nm Argon ion laser (Melles Griot, Model: 35-MAP-321-240) and a 532 nm DPSS laser (Melles Griot, Model: LD-WL206) were used to illuminate the same area of the sample (field of view ~1000 μm^2) via an objective lens (Nikon, 1.49NA, 60X TIRF). The emission from the sample was collected by the same objective and passed through appropriate dichroic/long pass filters and detected by a CCD camera (DVC 1412AM). For co-localization studies of individual GP-PICsomes labelled with two fluorophores, FITC and RhB was selectively excited at 488 and 532 nm, and their emission was collected using a 445-530 nm and 545–630 nm bandpass emission filters, respectively. The excitation power (50-200 μW) was varied for the two lasers using neutral density filters such that comparable intensity of emission (within a factor of 3) is observed in the two energetically separated detection channels (colored green for FITC and red for RhB). Typically movies were collected with an exposure time of 100 ms, and averaged over 100 frames before further image processing. To monitor aggregation dynamics of GP-PICsomes (labelled with RhB) in presence of Con-A and their deaggregation in excess mannose, movies were collected at 5 Hz. ImageJ was used to obtained montage images from acquired movies, these show single-frame sequential snapshots at regular time interval. To visualize the trajectories of single GP-PICsomes and their aggregates in solution maximum projection (MP) images [40] rather than time average images were generated over a certain time interval using ImageJ. All measurements were performed at 295 K.

2.2.19 Sample preparation for fluorescence imaging of GP-PICsomes

(1) For hollowness and dye encapsulation in GP-PICsomes

Fluorescence imaging in solution was performed by placing 20 μL of FITC-Dextran encapsulated RhB-GP-PICsomes in between two glass cover slips and incubating for 10 min. For dry state measurements, the sample was spin coated (20 μL, 1000 rpm, 1 min; Ducom PRS-6K) on a clean cover slip and imaged after 30 min.

2.2.20 Sample preparation for fluorescence imaging of GP-PICsomes aggregation and de-aggregation

1.0 mg/mL solution of Con-A was prepared in 100 mM phosphate buffer (pH 7.4) containing 0.1 mM $MnCl_2$, 0.1 mM $CaCl_2$ and 0.1 M NaCl. The aggregation experiment was performed by preincubating RhB-GP-PICsomes with Con-A, and sandwiching this solution in between two glass coverslips. A reservoir of buffer solution was maintained on both sides of solution to prevent solvent evaporation. Alternatively, Con-A was introduced between the coverslips and incubated for 10 minutes for adsorption on glass surface and excess Con-A solution was washed out by capillary action using a filter paper at one end while maintaining enough buffer in the reservoir on the other end. Finally, RhB-GP-PICsomes solution was introduced from reservoir end of the coverslips while imaging. Movies were collected at 3 Hz to visualize the aggregates. For de-aggregation studies, preformed aggregates were prepared by mixing Con-A solution (50μL) and RhB-GP-PICsomes solution (100μL) for different times (10-30 min). This mixture was then introduced into a home-made flow chamber through an injection pump where flow rates can be controlled. After visualizing aggregates of RhB-GP-PICsomes, enough buffer was injected to wash off excess aggregates and unbound Con-A, followed by introduction of buffer containing 300 mM mannose. Flow of solution was controlled using the syringe pump. The control experiment for deaggregation process with 300 mM galactose solution was not only performed under identical conditions but also for much longer time (10 min) incubation with excess galactose.

2.3 Results and Discussion

2.3.1 Synthesis and characterization of cationic block copolymers

The cationic block copolymer (catiomer: GP_{20}-PLL_{100}) was obtained by independently synthesizing alkyne-functionalized GP_{20} and azide-functionalized PLL_{100} and then conjugating them using "click chemistry". GP_{20} containing pendent carbohydrate moieties with an alkyne at the chain end were synthesized by following the previously developed methodology that involves propargyl amine initiated ROP of the mannosyl-N-

carboxyanhydride (NCA) monomer.[37] The removal of acetyl protection followed by purification led to fully water-soluble alkyne terminated GP (Scheme 2.1).

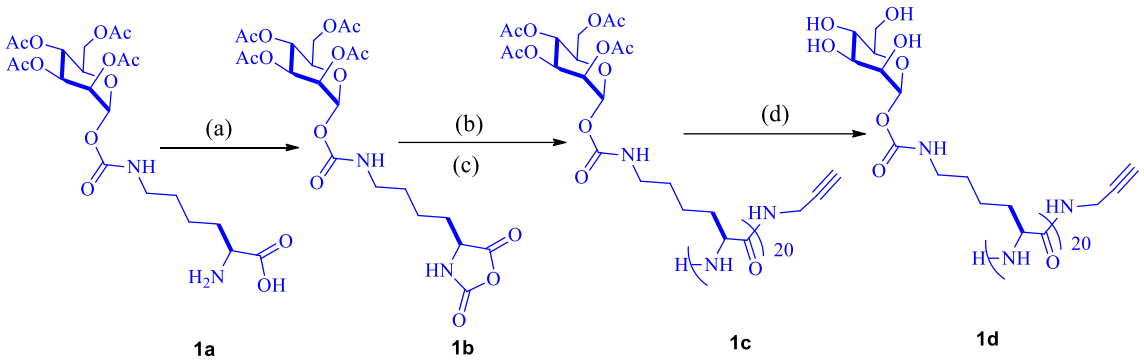

(a) Triphosgene, α-pinene, dry THF, 60°C (b) Propargylamine, dioxane (c) Proton Sponge (1.0 eq), 24 h, room temperature (d) THF, Hydrazine hydrate (25 equiv), 12 h.

Scheme 2.1 Synthesis of alkyne-functionalized mannose glycopolypeptide (Pr-GP_{20}).

The cationic azide-functionalized poly-*L*-lysine block (N_3-PLL_{100}) was synthesized from ring opening polymerization of triflouroacetyl-protected lysine NCA and then triflouroacetyl groups were deprotected in the presence of KOH (Scheme 2.2). All of the protected copolymer building blocks which contain alkyne-$AcGP_{20}$ and azide-$PLL(TFA)_{100}$ had low dispersity (Figure 2.2) and the chain length of each polymer (M_n) was determined from ^{1}H NMR spectra using end-group analysis (Table 2.1 and Appendix A:NMR section).

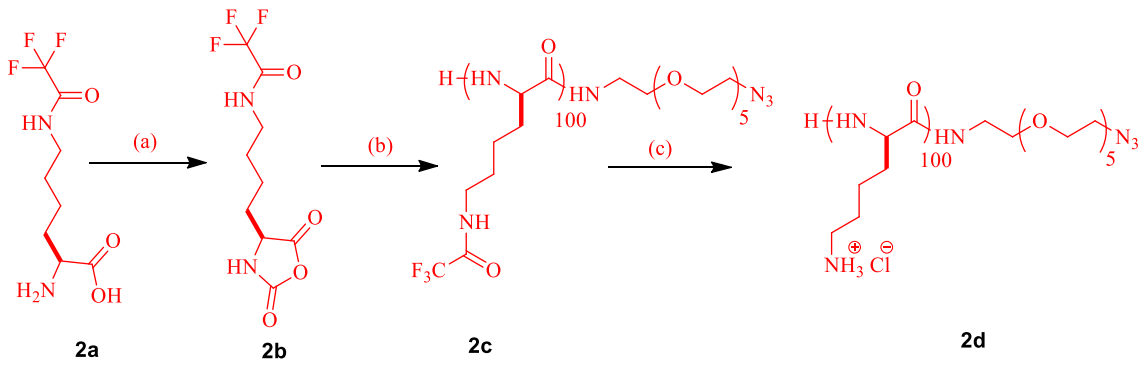

(a) Triphosgene, α- pinene, dry THF, 60°C (b) N_3-PEG-NH_2, DMF (c) THF, KOH (1.5eq)

Scheme 2.2 Synthesis of azide-terminated poly-L-lysine (N_3-PLL_{100}).

The M_n values determined matched closely to that expected from M/I values. After deprotection of copolymers, both alkyne-GP_{20} and azide-PLL_{100} were conjugated using copper-catalyzed azide-alkyne click reaction to synthesize cationic block-co-glycopolypeptides (GP_{20}-PLL_{100}) (Scheme 2.3).

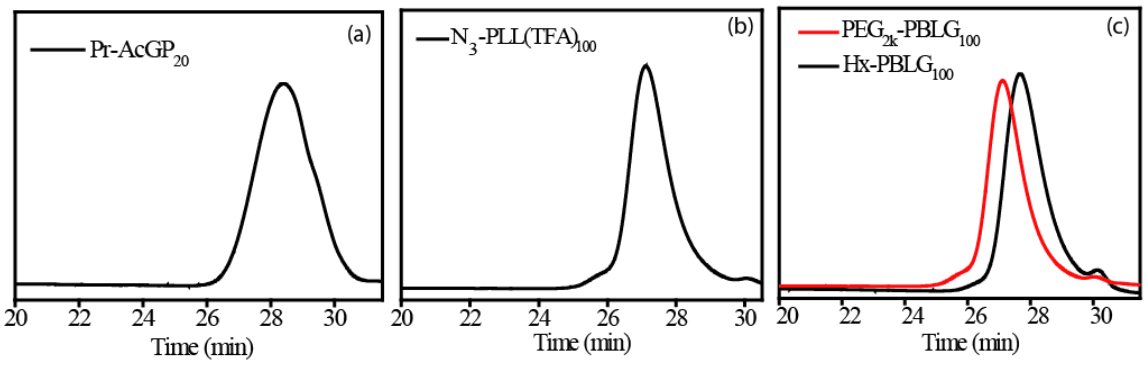

Figure 2.2: Size exclusion chromatograms of (a) Pr-$AcGP_{20}$ (b) N_3-$PLL(TFA)_{100}$ (c) PEG_{2k}-$PBLG_{100}$ and Hexyl-$PBLG_{100}$.

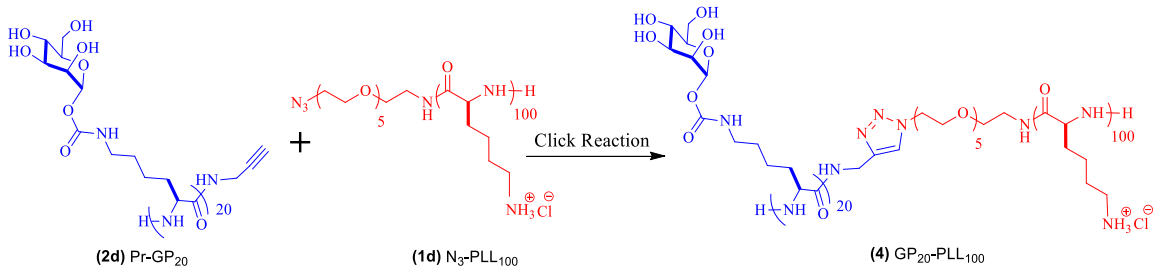

Scheme 2.3 Synthesis of glycopolypeptide-b-poly-*L*-lysine (GP_{20}-PLL_{100}) (4).

The progress of the reaction was monitored using FT-IR spectra by following the decrease in the characteristic azide stretch at 2117 cm^{-1} (Figure 2.3a).

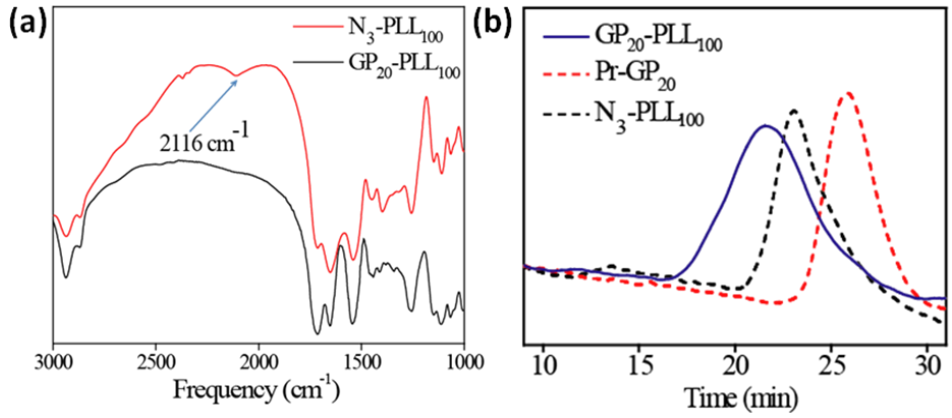

Figure 2.3: Characterisation of cationic block copolymer (a) FTIR spectra of the precursor polymer N_3-PLL_{100} and GP_{20}-PLL_{100} (catiomer) after "click" reaction. (b) Aqueous GPC curves of the GP_{20}-PLL_{100} from reaction mixture overlaid with curves of parent polymers.

After the reaction was complete, dialysis against EDTA solution was performed to remove all the residual copper followed by dialysis (using 12 kDa MWCO dialysis membrane) against DI water to remove the excess GP (molecular weight of deprotected GP is 7 kDa) used in the click reaction. SEC analysis of this purified GP_{20}-PLL_{100} block co-polypeptides was performed to ascertain the efficiency of click reaction. Aqueous GPC of the purified "clicked" product (Figure 2.3b) displayed a new peak at higher molecular weight, which was distinctly shifted from the parent GP and poly-lysine, suggesting the formation of the clicked product. Moreover, the complete absence of characteristic organic azide stretch (2115 cm^{-1}) in IR analysis (Figure 2.3a) suggests a near-quantitative click reaction. The exact composition of the block co-polypeptide was determined from ^1H NMR by comparing the integration of characteristic peaks present in GP and PLL segments which were in the expected molar ratio of 1:1 (Figure 2.4).

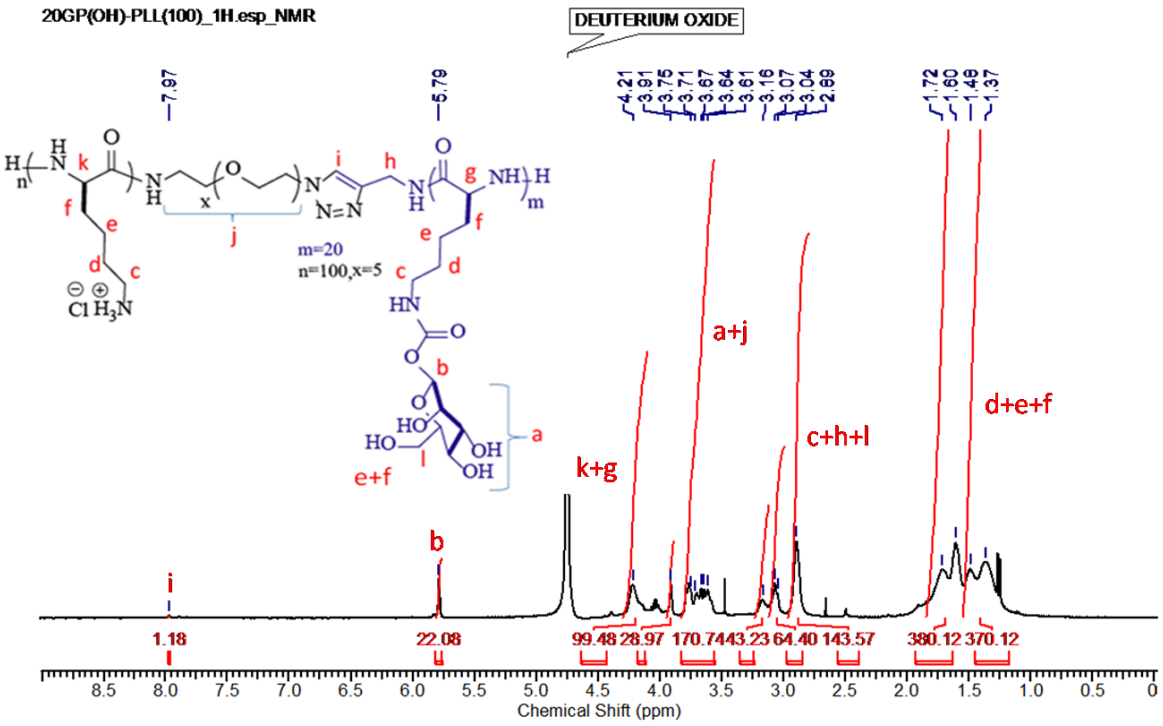

Figure 2.4: ^1H NMR spectrum of the synthesized GP_{20}-PLL_{100} (**4**) block copolymer (catiomer).

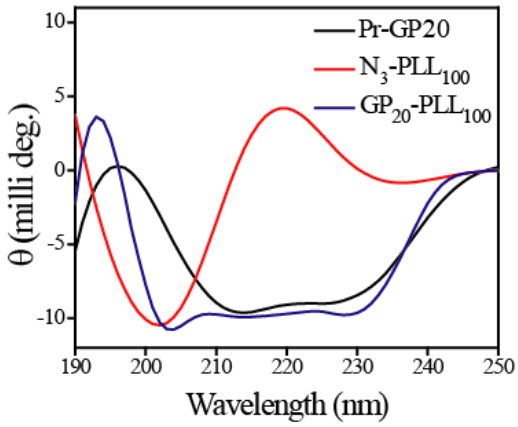

Figure 2.5: Circular dichroism spectra of parent polymers Pr-GP_{20}, N_3-PLL_{100} and block catiomer GP_{20}-PLL_{100} in 10 mM phosphate buffer (pH 7.4).

2.3.2 Synthesis and characterization anionic block copolymers

For anionic block co-polypeptides, ROP of γ–benzyl-*L*–glutamate N-carboxyanhydride was performed by using PEG_{2k}–NH_2 as the macroinitiator (M/I = 100) in dry DMF (Scheme 2.4 and Table 2.1). The completion of the reaction was confirmed by the complete disappearance of the anhydride stretch of initial NCA at 1785 and 1858 cm^{-1} in the FT-IR spectra (Figure A1c) The number average molecular weight (M_n) was calculated by ^{1}H NMR from the relative intensity of the peak at 3.68 ppm corresponding to the characteristic proton (-OCH_2CH_2) present in the initiator PEG-amine with the proton peaks of the phenyl ring (-C_6H_5) present in the benzyl-ester moiety of the polymer (7.30 ppm). The molecular weight distribution observed from GPC was monomodal and the dispersity was reasonably narrow (1.11) (Figure 2.2c and Table 1). PEG_{2k}-PLG_{100} was prepared by benzyl-ester deprotection of PEG_{2k}-$PBLG_{100}$ using base hydrolysis. ^{1}H-NMR of resulting polymer showed complete disappearance of the signals corresponding to the benzyl group and rest of the signals were assigned to PEG_{2k}-PLG_{100} (Figure 2.6).

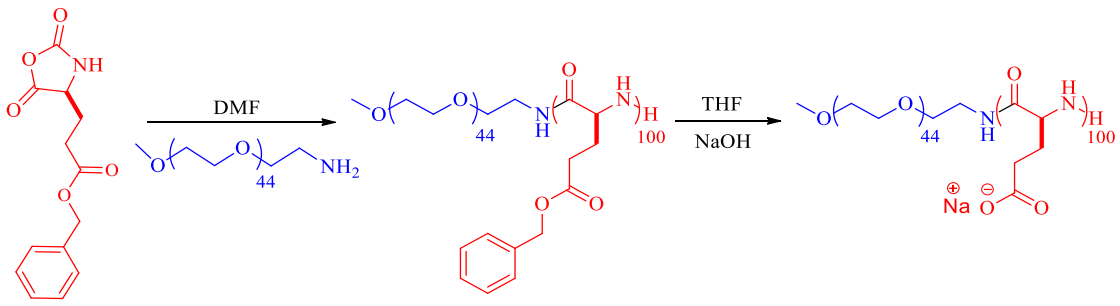

(3a) Bn-Glu-NCA **(3b)** PEG_{2k}-$PBLG_{100}$ **(3c)** PEG_{2k}-PLG_{100}

Scheme 2.4 Synthesis of *PEG*$_{2k}$-PLG_{100} by ROP of Bn-Glu-NCA using PEG_{2k}-NH_2 as the macroinitiator.

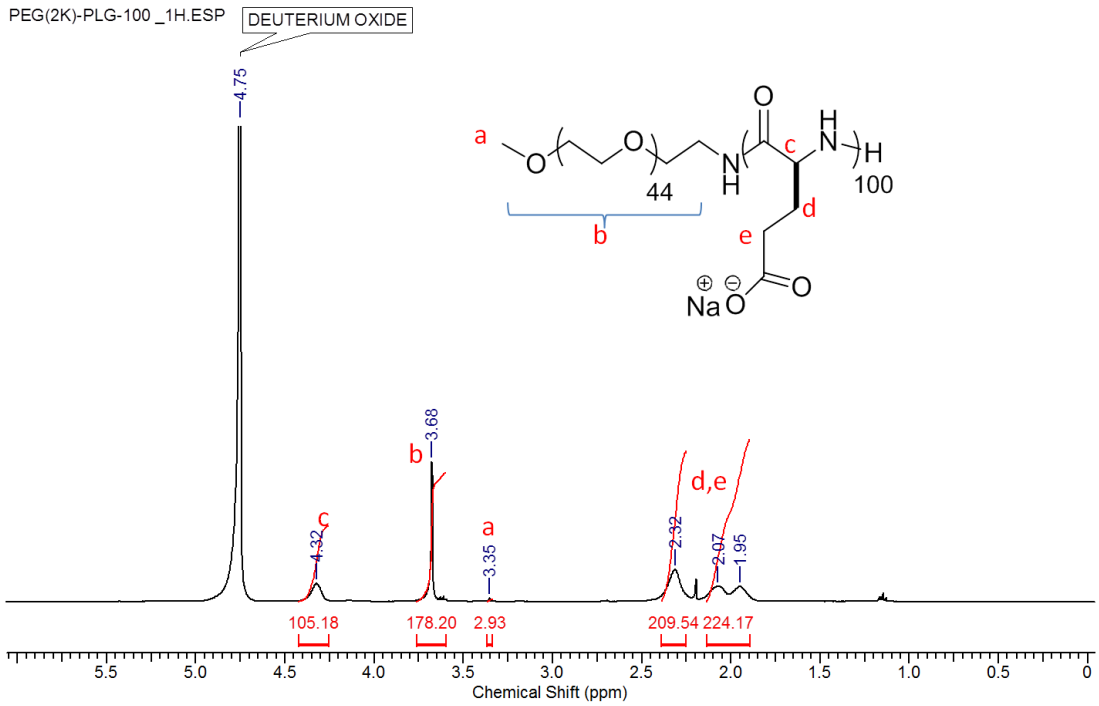

Figure 2.6: ^{1}H NMR spectrum of the synthesized PEG_{2k}-PLG_{100} (3c) block copolymer.

Table: 2.1: Characterization data for alkyne-AcGP, azide-PLL(TFA), PEG_{2k}-PBLG and their corresponding deprotected polymers.

Entry no.	Initiator (I)	Protected polymers	M/I[a]	M_n[b] (10^3g/mol)	DP[c]	M_w/M_n[d]	DP[e]	Deprotected polymers	DP[f]
1	Propargyl amine	$AcGP_{20}$	20	11.0	22	1.15	24	GP_{20}	22
2	N_3PEGNH_2	$PLL(TFA)_{100}$	100	22.9	102	1.12	106	PLL_{100}	102
3	$PEG_{(2k)}$-NH_2	$PBLG_{100}$	100	24.9	105	1.10	110	PLG_{100}	105
4	Hexylamine	$PBLG_{100}$	100	21.8	97	1.11	111	PLG_{100}	97
5								GP_{20}-PLL_{100}	22+102

[a]Monomer to initiator ratio. [b]Number average molecular weight calculated from GPC. [c]DP was calculated from 1H NMR. [d]M_w/M_n were calculated from GPC. [e] DP was calculated from GPC, [f] DP was calculated from ^{1}H NMR (Appendix A: NMR section).

2.3.3 Self-assembly of charged block copolymers

GP-PICsomes were prepared by self-assembly of oppositely charged double hydrophilic block copolymer *via* the electrostatic interaction between GP containing catiomer and PEG containing aniomer. Kataoka had previously demonstrated that uniform PICsomes were formed by mixing of cationic PEG_{2k}-*b*-poly(aspartamide)$_{100}$ and PEG_{2k}-*b*-

poly(aspartate)$_{100}$.[23] They subsequently demonstrated that the usage of large volume of PEGs, or higher PEG weight fraction (f_{PEG}) in the block copolymers, prevented the growth of PIC and drove micelle formation due to the immiscibility of PEG part and PIC part, as well as large steric hindrance of the PEG strands. [24,25] Therefore, for the preparation of GP-PICsomes synthesis of a double hydrophilic catiomer GP$_{20}$-*b*-poly(*L*-lysine)$_{100}$ and aniomer PEG$_{2k}$-*b*-poly(*L*-glutamate)$_{100}$ was attempted such that upon mixing, the 100-mer poly-*L*-lysine and poly-*L*-glutamate would generate the stable PIC membrane where most of the GP$_{20}$ and PEG$_{2k}$ moieties would form the outer and inner layers, respectively. Since the carbohydrate side chains are very bulky (M.W. 7 kDa), using GP in both the catiomer and aniomer was avoided to prevent formation of micelles. A short PEG$_{2k}$ was used in the aniomer instead to help the PIC transform into PICsomes. In order to confirm the type of supramolecular structure formed upon self-assembly of oppositely charged block copolymers, SEM was performed on GP-PICsomes cast on a surface under solvent evaporated conditions. SEM measurements showed the presence of a spherical morphology (Figure 2.7a) having an average diameter of 1.67 µm with sizes ranging between 1.2 µm and 2.2 µm (Figure 2.7b). GP-PICsomes were also characterized by TEM after negatively staining with uranyl acetate (0.2 wt %) solution. TEM analysis also indicated presence of well-dispersed PICsomes with spherical structure having a characteristic dark rim on the outer surface, indicating their hollow morphology (Figure 2.7c). Further evidence of hollow morphology was obtained from AFM measurements on silicon wafer (Figure 2.7d) which revealed a wall thickness of ~30 nm and a height/diameter ratio of ~0.08, which is consistent with a spherical hollow vesicular morphology.[41] Since all the above microscopic analyses were performed in the dried state, the size of the PICsomes formed after 24 h incubation of the GP$_{20}$-PLL$_{100}$ and PEG$_{2k}$-PLG$_{100}$ with was analyzed by DLS technique from which an average diameter of 1.46 µm was determined. This was again consistent with SEM and TEM measurements (Figure A2). The sizes and distribution of GP-PICsomes were also determined by optical micrograph which also showed an average diameter of 1.43µm (Figure A4). The vesicle wall thickness of 25-30 nm obtained from both TEM and AFM approximately equals the size of a fully extended chain length of the constituent polyelectrolyte strands (~25 nm), roughly estimated by summation of the average backbone length of each amino acid unit in the polypeptide chain (C-C-N, 0.24nm).[27] This suggests that the vesicle wall is composed of a monolayer of PIC sandwiched by PEG and GPs palisades or the mixture of both PEG and GP part in the inner and outer surface.

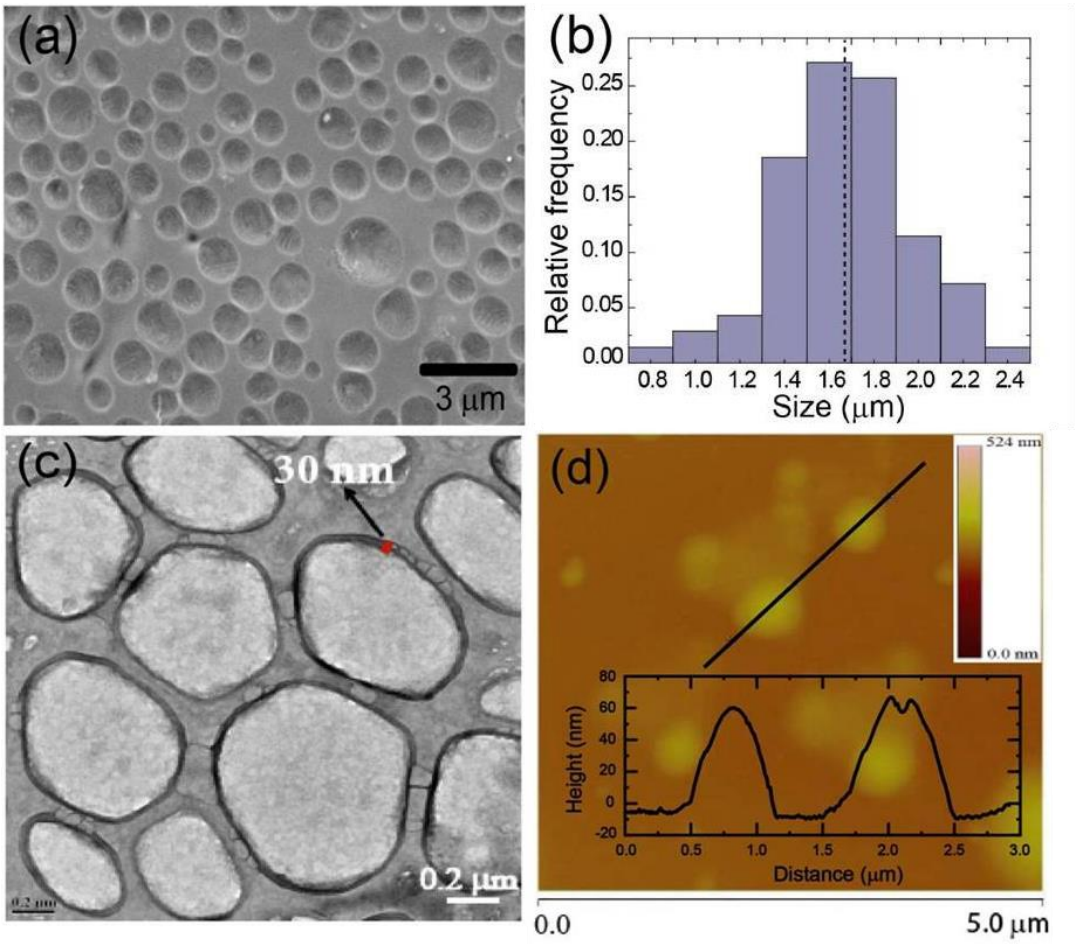

Figure 2.7: GP-PICsomes formed via self-assembly upon addition of equimolar amounts of GP_{20}-PLL_{100} and PEG_{2k}-PLG_{100} (a) SEM image of GP-PICsomes (b) Size distribution of GP-PICsomes from SEM images (c) TEM image of GP-PICsomes (d) AFM image of the GP-PICsomes drop cast from aqueous solution on silicon wafer and corresponding height profile.

It is hypothesized that in this system the growth of GP-PICsomes in aqueous medium is initiated by uPIC formation, which is a result of the bilayer formed due to the interaction between cationic amino groups in (GP_{20}-PLL_{100}) and anionic glutamate groups in PEG_{2k}-PLG_{100} resulting in charge neutralization.[28] This uPIC units grow over time resulting in an initial formation of a three-layered membrane structure consisting of a middle PIC phase sandwiched by external and internal hydrophilic shell layers (PEG and GP). When the membrane-like aggregates become so large that the interfacial energy is predominant, the membrane-like bilayer closes to form vesicles. The bending of the three layer lamellar structure would reduce the interfacial free energy and enclose it into a vesicular morphology.[42-45] Since the uPIC is composed of 100-mer PLL and 100-mer PLG, it would behave as a stiff polymer unit with low internal degrees of freedom, as well as low formational entropy. Following the general rule that increasing order inherently leads to

an increased bending modulus (κ) of the bilayers, a vesicle with relatively low interfacial curvature leading to large sizes (micron diameter) is expected. It is to be noted that the molecular weight of the shell layer GP_{20} (M.Wt. 7 KDa) was significantly higher than that of PEG_{2k} and such high weight fractions have been earlier shown to prevent formation of PICsomes. However, their self-assembly into PICsomes is likely due to the efficient packing of the helical GP_{20} unit (see circular dichroism data in Figure 2.5) at the surface of GP-PICsomes which induces morphology bearing a lower curvature as has been observed earlier with amphiphilic glycopolypeptides.[11,12,14,16] In GP-PICsomes, three possibilities exist during the formation of the three layer lamellar structure with respect the position of GP_{20} and PEG_{2k} in the inner layer (I) or outer layer (O) of the PICsomes: [(I)PEG-PIC-(O)GP], [(I)PEG,GP-PIC-(O)PEG,GP], [(I)GP-PIC-(O)PEG]. Since GP_{20} is much more bulky than PEG_{2k}, the assemblies will prefer a morphology with less curvature and hence GP_{20} chains are expected be present on the outer surface of the PICsomes (the first two of the three possible structures mentioned above). The presence of glycopolypeptide part on PICsomes outer surface is later confirmed by investigating their interaction with carbohydrate binding protein (lectins). It is possible that some of the PEG_{2k} chains are also present in the outer layer, however it was not possible to determine the extent of heterogeneity. The presence of PEG_{2k} in the aniomer was critical to the formation of PICsomes. Upon mixing equimolar solutions of GP_{20}-PLL_{100} with the homoaniomer Hx-PLG_{100}, formation of no well-defined structures was observed (Figure A5).

2.3.4 Stability and dye encapsulation studies of GP-PICsomes

In aqueous solution the hollow nature of the spherical particles were tested by encapsulating hydrophilic macromolecule FITC-Dextran. UV-Vis spectra of FITC-Dextran encapsulated GP-PICsomes shows a characteristic peak (λ_{max}) at 490 nm (Figure 2.8). The encapsulation efficiency (EE) was determined as $EE = (W_1/W_2) \times 100$, where W_1 is the amount of FITC-Dextran encapsulated and W_2 is the amount of FITC-Dextran added initially for encapsulation. The value of W_1 was calculated by measuring the optical density at 493 nm (molar absorption coefficient of FITC-Dextran in water is taken as 75000 L mol^{-1}). The percentage encapsulation efficiency of FITC-Dextran was determined to be ~2.06 %.

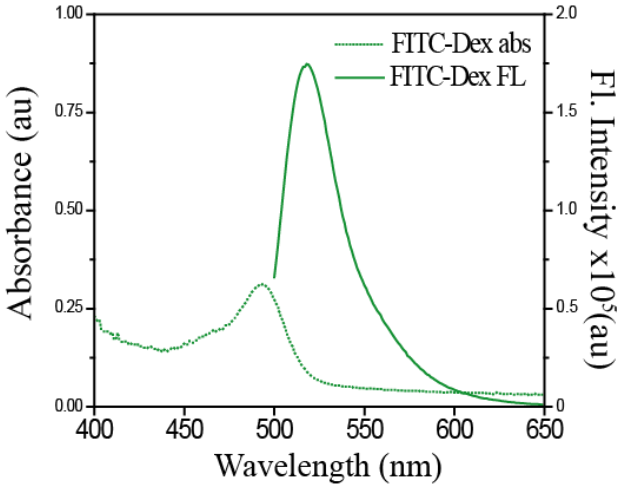

Figure 2.8: Absorption and emission spectra of FITC-Dextran loaded GP-PICsomes.

To test release of FITC-Dextran from GP-PICsomes, the aqueous solution of FITC-Dextran encapsulated GP-PICsomes was dialyzed against phosphate buffer solution for 2 days. Emission spectra of the phosphate buffer outside the dialysis tube indicated leakage of FITC-Dextran with passage of time (Figure 2.9a). After 48 hours, the leakage of FITC-Dextran was estimated by comparing the absorption spectra of FITC-Dextran encapsulated GP-PICsomes inside dialysis tubing before and after the release experiment. The percentage of FITC-Dextran released in this period of 48 h was determined to be approx 63.2% (Figure 2.9b), which indicates its slow release from the GP-PICsomes.

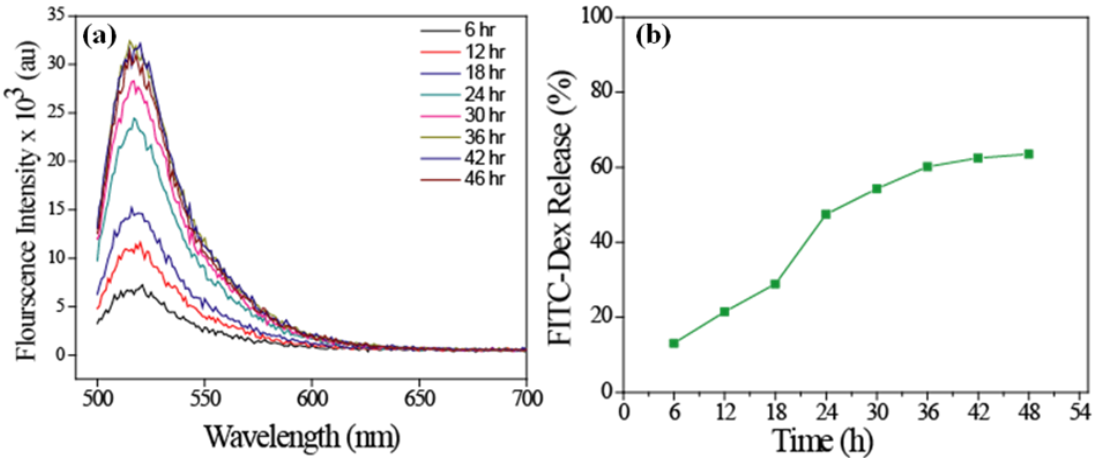

Figure 2.9: (a) Emission spectrum of FITC-Dextran in PBS released from the dialysis tube over a time period of 48 h (b) Plot of % of FITC-Dextran as a function of time.

2.3.5 Visualization of individual GP-PICsomes

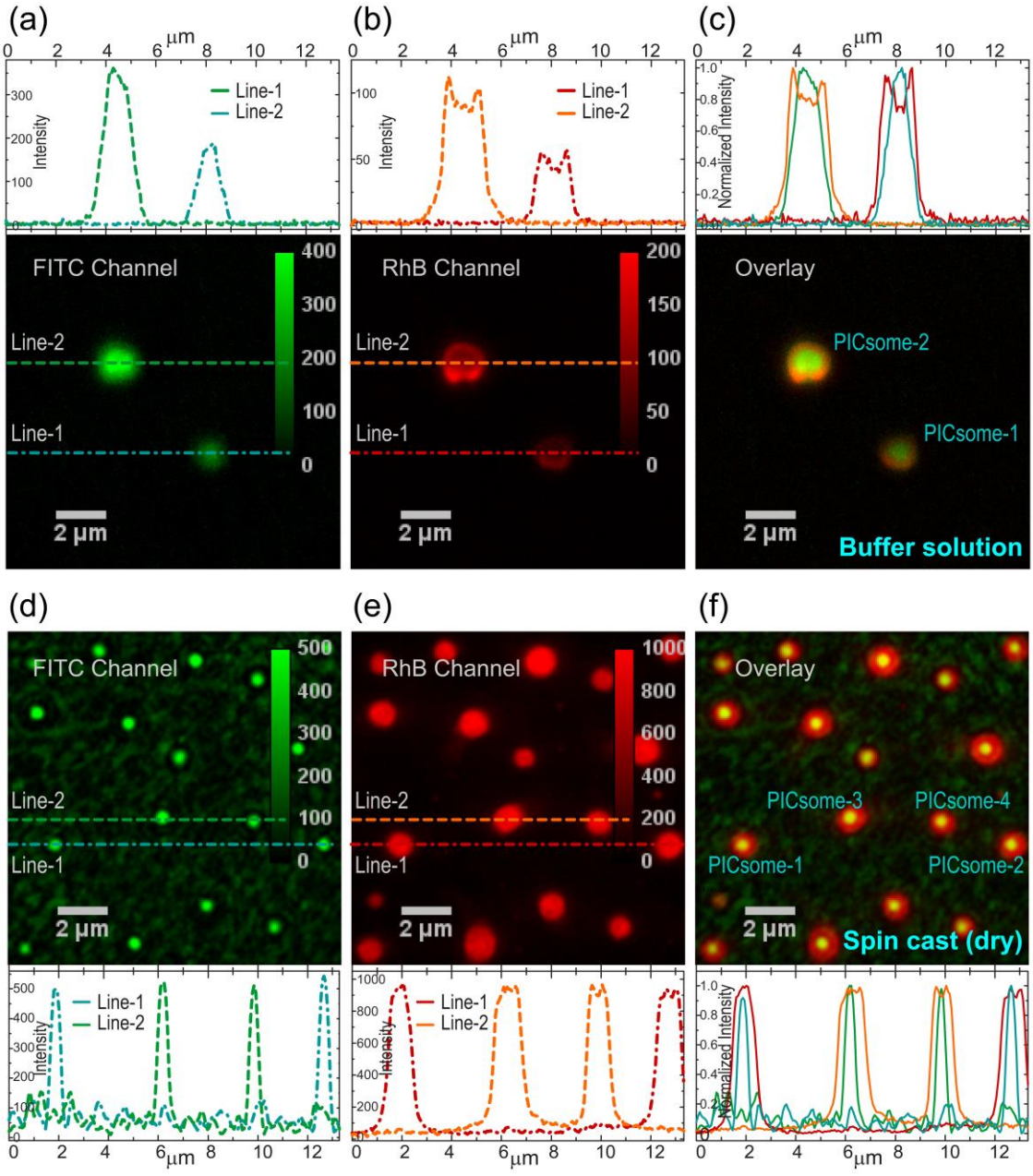

Figure 2.10: Fluorescence images of individual GP-PICsomes labeled with both FITC and RhB in solution (a-c) and spin cast on glass coverslips (d-f), collected through band pass filters for FITC (a, d) and RhB (b, e) emission (colored green and red, respectively), along with pseudo color images (c,f) obtained via quantitative superposition of intensity images acquired for the same area through two detection channels.

Although both AFM and electron microscopy measurements provide crucial information on the size distributions and shape of the GP-PICsomes under dried conditions, it is difficult to conclusively comment whether the solution structures are indeed preserved upon solvent evaporation (for drop cast samples). Further, it is also challenging to

conclude directly from AFM or TEM measurements whether the morphology of GP-PICsomes are indeed hollow, as indicated by dye encapsulation studies. As the dimensions of these GP-PICsomes are much larger than the diffraction limit, the most direct way to test their morphology (and dimensions) in solution is to image individual PICsomes with two fluorescent dyes located in different spatial regions (central water pool and PIC shell regions).

To study co-localization behaviour, RhB labeled GP-PICsomes were synthesized by the self-assembly of block aniomer RhB-PEG_{2k}-PLG_{100} and block catiomer (GP_{20}-PLL_{100}), following which hydrophilic FITC-Dextran dye was encapsulated within the RhB-GP-PICsomes. Careful optimization on the relative proportion of encapsulated FITC-Dextran and sequential excitation of the two dyes was done by using 488 nm and 532 nm lasers and it allowed us to visualize GP-PICsomes in solution with comparable emission intensity (within a factor of 3) in energetically separated detection channels. Figure 2.10(a-c) shows two such individual FITC encapsulated RhB-GP-PICsomes in buffer solution. It is important to note that the vast majority of the GP-PICsomes undergo diffusion in solution; however, it was possible to image few spatially segregated PICsomes which adhere to the glass surface and do not undergo any translational motion. The images obtained from both the emission channels show that in solution, GP-PICsomes are quasi-spherical and have dimensions of 1-2 μm, consistent with AFM and electron microscopy measurements (Figure 2.7). More importantly, the spatial intensity profiles in the two detection channels display contrasting (filled and ring-like) emission patterns (Figure 2.10a, 2.10b), which can be readily visualized in the pseudo color overlay images (Figure 2.10c) as well as in the intensity line profiles, as expected for a hollow morphology.

In contrast, the emission behaviour of GP-PICsomes in the absence of solvents are quite different, as observed from dual-color imaging of FITC encapsulated RhB-GP-PICsomes spin-cast on glass coverslip from the solution described in Figure 2.10(d-f). First, solvent evaporation leads to higher density of individual PICsomes that can be imaged in the same field of view. Interestingly, the relative background emission in the FITC channel (Figure 2.10d) is significantly higher as compared to that in solution (Figure 2.10a), which suggests partial leaching of encapsulated FITC upon solvent removal. This inference is further supported by the images of single GP-PICsomes (and corresponding line profiles) observed in the RhB channel (Figure 2.10e), which have much higher intensity as well as

spatial uniformity in emission (in edges and central regions) as compared to that in solution, presumably due to shrinkage of GP-PICsomes during dehydration (leaching). Furthermore, it is also evident from the overlay image (Figure 2.10f) and intensity line-profiles that the emission originating from FITC within GP-PICsomes is far more localized (300-500 nm) as compared to those in buffer solution. This indicates that existence of water pools of relatively smaller dimensions within flattened PICsomes, where remaining hydrophilic FITC-Dextran accumulate and increase the effective local concentration thereby producing a relatively intense localized emission from within constricted GP-PICsomes. Nonetheless, both these measurements performed in buffer solution and under dry conditions provide direct evidence on the existence of hollow morphology for such large GP-PICsomes.

2.3.6 Dynamics of GP-PICsomes and their interaction with Con A

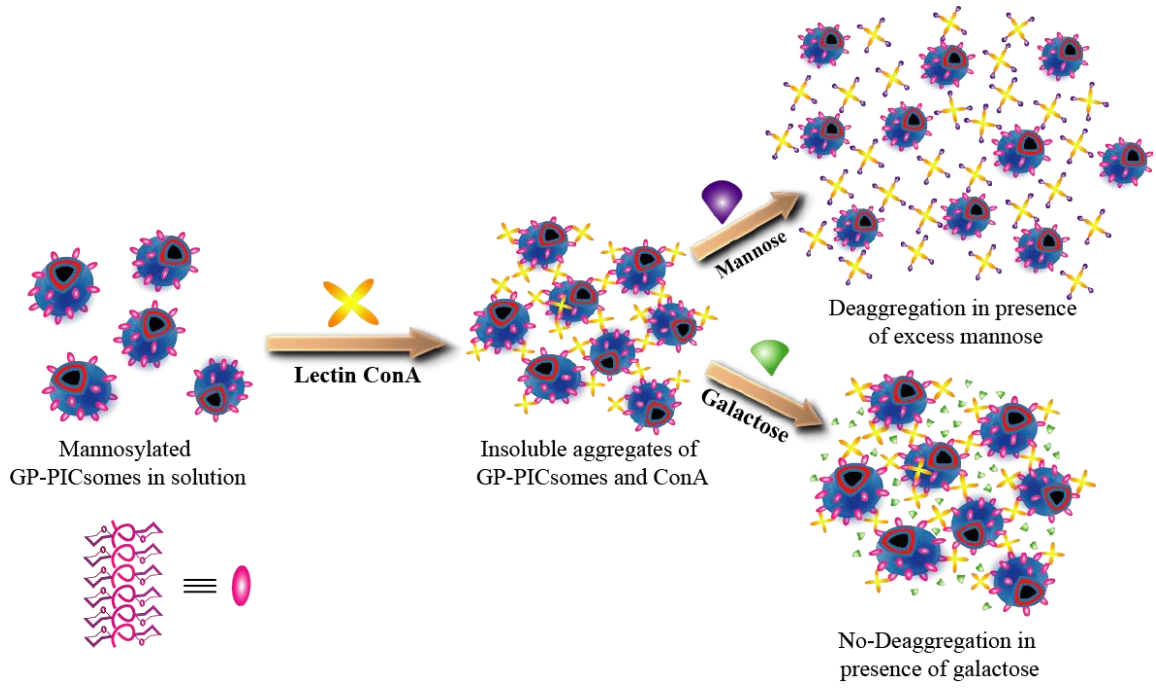

Figure 2.11: Schematic depiction of multivalent association of GP-PICsomes mediated by mannose binding lectin (Con-A) which lead to aggregation, and disassembly of aggregates only in presence of excess free mannose (not galactose) in solution.

To address whether glycopolypeptides were displayed on the outer-surface of the mannose-containing PICsomes and verify that surface remained bioactive upon self-assembly, the aggregation behaviour of GP-PICsomes upon addition of the mannose specific lectin, ConA, as well as de-aggregation of clustered PICsomes in excess of free

mannose was studied. Simple turbidimetic assays were not performed, as free GP_{20}-PLL_{100}, if still present in solution, could also cross-link with Con-A to form turbid solutions. The relatively large (~μm) size of the GP-PICsomes, which is expected to diffuse sluggishly in solution, allowed us to probe Con-A induced aggregation dynamics of individual assemblies in buffer solution using epifluorescence video microscopy. As depicted in Figure 2.11, if the mannose moieties are present on the outer surface of the GP-PICsomes, their polyvalent interaction with the tetrameric Con-A would lead to formation of large PICsomes aggregates. In contrast, if the GP moieties are present in the inner-membrane post self-assembly, addition of Con-A would show not lead to association of two or more GP-PICsomes, and therefore would not induce aggregation. The dynamics of two single RhB-GP-PICsomes in buffer solution in absence of any external hydrodynamic force is shown in Figure 2.12a, where each PICsome undergo 3D translational motion as evidenced from the spatial intensity distributions of their trajectories. The diffusion dynamics of GP-PICsomes can be easily captured at 0.5-1 Hz due to their relatively large size, however, diffusion constants were not extracted because it is unclear whether they interact with the glass surface intermittently. Upon incubation (for 15 min) with 0.5 mg/mL lectin receptor (Con-A), which has four mannose binding sites, individual PICsomes were rarely detected even under dilute conditions. Rather, the diffusion of small aggregates constituting of few (typically 3-6) GP-PICsomes can be readily visualized upon addition of Con-A (Figure A6). The tumbling dynamics (without any hydrodynamic drag) of one such small aggregate assembly, constituting of 5 or 6 GP-PICsomes attached to each other, is shown as single-frame snapshots in Figure 2.12b (from 0-20s) along with their trajectory (Figure A7: Movie 3). It was noticed that this small aggregate eventually gets attached to the surface (after ~20 s) presumably due to binding to surface adsorbed Con-A. To test this, excess Con-A solution (1 mg/mL) was introduced on a glass cover slip and incubated for 10 min, so that some of it adsorbs on the substrate. After removal of excess Con-A with buffer solution, GP-PICsomes were introduced in the flow chamber. Here, surface attachment of aggregates and their eventual immobilization in presence of slight hydrodynamic flow can be observed frequently, as exemplified for another aggregate shown in Figure 2.12c. It was noticed that in presence of excess (1mg/mL) Con-A in solution, higher order aggregation is induced (Figure 2.12d), where all the GP-PICsomes within the aggregate tumble (and move) synchronously, while the entire aggregate assembly diffuse sluggishly even in presence of weak flow.

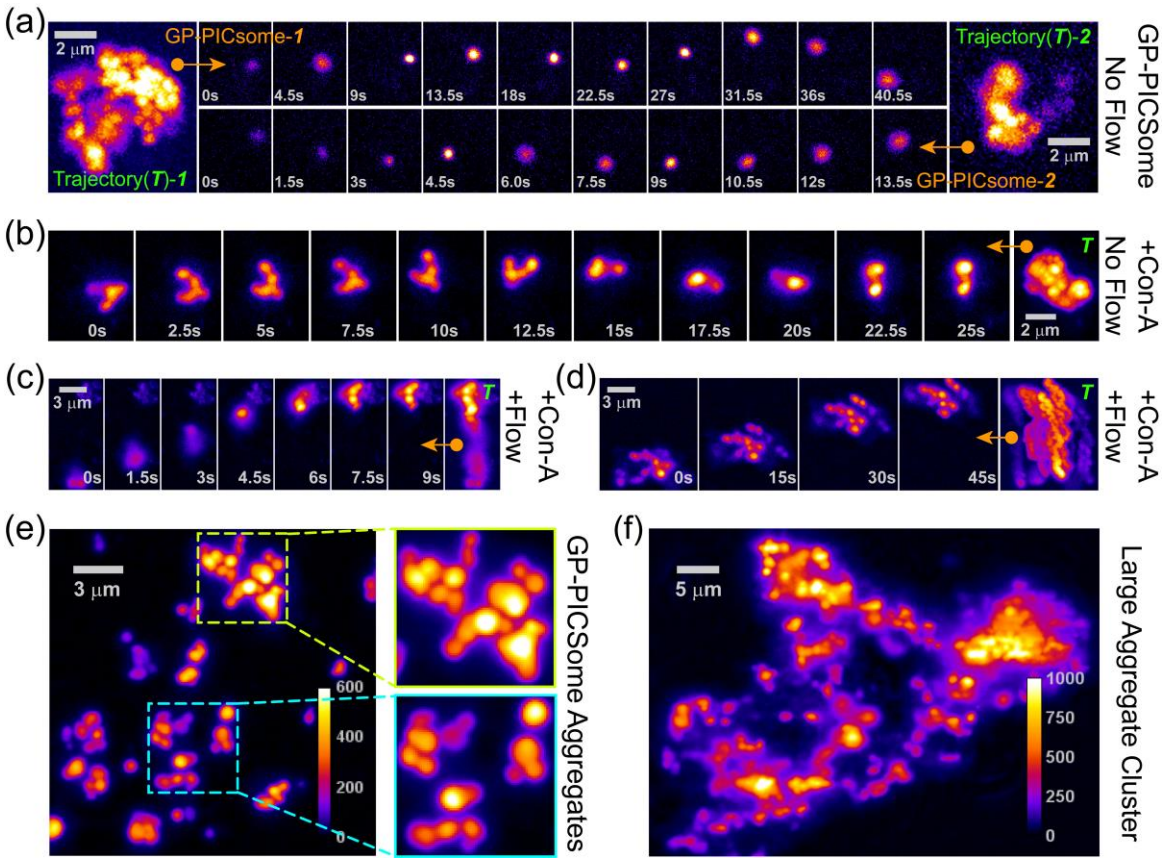

Figure 2.12: (a) Dynamics of individual RhB labeled GP-PICsomes in the absence of any external hydrodynamic force. Top and bottom rows represent ten single-frame sequential snapshots for two representative GP-PICsomes in solution. Left and right panels represent corresponding maximum projection (MP) images[40] of same area (at 2× magnification) for trajectory duration of 40.5s and 13.5s. (Movie 1 and 2) (b-d) Solution dynamics and eventual surface association of GP-PICsome aggregates of various sizes formed upon addition of Con-A, in absence (b) and presence (c-d) of weak hydrodynamic flow. Rightmost panels in (b-d) depict MP images over entire trajectories from which representative single-frame sequential snapshots are shown for each aggregate. (Movies 3, 4 and 5) (e) Variety of multiple scattered GP-PICsome aggregates attached on to glass surface with blowups (5×5 μm) depicting the presence of many GP-PICsomes within each aggregate. (f) Formation of very large extended aggregate clusters of GP-PICsomes upon incubation with Con-A for 30 min. Movie 6 provided in Figure: A7 depicts clustering of aggregates in three dimensions. Movie links are provided below and in Figure A7.

For Movie 1 see:

https://pubs.acs.org/doi/suppl/10.1021/acsomega.6b00142/suppl_file/ao6b00142_si_002.avi

For Movie 2 see:

https://pubs.acs.org/doi/suppl/10.1021/acsomega.6b00142/suppl_file/ao6b00142_si_003.avi

For Movie 3 see:

https://pubs.acs.org/doi/suppl/10.1021/acsomega.6b00142/suppl_file/ao6b00142_si_004.avi

For Movie 4 see:

https://pubs.acs.org/doi/suppl/10.1021/acsomega.6b00142/suppl_file/ao6b00142_si_005.avi

For Movie 5 see:

https://pubs.acs.org/doi/suppl/10.1021/acsomega.6b00142/suppl_file/ao6b00142_si_006.avi

For Movie 6 see:

https://pubs.acs.org/doi/suppl/10.1021/acsomega.6b00142/suppl_file/ao6b00142_si_007.avi

Typically, over several minutes, it was found that more number of smaller aggregates coalesce with each other and eventually adhere directly to the surface or attach onto existing surface bound aggregates (Figure 2.12e). Further, it was observed that some of these aggregates (similar to those shown in blow up in bottom of Figure 2.12e) tend to undergo anchored or restricted motion in solution even when attached to the surface (Figure A6). Such restricted anchored movement may also be responsible for the Con-A induced bridging (or connection) of two or more nearby aggregates, eventually leading to formation of higher order aggregates shown in Figure 2.12e (blow up on top). It is worth mentioning that estimation of the number of GP-PICsomes within each surface-bound aggregate using static fluorescence images (as in Figure 2.12e) can be very challenging if not impossible; for instance, single snapshot image at 25s in Figure 2.12b seems to portray the existence of only 2-3 GP-PICsomes within the aggregate, while observation of the entire movie reveals a more realistic picture. In fact, all the large aggregates are 3D assemblies which constitute much more number of PICsomes as compared to those seen from the static fluorescence images. This is further evident for very large extended clusters of aggregates (Figure 2.12f) that are generated on the surface over several hours in presence of Con-A, and such 3D assembly of PICsomes in these large aggregate clusters can be readily visualized upon changing the (z-) focus of the objective during fluorescence imaging (movie 6).

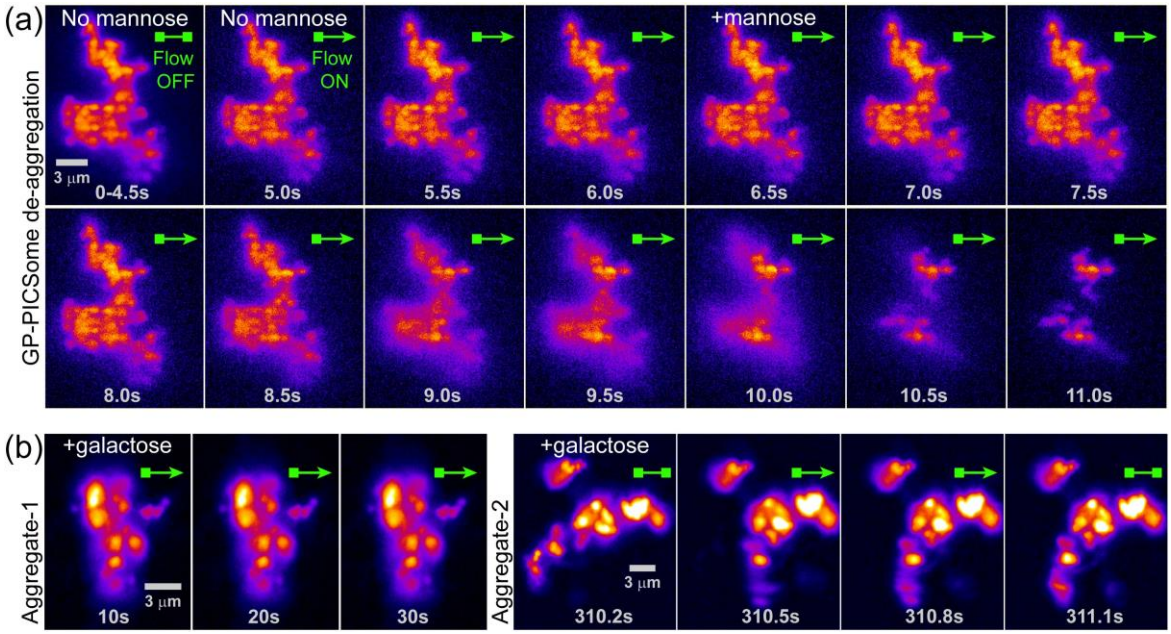

Figure 2.13: (a) Dissociation/de-aggregation of an immobile RhB-GP-PICsome aggregate cluster upon addition of excess monomeric mannose solution. The first panel (0-4.5s) depicts the time-average image of the aggregate-cluster in absence of flow, while other panels are sequential single-frame snapshots under flow in absence (5-6s) and presence (>6s) of mannose (300 mM) containing buffer. (Movie 7) (b) Sequential single-frame snapshots of an immobile GP-PICsome aggregate cluster (Aggregate-1) attached to glass surface under continuous flow of 300 mM galactose containing buffer. Single-frame snapshots of a larger aggregate cluster (Aggregate-2, right) incubated with 300 mM galactose for 5 min, under momentary buffer flow (suddenly turned on and off, as represented by arrowheads) (Movie 8). Movie links are provided below and in Figure A7.

For Movie 7 see:

https://pubs.acs.org/doi/suppl/10.1021/acsomega.6b00142/suppl_file/ao6b00142_si_008.avi

For Movie 8 see:

https://pubs.acs.org/doi/suppl/10.1021/acsomega.6b00142/suppl_file/ao6b00142_si_009.avi

To ensure that the observed aggregation of RhB-GP-PICsomes was indeed induced by specific interaction of the mannose binding domain in Con-A interacting with surface grafted mannose moieties of GP-PICsomes (Figure 2.11), challenge experiments were performed with excess (300 mM) of free mannose and monitored surface-bound large aggregates and aggregate-clusters using fluorescence video imaging. The results of such a competition experiment is depicted in Figure 2.13a, where a large aggregate cluster of RhB-GP-PICsomes is imaged under hydrodynamic flow in the absence and presence of excess mannose It was found that within a few seconds of the arrival of mannose containing buffer solution (at ~6s), the aggregate cluster disassembles rapidly (~seconds)

and only a small fraction of GP-PICsomes (or their smaller aggregates) still remain bound to the surface. A possible reason for the presence of these firmly adhered smaller aggregates is that mannose was unable to access all Con-A binding sites (buried within aggregates) with equal ease. As a control, the same experiments were performed with galactose, a carbohydrate which has no binding affinity towards Con-A (Figure 2.11). It was observed that excess (300 mM) of galactose does not affect the aggregates or large aggregate clusters in any way. For instance, as shown in Figure 2.13b, neither de-aggregation occurred nor any GP-PICsome was disassembled from Aggregate-1 under continuous flow of buffer containing excess galactose. It was possible to identify a few large GP-PICsome aggregate clusters, parts of which were not firmly anchored to the glass surface, such as Aggregte-2 in Figure 2.13b. Relatively long time (5 min) incubation with excess galactose followed by intermittent buffer flow (momentarily turned on and turned off) could only induce a part of this aggregate cluster to swivel rather than disassemble, which recoiled in absence of the hydrodynamic drag without altering the remaining structure. From these experiments it was concluded, that the GP-PICsomes formed displayed part or all of the GP present on its outer surface. The GP-PICsomes remained bioactive and the mannose residues in GP specifically interacted with Con-A to form large aggregate clusters.

2.4 Conclusions

To develop mimics of glycoproteins bearing cell surfaces, the oppositely charged hydrophilic block copolymers (catiomer and aniomer) based on glycopolypeptide-b-poly-*L*-lysine and PEG_{2k}-b-poly-*L*-glutamate was synthesized, and self-assembled in aqueous medium to form glycopolypeptide based polyionic complex vesicles (GP-PICsomes). Imaging of these microscopic assemblies in solution and in the dry state was demonstrated which shows the hollow structural morphology of few micrometers dimensions where several carbohydrate functional groups protrude out in solution, reminiscent of a biological cell. More importantly, the biochemically activity of surface grafted mannose moieties was retained, as evident from multivalent interaction dynamics of the GP-PICsomes to form aggregates, mediated by a carbohydrate binding protein (lectin). The bioactivity of surface grafted carbohydrate groups of PICsomes was demonstrated and is highly specific to the lectin Con-A which has multiple binding sites, and act as effective bridge between GP-PICsomes to induce strong inter-particle interactions. Using fluorescently labelled GP-PICsomes, the visualization of the

aggregation dynamics in presence of Con-A was studied, which show the formation of extended, three dimensional higher order aggregate clusters from the association of individual PICsomes over time, at times mediate by Con-A bound to glass surface. Finally, the PICsome-aggregate clusters are disassembled (de-aggregate) spontaneously in presence of excess mannose in solution, which reiterate the specificity of biomolecular interactions of surface pendant groups. Therefore, it was demonstrated from these studies that large surface bioactive GP-PICsomes (or further modifications thereof) have the potential to be used as suitable models to study various interactions on cellular surfaces and intercellular recognition.

2.5 References

1. Schatz, C.; Louguet, S.; Le Meins, J.-F.; Lecommandoux, S. *Angew. Chem., Int. Ed.* **2009**, *48*, 2572−2575.
2. Wu, D. Q.; Lu, B.; Chang, C.; Chen, C. S.; Wang, T.; Zhang, Y. Y.; Cheng, S. X.; Jiang, X. J.; Zhang, X. Z.; Zhuo, R. X. *Biomaterials.* **2009**, *30*, 1363−1371.
3. Cho, C. S.; Seo, S. J.; Park, I. K.; Kim, S. H.; Kim, T. H.; Hoshiba, T.; Harada, I.; Akaike, T. *Biomaterials.* **2006**, *27*, 576−585.
4. Chen, G.; Amajjahe, S.; Stenzel, M. H. *Chem. Commun*. **2009**, *10*, 1198−1200.
5. Bonduelle, C.; Lecommandoux, S. *Biomacromolecules.* **2013**, *14*, 2973−2983.
6. Herzner, H.; Reipen, T.; Schultz, M.; Kunz, H. *Chem. Rev.* **2000**, *100*, 4495−4537.
7. Pratt, M. A.; Bertozzi, C. R *Chem. Soc. Rev*. **2005**, *34*, 58−68.
8. Wang, Q.; Dordick, J. S.; Linhardt, R. J. *Chem. Mater.* **2002**, *14*, 3232−3244.
9. Kramer, J. R.; Deming, T. J. *Polym. Chem.* **2014**, *5*, 671-682.
10. Krannig, K. S.; Schlaad, H. *Soft Matter*. **2014**, *10*, 4228-4235.
11. Pati, D.; Kalva, N.; Das, S.; Kumaraswamy, G.; Sen Gupta, S.; Ambade, A. V. *J. Am. Chem. Soc*. **2012**, *134*, 7796−7802.
12. Das, S.; Sharma, D. K.; Chakrabarty, S.; Chowdhury, A.; Sen Gupta, S. *Langmuir*. **2015**, *31*, 3402−3412.
13. Dhaware, V.; Shaikh, A. Y.; Kar, M.; Hotha, S.; Sen Gupta, S. *Langmuir*. **2013**, *29*, 5659−5667.
14. Kramer, J. R.; Rodriguez, A. R.; Choe, U. J.; Kamei, D. T.; Deming, T. J. *Soft Matter*. **2013**, *9*, 3389-3395.
15. Bonduelle, C.; Huang, J.; Ibarboure, E.; Heise, A.; Lecommandoux, S. *Chem. Commun.* **2012**, *48*, 8353−8355.
16. Pati, D.; Das, S.; Patil, N. G.; Parekh, N.; Anjum, D. H.; Dhaware, V.; Ambade, A. V.; Sen Gupta, S. *Biomacromolecules.* **2016**, *17*, 466–475.
17. Onaca, O.; Nallani, M.; Ihle, S.; Schenk, A.; Schwaneberg, U. *Biotechnol. J*. 2006, *1*, 795–805.
18. Nyin, H.; Routh, A. F. *Soft Matter.* **2006**, *2*, 940–949.

19. Discher, B. M., Won, Y. Y., Ege, D. S., Lee, J. C-M., Bates, F. S., Discher, D. E. & Hammer, D. A. *Science*. **1999**, *284*, 1143–1146.
20. Lee, Y.; Kataoka, K. *Soft Matter*. **2009**, *5*, 3810–3817.
21. Kataoka, K.; Harada, A. *Prog. Polym. Sci*. **2006**, *31*, 949–982.
22. Hartig, S. M.; Greene, R. R.; Dikov, M. M.; Prokop, A.; Davidson, J. M. *Pharm. Res.* **2007**, *24*, 2353–2369.
23. Harada, K.; Kataoka, K. *Macromolecules.* **1996**, *28*, 5294-5299.
24. Chuanoi, S.; Kishimura, A.; Dong, W.F.; Anraku1, Y.; Yuichi, Y.; Kataoka, K. *Polymer Journal.* **2014**, *46*, 130–135.
25. Koide, Y.; Kishimura, A.; Osada, K.; Jang, W.D.; Yamasaki, Y.; Kataoka, K. *J. Am. Chem. Soc*. **2006**, *128*, 5988–5989.
26. Dong, W. F.; Kishimura, A.; Anraku, Y.; Chuanoi, S.; Yamasaki, Y.; Kataoka, K. *J. Am. Chem. Soc.* **2009**, *131*, 3804–3805.
27. Anraku, Y.; Kishimura, A.; Oba, M.; Yamasaki, Y.; Kataoka, K. *J. Am. Chem. Soc*. 2010, *132*, 1631–1636.
28. Anraku, Y.; Kishimura, A.; Yamasaki, Y.; Kataoka, K. *J. Am. Chem. Soc*. **2013**, *135*, 1423–1429.
29. Kishimura, A.; Koide, A.; Osada, K..; Yamasaki, Y.; Kataoka, K. *Angew. Chem., Int. Ed*. **2007**, *46*, 6085–6088.
30. Oana, H.; Kishimura, A.; Yonehara, K.; Yamasaki, Y.; Washizu, M.; Kataoka, K. *Angew. Chem. Int. Ed*. **2009**, *48*, 4613 –4616.
31. Munoz, E. M.; Correa, J.; Riguera, J.; Megia, E. F. *J. Am. Chem. Soc*. **2013**, *135*, 5966-5969.
32. Su, L.; Zhao, Y.; Chen, G; Jiang, M. *Polym. Chem.* **2012**, *3*, 1560-1566.
33. Yilmaz, G.; Becer, C.R. *Polym. Chem.* **2015**, *6*, 5503-5514.
34. Nagasaki, Y.; Yasugi, K.; Yamamoto, Y.; Harada, A.; Kataoka, K. *Biomacromolecules.* **2001**, *2*, 1067–1070.
35. Pati, D.; Shaikh, A.; Das, S.; Nareddy, P. K.; Swamy, M. J.; Hotha, S.; Sen Gupta, S. *Biomacromolecules.* **2012**, *13*, 1287−1295.
36. Duncan, G.A.; and Bevan, M.A. *Langmuir.* 2014, *30*, 15253–15260.
37. Das, S.; Pati, D.; Tiwari, N.; Nisal, A.; Sen Gupta, S. *Biomacromolecules.* 2012, *13*, 3695−3702.
38. Vu Hong, V.; Stanislav I. Presolski, S.I.; Celia Ma, C.; Finn, M. G. *Angew. Chem. Int. Ed*. **2009**, *48*, 9879–9883.
39. Vlist, J.V.D.; Faber, M.; Loen, L.; Dijkman, T.J.; Asri, L.A.T.W.; Loos, K. *Polymers.* **2012**, *4*, 674-690.
40. Bhattacharya, S.; Sharma, D.K.; Saurabh, S.; De, S.; Sain, A.; Nandi, A.; Chowdhury, A. *J. Phys. Chem.* B. **2013**, *117*, 7771-7782.
41. Kazakov, S.; Kaholek, M.; Kudasheva, D.; Teraoka, I.; Cowman, M. K.; Levon, K. *Langmuir.* **2003**, *19*, 8086−8093.
42. Mai, Y.; Eisenberg, A. *Chem. Soc. Rev*. 2012, *41*, 5969−5985.
43. Blanazs, A.; Armes, S. P.; Ryan, A. J. *Macromol. Rapid Commun*. **2009**, *30*, 267−277.
44. Antonietti, M.; Forster, S. Vesicles and Liposomes: *Adv. Mater*. **2003**, *15*, 1323−1333.

45. Discher, D. E.; Eisenberg, A. *Science.* **2002**, *297*, 967−973.

CHAPTER 3

Amphiphilic Glycopolypeptide based Crosslinked Nanocarriers for Dual Stimuli-Responsive Drug Delivery

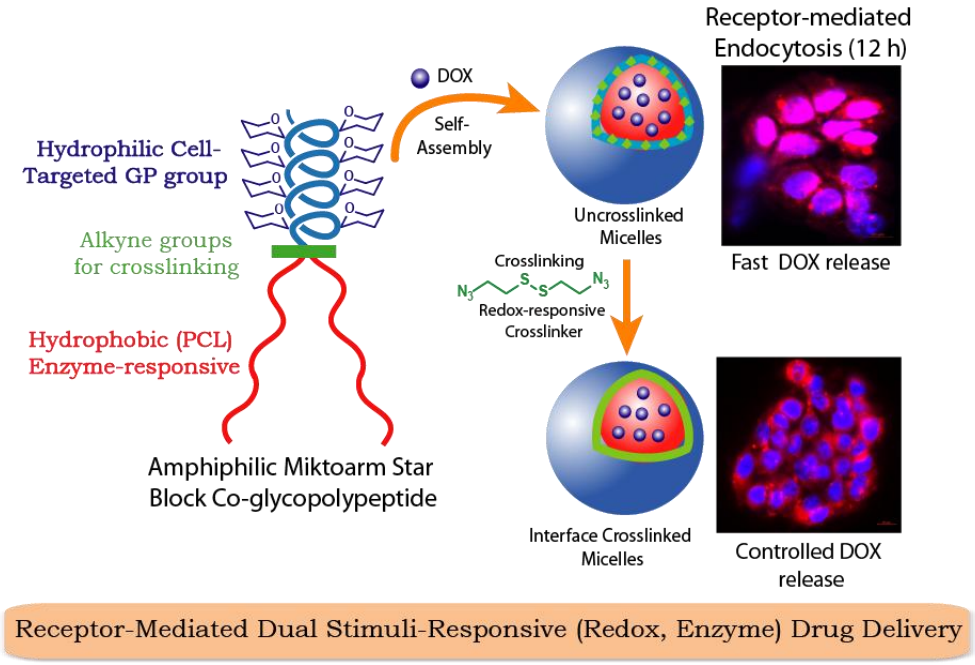

Pandey, B. *et al.* manuscript is under preparation **2018.**

3.1 Introduction

Several carbohydrate receptors are overexpressed on the surface of cancer cells as compared to normal cells.[1,2] The over-expression of specific carbohydrate receptors on the cancer cell surface, has accelerated the development of glyco-macromolecules for drug delivery and studies on their potential for targeting affected cells.[3-7] Several carbohydrate-containing nanocarriers-based delivery systems (*viz*. micelles, vesicles, nanorods, etc.) are being currently explored for such applications.[8-14] Amphiphilic glycopolypeptides undergo self-assembly process to form micellar nanostructures displaying carbohydrates on their surface, which can be explored for targeted drug delivery applications.[8,15-21] However, there are very few literature reports wherein glycopolypeptide-based micelles have been evaluated for drug delivery by studying cellular uptake of drug-loaded micelles.[17,18,20] Recently, Jiang and co-workers demonstrated formation of reduction-sensitive amphiphilic glycopolypeptide-poly(ε-caprolactone) (GP–SS–PCL) block copolymer micelles as theranostic nanocarriers for application in chemotherapy and MR imaging.[17] Jan and co-workers demonstrate the synthesis and self assembly of poly(L-lysine) based random copolymer containing bioactive pendent lactobionolactone and hexanoyl units into crosslinked vesicles for controlled release in cancerous cells.[22] Biocompatible amphiphilic nGP-$(PCL_m)_2$ star copolymers have been reported but their assemblies were not explored for biological studies due to low stability *in vitro*.[16]

In the conventional polymeric micelles there is a thermodynamic equilibrium between the micelles and their unimers in the aqueous phase.[23] Due to this, during intravenous administration, the micelles are likely to be diluted below (CMC) and vulnerable to dissociation that may lead to premature drug release. This is one of the central issues regarding the biological application of self-assembled micelles.[48] Additionally, interaction with the plasma proteins (high and low-density proteins) may disrupt the micellar assembly.[24,25] All these factors reduce the therapeutic efficacy of drugs before reaching the target and may cause undesired side effects.[26,27] To improve the stability of micelle-like nanostructures, Wooley and co-workers, in their pioneering work, have introduced the concept of covalently crosslinked intramicellar assemblies.[28] This strategy has proved to be a powerful tool for the stabilization of micellar assemblies. Intramicellar crosslinking in the assemblies not only creates a barrier for the external agents that are responsible for the degradation of micelles but also provides them a robust character.[28,29] The crosslinking of micelles can be carried out on the hydrophilic shell,[30,31]within the

hydrophobic core,[32,33] or at the core-shell interface (interfacial crosslinking).[34-36,29] Out of these three, interfacial crosslinking is a unique and interesting approach, which combines the advantage of core and shell crosslinking.[29] It not only permits crosslinking at high micellar concentrations without inter-micellar crosslinking but also limits the alteration in the properties of micellar core that may occur during crosslinking.[36,37] Another significant advantage of the crosslinking approach is that it allows incorporation of several stimuli-responsive groups in polymeric micelles such as reducible disulfide bonds,[32,35] pH-cleavable linkages,[35,38] and hydrolyzable ester bonds.[39] Utilizing this approach, a stable micellar system, which can respond to different types of stimuli and aid in the controlled release of cargo can be designed.

For amphiphilic glycopolypeptide-based micellar systems, this crosslinking approach for enhanced micelle stability has not been explored yet. This chapter describes glycopolypeptide-based interface crosslinked (ICL) micellar nanostructures that exhibit dual stimuli-responsive (redox and enzyme-responsive) nature as potential candidates for targeted and controlled drug delivery (Figure 3.1). Amphiphilic biocompatible miktoarm star copolymer [$(PCL_{50})_2$-*b*-Pr-gly_6-*b*-GP_{40}], which comprises two hydrophobic poly(ε-caprolactone) blocks, a short poly(propargylglycine) middle block and the hydrophilic glycopolypeptide block was designed and synthesized. Poly(ε-caprolactone), a well-known biocompatible and FDA-approved polymer,[40a] was chosen as the degradable enzyme-responsive block. The star copolymer initially self-assembled into uncrosslinked (UCL) micellar structures. Then, free alkyne groups of the middle block at core-shell interface of the UCL micelles were utilized for crosslinking using click chemistry with the azide-terminated redox-responsive molecule to form interface crosslinked (ICL) micelles. Stability of ICL micelles to dilution compared to UCL micelles was investigated. Redox and enzyme-responsive drug release behaviour from ICL micelles was studied independently as well as simultaneously using the anti-cancer drug doxorubicin (DOX). Finally, stimuli-mediated time-dependent DOX release from DOX-loaded UCL and ICL micelles was evaluated in living cells to test whether the ICL micelles display controlled release in the intracellular environment.

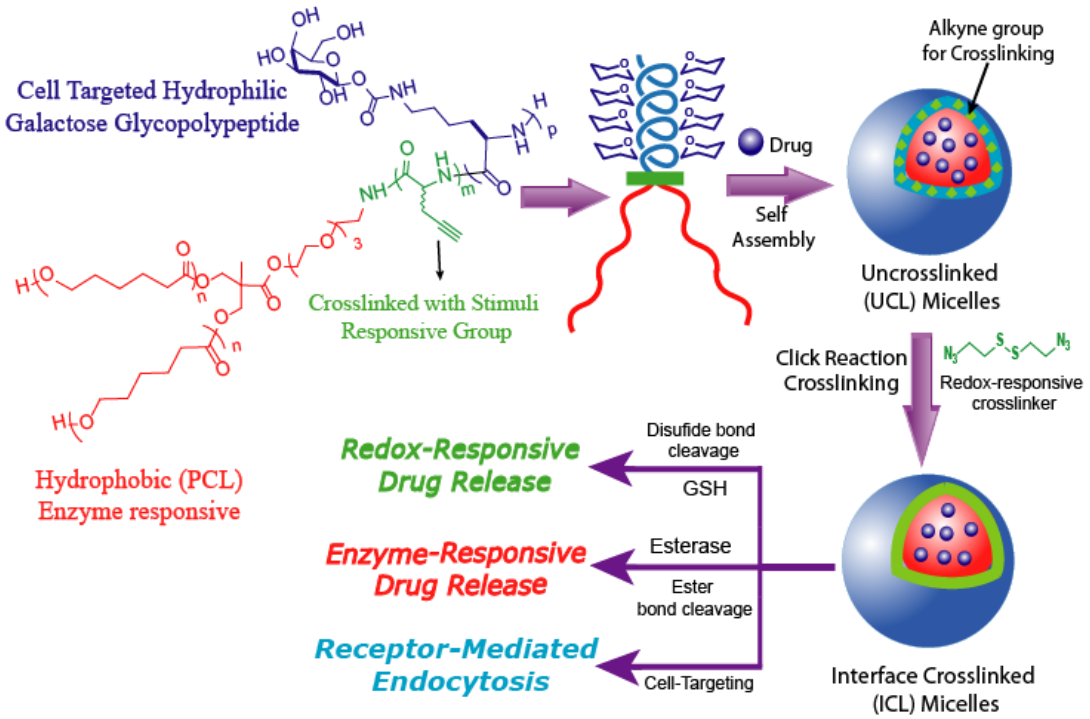

Figure 3.1: Schematic representation of the synthesized amphiphilic block coglycopolypeptides and their self-assembly into uncrosslinked (UCL) and interface crosslinked (ICL) nanostructures for targeted and controlled drug delivery.

3.2 Experimental Section

3.2.1 General

Tetraethylene glycol, ε-caprolactone, stannous octanoate (Sn(oct)2), triphosgene Rhodamine B octadecyl ester (RBOE), $HAuCl_4$, 2,2-bis-methylolpropionic acid (bis-MPA), dimethyl formamide (DMF), 2-hydroxyethyl disulfide, D,L-propargylglycine, esterase enzyme from horse liver, dialysis tubing (MW cut off 12 kDa) and glutathione (GSH) were purchased from Aldrich Chemical. $CuSO_4$ and sodium ascorbate were purchased from Fisher Scientific. Dialysis tubing (MW cut-off 3.5 kD) was purchased from Thermo-Fisher Scientific. Triethylamine, toluene, methanol, THF, chloroform, n-hexane and ethyl acetate were purchased from Merck. Toluene and tetrahydrofuran were dried over sodium and distilled before use. n-hexane and ethyl acetate were dried on CaH_2. DCC was purchased from Spectrochem. 4-(N,N-dimethylamino)pyridine p-toluenesulfonate (DPTS) was synthesized by following reported procedure.[40b] ε-caprolactone was purified by vacuum distillation. GPC chromatograms of all the polycaprolactone sample were recorded on a Thermo Quest (TQ) GPC at 25 °C with RI detector against polystyrene standards using $CHCl_3$ as eluent with flow rate 1 mL/min.

Circular dichroism (CD) spectra of solution was recorded in the range of 190 nm to 250 nm using JASCO CD Spectropolarimeter (J-815) in a cuvette with a 1 mm path length.

3.2.2 Synthesis of branched hydrophobic initiator [$(PCL_{50})_2$-NH_2]

*3.2.2.1 Synthesis of tetraethylene glycol monotosylate **(1)***

A 100 mL two-neck round-bottom flask was attached with a dropping funnel and then charged with tetraethylene glycol (TEG) (5 g, 25.74 mmol), dry triethylamine (3.61 mL, 25.74 mmol), and dry dichloromethane (50 mL) under an inert atmosphere. Initially, the reaction was maintained at 0°C and then the solution of p-toluenesulfonyl chloride (4.65 g, 24.45 mmol) in dry DCM (25 mL) was added dropwise with the constant stirring at 0 °C. The reaction mixture was allowed to stir at 0 °C for initial 1 h and then for overnight at room temperature. After completion of the reaction, the reaction mixture was washed with 5% aqueous $NaHCO_3$ solution then with water (2 × 100 mL) twice. The organic layer was dried over anhydrous sodium sulfate, filtered and DCM was evaporated under reduced pressure. The crude product was purified by silica gel column chromatography using a mixture of pet ether: ethyl acetate (60:40, v/v) two parts and DCM: methanol (95:5) one part as eluent to afford desired monotosylated TEG **(1)** as a colorless viscous liquid (Yield: 3.5 g, 44.6 %).

^{1}H NMR (400 MHz, $CDCl_3$), δ (ppm): 2.44 (s, 3H,), 2.47 (s, 1H), 3.55-3.75 (m, 14H), 4.15 (t, 2H), 7.32 (d, 2H), 7.78 (d, 2H).

*3.2.2.2 Synthesis of azido-etraethylene glycol **(2)***

A 250 mL round bottom flask was charged with compound **1** (3.5 g, 10.04 mmol) and sodium azide (6.75 g, 100.4 mmol) and refluxed in 100 mL DMF at 60 ^{0}C for 24 h. The crude product was initially extracted with DCM and water and then the organic layer was dried over anhydrous sodium sulfate, filtered and removed by reduced pressure. The crude product was purified by silica gel column chromatography using a mixture of ethyl acetate:pet ether (40:60, v/v) two parts and DCM: methanol (95:5) one part as eluent to afford desired product **(2)** as a colourless viscous liquid (Yield: 2.97g, 85 %).

^{1}H NMR (200 MHz, $CDCl_3$), δ (ppm): 2.47 (bs, 1H), 3.39 (t, 2H), 3.55-3.75 (m, 14H).

*3.2.2.3 Synthesis of azido-tetraethylene glycol diol **(3)***

In a 250 mL round bottom flask, compound **2** (2 g, 9.10 mmol), isopropylidene-2,2-bis(methoxy)propionic acid (1.9 g, 10.92 mmol), DCC (2.06 g, 10.01 mmol) and DPTS (1.06 g, 3.64 mmol) were dissolved in 60 mL dry DCM and allowed to stir at room

temperature for 12 h under inert atmosphere. The crude product purified by the silica gel column chromatography using a mixture of ethyl acetate: pet ether (40:60, v/v) two parts and DCM: methanol (95:5) one part as eluent to afford azido-tetraethylene glycol acetonide. Acetonide was deprotected with Dowex $50H^+$ resin in methanol at 40 °C for 4h to get crude azido-tetraethylene glycol diol. Further crude product was purified by silica gel column chromatography using a mixture of ethyl acetate: pet ether (50:50, v/v) two parts and DCM: methanol (95:5) one part as eluent to afford desired product (difunctional initiator) as a colourless viscous liquid **(3)** (Yield: 2.9 g, 87 %).

^{1}H NMR (200 MHz, $CDCl_3$), δ (ppm): 1.07 (s, 3H), 3.23 (bs, 2H), 3.34 (t, Hz, 2H), 3.55-3.65 (12H), 3.68 (d, 2H), 3.78 (d, 2H), 4.28 (t, 2H).

3.2.2.4 Synthesis of azide-terminated branched polycaprolactone $(PCL_{50})_2$-N_3 ***(4)***

Difunctional initiator (3) (0.574 mmol), ε-caprolactone (74.62 mmol) and stannous (II) octanoate (0.18 mmol) were transferred to the Schlenk tube under inert atmosphere. The reaction mixture was degassed by three freeze-pump-thaw cycles. Polymerization was carried out under vacuum at 85 ˚C. When the solution became viscous the reaction was terminated by cooling to room temperature and by releasing the vacuum. DCM was added to dissolve the viscous polymer, the resulting solution was precipitated thrice in methanol, and the residue was filtered and dried in vacuum for 12 h to obtain a solid white powder (Yield 75%).

^{1}H NMR (400 MHz, $CDCl_3$), δ (ppm): 1.35-1.42 (m, 200H), 1.62-1.65 (m, 402H), 2.28-2.32 (m, 196H), 3.36-3.39 (t, 2H), 3.66-3.64 (m, 194), 4.04-4.09 (m, 195H), 4.21-4.26 (m, 7H).

3.2.2.5 Synthesis of amine-terminated and acetyl protected branched polycaprolactone $(PCL_{50})_2$-NH_2 ***(5)***

A 50 mL two-neck round-bottom flask was attached with a dropping funnel and was charged with $(PCL_{50})_2$-N_3 (1 g, 0.0892 mmol), triethylamine (0.024 mL, 0.1785 mmol), and dry dichloromethane (20 mL). The reaction mixture was allowed to cool at 0 °C. The solution of acetyl chloride (14 mg, 1.785 mmol) in dry dichloromethane (50 mL) was added dropwise under constant stirring at 0 °C. The reaction mixture was allowed to stir at 0 °C for 1 h and at room temperature overnight. The reaction mixture was washed with 5% aqueous $NaHCO_3$ solution then with water (2 × 100 mL). The organic layer (DCM) was dried over anhydrous sodium sulfate, filtered and then precipitated in methanol and residue was filtered and dried in vacuum for 12 h to obtain white solid powder. Further,

terminal azide group of $(PCL_{50})_2$-N_3 is then reduced to an amine *via* hydrogenation in the presence of 10% Pd/C catalyst. The obtained white powder $(PCL_{50})_2$-NH_2 was dried under vacuum and transferred to the glove box (Yield 78%).

^{1}H NMR (400MHz, $CDCl_3$), δ (ppm): 1.35-1.42 (m, 200H), 1.62-1.65 (m, 402H), 2.02 (s, 6H), 2.28-2.32 (m, 196H), 3.36-3.39 (t, 2H), 3.66-3.64 (m, 194), 4.04-4.09 (m, 195H), 4.21-4.26 (m, 9H).

3.2.3. Synthesis of N-carboxyanhydrides (NCA)

3.2.3.1 Synthesis of galacto-N-carboxyanhydrides ***(6)***

Per-*O*-acetylated-D-galactose-*L*-lysine carbamate (500 mg, 0.96 mmol) was dissolved in freshly distilled tetrahydrofuran (7 mL) and a solution of triphosgene (142 mg, 0.480 mmol) in anhydrous tetrahydrofuran (2 mL) was added to it under argon atmosphere and the reaction mixture was heated to 60°C. α- pinene (0.228 mL, 1.44 mmol) was then added to the reaction mixture and allowed for additional 1 h stirring. The reaction mixture was cooled to room temperature and precipitated into dry hexane (200 mL) to yield a white precipitate, which was quickly filtered and crystallized by a mixture of dry ethyl acetate and petroleum ether. The crystallized product was re-dissolved in a minimum amount of ethyl acetate (dry) and further purified by silica gel column chromatography in an inert atmosphere using a mixture of ethyl acetate: pet ether (75:25, v/v) two parts as eluent. The solvent was removed by reduced pressure and dried under vacuum for 1 h and transferred into the glove box to get white solid of galacto-*N*-carboxyanhydride (yield: 425 mg, 85%).

^{1}H NMR (400 MHz, $CDCl_3$): δ (ppm): 1.35−1.82 (m, 6H), 1.98, 2.03, 2.04, 2.14 (4s, 12H), 3.12 (td, 2H,), 4.04−4.20 (m, 3H), 4.33 (bs, 1H), 5.09 (dd, 1H, 10.5Hz), 4.25 (dd, 1H, 10.3 Hz), 5.30 (m, 1H), 5.42 (d, 1H, Hz), 5.62 (d, 1H), 7.14 (bs, 1H); ^{13}C NMR (100 MHz, $CDCl_3$): δ (ppm): 20.5, 20.6, 20.7, 21.6, 28.8, 31.0, 40.3, 57.4, 60.9, 66.8, 68.0, 70.7, 71.4, 93.3, 152.4, 154.1, 169.8, 170.0, 170.1, 170.5.

3.2.3.2 Synthesis of D, L-propargylglycine N-carboxyanhydride ***(7)***

To D,L-propargylglycine (100 mg, 0.88 mmol) dissolved in freshly distilled tetrahydrofuran (3 mL), triphosgene solution (78.6 mg, 0.265 mmol) in dry THF (1 mL) was added under argon and the reaction mixture was allowed to heat to 60°C. Subsequently, α- pinene (0.069 mL, 0.44 mmol) was added to the above reaction mixture and allowed to continue for 3-4 h until the reaction mixture becomes clear solution. After completion of reaction, solvent was removed by reduced pressure and the NCA was

precipitated in 100 mL n-hexane (dry) and placed in a -20°C freezer overnight for complete precipitation. The precipitated product was filtered off, dissolved in dry THF, and re-crystallized twice in dry n-hexane . The obtained solid product was washed with dry n-hexane and vacuum dried to get white crystals in 80% yield.

^{1}H-NMR (400 MHz, acetone-d^6) δ (ppm): 2.62 (t, 1H), 2.86 (dd, 2H), 4.75 (t, 1H), 8.05 (s, 1H); ^{13}C-NMR (100 MHz, acetone-d^6), δ (ppm): 22.26, 57.30, 73.64, 78.23, 152.71, 170.62.

3.2.4. Synthesis of cleavable disulfide crosslinker: Bis-(azidoethyl) disulfide (BADS)

*3.2.4.1 Synthesis of bis-(tosylate ethyl) disulfide **(8)***

A 100 mL round bottom flask was charged with 2-hydroxyethyl disulfide (3g, 0.02mol) and triethylamine (10.8g, 0.05mol) in chloroform (30 mL) and allowed to cool to 0 °C in an ice bath. Further, crystallised *p*-toluenesulfonyl chloride (28.6g, 0.15 mol) was dissolved in chloroform (30 mL) and added dropwise to the above solution. The reaction was allowed to proceed under stirring at room temperature for 14 h. The reaction mixture was filtered to remove the triethylamine salts. The filtrate was washed with saturated $NaHCO_3$ (200 mL) and then with water (100 mL). The organic solvent was dried over anhydrous sodium sulphate and filtered. Finally, chloroform was evaporated under vacuum to give the product (6.9 g, 78.6 % yield).

^{1}H NMR ($CDCl_3$, 400 MHz): δ (ppm): 2.44 (s, 6H), 2.83 (t, 4H), 4.19 (t, 4H), 7.35 (d, 2H), 7.78 (d, 2H).

*3.2.4.2 Synthesis of cross-linker bis-(azidoethyl) disulfide **(9)***

In a 100 mL round bottom flask, compound **(8)** (2g, 4.0 mmol) obtained from the above step was dissolved in acetone (50 mL). Further, sodium azide (1.4g, 23 mmol) was dissolved in water (30 mL) and added to the above acetone solution. The reaction mixture was refluxed at 80 °C. The product was extracted with diethyl ether (200 mL), and the organic layers were combined, dried over anhydrous sodium sulphate, filtered, and concentrated to give an orange-yellow oil (82 % yield).

^{1}H NMR ($CDCl_3$, 400 MHz): δ 2.85 (t, 4H), δ 3.57 (t, 4H).

*3.2.5 Synthesis of miktoarm star block copolymer [$(PCL_{50})_2$-b-Pr-gly_6-b-$AcGP_{40}$] by ROP of N-carboxyanhydrides **(P1)***

Inside the glove box, a solution of the first NCA monomer (DL-propargylglycine NCA) (7 eq. 100 mg mL^{-1}) in DMF was added to the amine functionalized branched

polycaprolactone $(PCL_{50})_2$-NH_2 as macroinitiator (1 eq.). The progress of polymerisation reaction was checked by FT-IR spectroscopy. After >95% consumption of the first monomer (confirmed by IR), the second monomer, α-*galacto*-*O*-lysNCA (40 eq.) along with the proton sponge (0.5 eq. of the second NCA monomer) in dry DMF (100 mg mL^{-1}) was added and the reaction progress was monitored by FT-IR spectroscopy. The reactions were generally finished within 48 h. After completion of reaction, aliquots were removed from the reaction mixture for GPC analysis. Finally, the solvent was removed under reduced pressure to get a solid residue. The resulting product was re-dissolved in DCM, washed with 1N HCl to remove "proton sponge" and the polymer was purified by precipitation in diethyl ether. The precipitated polymer was centrifuged and dried to get block co-glycopolypeptides (P1) as white solid in 80% yield.

^{1}H NMR (400 MHz, $CDCl_3$): δ (ppm): 1.36-1.80 (m, 12H), 1.82-1.95 (m, 2H), 1.98-2.10 (m, 12H), 2.90-3.24 (m, 3H), 3.70-4.0 (m, 1H), 4.0-4.15 (m, 1H), 4.17-4.35 (m, 3H), 4.9-5.15 (m, 2H), 5.2-5.5 (m, 1H), 5.6-5.80 (m, 1H).

3.2.6 Acetyl group deprotection of $[(PCL_{50})_2$-b-Pr-gly_6-b-$AcGP_{40}]$ ***(P2)***

The acetyl-protected block copolypeptide $(PCL_{50})_2$-*b*-Pr-gly_6-*b*-$AcGP_{40}$ was dissolved in tetrahydrofuran and hydrazine monohydrate (25 eq.) was added. The reaction mixture was allowed to stir for 12 h at room temperature. After reaction completion, acetone was added for quenching and finally solvent was removed under reduced pressure to get solid residue. The obtained product was dissolved in deionized water/ DMSO (1:1) mixture and filtered through 0.45 μm membrane filter. Finally, the polymer was purified by dialysing the filtered solution against DI water using dialysis membrane of 12 kDa MWCO. Dialysis was done for 2 days by changing water every 6 h. Dialyzed block copolymer (P2) was lyophilised to obtain white fluffy solid (70%) yield.

^{1}H NMR (400 MHz, DMSO-d6): δ (ppm): 0.90-1.80 (m, 10H), 2.08 (m, 1H), 2.20-2.30 (m, 1H), 2.75-3.15 (m, 2H), 3.20-3.50 (m, 5H), 3.66 (s, 1H), 3.93-4.10 (m, 1H), 4.22 (s, 1H), 4.49 (s, 1H), 4.65 (s, 1H), 4.84 (s, 1H), 5.17-5.22 (m,1H).

3.2.7 Determination of presence of propargyl group in $[(PCL_{50})_2$-b-Pr-gly_6-b-$AcGP_{40}]$ via click chemistry ***(P3)***

For the estimation of alkyne groups in the block copolymer (P1), it was clicked with excess of benzyl azide. The block glycopolypeptide (P1) was reacted with an excess amount of benzyl azide (5 eq.) in the presence of $CuSO_4.5H_2O$ (5 eq.) and sodium ascorbate (5 eq.) in amixture of THF: MeOH: H_2O (2: 2: 0.1). The reaction was allowed

to stir for 24 h under argon atmosphere. The solvent was removed under reduced pressure and residue was re-dissolved in dichloromethane. It was then washed multiple times using aqueous ammonia solution (dilute) to remove copper salt. Solvent was removed and the residue was re-dissolved in DCM. The resultant polymer was re-precipitated for a couple of times by addition of diethyl ether to the DCM solution. The precipitated white copolymer (P3) was dried under vacuum to get solid white powder.

^{1}H NMR (400 MHz, $CDCl_3$): δ (ppm): 0.50-1.80(m, 12H), 1.82-1.95 (m, 2H), 1.98-2.10 (m, 12H), 2.90-3.24 (m, 3H), 3.70-4.0 (m, 1H), 4.0-4.15 (m, 1H), 4.17-4.35 (m, 3H), 4.9-5.15 (m, 2H), 5.2-5.5 (m, 1H), 5.6-5.80 (m, 1H),7.29-7.42 (m, 5H).

3.2.8 Self-Assembly of deprotected $(PCL_{50})_2$-b-Pr-gly_6-b-GP_{40} copolymer in aqueous solution

3.2.8.1 Preparation of uncrosslinked (UCL) micelles

Fully deprotected polymers [$(PCL_{50})_2$-*b*-Pr-gly_6-*b*-GP_{40}] were dissolved in DMSO and water/DMSO mixture (1:1) was added slowly under stirring, to maintain the final polymer concentration at 0.5 mg mL^{-1}. The solution was allowed to stir for 4 h. The micellar solution was filtered through 0.45 μm membrane filter and dialyzed against DI water (MWCO = 12 kDa) for two days. DI water was changed every 6 h to remove DMSO.

3.2.8.2 Preparation of interface cross-linked (ICL) micelles

Deprotected block copolymer (2.0 mg, 0.082 μmol) and cross-linker bis-(azidoethyl) disulfide (60 μg, 0.295 μmol, 0.6 mol eq. of alkynyl group) were dissolved in DMSO and water/DMSO (1:1) mixture was added slowly under stirring to maintain the final polymer concentration at 0.5 mg mL^{-1}. The solution was allowed to stir for 4 h. Further, aqueous solution of $CuSO_4$, (3.6 μL, 5 mg/mL, 0.25 mol eq. of alkynyl group) and sodium ascorbate (5 μL, 5 mg/mL, 0.5 mol eq. of alkynyl group) were added to the above mixture and stirred overnight at room temperature. The solution was filtered using 0.45 μm membrane filter paper and subsequently purified by dialysis against DI water (MWCO = 12 kDa) for three days, changing water every 6 h to remove DMSO, copper salt and sodium ascorbate.

3.2.8.3 Determination of critical micelle concentration (CMC)

Critical micelle concentration (CMC) of UCL and ICL micelles was determined by fluorescence spectroscopy using rhodamine B octadecyl ester (RBOE) as a hydrophobic fluorescence probe. Micelles were serially diluted and concentration was varied from 0.5

mg mL^{-1} to 9.76 μg mL^{-1}. RBOE (10μL from stock solution of 1 mg/mL in acetone, 1.25 mM) was added to each of the different concentration of micelles. The solutions are allowed to stir overnight. The emission spectra were recorded with the excitation wavelength at 560 nm. The fluorescence intensity of RBOE at 578 nm was plotted against the solution concentration.

3.2.9 Sample preparation for TEM, AFM and DLS analysis

The polymer solution in DI water (0.05 wt%) was used for analysis. The polymer solution (10 μL) was spotted on carbon-coated 400 mesh copper grid , kept for 15-20 min and the excess solvent was removed by touching the edge of the grid with Whatman filter paper. Then grid was negatively stained by 0.2 wt% uranyl acetate for 10 s and washed twice with deionized water to remove excess unbound uranyl acetate from the grid. Grids were dried in desiccators for 20 h and analysed by TEM. For AFM analysis, aqueous solution was drop cast on silicon wafer and dried for 24 h. The aqueous solution of polymer wasfiltered using 0.45μm filter paper and hydrodynamic diameters were determined by DLS.

3.2.10 Circular dichroism measurements

Solution of $(PCL_{50})_2$-b-Pr-$gly_{5\text{-}6}$-b-$AcGP_{40}$ in DI water (0.25 to 1.0 mg/mL) was filtered through 0.22 μm membrane syringe filters. Spectra were recorded with an average of three scans and were reported as a plot of molar ellipticity [θ] versus wavelength. The molar ellipticity value for the block copolymer solution was determined using the standard formula, $[\theta]= (\theta \times 100 \times M_w)/(C \times l)$, where θ = experimental ellipticity values in milli degrees, M_w = average molecular weight of block copolymer, C= concentration in mg/mL, and l = path length in cm. The α-helicity percentage was calculated by using the formula: % α-helicity = (−[θ]222 nm + 3000)/ 39000.

3.2.11 Doxorubicin (DOX) encapsulation in UCL and ICL micelles

3.2.11.1 Preparation of DOX-loaded UCL micelles

DOX.HCl was neutralised with triethylamine in DMSO and mixed with solution of the block copolymer in DMSO and water/DMSO (1:1) was added slowly under stirring to maintain the final polymer concentration at 0.5 mg mL^{-1}. The above solution was allowed to stir for 4 h. The solution was then transferred to a dialysis bag (MWCO = 12.5 kDa) and purified by extensive dialysing against deionized water for 48 h. The solution was filtered through a 0.45μm membrane filter and used for further studies.

3.2.11.2 Preparation of DOX-loaded ICL micelles

Block copolymer solution and crosslinker in DMSO was mixed with deprotonated DOX and add water/dimethyl sulfoxide (1:1) slowly under stirring to maintain the final polymer concentration at 0.5 mg mL^{-1}. The above solution was stirred for 4 h to from UCL micelles, and then further, copper sulphate and sodium ascorbate were added to the above mixture and was allowed for overnight crosslinking at room temperature. The solution was then transferred to a dialysis bag (MWCO = 12 kDa) and purified by extensive dialysing against DI water for 48 h. The DOX encapsulated micellar solution was filtered using a 0.45μm membrane filter for further studies. The concentration of DOX-Loaded in micelles was calculated using UV-Vis spectroscopy, and drug loading efficiency (DLE) was determined using the equation:

$$\text{Drug Loading Efficiency (DLE)} = (W_e / W_f) \times 100$$

Where W_e is the amount of encapsulated DOX in micelles, W_f is the amount of feed DOX.

3.2.12 In-vitro drug release studies

3.2.12.1 Glutathione-mediated drug release studies

The release DOX from ICL micelles was studied in the presence of glutathione using the dialysis method. Briefly, 2.0 mL of drug loaded ICL micelles was transferred to a dialysis bag (MWCO=1,000) and placing it in 10 mL release media (PBS, 10 mM, pH 7.4) of various GSH concentrations (0, 2 μM and 10 mM). The release medium was shaken at 100 rpm at 37 ºC. At predetermined time intervals, 3.0 mL of solution was taken out from the medium and replaced with 3.0 mL of fresh release medium. The amount of DOX released was calculated from fluorescence measurements using linear standard calibration curve with the concentration range of 0.001-10 μg mL^{-1}. The excitation and emission wavelengths were 480 and 560 nm, respectively. The release experiments were performed in triplicate.

3.2.12.2 Enzyme-mediated drug release studies

The release DOX from ICL micelles was studied in the presence of esterase enzyme using the dialysis method. DOX-loaded ICL micellar solution (1 mL) was incubated with 5 units of esterase enzyme and transferred to a dialysis membrane (MWCO =1,000 kDa). Further, the dialysis membrane was placed in release media (PBS , pH 7.4, 10 mM) and was shaken at 100 rpm at 37 ºC. Periodically, 1.0 mL of aliquot was taken from the medium and replaced with 1.0 mL of fresh release medium. The amount of DOX

released was calculated by using the similar method used for GSH. Similarly, release of DOX from the ICL micelles was studied by the sequential application of dual stimuli (Case 1: Glutathione/enzyme and Case 2: enzyme/Glutathione).

3.2.13 In vitro cytotoxicity studies

In vitro cytotoxicity assay of blank UCL and ICL micelles was done by seeding the HepG2 cells in 96-well plate (flat-bottomed) with a density of 10,000 cells per well in minimum essential medium (MEM) having 10% FBS. The cell-seeded plate was placed in a incubator (37 °C with 5% CO_2) for 24 h. Further, UCL and ICL micelles were prepared in the serum-free MEM with a final concentration of 10, 20, 40, 60, 80, 100, 200, and 300 μg mL^{-1} and further incubated for 4 h at 37 °C with 5% CO_2. The cells were further incubated for another 40 h. After 40 h, the media was exchanged with 110 μL of solution of MEM containing 10% FBS. Then, filter-sterilized MTT (3-(4,5- dimethylthiazol-2-yl)-2,5-diphenyltetrazolium bromide) reagent (0.45 mg/mL) was added to each well and further incubated for 4 h at 37 °C with 5% CO_2. To dissolve the insoluble purple coloured formazan crystals formed after incubation for 4 h, media was exchanged with100 μL of DMSO was added. The absorbance of the coloured solution was measured at 550 nm using a microtiter plate reader and the relative percent cell viability was obtained from the following equation:

$$\text{Relative percent cell viability} = (A_{test}/A_{control}) \times 100\%.$$

Where A_{test} is the absorbance of the sample treated cells, $A_{control}$ is the absorbance of the untreated cells (control).

Experiments were performed in triplicate and absorbance was measured as a mean of triplicate measurements. The cell viability data was plotted against the concentration of blank UCL and SCL micelles by representing the percentage relative to untreated cells (control). Similarly, MTT assay of free DOX, DOX-Loaded UCL and ICL micelles were performed following the same procedure.

3.2.14 Cellular uptake study using epifluorescence microscopy

Cellular uptake studies on the HepG2 cells was done by seeding the cells in the 24-well plate with a density of 50000 cells per well in minimum essential medium (MEM) having 10% FBS. Further, the cell-seeded plate was placed in an incubator (37 °C with 5% CO_2) for 24 h. After that, media was exchanged with MEM containing 100μg/mL of DOX-encapsulated UCL and ICL respectively, and incubated for 2, 12, 24 and 48 h respectively at 37 °C with 5% CO_2. After incubation for specific hours, incubated cells were washed

with PBS three times, and the fixation of cells was done by using 4% paraformaldehyde solution. For nucleus staining, DAPI was used. All the images for DOX containing micelles were taken at 500 ms exposure time using an epifluorescence microscope (Carl Zeiss).

3.3 Results and Discussions

3.3.1 Synthesis and characterization of amine-terminated branched polycaprolactone initiator ($PCL_{50})_2$-NH_2

Towards the synthesis of the miktoarm star copolymer $(PCL_{50})_2$-b-Pr-gly_6-b-GP_{40}, initially amine end-functionalized branched functional initiator $(PCL_{50})_2$-NH_2 was prepared *via* ROP of ε-caprolactone from the diol initiator, acetylation of two free terminal -OH groups of PCL chains and reduction of azide groups (Scheme 3.1 and 3.2). Synthesis of azide-functionalized diol initiator (3) was carried out starting from tetraethylene glycol (TEG). TEG was first monotosylated (1) and then reacted with sodium azide to afford monoazido-TEG (2), which was converted to azido-tetraethylene glycol diol (3) using bis-MPA anhydride followed by stirring with Dowex 50 H^+. ROP of ε-caprolactone was carried out from diol initiator (3) to get $[(PCL_{50})_2$-$N_3]$ (4) functionalized with azide group at one end and two free -OH groups at the end of branched PCL chains (Scheme 3.1). The polymer was obtained by precipitation in methanol.

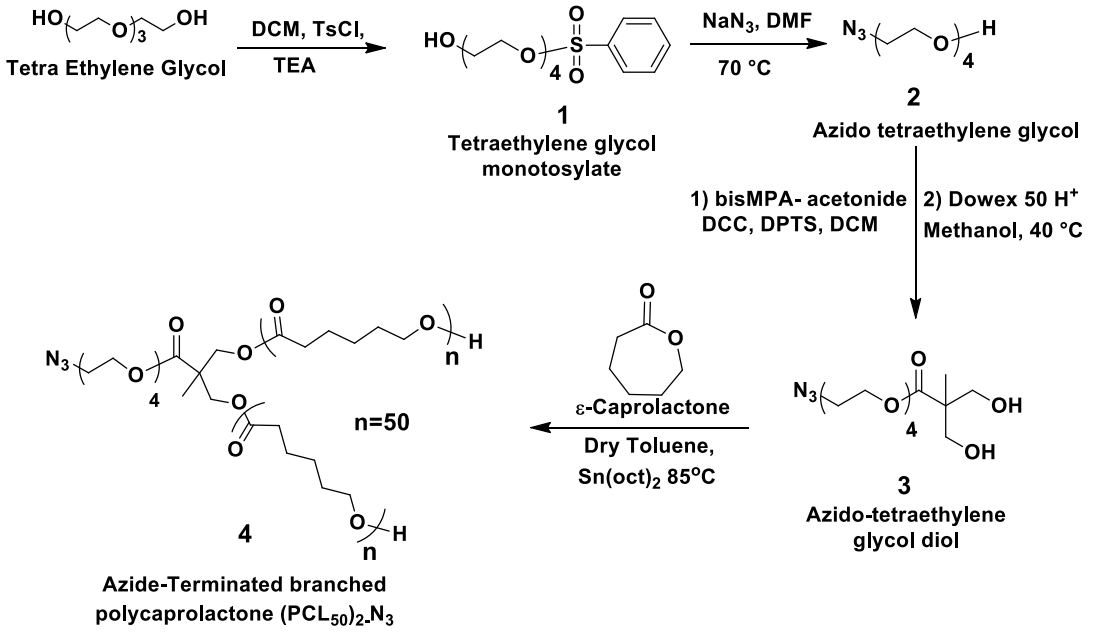

Scheme 3.1: Synthesis of azide-terminated branched polycaprolactone $(PCL_{50})_2$-N_3.

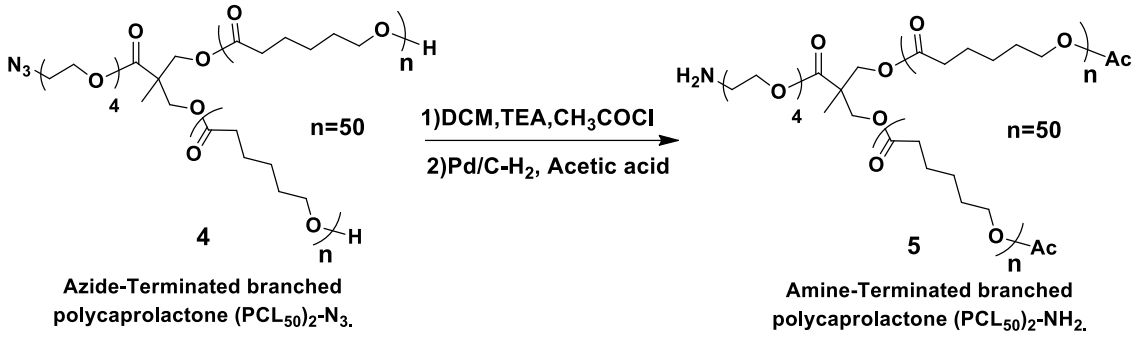

Scheme 3.2: Synthesis of amine-terminated branched polycaprolactone $(PCL_{50})_2$-NH_2.

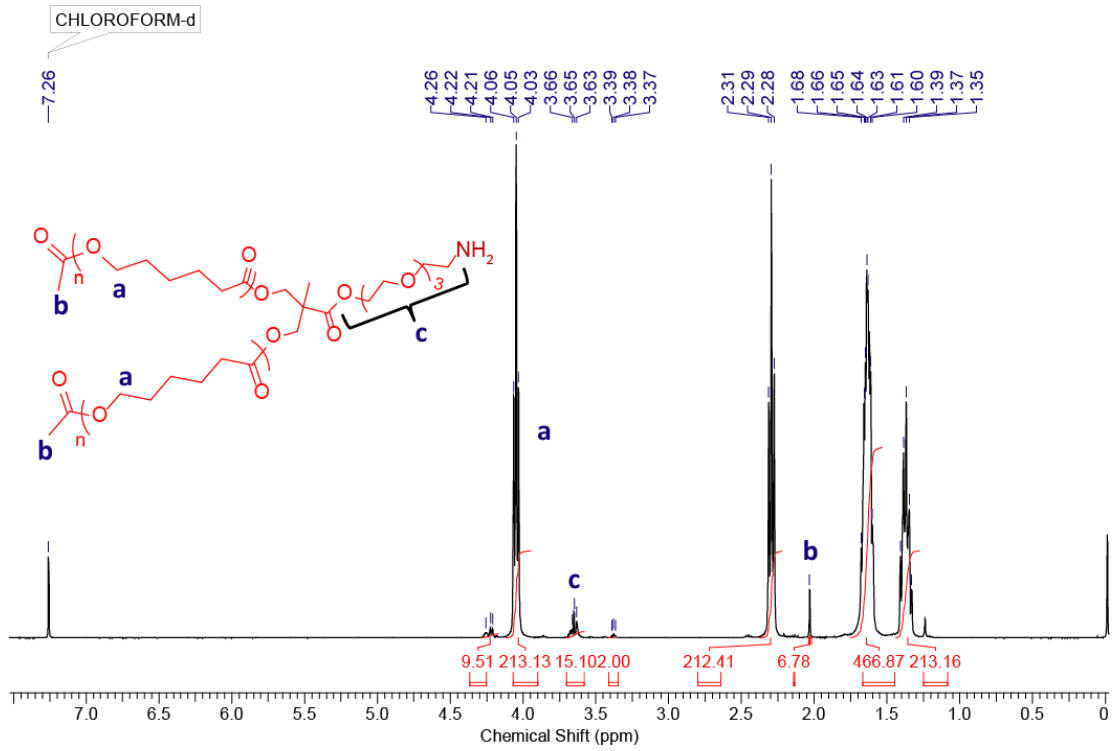

Figure 3.2: ^{1}H NMR spectrum of amine-terminated branched polycaprolactone initiator $(PCL_{50})_2$-NH_2.

M_n was calculated using ^{1}H NMR spectroscopy by integrating the peak at 2.27-2.31 (ppm) of terminal methylene proton ($C\underline{H}_2$-OH) of PCL chain with respect to peak for TEG protons ($-C\underline{H}_2-C\underline{H}_2$) at 3.63-3.65 (ppm) (Figure B4). Terminal -OH groups of azide-functionalized branched PCL (4) is acetylated to prevent the side reactions during NCA polymerization. The azide group of acetylated [$(PCL_{50})_2$-N_3] polymer was further reduced to generate amine-functionalized branched polycaprolactone (5) as a hydrophobic initiator (Scheme 3.2) The polymer was obtained by precipitation in methanol and characterized by ^{1}H NMR spectroscopy by integrating the peak at 2.02 (ppm) ($-CO-CH_3$)

with respect to TEG protons (−CH_2−CH_2) at 3.63-3.65 (ppm) (Figure 3.2). GPC analysis was used to confirm the purity of the polymer (Figure 3.5a).

3.3.2 Synthesis and characterization of mikto-arm star copolymer :$(PCL_{50})_2$-b-Pr-gly_6-b-GP_{40}

In a previous report, nGP-$(PCL_m)_2$ star copolymers with varying block lengths of PCL (25, 50) and GP (10, 20, 40) were prepared and shown to assemble into different type of nanostructures such as micelles, vesicle and rods.[16] Although the block co-polymer 40GP-$(PCL50)_2$ formed micellar aggregates in aqueous solution, it was not explored for biological applications due to their limited stability in media under dilute conditions. In an attempt to develop stable micellar system from 40GP-$(PCL50)_2$ copolymers, an amphiphilic miktoarm star copolypeptide $(PCL_{50})_2$-b-Pr-gly_6-b-GP_{40} was designed. This construct contains in addition to the hydrophobic $(PCL_{50})_2$ and a hydrophilic (GP_{40}) block, an additional short (Pr-gly_6) block, which could be further used to form cross-linked micelles. To obtain the final polymer architecture, sequential ROP was used in proper sequence to minimize purification efforts. Amphiphilic miktoarm star copolymer [$(PCL_{50})_2$-*b*-Pr-gly_6-*b*-GP_{40}] was prepared by ROP of two conventional NCA's (DL-propargylglycine NCA and α-*galacto*-*O*-lys NCA) sequentially using amine-terminated branched polycaprolactone $(PCL_{50})_2$-NH_2 as macroinitiator. Firstly, α-*galacto*-*O*-lys NCA was synthesized by following a previous methodology (Scheme 3.3)[3] and DL-propargylglycine NCA was prepared by following the method of Heise et al.[8] (Scheme 3.4) The polymerization of propargylglycine NCA was initiated by $(PCL_{50})_2$-NH_2**(5)** as a macroinitiator (M/I = 7) in dry DMF. The second monomer, α-*galacto*-*O*-lys NCA (I: M1: M2 =1:7: 40) and ''proton sponge'' (0.5 eq.) were added to the above reaction mixture after completion of the first stage polymerization (10 min) as monitored by FT-IR spectroscopy. The progress of second polymerisation reaction was checked by the complete disappearance of characteristic NCA anhydride stretching at 1785 cm^{-1} and 1858 cm^{-1} in the FT-IR spectra (Figure B1). A monomodal peak and narrow molecular weight distribution was observed for the resulting acetyl protected block copolymer after GPC analysis with a dispersity (Đ) value of 1.18. The molecular weight of the resulting star copolymer was also calculated by ^{1}H NMR analysis by combined integration of the peaks for terminal –C<u>H</u>$_2$ proton of PCL block denoted as (i) and methylene/ methane proton (-C<u>H</u>$_2$/-C<u>H</u>) of galactose (denoted as k) at 4.04-4.30 (ppm) (combinedly denoted as i, k) with respect to the characteristic anomeric proton of the GP segment at 5.67 (ppm)

denoted as (a) (Figure 3.3). The M_n values determined from NMR spectra closely matched to that expected from M/I values. Acetyl groups in the GP segment of block copolymer P1 were deprotected by using hydrazine hydrate under very mild conditions. Deprotection of acetyl groups was affirmed by the absence of peaks for acetyl protons in the ^{1}H NMR spectra (Figure B11).

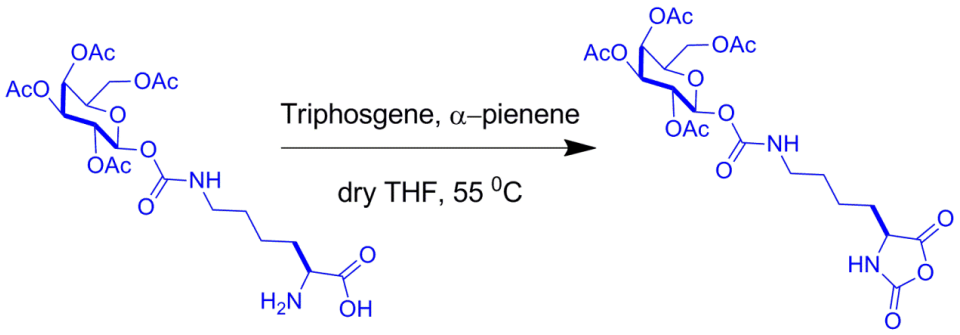

Scheme 3.3: Synthesis of galacto-N-carboxyanhydride.

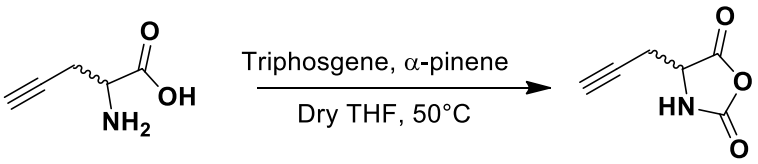

Scheme 3.4: Synthesis of D,L- propargylglycine N-carboxyanhydride.

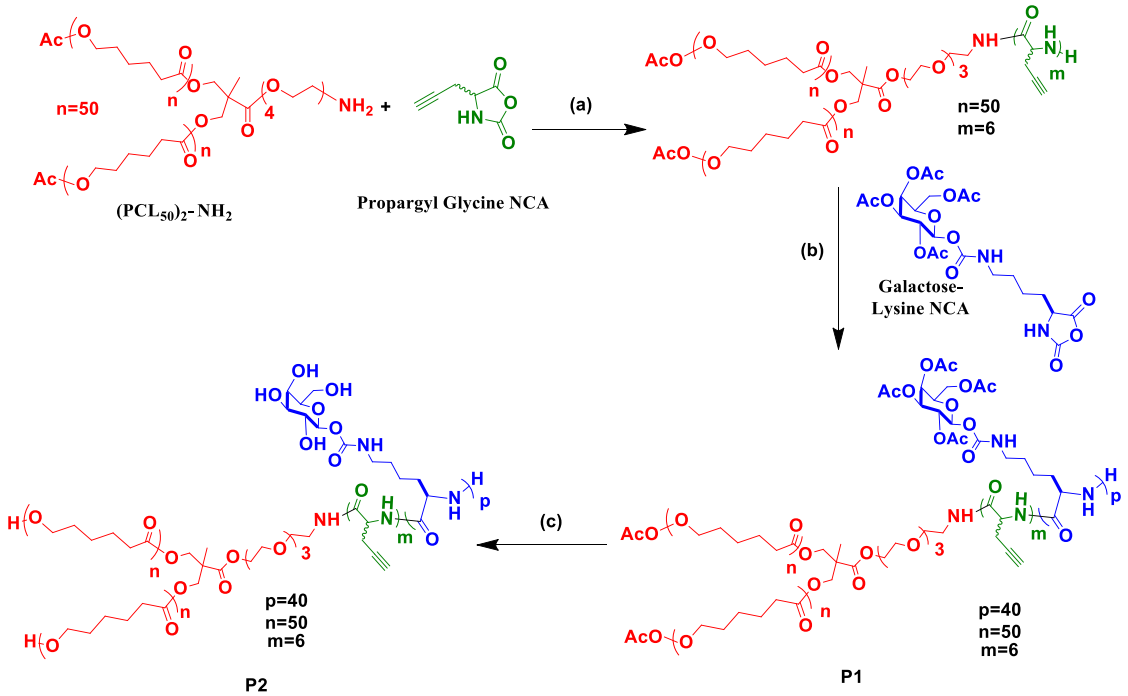

(a) DMF, RT (b) Proton Sponge (1.0 eq.), 38 h, RT (c) THF, Hydrazine hydrate (25 eq.),12 h.

Scheme 3.5: Synthesis of amphiphilic mikto-arm star copolymer $(PCL_{50})_2$-b-Pr-gly_6-b-GP_{40}.

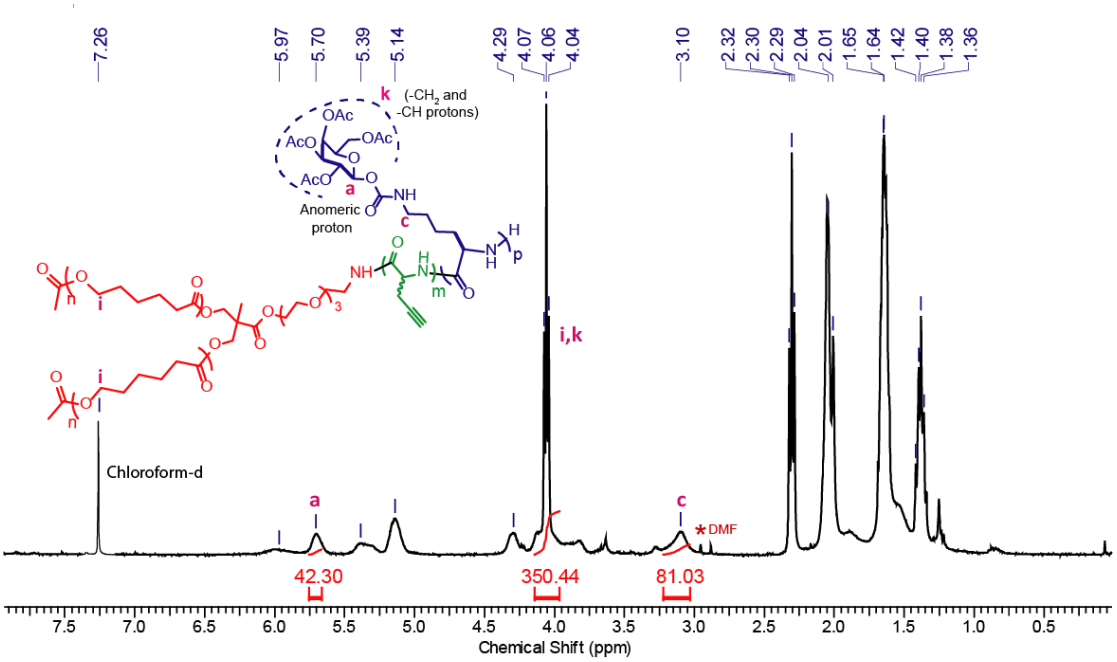

Figure 3.3: ^{1}H NMR spectrum of protected mikto-arm star copolymer $(PCL_{50})_2$-b-Pr-gly$_6$-b-AcGP$_{40}$

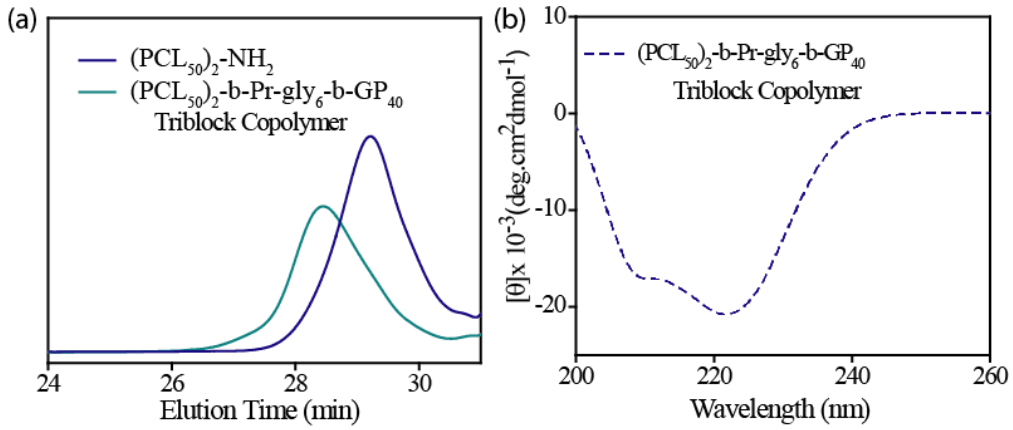

Figure 3.4: (a) GPC chromatograms of amine-terminated branched $(PCL_{50})_2$-NH_2) and protected star copolymer (P1) (b) CD spectrum of deprotected star copolymer (P2) in DI water.

The GP segment in the deprotected star copolymer $(PCL_{50})_2$-b-Pr-gly$_6$-b-GP$_{40}$ which is synthesized by the polymerization of racemic DL-propargylglycine NCA and enantiomerically pure α-*galacto*-*O*-lys NCA affords a polypeptide backbone composed of racemic poly DL-Pr(gly) and enantiomerically pure poly-L-lysine. Hence, the secondary structure of block copolypeptide in deionized water was determined by circular dichroism (CD) spectroscopy, which showed characteristic minima at 208 and 222 nm that confirms α-helical nature (Figure 3.4b). It is revealed that helical nature of the GP arm in the star

copolymer was not disturbed by incorporating a random and short poly(propargylglycine) block.

3.3.3 Estimation of alkyne groups in star block copolymer [$(PCL_{50})_2$-b-Pr-gly_6-b-$AcGP_{40}$]

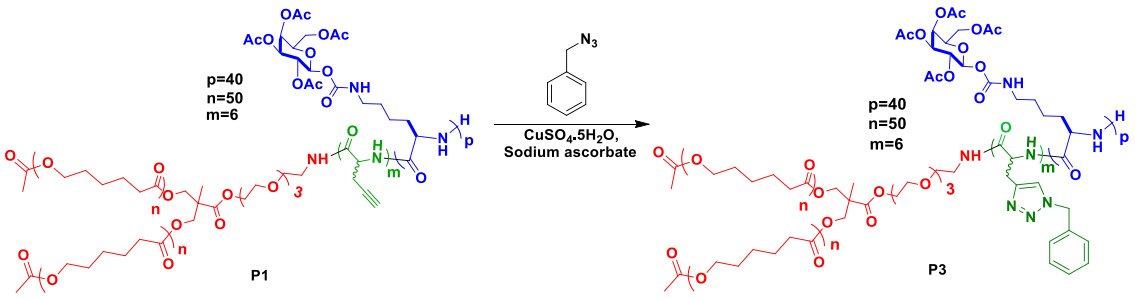

Scheme 3.6 Click reaction of alkyne-containing miktoarm star copolymer (P1) with benzyl azide to obtain P3.

From the NMR spectrum the significant peaks of propargylglycine protons in star copolymer (P1) were not visible due to overlapping with other peaks, hence to confirm the presence of short poly(propargylglycine) block in copolymer, polymer P1 was reacted with benzyl azide using Cu(I) catalyzed azide-alkyne ‘‘click chemistry’’(Scheme 3.6).

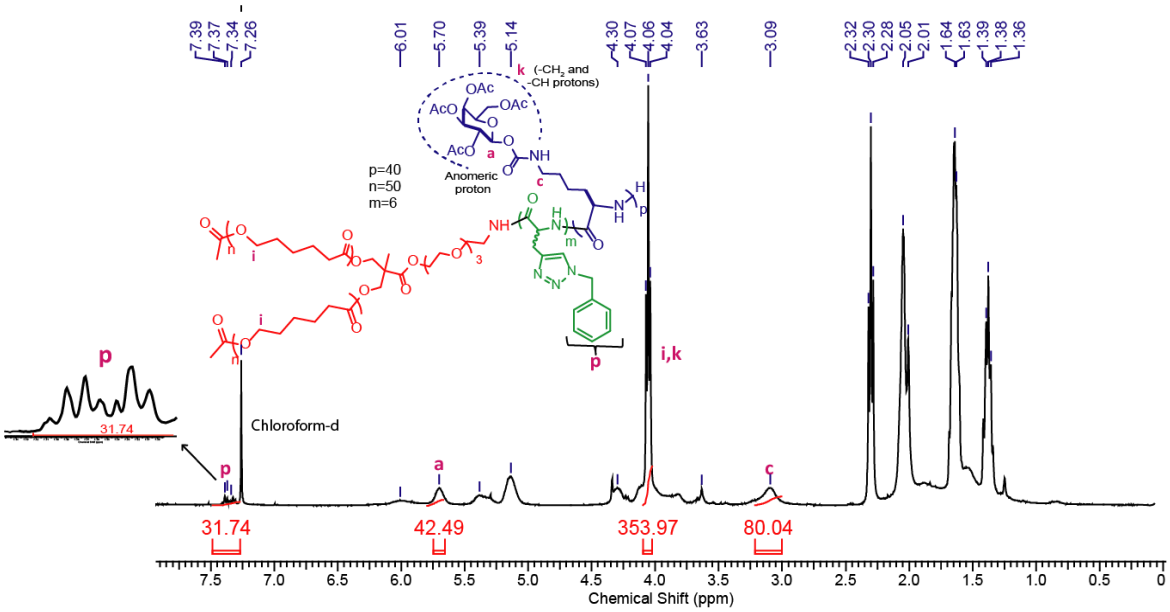

Figure 3.5: ^{1}H NMR spectrum of polymer **P1** after click reaction with benzyl azide.

The number of benzyl groups incorporated in the star copolymer P1 was estimated from ^{1}H NMR by integrating the characteristic anomeric proton of the GP segment at 5.67

(ppm) denoted as 'a' with respect to the characteristic aromatic protons at 7.3-7.43 (ppm) denoted as 'p'. It showed the incorporation of ~6 units of propargylglycine in the star copolymer (P1) (Figure 2). The overall ratio of initiator $(PCL_{50})_2$-NH_2, DL-propargylglycine and α-*galacto*-*O*-lysine in the block copolymer (P1) was found to be 1: 6: 40 as expected.

3.3.4 Self-assembly of mikto-arm star copolymer in aqueous medium

Out of many efficacious nanocarriers, polymeric micelles assembled from amphiphilic block copolymers are very popular and have been a major research theme in the area of drug delivery. Polymeric micelles were one of the first polymer based self-assemblies reported as a nano-drug delivery system.[23] These are the nano-sized colloidal particles, prepared from the self-assembly of amphiphilic block copolymers and consist of inner hydrophobic core and outer hydrophilic shell. Micelles have been extensively used as a carrier to deliver conventional hydrophobic anticancer drugs, such as paclitaxel (PTX) and doxorubicin (DOX) as they improved poor drug solubility, prolonged in vivo circulation time and preferential accumulation at tumor site via the enhanced permeability and retention (EPR) effect.[24-26] The synthesized amphiphilic three-arm star copolymer was dissolved in DMSO, and then same volume of water was added to maintain the final polymer concentration at 0.05 wt%. During this process, the amphiphilic block copolymer which comprises of heterogeneous block undergoes self-assembly process in the suitable solvent (a good solvent for one block and a poor solvent for another block).[41] During self-assembly of block copolymer, diffusion of common solvent (DMSO) in the aqueous medium occurs which forces the PCL (hydrophobic block) to undergo microphase separation and leads to the formation of self-assembled structures. This clear solution was dialyzed thoroughly against deionized water to remove the DMSO. To determine the morphology of the self-assembled structures, a drop of above solution was placed on carbon-coated grid and examined under transmission electron microscope using uranyl acetate (0.2 wt %) as negative stain. Well dispersed particles with spherical core-shell morphology with having an average size of ~140 nm ± 23 nm was observed (Figure 3.6a and Table 3.1). For further evidence, the morphology of self-assembled structures was also determined by (AFM) analysis (Figure 3.6b) which also corroborated with the TEM results. (DLS) analysis was performed to determine the hydrodynamic diameter of the spherical morphology in solution phase. A hydrodynamic diameter of ~163 nm ± 19 nm was observed by DLS measurements (Figure 3.7). The obtained higher values for the

hydrodynamic diameter in DLS analysis is probably due to the presence of solvation layer along with the particle in the aqueous phase. The obtained spherical morphology is called as uncrosslinked (UCL) micelles.

In the previous studies on GP-PCL block copolymers self-assembly behavior was well explained, as different types of morphologies were formed by tuning molecular parameters of GP-PCL copolymer system. Herein, formation of final morphological structures self-assembled from star block copolymer was governed by three important parameters *viz*. W_{philic}, helicity of GP block, and crystallinity of branched PCL chains.[16] Generally, in an amphiphile where hydrophilic to hydrophobic ratio is less than 0.5, it forms polymersomes while those with a ratio greater than 1.0 usually form micelles.[42] But in GP-PCL copolymer system two different morphologies were formed although they exhibit same hydrophilic weight fraction (W_{philic}), therefore W_{philic} was not a sufficient and only factor in the formation of these morphologies.[16] It has been reported that GP segment exhibits secondary conformation (helical nature) and the helicity can be varied by varying the chain length of GP segment. The extent of helicity shows strong correlation with the self-assembly of GP based nanocarriers system. For example, a short GP segment present in 10GP-$(PCL_{25})_2$[16] and 12GP-PPO[43] system was shown to be roughly helix-coil or weak helix system exhibiting about ~23% of helicity, which makes the GP segment flexible and dynamic in solution. This flexible helix conformation of GP segment helps in efficient packing during self-assembly and resulting in a morphology bearing lower curvature like nanorods or polymersome. As the length of GP segment was increased, the percent helicity also increased and led to formation of assembly with higher curvature like micelles and worm-like micelles.[15,16,43] Similar result was obtained in a previous study, wherein GP-dendron block copolymer conjugates containing longer GP block formed micelles and that with smaller GP block formed nanorods.[15] PCL as a hydrophobic block also shows a significant role in the formation of the self-assembled structures. Crystalline behaviour of PCL depends on type of block copolymer and regularity of crystalline domain in the copolymer usually increases with the PCL chain length.[44] Therefore, it seems to be a combined role of three factors *viz*. hydrophilic weight fraction, crystallinity of PCL blocks and helicity of GP block that determines the formation of the final morphologies from these star block copolymers. Similarly, in the amphiphilic star copolymer $(PCL_{50})_2$-*b*-Pr-gly_6-*b*-GP_{40} all three factors would play an important role in the formation of final morphological structures. The star copolymer was calculated to have

hydrophilic to hydrophobic ratio of ~1.08, therefore it was expected to self-assemble into micelles. Further, percent helicity of ~52 would also lead to the formation of morphology with high curvature like micelles. Hydrophobic segment PCL containing chain length of 50 in each arm, will impart larger crystalline domain, offers substantial reinforcement to the nanostructures and controls their shape and size.[45] It is also suitable for formation of micelles. Incorporation of short poly Pr(gly) random block between the two individual blocks (GP and PCL) for crosslinking with diazide crosslinker does not show any effect on the overall structural morphology however. it is surmised to have some role in determining the the arrangements of blocks in the formation of micellar structure of larger size compared to the previously reported GP-PCL system.

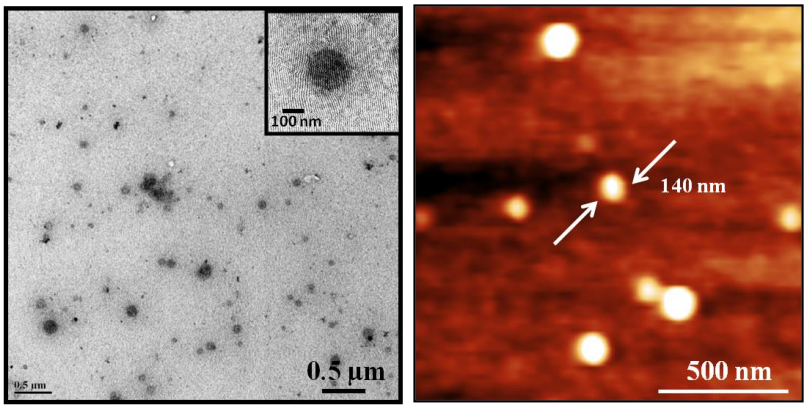

Figure 3.6: (a) Transmission electron microscopic (TEM) image of UCL micelles (inset shows individual micelles) (b) Atomic force microscopic (AFM) image of UCL micelles.

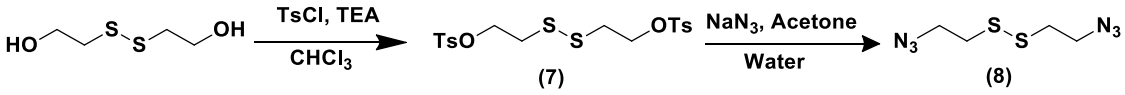

Scheme 3.7: Synthesis of cleavable bis-(azidoethyl) disulfide crosslinker (BADS).

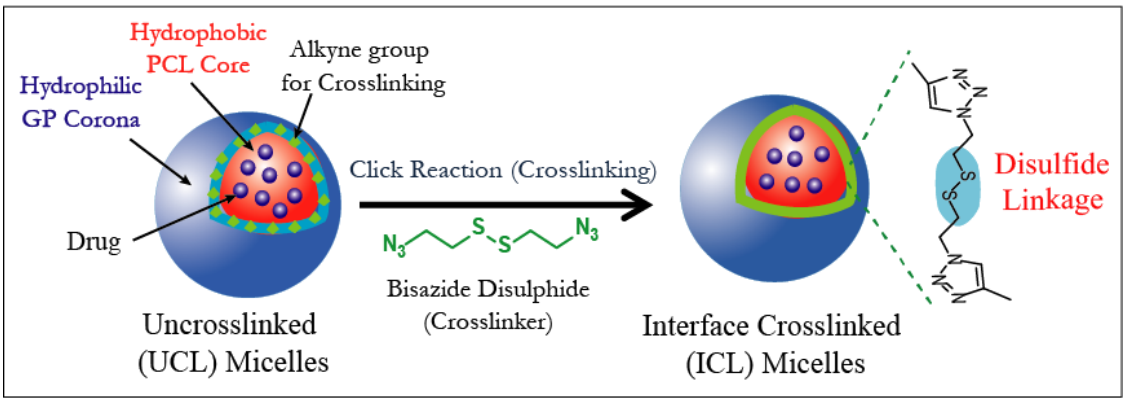

Scheme 3.8: Schematic for the synthesis of interface crosslinked micelles (ICL) via click chemistry.

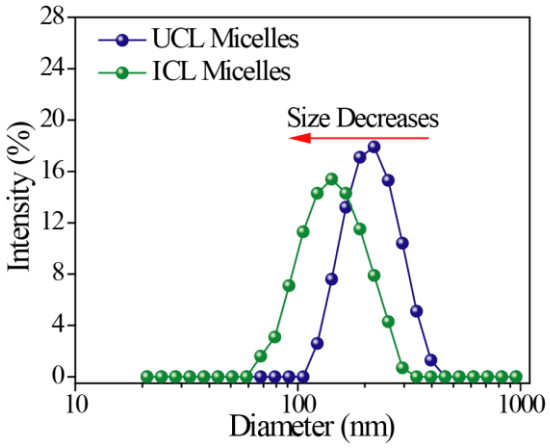

Figure 3.7: DLS size distribution of UCL and ICL micelles.

3.3.5 Preparation of interface crosslinked (ICL) micelles

The $(PCL_{50})_2$-b-Pr-gly_6-b-GP_{40} star copolymer was designed in such a way that alkyne groups of middle poly Pr(gly) block can be covalently crosslinked with azide groups of diazide crosslinker *via* click chemistry. Further, redox-responsive groups in the star copolymer micelles were introduced by using dithiol containing diazide crosslinker, i.e. bis-(azidoethyl) disulfide (BADS). As the alkyne groups containing middle block was present at the core-shell interface of the preformed UCL micelles, the prepared cross-linked micelles are known as interface crosslinked (ICL) micelles (Scheme 3.8). Crosslinking in the micellar assemblies will not only retain their three-dimensional structure in the solution but also enhance their stability below a particular concentration i.e. CMC so that they can be successfully used for the drug delivery application. The crosslinking of the interface is not only an effective strategy to decrease the micellar disruption during blood circulation but also creates the barrier to prevent the leakage of entrapped drug molecules and thereby decrease the burst release to a large extent. The preparation of the cross-linked micelles requires a combination of self-assembly and covalent bond formation between the polymer chains for the production of stable nanostructures. For this purpose, UCL micelles were reacted with diazide disulfide crosslinker in DMSO: water (1:1) in the presence of copper sulfate and sodium ascorbate to cross-link the middle block. The obtained ICL micelles were analyzed by TEM (Figure 3.8a) and AFM (Figure 3.8b) techniques, which show the average particle size of ~105 nm ± 16 nm whereas the hydrodynamic diameter of 129 ± 26 nm was obtained from DLS analysis (Figure 3.6 and Table 3.1).

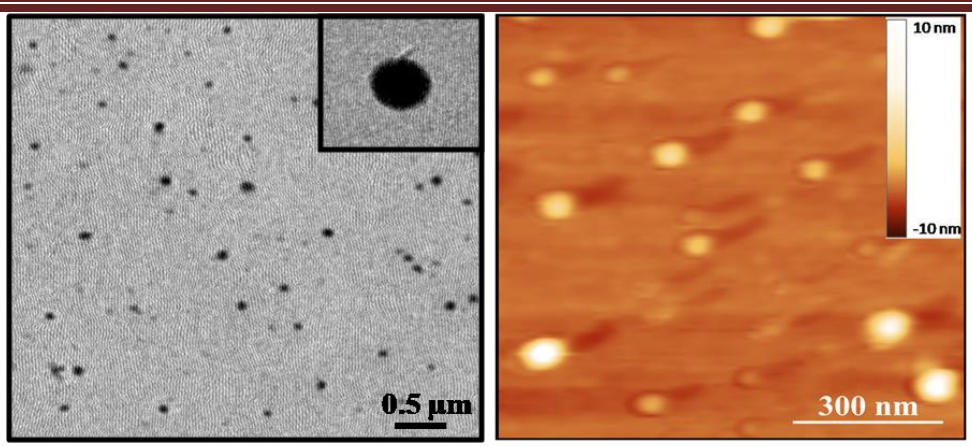

Figure: 3.8 Images from (a) TEM (inset shows individual micelles) and (b) AFM analysis of ICL micelles.

Moreover, all particles were well dispersed, and almost no aggregation was found during crosslinking reaction, implying that there was no intermicellar reaction during crosslinking. These results were also in concurrence with the previous studies for the preparation of ICL micelles wherein outer coronal hydrophilic part prevents crosslinkable inner shell to undergo intermicellar crosslinking due to steric hindrance.[37] This is the major advantage of interface crosslinked micelles over others such as core or shell cross-linked micelles. From all techniques, it was observed that ICL micelles have a lower diameter compared to UCL micelles. This decrement in size of ICL micelles might be due to the crosslinking which results in the formation of a fixed chemical network between the randomly oriented free propargyl groups of propargylglycine. This leads to the formation of a condensed structure with lower diameter. This trend was also in concurrence with the previous studies on the crosslinked micellar structure confirming the covalent bond formation between the cross-linkable groups of polymer. For example, folate conjugated interlayer crosslinked micelles prepared through photo-crosslinking of PEG-PAC-PLA/FA-PEG-PLA block copolymer micelles showed shrinkage in size by 10-15 nm because of the formation of the compact layer around the hydrophobic core.[34] All these results clearly reveal that crosslinking has an effect on the micellar size.

3.3.6 Dye encapsulation and CMC determination

The determination of CMC values for newly formed amphiphilic star copolymer micelles was necessary for their further studies because CMC values are directly related to the thermodynamic stability of resultant micelles. CMC value of the UCL micelles was evaluated using rhodamine B octadecyl ester (RBOE), as a hydrophobic dye. Initially, the micelle structure was confirmed by RBOE dye encapsulation in UCL and ICL micelles.

The UV−Vis spectra of RBOE-encapsulated UCL micelles and ICL micelles (λ_{max}≈ 565 nm) show a clear blue shift compared to water (λ_{max}≈ 575 nm), which indicates that RBOE can predominantly locate in a relatively nonpolar environment i.e; hydrophobic core of the micelles. It was evidenced by a visual change in colour of the solution and from fluorescence emission spectrum, which showed a broad peak with λ_{max} at 578 nm when excited at 554 nm (Figure 3.9). This result suggests that these bioactive micellar assemblies are capable of encapsulating hydrophobic guest molecules. Therefore, to determine (CMC) value, fluorescence emission spectra of the encapsulated RBOE dye at different polymer concentrations was recorded by exciting at 554 nm and λ_{em} of RBOE was plotted versus concentration of polymer to give the typical CMC curve. A CMC value of 15.6µg/mL was obtained for UCL micelles (Figure 3.10a). Further, confirmation of crosslinking in UCL micelles was done by CMC experiments, which show that ICL micelles do not have detectable CMC value (Figure 3.10b). The results are similar to observations made in previous reports[46,47] and show that crosslinking of UCL micelles was successful. By decreasing the concentration below a particular value (CMC), UCL micelles would dissociate into unimers whereas ICL micelles would not. Due to core-shell interface crosslinking, RBOE dye was stabilized within the hydrophobic core of ICL micelles even at very low concentration. Therefore; these nanomaterials could be used at both low and high concentrations.[48]

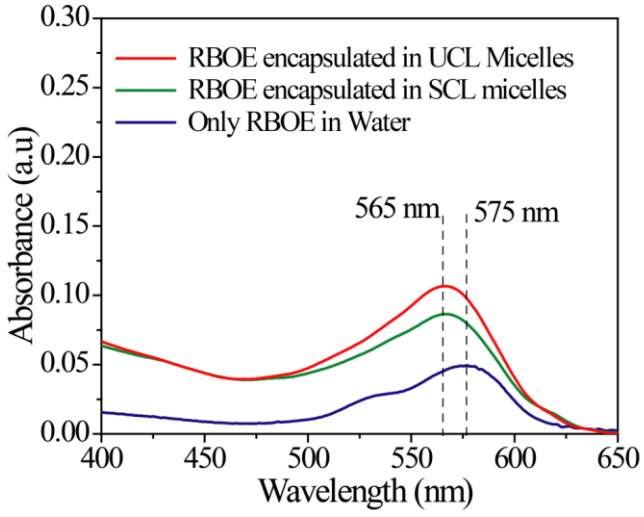

Figure 3.9: UV-Vis absorption spectra of free RBOE in water and RBOE encapsulated in UCL and ICL micelles.

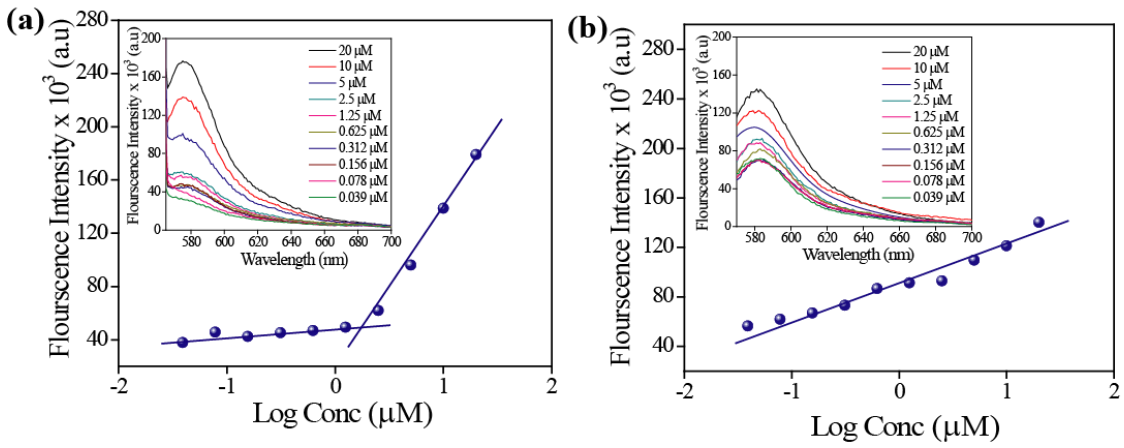

Figure 3.10: Plot of fluorescence intensity versus the logarithm of the polymer concentration (μM) in aqueous solution (a) Uncrosslinked (UCL) micelles (b) Interface crosslinked (ICL) micelles. Inset: Fluorescence emission spectra of RBOE in an aqueous solution of the polymer at different concentrations.

3.3.7 Stability studies of micelles

For further confirmation of the crosslinking and to check the stability of micelles, three experiments, *viz.* dilution assay, size determination below CMC and time-dependent dye release were performed with both UCL and ICL micelles. Firstly, for dilution assay, preformed ICL and UCL micelles in aqueous medium were diluted with a 10-fold volume of DMF. After dilution, the disappearance of DLS signal in the range of 100-200 nm and appearance of the new signal in the range of ~10 nm was observed for the UCL micelles, which confirms their disruption probably due to the dissolution of the polymer in DMF. On the other hand, particle size in the same range (100-200 nm) was observed for the ICL micelles even after dilution (Figure 3.11a). In the previous reports, crosslinked micelles prepared *via* crosslinking in either core, shell or core-shell interface show similar results.[32,34] For example, in a report, dissociation of normal micelles into the unimers was observed by DLS after dilution with 5-fold THF as an organic solvent whereas, UV-irradiated crosslinked micelles showed stability against dilution.[34] This confirms that ICL micelles retain their structural stability after dilution and cross-linking allows them to withstand in DMF, which is a suitable solvent for both the blocks.

Further, the stability of micelles was also evaluated by DLS technique above and below CMC. In case of UCL micelles, a huge change in PDI and particle size (both high and low values) was observed by DLS measurement above and below CMC value compared to ICL micelles (Figure 3.11b), which show similar value as shown above CMC. The

disassembly of the UCL micelles after dilution (below CMC) can be compared with the disruption that occurs when injected *in vivo* which leads to the premature and burst release of encapsulated drugs during circulation in the bloodstream. Here, the polydispersity change in UCL micelles upon dilution can be well explained by the solubility behaviour of two individual blocks (PCL and glycopolypeptide) in the aqueous medium after dissociation of UCL micelles into free polymer below CMC value. PCL is hydrophobic while GP is hydrophilic in nature and hence a range of particle sizes was observed in DLS analysis due to aggregation of individual amphiphilic block copolymers. This study further confirms the stability of ICL micelles below CMC values. There are previous reports where the similar experiment was performed to check the stability of micelles. For example, when the crosslinked micelles prepared from PEG-DTT-PCL based block copolymer were diluted by addition of 1000-fold water (C << CMC), no significant change in the particle size and distribution was observed whereas uncrosslinked micelles underwent a dramatic change in both particle size and distribution.[49] Similar observations are found in the other reports which also confirm their thermodynamic stability against dilution.[34] All the above results indicate the micellar stability against extensive dilution by introducing the crosslinking, which enhance their stability during circulation in the bloodstream.

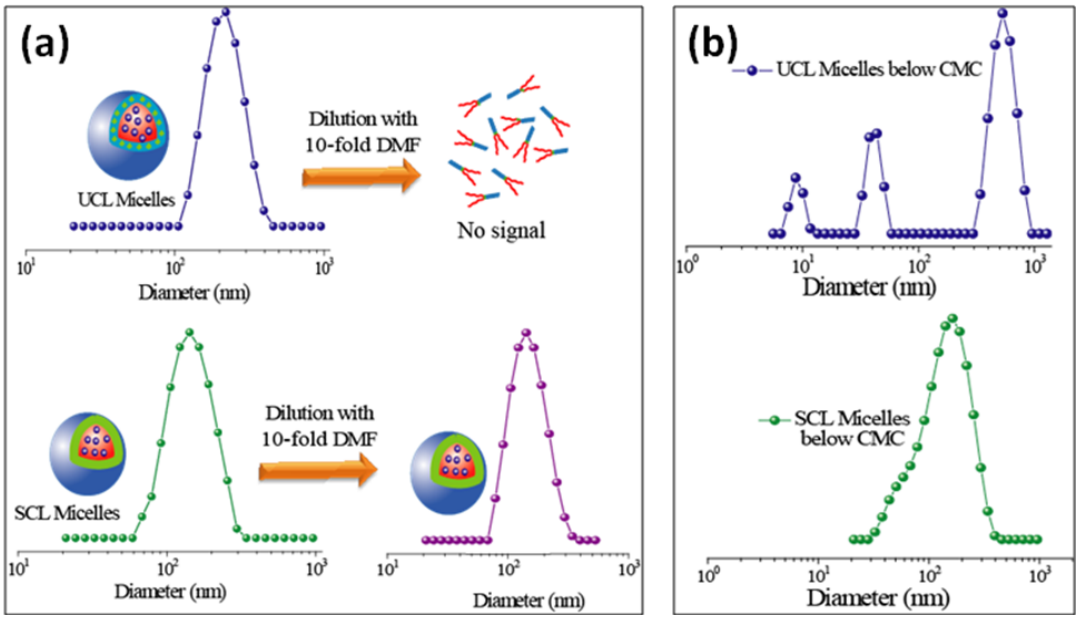

Figure 3.11: Stability studies of UCL and ICL micelles: DLS size distribution curves (a) upon dilution by 10-fold volume of DMF and (b) below CMC.

Time-dependent stability studies of UCL and ICL micelles were also studied using fluorescence spectroscopy. Changes in the fluorescence intensity of RBOE encapsulated in UCL and ICL micelles were observed with time (Figure 3.12). In case of UCL micelles, a substantial decrease in the fluorescence intensity was observed with time whereas ICL micelles maintained significant fluorescence intensity.

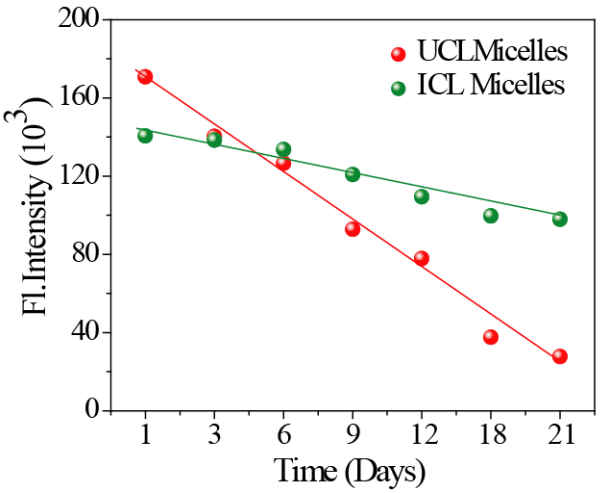

Figure 3.12: Changes in RBOE fluorescence intensity encapsulated in UCL and ICL micelles with time.

This can be explained by the dissociation of UCL micelles with time which leads to the fast release of RBOE as compared to ICL micelles. As RBOE forms non-fluorescent dimers in aqueous medium but shows strong emission in the hydrophobic core of micelles[50] the fluorescence intensity of RBOE released from UCL micelles in aqueous medium continuously decreased with time whereas ICL micelles showed significant fluorescence intensity within specific time period. The obtained results confirmed the higher stability of ICL micelles due to crosslinking compared to UCL micelles and that ICL micelles are capable of storing the encapsulated molecules for substantially longer period of time.

3.3.8 Doxorubicin loading in UCL and ICL micelles

To demonstrate the ability of micelles to encapsulate hydrophobic anticancer drug molecules in their hydrophobic core, doxorubicin (DOX) was chosen. It was loaded into the UCL and ICL micelles by simply mixing with the star copolymer during self-assembly and subsequent dialysis against deionised water removed the free DOX. DOX loading efficiencies (DLE) in UCL and ICL micelles were estimated by UV-Vis spectroscopy (Figure 3.13a). The obtained DLE of UCL and ICL micelles are 36.7% and

32.86%, respectively (Table 3.1). The lower DLE value for ICL micelles compared to UCL micelles is probably due to the loss of drug during crosslinking process. A small increment in the size of UCL and ICL micelles was also observed after drug (DOX) encapsulation. The hydrodynamic size of DOX-loaded UCL and ICL micelles observed from DLS analysis was 179 and 147 nm, respectively (Figure 3.13b) while the average size of DOX encapsulated ICL and UCL micelles measured from TEM analysis was ~168 nm and ~132 nm, respectively (Figure 3.13c and 3.13d and Table 3.1). These results demonstrated that the particle size of DOX-loaded UCL and ICL micelles was larger than that of blank UCL and ICL micelles. Previous studies based on the DOX encapsulation in the inner hydrophobic core of micelles also demonstrate that the size of micelles increases after sufficient loading of hydrophobic drugs and is also comparable to micellar system described here.[35] It can be mainly attributed due to the encapsulation of hydrophobic DOX in the core of both the micelles which increases the inner space and increases overall particle size.

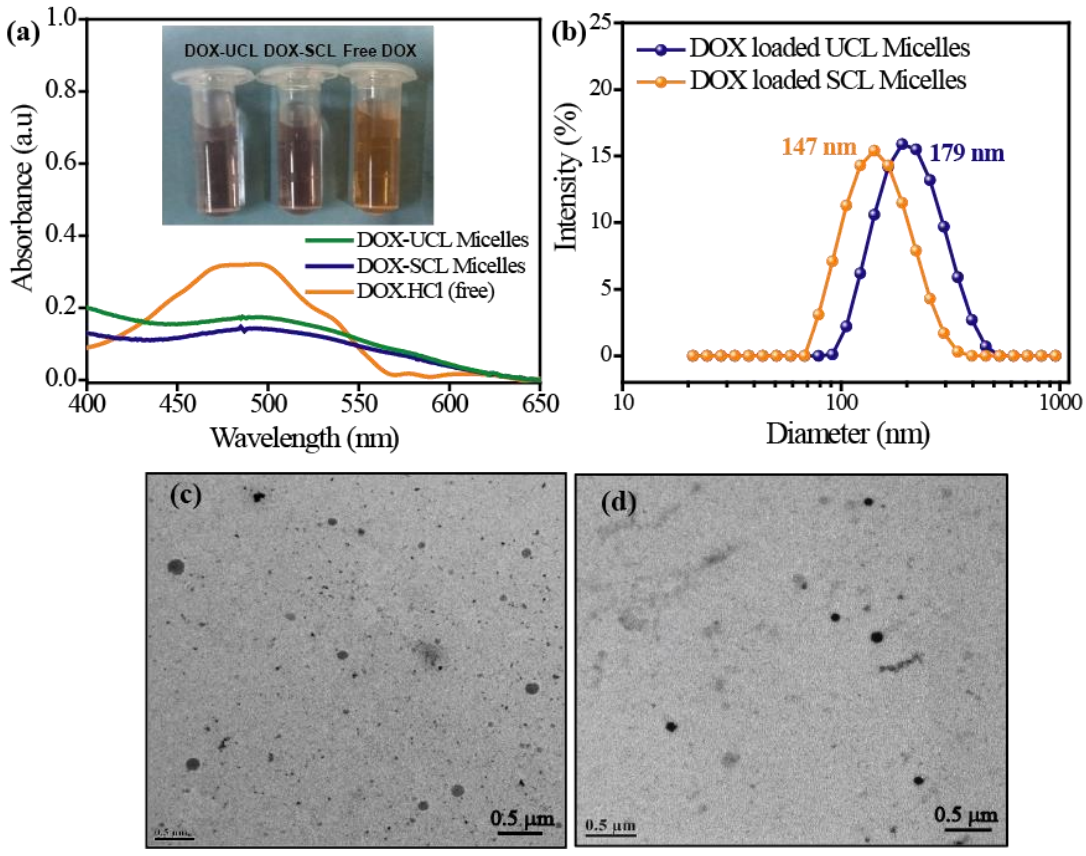

Figure 3.13: (a) UV-Vis absorption spectra of free DOX and DOX encapsulated in UCL and ICL micelles (b) DLS measurement of DOX encapsulated UCL and ICL micelles (c) TEM image of DOX-loaded UCL micelles (d) TEM image of DOX-loaded ICL micelles.

Table 3.1. Characteristics of blank and DOX-loaded UCL and ICL micelles.

Entry no.	Micelles	D_h (nm)	PDI	DLE (%)
a)	UCL Micelles	140 nm ± 23 nm	0.218	-
b)	ICL Micelles	105 nm ± 16 nm	0.209	-
c)	DOX-UCL Micelles	168 nm ± 19 nm	0.254	36.7 %
d)	DOX-ICL Micelles	132 nm ± 17 nm	0.236	32.8 %

3.3.9 In vitro drug release studies: redox and enzyme responsive release studies

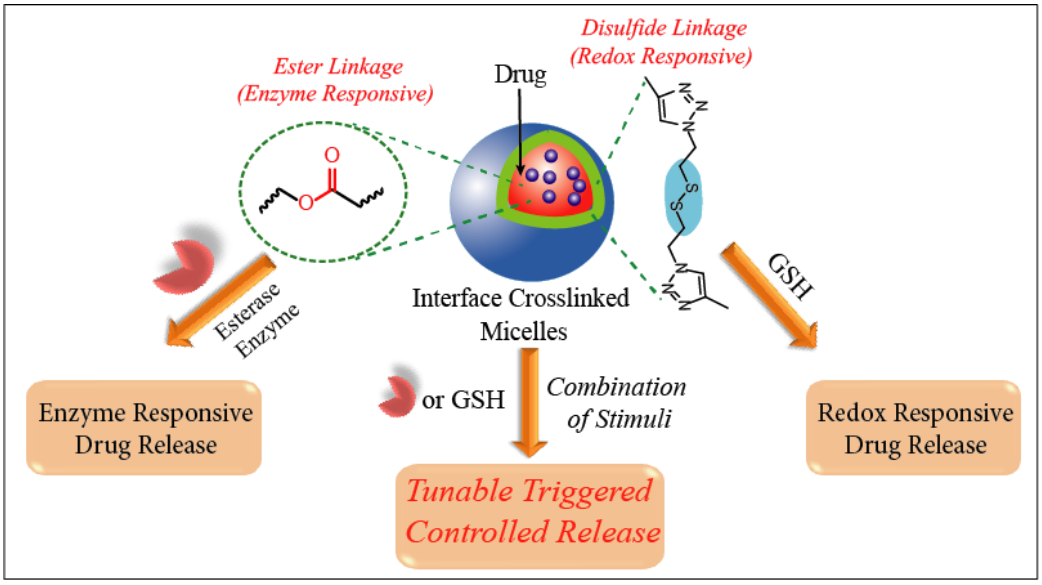

Scheme 3.9: Schematic representation of release of drugs from ICL micelles in response to single and dual stimuli.

In vitro release studies were performed for the ICL micelles as these micelles comprise of both redox-responsive (disulfide bond in interface crosslinked region) and enzyme responsive (ester group in hydrophobic core: PCL block) groups(Scheme 3.9). For all the release studies, doxorubicin (DOX) was used as a hydrophobic drug, which is widely used as an antineoplastic agent in adult and pediatric cancer therapy. It shows an anticancer effect after insertion into DNA strands which inhibits the synthesis of bioactive macromolecules and leads to cell death.[51] Herein, the release behavior of ICL micelles was studied by applying the stimuli individually as well as simultaneously. Recently, redox-responsive nanocarriers are of great interest because of the active intracellular drug release due to the presence of GSH concentration gradient in the intracellular environment.[34,35,52,53] Firstly, the DOX release from ICL micelles was studied by using

reducing agent glutathione (GSH) as a redox stimulus. The intracellular environments in tumor tissues are unusually different from the normal tissues. The difference between the amount of glutathione (GSH, ~10 mM) in the tumor cells compared to that in the blood (1-2 µM) or normal tissues (2-20 µM) makes it an ideal trigger system for the designing of redox-responsive micelles.[35,52,53] To explore redox-responsive behavior of ICL micelles, the DOX release at two different concentration of GSH (~2 µM GSH and ~10 mM GSH) under physiological condition (PBS, pH 7.4, 37 °C) was studied (Figure 3.14a).

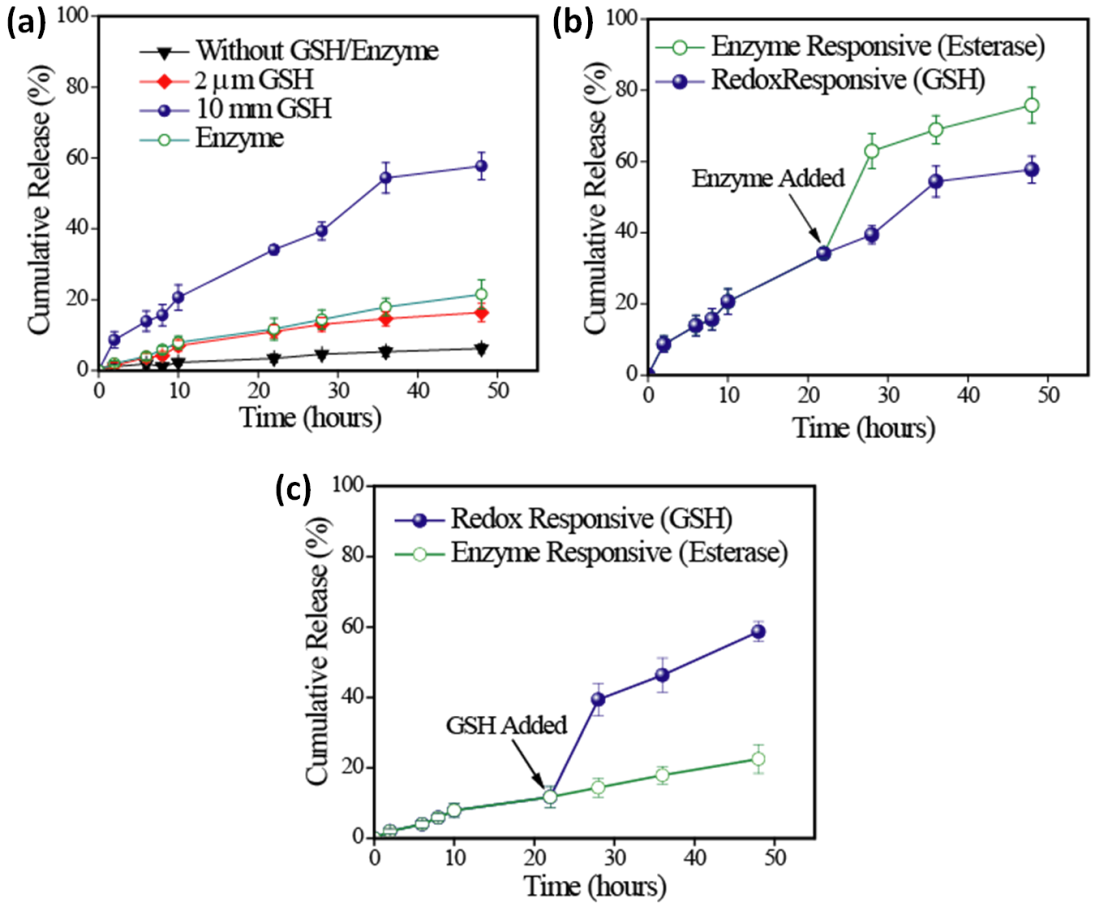

Figure 3.14: Release of DOX from ICL micelles (a) in presence of esterase and GSH (~2 µM GSH and ~10 mM GSH) (b) by applying dual stimuli (Case 1: Redox and Enzyme) (c) by applying dual stimuli (Case 2: Enzyme and Redox).

In the presence of ~2 µM GSH, the cumulative release of only ~10% of the drug was observed in 48 h compared to ~10 mM GSH where ~60% of DOX release occured in 48 h. In the absence of GSH as a control, only 5% DOX released was observed (Figure 3.14a). The controlled release of DOX could be attributed to the cleavage of disulfide linkages by GSH and is consistent with results observed by Zhong and co-workers.[10] These results are also in concurrence with several other studies, which show that redox-

responsive micelle shows different release behaviour at two different GSH concentration (~2 μM GSH and ~10 mM GSH). These results indicate that micellar assembly is only disrupted by GSH-mediated cleavage of disulfide bonds. It is demonstrated from these studies that the disulfide containing interface cross-linked micelles can encapsulate hydrophobic molecules and release them selectively into the affected site in response to changes in the redox environment. Therefore, it is expected that these micelles would show similar stability in blood circulation with minimum drug release, but undergo disruption rapidly and show burst drug release in intracellular environment of tumor sites.

Enzymes play an important role in various biological and metabolic processes inside the intracellular environment by catalyzing several chemical reactions.[54,55] As they naturally exist inside the biological system these enzymes can be used as a trigger for the stimuli-responsive nanomaterials in controlled drug delivery application.[55] Therefore, the release of DOX from ICL micelles was also studied by applying another stimulus i.e. esterase enzyme. Enzyme triggered drug release was also investigated in different system using esterase enzyme.[56,57] The block copolymer, apart from being redox-responsive, can also be responsive to the enzyme as the hydrophobic segment branched PCL of the copolymer consists of ester bond and act as a degradable enzyme-responsive block. Esterase enzyme as external stimuli can also cleave copolymer structure and should disassemble the whole micellar structure. Similar to the redox-responsive studies, the enzyme-responsive DOX release studies were performed under physiological conditions (PBS, pH 7.4, 10 units of esterase enzyme, 37°C) [57] and the release kinetics of DOX were studied in both absence and presence of esterase enzyme. In the absence of esterase enzyme, ~5% DOX releas was observed, whereas in the presence of enzyme only ~22% of the drug was released in 48 h (Figure 3.14a). These results are quite different from redox-responsive studies because of the different location of stimuli-responsive group (PCL chains) in star copolymer and type of stimuli used. Here, in the presence of an enzyme, the slow release of DOX from ICL micelles might occur due to the low permeability of esterase enzyme into the hydrophobic core to cleave the ester bond. As the inner hydrophobic core is more stabilized by the crosslinking at the interface, there is resistance to the esterase enzyme to enter inside the core. Sometimes, in a biological system, the extracellular enzymes acting as an external stimulus can also degrade the structure of nanoparticle before reaching the targets, and this can be a limitation for such type of drug delivery system. Here, this limitation can be overcome by crosslinking the micelles or by using a dual stimuli-

responsive system where control over the release of drugs is possible by applying two stimuli synergistically or by reversing their order.

Designing of the multi-stimuli-responsive systems, which show tunable drug release at the active site is an important goal in the development of smart drug delivery vehicles.[58] It will not only increase the efficacy of drug therapies but also support the diagnosis of diseases by monitoring various physiological changes at a time.[58] To explore this possibility, combined effect of both the stimuli i.e. redox-responsive and enzyme on drug release profile of ICL micelles was studied., The release behaviour from ICL micelles was investigated by applying both the stimuli simultaneously (Case 1: Redox and enzyme) and also by employing them in reverse order (Case 2: Enzyme and redox) (Scheme 3.9). In case 1, redox stimulus was applied on ICL micelles, which showed about 38% DOX release in the initial 22 h and total 56% in 48 h. When second stimulus (esterase enzyme) was applied after 22 h, a sudden increase in the release with an additional value of ~40% was observed in the next 26 h (total ~78% release in 48 h). Thus, ICL micelles on simultaneous exposure to both the stimuli lead to ~22% higher DOX release in 48 h as compared to a single stimulus (redox) in same period of time (Figure 3.14b). This sudden change in release profile after addition of enzyme was observed by the concurrent cleaving of disulfide as well as ester linkage in the micellar assembly. Initially, only one stimulus is responsible for DOX release by cleaving the disulfide bond at the interface but as the second stimulus is applied, both the stimuli work simultaneously and finally disassemble the entire micelle to release the drug. In the second case when the sequence of stimuli was reversed, and the DOX encapsulated ICL micelles were initially subjected to esterase enzyme for 22 h, a small release of ~16% was observed with the total release of 22% in 48 h. However, when GSH (10 mM) was added after 22 h, an abrupt increase in the release with an additional value of ~38% was observed within next 26 h (total ~60% release in 48 h). Thus, ICL micelles on simultaneous exposure to both the stimuli lead to ~38% higher DOX release in 48 h compared to a single stimulus (esterase enzyme) in same period of time (Figure 3.14c). A The enzyme is already present in the system when GSH was added after 22 h. The disulfide bonds at the interface crosslinking start cleaving and simultaneously enzyme gets access to the inner hydrophobic core to cleave the ester linkage which leads to sudden increase in the release of drug. From these results, it can be seen that by bringing temporal control and faster release in both the cases, the tuning

ability of drug release can be achieved. Additionally, these studies show that the enzyme remains active under redox condition and high GSH concentration.

3.3.10 Cytotoxicity studies

This dual stimuli-responsive nature of nanocarriers may be sequential or simultaneous, but these it allows to explore the different environments of cancer as well as the other stimuli in intracellular conditions. From the above drug releases studies, it can be demonstrated that the prepared micellar system would help in local distribution of drug in cancer tissues *via* the effect of both stimuli in the intracellular compartments. Therefore, both slow and fast release of DOX can be achieved via redox and enzyme responsiveness in a single micellar structure for cancer therapy.

Cellular entry experiments of both UCL and ICL micelles were investigated to ascertain whether they were capable of controlled drug delivery in mammalian cells. As cell viability is the necessary condition, cytotoxicity assay (MTT assay) of the star copolymer self-assembled into the micellar system (both ICL and UCL micelles) was performed. The experiments were conducted by incubating the micelles with liver cancer (HepG2) cells for 40 h. The concentration of the polymer assemblies was varied from 10 to 300 μg/mL. From MTT assay results, the non-toxicity of both UCL and ICL micelles was observed up to a concentration of 300 μg/mL as ~80% of the cells remained viable at this concentration up to 48 h, and it affirmed that the crosslinking of UCL micelles would not affect the cytotoxicity (Figure 3.15a). The cell viability results indicated the biocompatibility of both UCL and ICL micelles for further drug delivery application.

MTT assay of free DOX and DOX-loaded UCL and ICL micelles was also performed in HepG2 cell line by maintaining the similar experimental conditions used for blank UCL and ICL micelles for 24 h. The DOX concentration for MTT assay was chosen depending on the amount of DOX present in the micelles i.e. DOX concentration was varied from 0 μg/mL to 0.8 μg/mL corresponding to the particular micellar concentration. For comparison, the same concentration of free DOX was used for the control experiment. The MTT assay results corresponding to free DOX, DOX-loaded UCL and ICL micelles in HepG2 cells are shown in figure 3.15b. It is observed that free DOX had greater cytotoxicity than the DOX-loaded UCL and ICL micelles within 24 h, which suggests that the penetration of free DOX in cells is faster as compared to DOX release from the micelles, which is a slow process. Figure 3.15b also reveals higher cytotoxicity of DOX-

loaded UCL micelles compared to ICL micelles indicating that DOX release was faster from UCL micelles. ICL micelles showed slower release of DOX, as crosslinking leads to stabilisation and disulfide bond is slowly cleaved by intracellular GSH. The results demonstrated that the UCL and ICL micelles are non-toxic but DOX-loaded micelles had an apparent inhibitory effect on the growth of HepG2 cells.

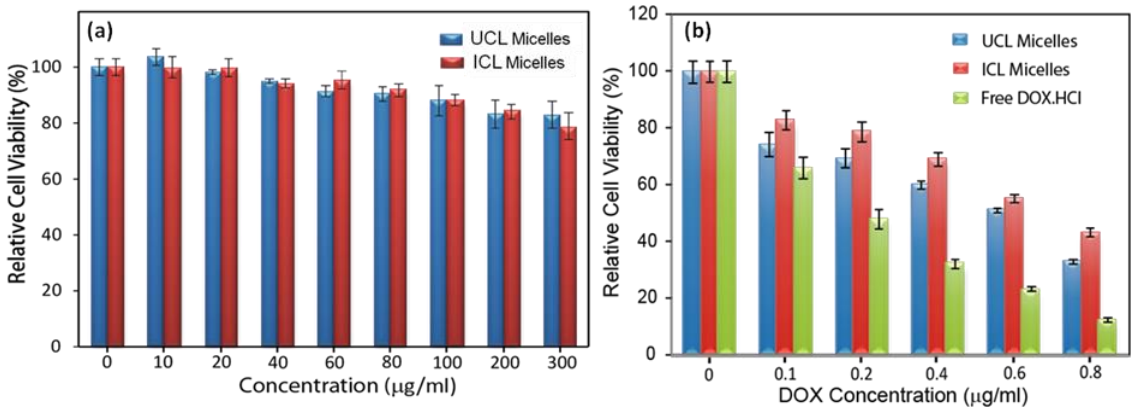

Figure 3.15: MTT assay data of (a) UCL and ICL micelles (b) DOX-loaded UCL and ICL micelles.

3.3.11 Cellular uptake studies

Cellular internalization and intracellular release behaviour of DOX-loaded UCL and ICL micelles were investigated in liver cancer (HepG2) cells by epifluorescence microscopy (Figure 3.16b). HepG2 cells are known to have over-expressed galactose binding asialoglycoprotein (ASGPR) receptor.[1] In a previous work, the uptake of carbohydrate decorated nanoparticle was explained by receptor-mediated endocytosis as carbohydrate receptors are responsible for this mechanism.[16] Further to understand the stimuli-responsive behaviour of DOX-loaded micelles for better drug accumulation, time-dependent intracellular uptake of DOX-Loaded UCL and ICL micelles was studied. HepG2 cells were incubated with DOX-Loaded UCL and ICL micelles and free DOX.HCl for 2, 12, 24 and 48 h at 37 °C.

As a control, when free DOX·HCl was incubated for 2 h, strong red fluorescence was observed both in the nuclei (mostly) and cytosol of the HepG2 cells compared to DOX-loaded UCL and ICL micelles (Figure 3.16c). When the HepG2 cells were treated with free DOX, a better overlap between DOX and DAPI staining dye was found in the nucleus as observed from fluorescence microscopic images. This occurred because the DOX molecules have the tendency to accumulate mostly inside the nucleus, which was evident in cells treated with free DOX. Furthermore, perinuclear localization of DOX-

loaded UCL and ICL micelles inside the cells was confirmed from the fluorescence microscopy image after 2 h of incubation (Figure 3.16a and 3.16b for 2h data). This was observed because of rapid internalization of water-soluble DOX·HCl, as DOX quickly enters into cells *via* passive diffusion whereas uptake of micelles occurred *via* receptor-mediated endocytosis. In case of UCL micelles, when the incubation time increased from 2 h to 12 h, DOX fluorescence was observed mainly in the nucleus which remained constant in next 24 and 48 h. This was easily noticed through the overlapping of DOX and DAPI fluorescence in the microscopic images (Figure 3.16a for 12, 24, 24 h data). However, in case of ICL micelles, increase in DOX fluorescence was observed in cytoplasm within 12 h, became more intense in 24 h in the perinuclear region and finally reached to the nucleus in 48 h (Figure 3.16b).

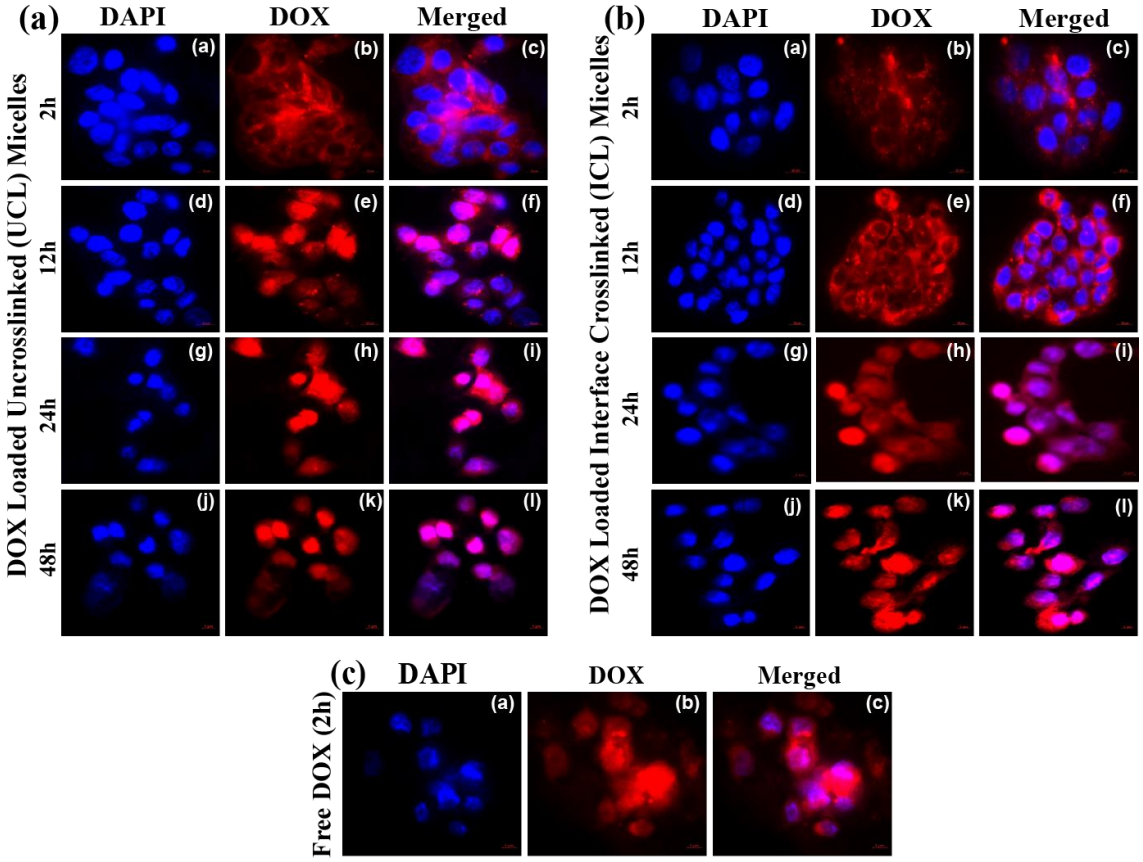

Figure 3.16: Epifluorescence microscopic images of intracellular distribution of (a) DOX loaded UCL and (b) DOX loaded ICL micelles at different time intervals (2, 12, 24, 48h) (c) free DOX, in HepG2 cell. For each panel, the images from the left to right show staining of cell nuclei by DAPI (shown in blue), DOX fluorescence in the cells (shown in red), overlay of the two images. The scale bars are 10 μm in all the images.

From these results, an efficient internalization of DOX-loaded UCL and ICL micelles and enhanced intracellular release of DOX upon micellar degradation was observed by HepG2 cells. Closer observation further reveals fast degradation of UCL micelles as compared to ICL micelles, leading to slower release of DOX from ICL micelles. The accumulation of DOX in the nucleus after release from ICL micelles was observed within ~24 h whereas it took only 12 h for DOX to accumulate in nucleus from UCL micelles. This result showed that, up to ~24 h, DOX molecules mostly reside in the ICL micelles and show prominent fluorescence in the cytosol, whereas they are easily released from UCL micelles after 12 h and accumulate in the nucleus. Therefore, it was confirmed that release of DOX occurs slowly from ICL micelles compared to UCL micelles. It can be explained by the slow cleavage of the disulfide linkage (crosslinking) by intracellular GSH to release the drug from the stabilized ICL micelles. The current investigation demonstrated that the cellular uptake of DOX from ICL micelles occurs due to stimuli-responsive release and it occurs in a time-dependent manner in HepG2 cells.

3.4 Conclusions

In conclusion, the design and synthesis of amphiphilic glycopolypeptide star copolymer based stimuli-responsive interface crosslinked (ICL) micelles for programmed and targeted drug delivery was demonstrated. For this purpose, miktoarm star block copolymer $(PCL_{50})_2$-b-Pr-$gly_{5\text{-}6}$-b-GP_{40} was synthesized by ROP of two conventional NCA's (DL-propargyl glycine NCA and α-*galacto*-*O*-lys NCA) sequentially initiated by amine-terminated branched hydrophobic polycaprolactone, $(PCL_{50})_2$-NH_2. The star copolymer was initially self–assembled into uncrosslinked (UCL) micelles depending upon three different factors *viz.* helicity of GP block, hydrophilic−hydrophobic ratio and crystallinity of PCL. Further, free alkyne groups of the middle block at core-shell interface of the UCL micelles were reacted with bis-(azidoethyl) disulfide (BADS) as redox-responsive crosslinker *via* click chemistry to form interface crosslinked (ICL) micelles. The synergistic effect of dual stimuli (redox and enzyme) on the drug release behaviour from ICL micelles was studied using doxorubicin (DOX) as a model drug. Furthermore, the presented UCL and ICL micelles were explored towards their biological application as potent drug vehicles with low *in vitro* cytotoxicity and their ability to target the specific cancer cells and release the drugs in a time-dependent manner was demonstrated.

3.5 References

(1) Cho, C. S.; Seo, S. J.; Park, I. K.; Kim, S. H.; Kim, T. H.; Hoshiba, T.; Harada, I.; Akaike, T. *Biomaterials* **2006**, *27*, 576−585.

(2) Parry, A. L.; Clemson, N. A.; Ellis, J.; Bernhard, S. S. R.; Davis, B. G.; Cameron, N. R. *J. Am. Chem. Soc*. **2013**, *135*, 9362−9365.

(3) Pati, D.; Shaikh, A.; Das, S.; Nareddy, P. K.; Swamy, M. J.; Hotha, S.; Sen Gupta, S. *Biomacromolecules* **2012**, *13*, 1287−1295.

(4) Pati, D.; Shaikh, A. Y.; Hotha, S.; Sen Gupta, S. *Polym. Chem*. **2011**, *2*, 805−811.

(5) Krannig, K.-S.; Schlaad, H. *J. Am. Chem. Soc.* **2012**, *134*, 18542−18545.

(6) Kramer, J. R.; Deming, T. J. *J. Am.* Chem. Soc. **2010**, *132*, 15068−15071.

(7) Wienke, D.; Davies, G. C.; Johnson, D. a.; Sturge, J.; Lambros, M. B. K.; Savage, K.; Elsheikh, S. E.; Green, a. R.; Ellis, I. O.; Robertson, D.; Reis-Filho, J. S.; Isacke, C. M. *Cancer Res.* **2007**, *67*,10230−10240.

(8) Bonduelle, C.; Huang, J.; Mena-Barragán, T.; Mellet, C. O.; Decroocq, C.; Etamé, E.; Heise, A.; Compain, P.; Lecommandoux, S. *Chem. Commun*. **2014**, *50*, 3350−3352.

(9) Wu, D. Q.; Lu, B.; Chang, C.; Chen, S. C.; Wang, T.; Zhang, Y.Y.; Cheng, S. X.; Jiang, X. J.; Zhang, X. Z.; Zhuo, R. X. *Biomaterials* **2009**, *30*, 1363−1371.

(10) Wang, X.; Sun, H.; Meng, F.; Cheng, R.; Deng, C.; Zhong, Z. *Biomacromolecules* **2013**, *14*, 2873−2882.

(11) You, L.; Schlaad, H. *J. Am. Chem. Soc.* **2006**, *128*, 13336−13337.

(12) Schatz, C.; Louguet, S.; Le Meins, J.-F.; Lecommandoux, S. *Angew. Chem., Int. Ed.* **2009**, *48*, 2572−2575.

(13) Ladmiral, V.; Semsarilar, M.; Canton, I.; Armes, S. P. *J. Am. Chem. Soc.* **2013**, *135*, 13574−13581.

(14) Chen, G.; Amajjahe, S.; Stenzel, M. H. *Chem. Commun*. **2009**, *10*, 1198−1200.

(15) Pati, D.; Kalva, N.; Das, S.; Kumaraswamy, G.; Sen Gupta, S.; Ambade, A. V. *J. Am. Chem. Soc.* **2012**, *134*, 7796−7802.

(16) Pati, D.; Das, S.; Patil, N. G.; Parekh, N.; Anjum, D. H.; Dhaware, V.; Ambade, A. V.; Sen Gupta, S. *Biomacromolecules* **2016**, *17*, 466−475.

(17) Yang, H.-K.; Bao, J.-F.; Mo, L.; Yang, R.-M.; Xu, X.-D.; Tang, W.-J.; Lin, J.-T.; Zhang, L.-M.; Jiang, X.-Q. *RSC. Adv.* **2017**, *7*, 21093-21106.

(18) Wang, S.S.S.; How, S.C.; Chen, Y.D.; Tsai, Y.H.; Jan, J.-S. *J. Mater. Chem. B.* **2015**, *3*, 5220–5231.

(19) Liu, Y.; Zhang, Y.; Wang, Z.; Wang, J.; Wei, K.; Chen, G.; Jiang, M. *J. Am. Chem. Soc.* **2016**, *138*, 12387− 12394.

(20) Wang, Z.; Sheng, R. L.; Luo, T.; Sun, J. J.; Cao. A. M. *Polym. Chem.* **2017**, *8*, 472–484.

(21) Gauche, C.; Lecommandoux, S. *Polymer* **2016**, *107*, 474–484.

(22) Huang, Y.-C.; Arham, M.; Jan, J.-S. *Euro Polym. J.* **2013**, *49*, 726–737.

(23) Hoffman, A. S. *J. Control. Release.* **2008**, *132*, 153-163.

(24) Torchilin, V. P. *Pharmaceutical. Research.* **2006**, *24*, 1-15.

(25) Nishiyama, N.; Kataoka, K. *Pharmacol Ther*. **2006**, *112*, 630–648.

(26) Deng, C.; Jiang, Y.; Cheng, R.; Meng, F.; Zhong Z. *Nano. Today*. **2012**, 7, 467—480.

(27) Bae, Y. H.; Yin, H. Q. *J. Controlled Release*, **2008**, *131*, 2–4.

(28) O'Reilly, R. K.; Hawker, C. J.; Wooley, K.L. *Chem. Soc. Rev.* **2006**, *35*, 1068—1083.

(29) Read, E. S.; Armes, S. P. *Chem. Commun*., **2007**, *29*, 3021–3035.

(30) Huang, H. Y.; Remsen, E. E.; Wooley, K. L.. *Chem. Commun*. **1998**, *13*, 1415–1416.

(31) Cheng, C.; Qi, K.; Khoshdel, E.; Wooley, K. L. *J. Am. Chem. Soc.* **2006**, *128*, 6808-6809.

(32) Zhang, Z.; Yin, L.; Zhang, Y.; Xu, Y.; Tong, R.; Zhou, Q.; Ren, J.; Cheng, J. *ACS Macro Lett.* **2013**, *2*, 40−44.

(33) Talelli, M.; Barz, M.; Rijcken, C. J.; Kiessling, F.; Hennink, W. E.; Lammers, T. *Nano Today.* **2015**, *10*, 93–117.

(34) Xiong, J.; Meng, F.; Wang, C.; Cheng, R.; Liu, Z.; Zhong, Z. *J. Mater. Chem.* **2011**, *21*, 5786-5794.

(35) Xiong, D.; Yao, N.; Gu, H.; Wang, J.; Zhang, L. *Polymer* **2017**, *114*, 161– 172.

(36) Chen, C.-K.; Lin, W.-J.; Hsia, Y.; Lo. L.-W. *Macromol. Biosci.* **2017**, *17*, 160019.

(37) Liu, S.; Weaver, J. V. M.; Tang, Y.; Billingham, N. C.; Armes, S. P.; Tribe, K. *Macromolecules* **2002**, *35*, 6121-6131.

(38) Dai, J.; Lin, S.; Cheng, D.; Zou, S.; Shuai, X. *Angew. Chem. Int. Ed.* **2011**, *50*, 9404–9408.

(39) Zelzer, M.; Todd, S. J.; Hirst, A. R.; McDonald, T. O.; Ulijn, R. V. *Biomater. Sci.* **2013**, *1*, 11-39.

(40) Ghoroghchian, P. P.; Li, G.; Levine, D. H.; Davis, K. P.; Bates, F. S.; Hammer, D. A.; Therien, M. J. *Macromolecules* **2006**, *39*, 1673−1675.

(41) Mai, Y.; Eisenberg, A. *Chem. Soc. Rev.* **2012**, *41*, 5969−5985.

(42) Antonietti, M.; Förster, S. *Adv. Mater.* **2003**, *15*, 1323−1333.

(43) Das, S.; Sharma, D. K.; Chakrabarty, S.; Chowdhury, A.; Sen Gupta, S. *Langmuir* **2015**, *31*, 3402−3412.

(44) Peponi, L.; Navarro-Baena, I.; Baez, J. E.; Kenny, J. M.; Marcos-Fernandez, A. *Polymer* **2012**, *53*, 4561– 4568.

(45) Rizis, G.; van de Ven, T. G. M.; Eisenberg, A. *Soft Matter* **2014**, *10*, 2825– 2835.

(46) Wu, S.; Kuang, H.; Meng, F.; Wu, Y.; Li, X.; Jing, X.; Huang, Y. *J. Mater. Chem*., **2012**, *22*, 15348-15356.

(47) Thurmond, K.B.; Kowalewski, T.; Wooley, K.L. *J. Am. Chem. Soc*. **1996**, *118*, 7239-7240.

(48) Zhao, Y. *Langmuir* **2016**, *32*, 5703-5713.

(49) Xu, Y. M.; Meng, F. H.; Cheng, R.; Zhong, Z. Y. *Macromol. Biosci.* **2009**, *9*, 1254– 1261.

(40) Nakashima, K.; Anzai, T.; Fujimoto, Y. *Langmuir* **1994**, *10*, 658−661.

(51) Mohan, P.; Rapoport, N. *Mol. Pharmaceutics*, **2010**, *7*, 1959-1973.

(52) Cheng, R.; Feng, F.; Meng, F.; Deng, C.; Feijen, J.; Zhong, Z. *J. Controlled Release,* **2011**, 152, 2-12

(53) Meng, F.; Hennink, W. E.; Zhong, Z. *Biomaterial*, **2009**, *30*, 2180-2198.

(54) Hu, Q.; Katti, P. S.; Gu, Z. *Nanoscale* **2014**, *6*, 12273– 12286.

(55) Hu, J.; Zhang, G.; Liu, S. *Chem. Soc. Rev.*, **2012**, *41*, 5933–5949.

(56) Harnoy, A. J.; Rosenbaum, I.; Tirosh, E.; Ebenstein, Y.; Shaharabani, R.; Beck R.; Amir, R. J. *J. Am. Chem. Soc.*, **2014**, *136*, 7531–7534.

(57) Pramod, P. S.; Takamura, K.; Chaphekar, S.; Balasubramanian, N.; Jayakannan, M. *Biomacromolecules* **2012**, *13*, 3627-3640.

(58) Zhuang, J.; Gordon, M. R.; Ventura, J.; Li, L.; Thayumanavan, S. *Chem. Soc. Rev*. **2013**, *42*, 7421 −7435.

CHAPTER 4

pH-Responsive Self-Assembled Nanostructures from Amphiphilic Mannose-6-phosphate Glycopolypeptides for Lysosome Targeted Drug Delivery

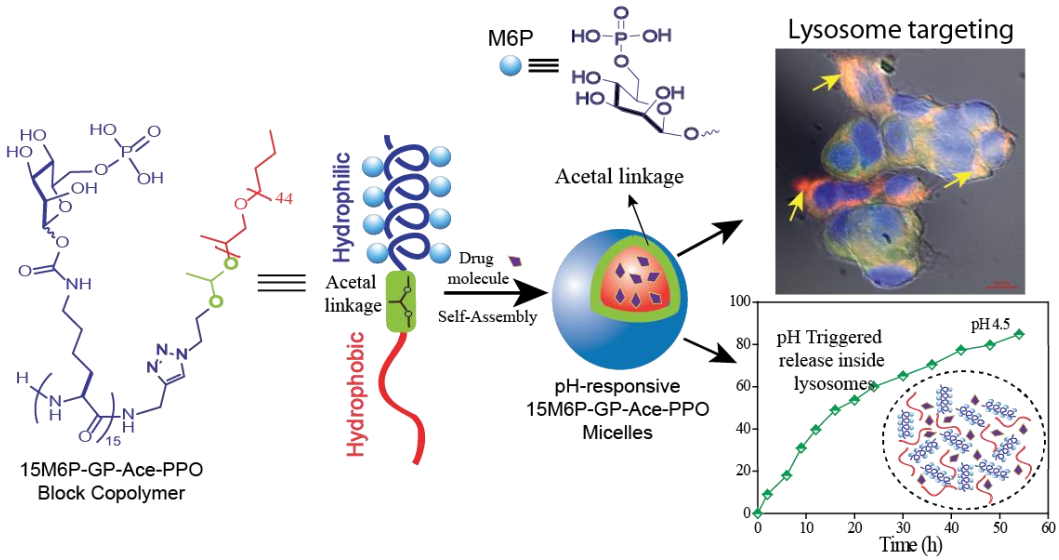

Pandey, B. *et al.* manuscript is under preparation **2018.**

4.1 Introduction

The mannose 6-phosphate receptor (M6PR) is a multifunctional protein which performs a major function of sorting the lysosomal enzymes from intracellular secretory proteins and deliver them to lysosomes in the mammalian cells.[1] M6P receptor includes cation-independent (CI) transmembrane multifunctional glycoprotein known as mannose-6-phosphate (M6P) receptor (CI-MPR) or insulin-like growth factor-II (IGF-II) (300 kDa), which is majorly involved in the transport of various cellular proteins from the cell surface or Trans-Golgi network (TGN) to lysosomes.[2-4] This receptor has a large extracellular domain with distinct binding sites especially for M6P-containing ligands, which help in the internalization of M6P-containing proteins.[3] CI-MPR, after binding to phosphomannosyl residues of the lysosomal enzymes in the Trans Golgi network (TGN) form a ligand-receptor complex which is internalized into endosomes and further degraded by low pH. To continue another cycle of same process, these receptors will return back to the TGN. Therefore, the CI-MPR abundantly resides in the intracellular compartments and shuffles in between the endosomes and TGN with only ~10% of the receptor localized on the cell surface.[3] Moreover, the receptor CI-MPR was found to be over-expressed in the early phase of prostate and breast cancer.[5,6] Therefore, alike with other overexpressed proteins, CI-MPR also acts as early marker for these cancers.

This innate property of the M6P receptor to bind mannose-6-phosphate-bound proteins and peptides exclusively in the lysosome can be used to selectively deliver the cytotoxic drugs specific to lysosomes.[7-11] Earlier reports reveal that CI-MPR exists in dimer state which permits the high-affinity binding to respective ligands which are multivalent in nature.[12-16] Glycoproteins which contain multiple M6P groups are expected to bind with the CI-MPR receptor with a higher binding affinity (K_d = 2−20 nM) as compared to monomeric M6P residues due to the "glycocluster effect".[17-19] Moreover, molecular structure and its ligand binding tendency show that flexible arranged M6P units lead to high binding affinity.[19] Therefore, the enhanced affinity and selectivity of proteins/peptides with polyvalently displayed M6P bearing ligands for CI-MPR receptor has motivated scientists to discover synthetic ligands that bear multiple copies of M6P moiety.[20-24] Few reports are available where synthetic peptide-based ligands bearing multiple copies of M6P have been prepared for the efficient targeting of CI-MPR receptor. Recently, the synthesis of a multivalent M6P (oligomeric) ligand has been investigated *via* solid phase peptide synthesis methodology.[20] This approach is limited in

several ways including tedious synthetic steps, incorporation of unnatural triazole moieties on ligand backbone and most importantly the lack of polyvalency (they are only multi-valent). All these drawbacks would compromise their function to mimic a natural biological ligand. A new methodology was recently developed for the preparation of high molecular weight (~22 kDa) end group-functionalized polyvalent mannose-6-phosphate glycopolypeptides (M6P-GPs) via ring-opening polymerization of M6P-N-carboxyanhydride (NCA).[25] The prepared M6P-GPs not only show minimal cytotoxicity but also have remarkable selectivity of lysosomes trafficking with various cell lines such as MCF-7, L929 and MDA-MB-231. The uptake of M6P-GPs in the lysosomes of mammalian cells was also demonstrated and shown to be affiliated with the CI-MPR mediated pathway. Multiple copies of M6P moieties present in these glycopolypeptide chains will have an effective impact on the trafficking nature, which makes them lysosome specific.

This chapter describes the development of M6P-polypeptide-based nanocarrier that can encapsulate and deliver the drugs to the lysosomes for the treatment of several diseases like cancer. The strategy involves the synthesis of the amphiphilic pH-responsive block copolymer with M6P-glycopolypeptide as one of the blocks similar to previous studies where glycopolypeptide-based nanocarriers were designed[26-30] and explored for receptor-mediated targeting of cancer cells.[30] This M6P-based block copolymer is self-assembled into a micellar-type nanoparticle in which the drug can be incorporated in the hydrophobic core. The M6P-glycopolypeptide on the surface of the nanoparticle would deliver the drug exclusively inside the lysosome where the acidic pH disrupts the nanoparticle by cleaving the acetal bond and the drug is released. This would result in significantly enhanced anti-tumor activity, minimal drug resistance and side effects. Therefore, pH-responsive M6P-GP's labeled micelles prepared from the self-assembly of amphiphilic M6P-glycopolypeptide bearing pH-responsive (acetal) group in an aqueous medium was demonstrated. Amphiphilic M6P-GP block copolymer (15M6P-GP-ace-PPO) with the pH-responsive group was synthesised by click reaction of alkyne end-functionalized M6P-glycopolypeptide and the azide functionalized acetal containing PPO (PPO−Ace-N_3) as a hydrophobic block. Therefore, this, pH-responsive M6P-GP labeled nanocarriers are not only capable of encapsulating therapeutics towards exclusive lysosome-targeted drug delivery but also delivers the drug in a controlled manner by trigger release mechanism (Figure 4.1).

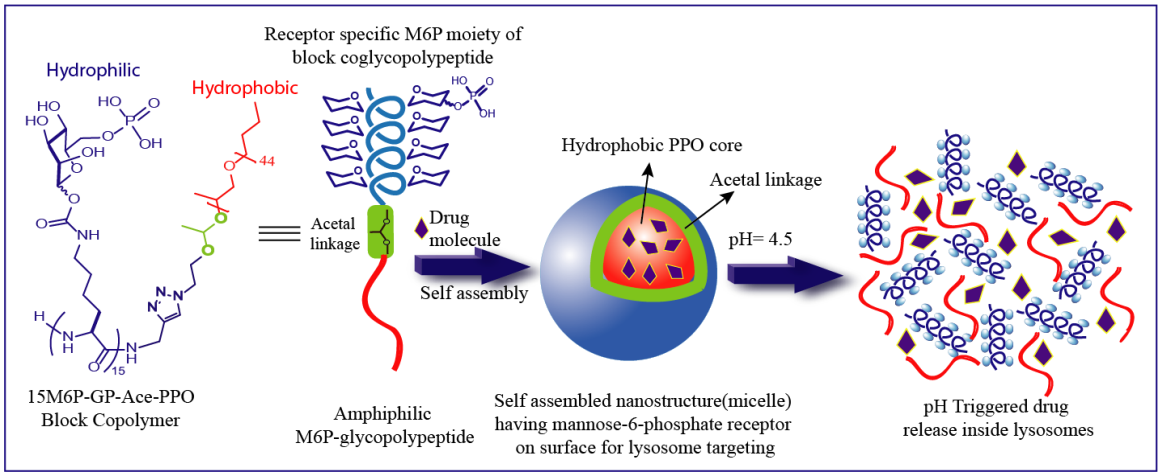

Figure 4.1: Schematic showing structures of amphiphilic pH-responsive mannose-6-phosphate containing block coglycopolypeptides (15M6P-GP-Ace-PPO) and their assembly into micelles for pH-triggered drug release inside lysosomes.

4.2 Experimental Section

4.2.1 General

Poly(propylene glycol) monobutyl ether (PPO−OH, M_n = 2500 g/mol), propargylamine, rhodamine B octadecyl ester perchlorate (RBOE) and triphosgene were purchased from Sigma-Aldrich. Other chemicals and solvents such as petroleum ether (b.p. 60˚-80˚C), ethyl acetate, diethyl ether, tetrahydrofuran, dioxane and dichloromethane were obtained from Merck, India. They are dried by using conventional drying methods and finally stored in glove- box prior to use. Mannose-6-phosphate-N-carboxyanhydride (M6P-NCA) was prepared by following previously published procedure.[25] 3.5 kDa (MWCO) dialysis membrane was obtained from Thermoscientific. The (3-(4,5-dimethylthiazol-2-yl)-2,5-diphenyltetrazolium bromide (MTT) reagent were procured from Invitrogen, India. Cell lines were purchased from ATCC and were maintained as per the manufacturer's instructions. Cells were maintained in minimum essential medium (MEM: Gibco) with 10% FBS (Fetal bovine serum). ^{31}P NMR spectra recorded on Bruker Spectrometer (202.46 MHz) using an internal 85% aqueous H_3PO_4 as reference standards.

4.2.2 Synthesis of acetal containing chloro-terminated poly(propylene glycol) monobutyl ether of (PPO−Ace-Cl) ***(1)***

Polypropylene glycol monobutyl ether (M_n = 2500 g/mol) (5g, 2.0 mmol) and pyridine p-toluene sulphonate (PPTS) (0.125g, 0.49 mmol) were dried by azeotropic distillation with toluene just before start of the reaction. The reaction mixture was then dissolved in 50 mL

dry DCM and chloroethyl vinyl ether (CEVE) (2.12g, 20mmol) was added by dissolving in 10 mL dry DCM dropwise over 15 min under an argon atmosphere at 0 ^{o}C. After 1 h, 20 mL of 5wt% Na_2CO_3 solution was added to quench the reaction and to avoid the cleavage of the acetal linkage. The reaction mixture was then diluted with 100 mL DCM and washed with brine solution. Finally, the reaction mixture was precipitated into cold hexane and the product was dried under vacuum.

^{1}H NMR (200MHz, $CDCl_3$): δ (ppm): 1.10-1.31(d, 130H), 3.36-3.56 (m, 131H), 4.80(q, 1H).

4.2.3 Synthesis of acetal containing azide terminated poly(propylene glycol) monobutyl ether PPO−Ace-N_3 ***(2)***

PPO-*Ace*-Cl (5g, 2.0 mmol), NaN_3 (1.3g, 20 mmol) was dissolved in DMF and stirred at 60 ^{o}C for 24 h. After completion of the reaction, DMF was removed under reduced pressure. The crude product was precipitated in cold diethyl ether and the obtained white product was dried under vacuum.

^{1}H NMR (200MHz, $CDCl_3$): δ (ppm): 1.10-1.31(d, 130H), 3.36-3.56 (m, 131H), 4.79(q, 1H).

4.2.4 General procedure for the synthesis of alkyne-functionalized M6P-glycopolypeptides ***(3)***

Inside the glove box, M6P-NCA solution with a concentration of 100 mg/mL in dry DMF was added with "proton sponge" N,N′-tetramethylnapthalene (0.5 eq. to monomer; 1 M) as an additive and propargylamine (0.5 M) as the initiator. M6P-NCA was prepared according to previous reports.[25] The reaction progress was checked by FT-IR spectroscopy. The polymerization reaction was usually completed within 38 h. After completion, aliquots were taken for GPC analysis. Finally, the solvent was removed under reduced pressure. The resulting residue was redissolved in dichloromethane and the polymer was precipitated out by addition of diethyl ether. The precipitated polymer was obtained by centrifugation and dried to get white M6P-glycopolypeptides in 90-95% yield.

^{1}H NMR (400 MHz, $CDCl_3$): δ (ppm): 1.28-1.57 (5H), 1.95-2.13 (10H), 2.15 (1H), 3.22-3.38 (2H), 3.98-4.12 (6H), 4.83-4.86 (1H), 5.05 (4H), 5.33 (3H), 6.71, 7.38 (10H), 7.78.
^{31}P NMR (202.46 MHz, $CDCl_3$): δ (ppm) -1.29.

*4.2.5 Synthesis of amphiphilic mannose-6-phosphate glycopolypeptide (15M6P-GP-ace-PPO) via click reaction **(4)***

Azide-functionalized acetal containing PPO and alkyne end-functionalized acetyl-protected M6P-glycopolypeptides (0.9 eq.) were dissolved in THF/DMSO/water/ methanol (2:1:0.2:1) solvent mixture and reaction mixture was degassed by three freeze-pump-thaw cycles. Further, a premixed solution of $CuSO_4 \cdot 5H_2O$ (0.2 eq.), tris(3-hydroxypropyltriazolylmethyl)amine (THPTA) (0.2 eq.) and sodium ascorbate (0.4 eq.) was added to the above reaction mixture and was allowed to stir at room temperature for 24 h under an argon atmosphere. The progress of the reaction was monitored by FT-IR spectroscopy. When >95% of the azide stretch disappeared, the solvent was removed by reduced pressure to get solid residue. The obtained residue was then dissolved in DCM and washed three times with dilute ammonia solution and then with water to remove the residual copper salt and sodium ascorbate. DCM was completely removed under reduced pressure and the product was precipitated in hexane and dried to get polymers as off-white solids.

^{1}H NMR (400MHz, $CDCl_3$): δ (ppm): 1.13 (m, 130H) 1.28-1.57 (m, 75H), 1.95-2.13 (m, 150H), 3.22-3.38 (m, 132H), 3.98-4.12 (m, 90H), 4.83-4.86 (m, 15H), 5.05 (6m, 60H), 5.33 (m, 45H), 6.71, 7.38 (m, 150H). ^{31}P NMR (202.46 MHz, $CDCl_3$): δ (ppm) -1.29

*4.2.6 Deprotection procedure for 15M6P-GP-ace-PPO block copolymers **(5)***

The benzyl phosphate deprotection of the protected 15M6P-GP-ace-PPO block copolymer was performed by hydrogenation process. Hydrogenolysis of block copolymers was carried out by using 10% Pd/C in methanol with hydrogen gas at balloon pressure for 18 h. Then, the reaction mixture was filtered and solvent was removed under reduced pressure to afford benzyl deprotected M6P-GP-ace-PPO in almost quantitative yield. The next step is the deprotection of acetyl groups of phosphate deprotected 15M6P-GP-ace-PPO block copolymer. Phosphate deprotected and acetyl-protected 15M6P-GP-ace-PPO block copolymer was dissolved in methanol and then hydrazine monohydrate (25 eq.) was added. The reaction was stirred for 12 h at room temperature. After reaction completion, acetone was added for quenching and finally solvent was removed under reduced pressure to get solid residue. The obtained product was dissolved in deionized water/ DMSO (1:1) mixture and filtered through 0.45 μm membrane filter. Finally, the polymer was purified by dialysing the filtered solution against DI water using dialysis membrane of 3.5 kDa MWCO. Dialysis was done for 2 days by changing water after every 6 h. Dialyzed

polymer was lyophilized to yield deprotected 15M6P-GP-ace-PPO (**6)** block copolymer as white fluffy solid (80% yield).

4.2.7 Self-assembly of deprotected copolymers 15M6P-GP-ace-PPO in aqueous solution

Fully deprotected 15M6P-GP-ace-PPO block copolymer (2.0 mg) was dissolved in 200 μL of dimethyl sulfoxide (DMSO) and filtered through a 0.22 μm hydrophilic membrane filter. The solution was then allowed to stir for 2 min in a 5 mL RB and then 1.8 mL of deionised water was quickly (<5 s) added to it and allowed to stir for another 3 h. The solution was placed in the dialysis bag (MWCO:12 kDa) and allowed to dialyze for 24 h against deionised water to remove DMSO completely.

4.2.8 Sample preparation for TEM, AFM and DLS analysis

The 0.1 wt% solution of the block copolymer was spotted on carbon-coated 400 mesh copper grid about 10 μL, kept for 15-20 min, the excess solvent was removed by touching the edge of the grid using Whatman filter paper. Then grid was negatively stained by 0.2 wt% uranyl acetate for 10 s and excess solvent was removed. The grid was washed twice with deionized water to remove excess unbound uranyl acetate from the grid. Grids were dried in desiccator for 20 h and analyzed by transmission electron microscopy. For AFM analysis, aqueous solution (0.02 wt%) was drop cast on a silicon wafer and then dried for 24 h. An aqueous solution (0.1 wt %) of block copolymer was filtered using 0.45μm filter and hydrodynamic diameter was determined by dynamic light scattering (DLS) analysis.

4.2.9 Circular dichroism measurements

Solution of deprotected block copolymer 15M6P-GP-ace-PPO (0.25 mg/mL) in phosphate buffer (pH 7.4) was filtered through 0.22 μm membrane syringe filter. Circular dichroism (CD) spectra of solution was recorded in the range of 190 nm to 250 nm using JASCO CD Spectropolarimeter (J-815) in a cuvette with a 1 mm path length. Spectra were recorded with an average of three scans and were reported as a plot of molar ellipticity [θ] versus wavelength.

4.2.10 Dye encapsulation studies and CMC determination

Micellar solution (1 mg/mL) was mixed with 20 μL of RBOE solution (1 mg/mL stock in acetone) and allowed to stir for 6 h. After 6 h, when the acetone was evaporated, the precipitated RBOE was filtered through 0.45 μm membrane filter. The concentration of RBOE loaded inside the micelles was calculated using UV-Vis spectroscopy and drug loading efficiency (DLE) was determined by using the following formula:

$$DLE\% = \frac{\text{Weight of encapsulated RBOE}}{\text{Weight of RBOE in Feed}} \text{x } 100$$

Critical micelle concentration

Critical micelle concentration (CMC) of micelles is determined by fluorescence spectroscopy using rhodamine B octadecyl ester (RBOE) as a hydrophobic fluorescence probe. The final stock solution of prepared micelles (142.9 μM) was serially diluted and concentration was varied from 1 mg mL^{-1} to 4.88 x 10^{-4} mg mL^{-1}. The serially diluted micellar solutions were mixed with RBOE in acetone to make a final concentration of RBOE of 1.25 μM. The solutions are allowed to stir overnight. Then the emission spectra were recorded with the excitation wavelength at 560 nm. The fluorescence intensity of RBOE at 580 nm was plotted against the concentration of micelles.

4.2.11 pH-responsive studies

The *in vitro* pH-responsive RBOE release study from the 15M6P-GP-ace-PPO micelles was carried out at two different pH values (7.4 and 4.5). Briefly 1 mg mL^{-1} solution of RBOE encapsulated micelles in buffer solution (pH 7.4) was placed in a pre-wetted cellulose membrane (MWCO: 3.5 kDa). The whole bag was placed into 5 mL buffer solution (pH 7.4) being stirred at a speed of 100 rpm at 37°C. For the dye release study at pH 4.5, the pH was adjusted by adding 1 M HCl to the micellar solution. At pre-determined time interval, the amounts of released RBOE were monitored by fluorescence spectroscopy at 580 nm.

4.2.12 In vitro cytotoxicity studies

In vitro cytotoxicity assay of 15M6P-ace-PPO micelles was done by seeding the MCF-7 cells in 96-well plate (flat-bottomed) with a density of 10,000 cells per well in minimum essential medium (MEM) having 10% FBS. The cell-seeded plate was placed in a incubator (37 °C with 5% CO_2) for 24 h. Further, micelles were prepared in the serum free MEM with a final concentration of 10, 20, 40, 60, 80, 100 and 200 μgmL^{-1} respectively and further incubated for 48 h at 37 °C with 5% CO2. After 48 h, the media was exchanged with 110 μL of MEM solution containing 10% FBS. Then, filter-sterilized MTT (3-(4,5-dimethylthiazol-2-yl)-2,5-diphenyltetrazolium bromide) reagent (0.45 mg/mL) was added to each well and further incubated for 4 h at 37 °C with 5% CO_2. To dissolve the insoluble purple coloured formazon crystals formed after incubation for 4 h, media was exchanged with100 μL of DMSO was added. The absorbance of the coloured

solution was measured at 550 nm using a microtiter plate reader and the relative percent cell viability was obtained from the following equation:

Relative percent cell viability = $(A_{test}/A_{control}) \times 100\%$.

Where A_{test} is the absorbance of the sample treated cells, $A_{control}$ is the absorbance of the untreated cells (control).

Experiments were performed in triplicate and absorbance was measured as a mean of triplicate measurements. The cell viability data was plotted against the concentration of blank UCL and SCL micelles by representing the percentage relative to untreated cells (control). Similarly MTT assays of free DOX, DOX-Loaded UCL and ICL micelles were performed following the same strategy.

4.2.13 Cellular uptake studies using epifluorescence microscopy

Cellular uptake studies of 15M6P-ace-PPO micelles with the MCF-7 cells (breast cancer cell line) was done by seeding the cells in the 24-well plate with a density of 50000 cells per well in minimum essential medium (MEM) having 10% FBS. Further, the cell-seeded plate was placed in a incubator (37 °C with 5% CO_2) for 24 h. After that, media was changed with MEM containing 200μg/mL of RBOE-encapsulated micelles respectively, and incubated for 4 h respectively at 37 °C with 5% CO2. After incubation for specific number of hours, incubated cells were washed with PBS three times and the fixation of cells was done by using 4% paraformaldehyde solution for 15 min. For lysosome staining, cells were treated with 50 nM LysoTracker green DND-26 (Invitrogen) for 30 minutes at 37 °C with 5% CO_2 followed by the nucleus staining with DAPI. All the images for RBOE containing micelles were taken at 500 ms exposure time using an epifluorescence microscope (Carl Zeiss). (Model: Axio Observer.Z1, Oil emersion objective, 63X). (Filters set 49 DAPI shift free EX G 365, BS FT 395, EM BP 445/50, Filter set 20 Rhodamine shift free EX BP 546/12, BS FT 560, EM BP 575-640, Filter set 10 shift free EX BP 450-490, BS FT 510, EM BP 515-565)

4.3. Results and discussions

4.3.1 Synthesis of acetal containing azide end-functionalised poly(propylene glycol) monobutyl ether (PPO−Ace-N_3)

Synthesis of azide-terminated acetal linkage containing PPO was done by following the procedure of Hawker *et al.* (Scheme 4.1).[31] Initially, hydroxyl group of PPO-OH (MW=2.5 kg mol^{-1}) was modified by incorporating an acid-cleavable acetal moiety using

2-chloroethyl vinyl ether (CEVE) in the presence of catalytic amount of pyridinium p-toluenesulfonate (PPTS), which is generally used for the preparation of an acetal bond from an alkyl vinyl ether and alcohol.[31] Reaction completion was confirmed by ^{1}H NMR spectroscopy by integrating the peak at 4.3 ppm (-CH of acetal) with respect to PPO protons (–CH-CH$_3$) at 1.11-1.13 ppm (Figure C1). In the next step, the chloro group was quantitatively transformed to the corresponding azide group by nucleophilic substitution of azide group at the C–Cl bond. The conversion of chloride into an azide without the loss of acetal group was quantitatively ascertained by NMR spectroscopy (Figure C2). Confirmation of azide group after substitution reaction was monitored by appearance of characteristic azide stretch (2115 cm^{-1}) in FT-IR analysis (Figure 4.2b). The number-average molecular weight (M_n) of the PPO block obtained from ^{1}H NMR by using ratio of the integration of characteristic peaks associated with the main chain and end groups did not change after the reaction and also correlated with the GPC analysis, ensuring the successful preparation of PPO with cleavable (acetal) and clickable (azide) groups.

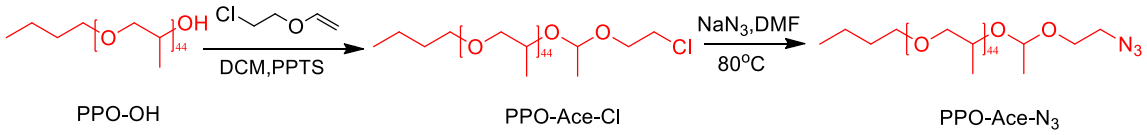

Scheme 4.1: Synthesis of acetal containing azide terminated poly (propylene glycol) monobutyl ether (PPO−Ace-N$_3$) as acid-cleavable hydrophobic block.

4.3.2 Synthesis of alkyne-functionalised M6P-glycopolypeptides

M6P-functionalized NCA monomer was synthesised by following the previous methodology.[25] M6P-NCA was polymerized by using primary amine as an initiator at room temperature and corresponding M6P-glycopolypeptide was obtained in quantitative yield (Scheme 4.2). The obtained M6P-glycopolypeptides were further purified by precipitation method and the number average molecular weight (M_n) was calculated from ^{1}H NMR spectra (Figure C3).

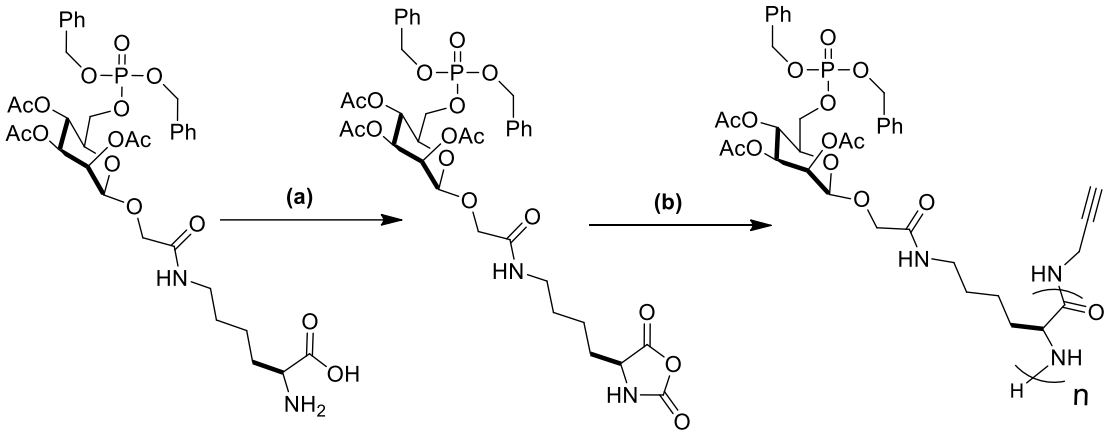

(a) Triphosgene, N-methyl morpholine, THF, 55 °C, 1h (58% yield); (b) propargylamine, proton sponge, DMF (~95% yield)

Scheme 4.2: Synthesis of alkyne functionalized M6P-glycopolypeptides.

After GPC analysis, the main peak for the Pr-15M6P-GP copolymer was observed along with a small shoulder peak possibly due to the presence of small oligomers. The molecular weight distribution (Đ) for the main peak was 1.18 (Figure 4.2b). The results suggested that calculated molecular weight corroborates well with the targeted monomer/initiator ratio and there is a control over polymerization. The resulted Pr-15M6P-GP copolymer was used as such for further synthesis and studies.

4.3.3 Synthesis of mannose-6-phosphate glycopolypeptide (15M6P-GP-ace-PPO) via click reaction

Alkyne end-functionalised mannose-6-phosphate group bearing acetyl-protected glycosyl unit (Pr-15M6P-GP) was synthesized by following the previously developed strategy which involves the ROP of mannose-6-phosphate (NCA) monomer with propargylamine as an initiator.[32] Further, alkyne-containing 15M6P-GP was conjugated with azide end-functionalized acetal containing PPO by using copper-catalyzed azide-alkyne cycloaddition (CuAAC) reaction, [33,34] a well-known type of the "click reaction" to form 15M6P-GP-ace-PPO block copolymer as shown in Scheme 4.3. GPC analysis of clicked 15M6P-GP-ace-PPO block copolymer was caried out to check the efficiency of the click reaction. The generation of a new peak at higher molecular weight was observed in GPC chromatogram, which is significantly shifted from that of the parent Pr-15M6P polymer and PPO-Ace-N_3 suggesting formation of the conjugated product. Moreover, IR analysis was performed, which showed the complete disappearance of characteristic azide stretch (2115 cm^{-1}) after click reaction (Figure 4.2a). The exact composition of the clicked block copolymer was calculated from ^1H NMR spectroscopy by comparing the characteristic

protons of PPO (−CH−CH_3) at 3.9 and 4.08 ppm (denoted as b+c) with respect to the benzylic protons of the M6P-GP segment at 7.32 ppm (denoted as a) which shows that the molar ratio of both the blocks is 1:1 as expected (Figure 4.3).

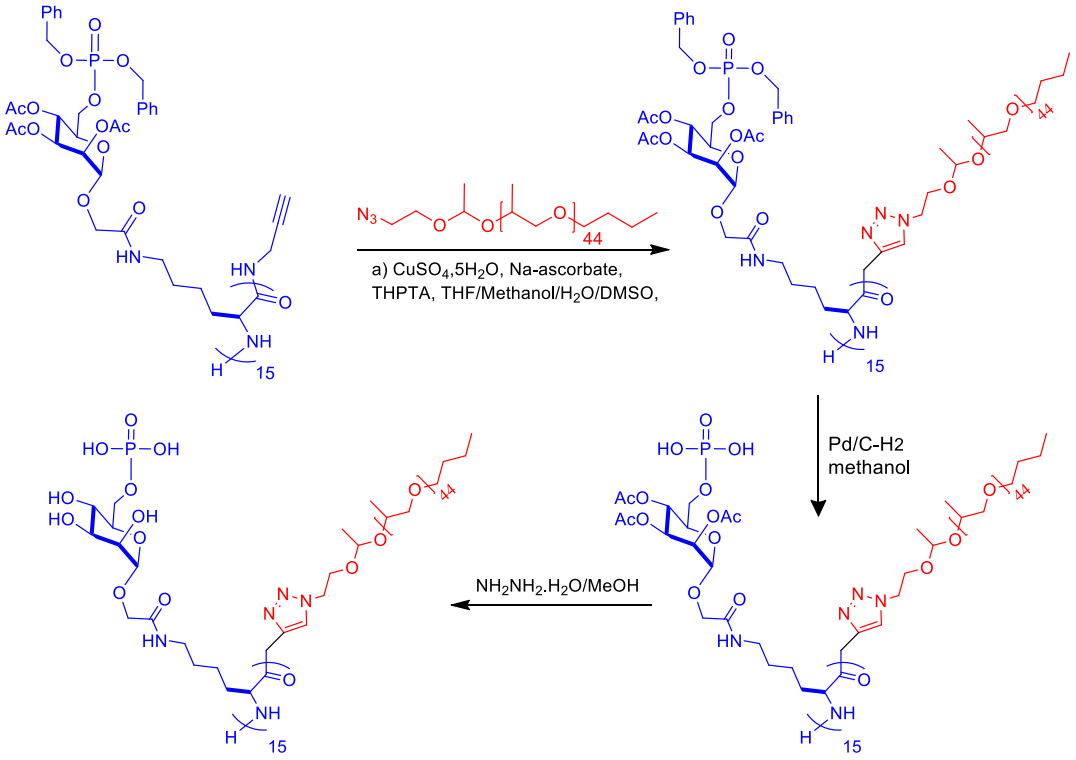

Scheme 4.3: Synthesis of amphiphilic 15M6P-GP-ace-PPO glycopolypeptide using click reaction.

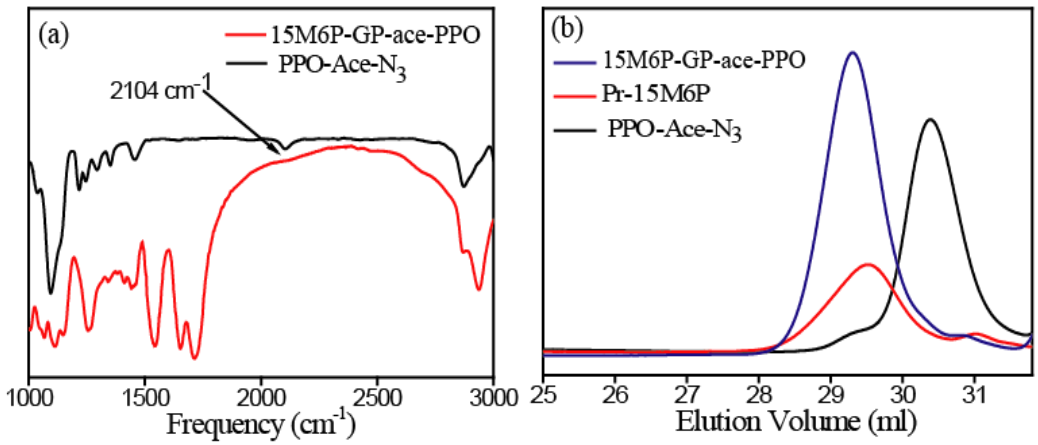

Figure 4.2: (a) FTIR spectra of the synthesized 15M6P-GP-ace-PPO block copolymer after "click" reaction. (b) Overlay of GPC curves of individual parent blocks (PPO and15M6P-GP) and 15M6P-GP-ace-PPO block copolymer prepared after "click" reaction.

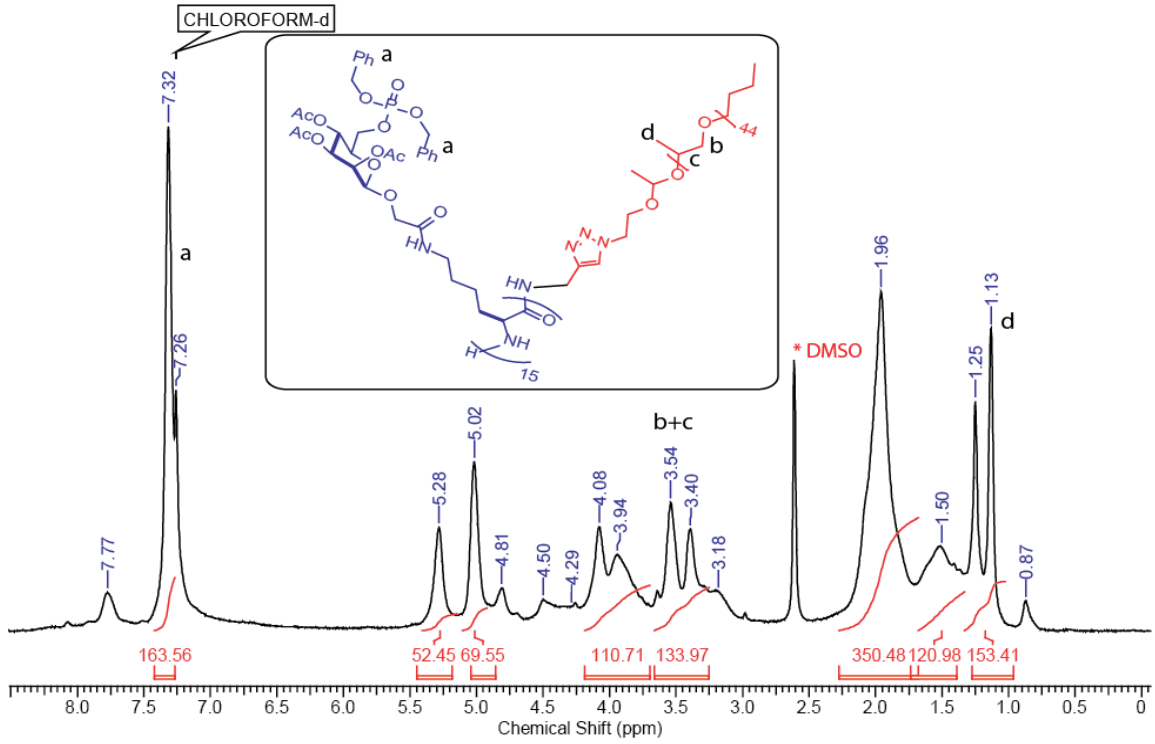

Figure 4.3: ^{1}H NMR spectrum of protected 15M6P-GP-ace-PPO block copolymer represents corresponding peaks to protons of PPO block and M6P-GP block.

Depending on the presence of the end-functional group in the M6P-GP's, the two benzyl protecting groups present on the phosphate moiety of M6P-glycopolypeptide were deprotected by using hydrogenation method. Further, the acetyl groups of the GP segment was deprotected by hydrazine hydrate in MeOH at room temperature. After completion of the reaction, the reaction mixture was quenched by addition of acetone and resultant polymer was dissolved in water before purification by dialysis method. Removal of acetyl groups was confirmed from ^{1}H NMR spectra of 15M6P-GP-ace-PPO in DMSO-d_6 (Figure C6). Further, removal of benzyl groups from M6P-GPs was determined by ^{31}P NMR spectrum, which shows a broad peak at -0.38 ppm indicating that the phosphate groups remain attached in the M6P-glycopolypeptide (Figure C5).

The synthesized deprotected 15M6P-GP-ace-PPO block copolymer from ROP of enantiomerically pure M6P-glyco-NCA contains hydrophilic M6P-GP segment bearing polypeptide backbone composed of enantiomerically pure poly-L-lysine. Therefore, secondary structure of amphiphilic M6P-GPs was determined in aqueous solution (phosphate buffer saline, pH 7.4) using circular dichroism (CD) spectroscopy. The CD spectrum shows the presence of α-helical chain conformation (characteristic peak at 208 and 222 nm) at neutral pH (7.4) (Figure 4.4). It clearly indicates that the incorporation of

charged phosphate group with a distance of 14 atoms from the polypeptide backbone does not have any effect on the secondary conformation as has been shown earlier.[35]

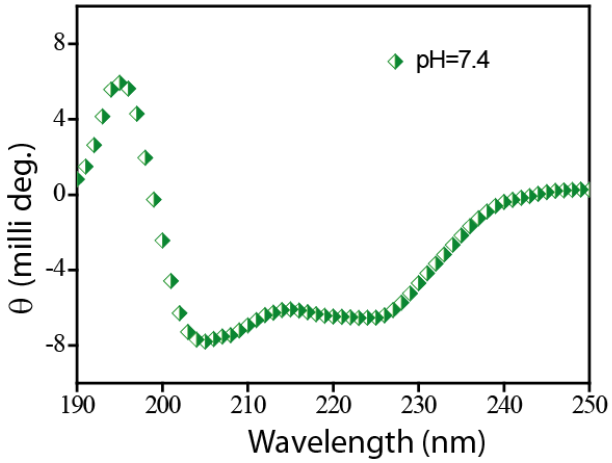

Figure 4.4: Circular dichroism spectra of the synthesized 15M6P-GP-ace-PPO block copolymer in buffer (pH 7.4).

4.3.4 Self-assembly of amphiphilic mannose-6-phosphate glycopolypeptide (15M6P-GP-ace-PPO)

Self-assembled mannose-6-phosphate glycopolypeptide-based nanostructures are important as they can be selectively used to deliver the drug inside lysosomes. Therefore, amphiphilic M6P-GPs are designed and synthesized so that they can be self-assembled into nanostructures as self-assembly of the amphiphilic block copolymer occurs due to the differential solubility of two individual blocks in selective solvents.[36] Here, 15M6P-GP-ace-PPO block copolymer exhibits M6P-GP as one of the blocks, which is highly hydrophilic and soluble in water while the other block is PPO, which is hydrophobic and insoluble in water. However, the whole polymer is completely soluble in DMSO which is common solvent for both the segments. When water was added to 15M6P-GP-ace-PPO dissolved in DMSO, the diffusion of DMSO into water occurs, which forces the PPO block to undergo microphase separation. Due to this, hydrophobic PPO chains tend to aggregate together in an aqueous environment to form an inner core with hydrophilic M6P-GP corona on the outer surface.

Earlier reports on the amphiphilic glycopolypeptide-based self-assembled structures demonstrated that three factors *viz.* hydrophilic weight fraction or hydrophilic to hydrophobic ratio, percentage helicity and nature of hydrophobic segment decide the formation of final nanostructures.[26-30,32] In a different system such as GP-PCL, GP-dendron[26] and 12GP-PPO,[29] different type of morphologies are obtained by tuning the

above three factors. Generally, an amphiphile where hydrophilic to hydrophobic ratio is less than 0.5, forms polymersomes while those with a ratio greater than 1.0 usually form micelles.[37] In 12GP-PPO system, where the hydrophilic/hydrophobic ratio is 1.6, it is expected to form micellar type morphologies however polymersomes are obtained. The presence of weak helix (28% helicity) and dynamic nature of peptide backbone of GP in the block copolymer provides more efficient packing towards formation of polymersomes. GP backbone of 15M6P-ace-PPO block copolymer system also exhibits weak helix character but the hydrophilic weight fraction is higher (2.8), which increases the tendency to self-assemble into micelles considering that the hydrophobic segment is same, i.e. PPO. Additionally, hydrophilicity of the block copolymer is also increased because of the presence of charged phosphate groups in the M6P-GP backbone that would not allow the weak helix to undergo efficient or close packing as was shown by uncharged 12GP-PPO block copolymer. All these factors would determine the final morphological structures formed by 15M6P-ace-PPO block copolymer system. After formation of self-assembled structures and complete removal of DMSO through dialysis process, the presence of self-assembled structures in the aqueous medium was revealed by DLS analysis that provided an average size of 65 nm (PDI = 0.28) (Figure 4.5c).

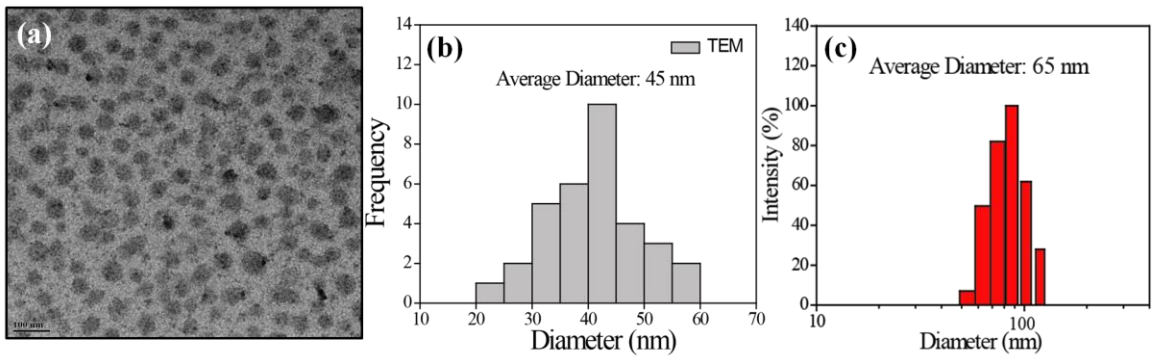

Figure 4.5: (a) TEM image of 15M6P-GP-ace-PPO micelles (scale: 100 nm) (b) size distribution of micelles from TEM image (c) DLS analysis of micelles from aqueous solution.

Further, TEM analysis was performed to understand the nature of particles in the dried state. It reveals the formation of small micellar aggregates with an average diameter of 45 nm (Figure 4.5a) with the size varying between 26−60 nm (Figure 4.5b). To further probe the exact nature of self-assembled structures, AFM and FE-SEM analysis was conducted, which also corroborated with the results of TEM, showing uniform particle size distribution within the range of 30-60 nm (Figure 4.6a and 4.6b). The corresponding

height profile image obtained from the AFM height contrast image shows the height to width (h/w) ratio of ratio of 0.14 which is consistent with micelles (Figure 4.6c).[38]

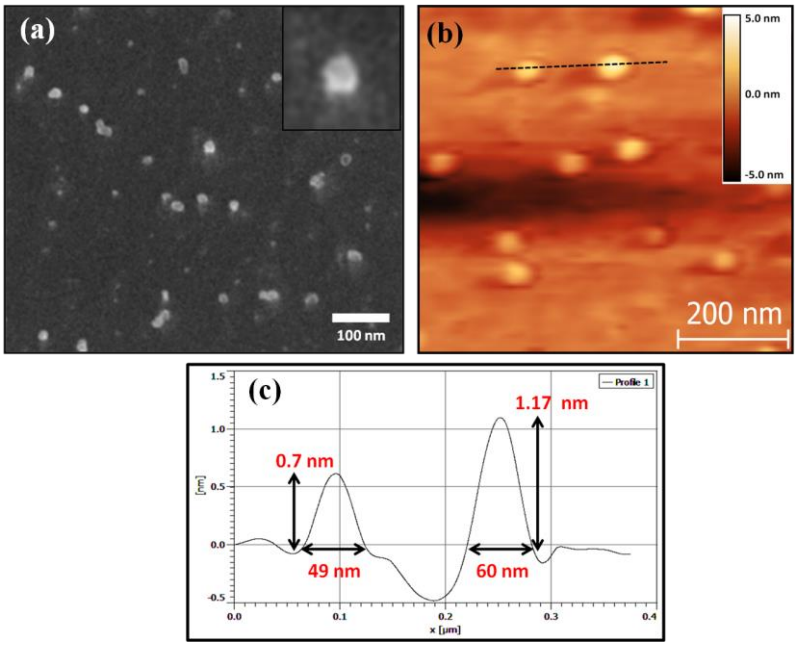

Figure 4.6: (a) FE-SEM image of micelles in water (inset shows a single micelle), (b) AFM image of the micelles drop cast from aqueous solution on a silicon wafer, (c) the corresponding height profile of micelles.

4.3.5 Dye encapsulation studies

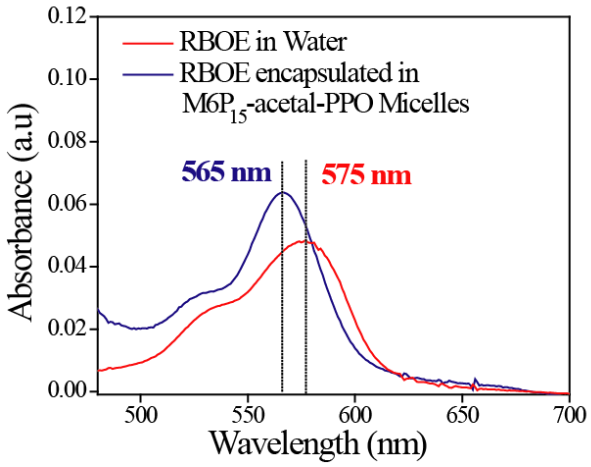

Figure 4.7: UV-Vis absorption spectra of free RBOE in water and RBOE encapsulated in 15M6P-GP-ace-PPO micelles in water.

The formation of micelle-like nanostructures was further confirmed by loading a non-polar RBOE dye that contains long octadecyl chain, which allows it to be encapsulated within the hydrophobic core of the micelles. The encapsulation efficiency (EE %) of RBOE dye (extinction coefficient = 112,000 $M^{-1}cm^{-1}$) was determined to be ~46%. The UV-Vis spectra of RBOE encapsulated 15M6P-GP-ace-PPO micelles (λ_{max} = 565 nm)

clearly shows a blue-shift (Figure 4.7) as compared to water (λ_{max}= 575 nm), which reveals that RBOE mainly resides in a relatively non-polar environment, i.e., encapsulated in the hydrophobic core of the micelles. The determination of CMC values for these novel 15M6P-GP-ace-PPO amphiphilic block copolymers is essential because CMC values directly relate to the thermodynamic stability of resultant micelles. CMC is also an important parameter for the self-assembly of an amphiphilic block copolymer as it determines whether the copolymers exist in self-assembled structure or as a unimer in aqueous solution at a given concentration.[39] Therefore, CMC of the micellar assembly was determined by the fluorescence spectroscopy technique using RBOE as a fluorescence probe. Fluorescence emission spectra of the encapsulated RBOE dye at different polymer concentrations (Figure 4.8b) were recorded by exciting at 554 nm and further λ_{em} of RBOE was plotted versus the concentration of polymer to give the typical CMC curve. The decrement in the RBOE fluorescence intensity with dilution was used to determine the CMC value for the self-assembled micelles and it was found to be 5.75 µM (Figure 4.8a).

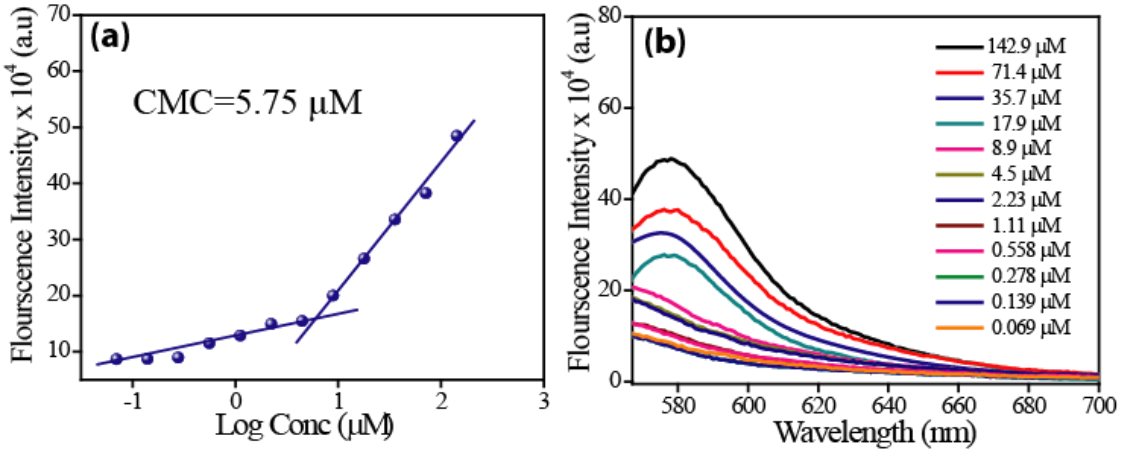

Figure 4.8: (a) Plot of fluorescence intensity versus the logarithm of the polymer concentration (µM) in aqueous solution. (b) Fluorescence emission spectra of RBOE in an aqueous solution of the polymer at different concentrations.

4.3.6 pH-responsive studies

pH as biological stimulus can act as an internal trigger for different type of nanoassemblies that are used for the tumour-targeted drug delivery. This is because pH is varied in different regions of biological systems for example, low pH is found in tumor (~5.0) and inflammatory tissues, in the intracellular compartments of cell such as lysosomes and endosomes (pH 4.5–6.5), which is comparatively more acidic compared to extracellular environment of normal tissues (pH 7.4).[40-44] Micellar degradation can be

achieved by incorporation of acid-cleavable groups such as acetals, orthoesters or anhydrides in the amphiphilic block copolymer as reported earlier.[45-47] Acetals as a pH-responsive systems are also attractive because of their easy incorporation in the block copolymer using simple synthetic steps, stability at higher pH and degradability in acidic (low pH) environment.[45,47] Herein, 15M6P-GP-ace-PPO block copolymer system contains acetal linkage as acid-cleavable and pH-responsive group so that self-assembled micelles can be disassembled by changing the pH of the surrounding environment. , To test this possibility, pH-responsive release of RBOE dye (as a model drug) from micellar assemblies was investigated at two different pH 7.4 and 4.5 by monitoring the emission spectra of RBOE at specific time intervals. The release studies were performed for about 2 days. Initially at pH 7.4, only ~8% release was observed which indicates that micellar structures maintain their morphological integrity at the neutral pH (Figure 4.9a). Further, the micellar disassembly under more acidic conditions (pH 4.5) was studied for the cleavage of acetal linkage in the micelles; pH 4.5 was maintained by adding 1 M HCl to the solution of pH 7.4. It was observed that about 63% of dye release occured in initial 1 day, which increased to 85% on 2nd day (Figure 4.9a). These results showed that acetal containing micelles are stable at neutral pH but degrade at low pH due to cleavage of acetal bonds. This study revealed that pH can act as stimulus or trigger for the micellar disassembly. These results are also in concurrence with the previous studies where acetal linkage was incorporated to study the pH responsiveness of different biodegradable micellar systems depending on the type of block copolymer.[48]

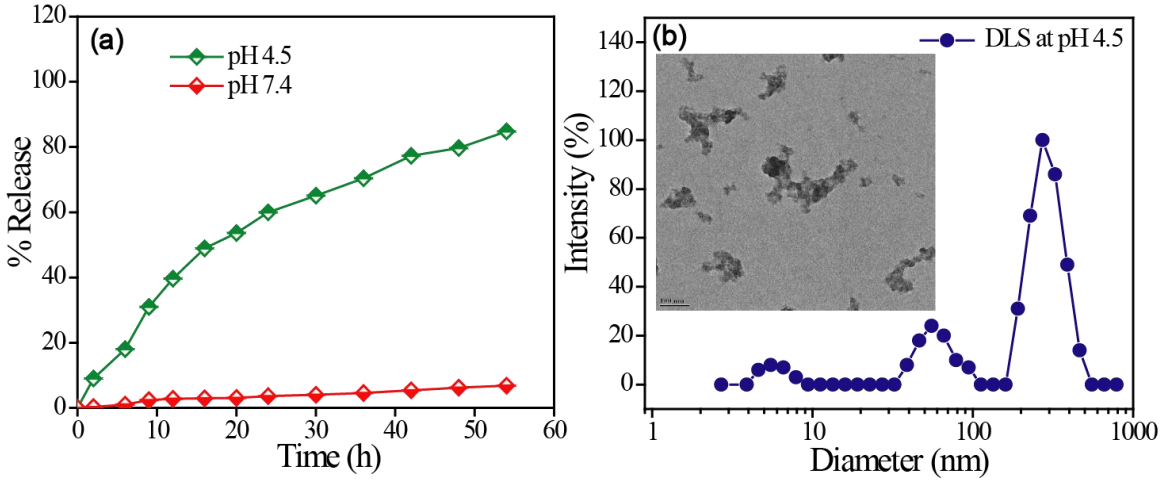

Figure 4.9: (a) pH-responsive dye release profile at two different pH values (7.4 and 4.5) at specific time intervals (b) Hydrodynamic diameter of the degraded micelles obtained by DLS analysis at pH 4.5. (inset: TEM image of the same solution).

Further, acetal cleavage in pH-responsive micelles was also confirmed by measuring change in size of the micelles using DLS and TEM techniques. At pH 7.4, an average size of ~65 nm had been observed for the micelles (Figure 4.5c). After stirring the micellar solution at pH 4.5 for 48 h, a huge change in the polydispersity of micellar size was observed (Figure 4.9b) which was also confirmed by TEM analysis, where only small aggregates were present (Figure 4.9b inset). The explanation is that the degradation of the micelles leads to formation of free polymer chains and their aggregation due to limited solubility.

4.3.7 In vitro cell cytotoxicity studies

The combination of lysosome-targeting M6P-GP group along with the controlled release of drugs at endosomal pH due to presence of acetal linkage may allow these pH-responsive micelles to act as smart nanocarriers for targeted specifically to lysosomes. Preliminary cellular uptake studies were performed to check whether the M6P-GP labeled micelles were able to enter inside the lysosomes selectively. Since cell viability studies of the prepared 15M6P-GP-ace-PPO polymer micelles is a prerequisite for such type of uptake study, so first a cytotoxicity assay (MTT assay) of 15M6P-GP-ace-PPO block copolymer that is self-assembled into the micellar system was performed with MCF-7 breast cancer cell line (Figure 4.10).

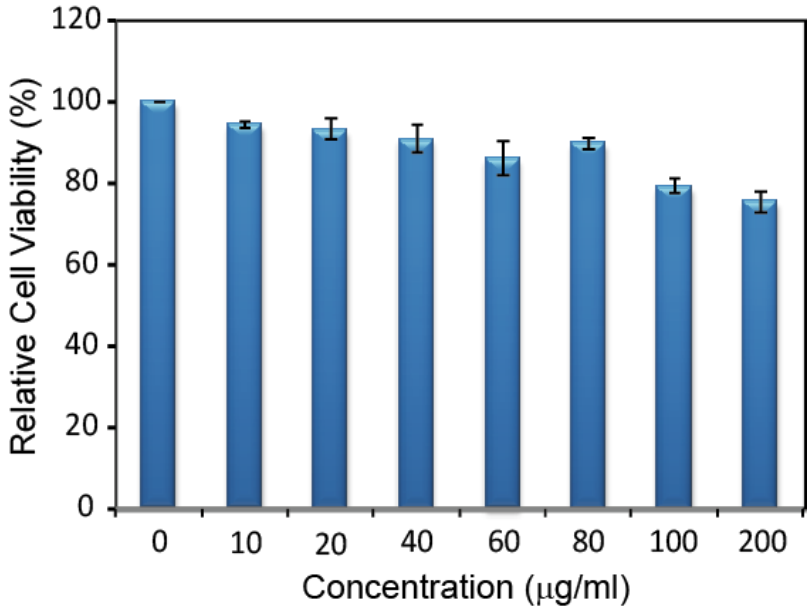

Figure 4.10: MTT assay for 15M6P-GP-ace-PPO block polymer micelles performed on MCF-7 cell line.

After incubating for 48 h, the cytotoxicity assay results revealed that M6P-GPs decorated micelles are least toxic to the MCF-7 cell *in vitro* since ~80% of the cells are viable up to

200 μg of polymer concentration. The cell viability results indicated the biocompatibility of the M6P-GP-labeled micelles for the further application towards lysosomal drug delivery.

4.3.8 Cellular uptake studies

Lysosomes are the major acidic intracellular compartments inside the cell which contain hydrolytic enzymes that can break down many kinds of biomolecules. The amount of lysosomes and acidity is significantly increased in the cancerous cell. Therefore, to check the potential efficacy of M6P-GP labeled nanocarriers for lysosome targeting, the MCF-7 breast cancer cells were incubated with 200 μg/mL of RBOE loaded for 4 h at 37 °C and further the cells were treated LysoTracker green DND-99 to specifically stain acidic cell organelle i.e., lysosomes.

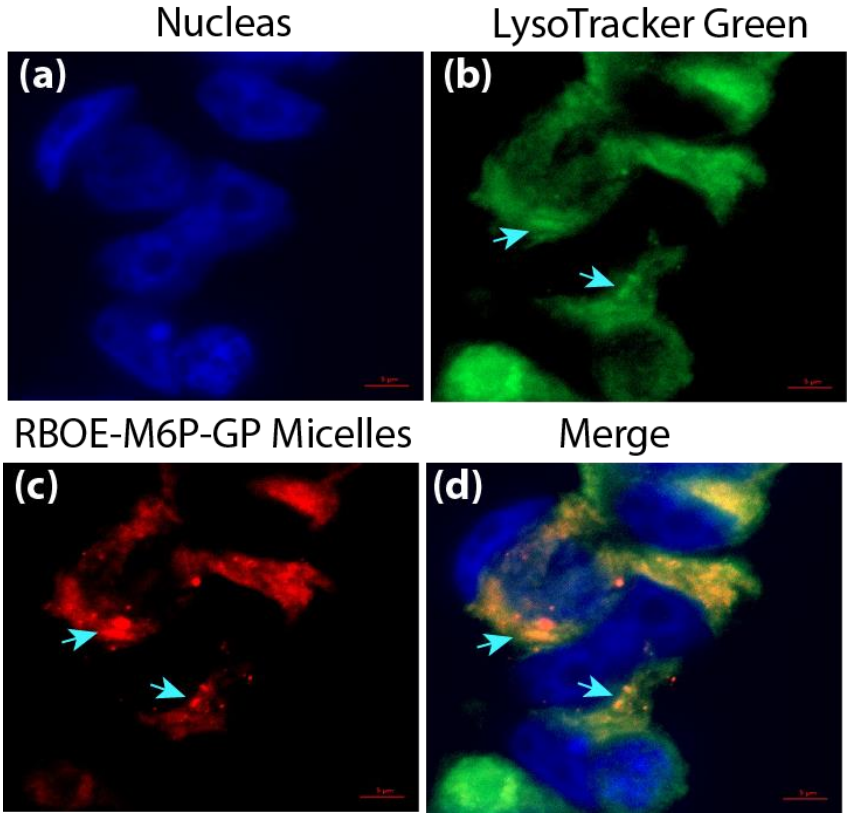

Figure 4.11: Lysosome targeting with RBOE encapsulated M6P-GP-ace-PPO micelles: MCF-7 (a-d) cells were cultured for 4 h, respectively, with RBOE encapsulated M6P-GP micelles (200 μg/mL) in DMEM and then stained with LysoTracker Green (50 nM) for 30 min. The cells were probed by epifluorescence microscopy. Merging of the RBOE signal (shown in green) and that of LysoTracker Green (shown in green) revealed colocalization as indicated by the orange-yellow spots/areas (bars, 5 μm); cyan color arrow indicates punctate-like vesicles.

An epifluorescence microscopy image shows an optimum number of red fluorescent scattered around spotted structures inside the different region of cells which is an indication of the presence of cell organelles such as lysosomes (Figure 4.11). Moreover, the presence of RBOE-loaded M6P-GP micelles inside the lysosomes of cells were confirmed by the fluorescence of RBOE and LysoTracker green. From figure 4.12, colocalization of red fluorescence from RBOE from the M6P-GP-labeled micelles and lysotracker green can be clearly observed. The overlap between the green fluorescence of lysotracker dye and red fluorescence of encapsulated RBOE, indicates the internalisation of M6P-GP labeled micelles inside acidic lysosomes. Additionally, the color intensity profile of both dyes obtained from the bright part of merged images exhibits similar variation in color intensity with distance for both red and green fluorescence channel (Figure 4.12). These observations further supported the hypothesis that both red (RBOE) and green (Lysotracker green) dyes were colocalized within individual lysosomes. These results show that M6P-GP labeled micelles are highly concentrated in the lysosome compared to the cytoplasm, confirming their excellent lysosome-targeting ability.

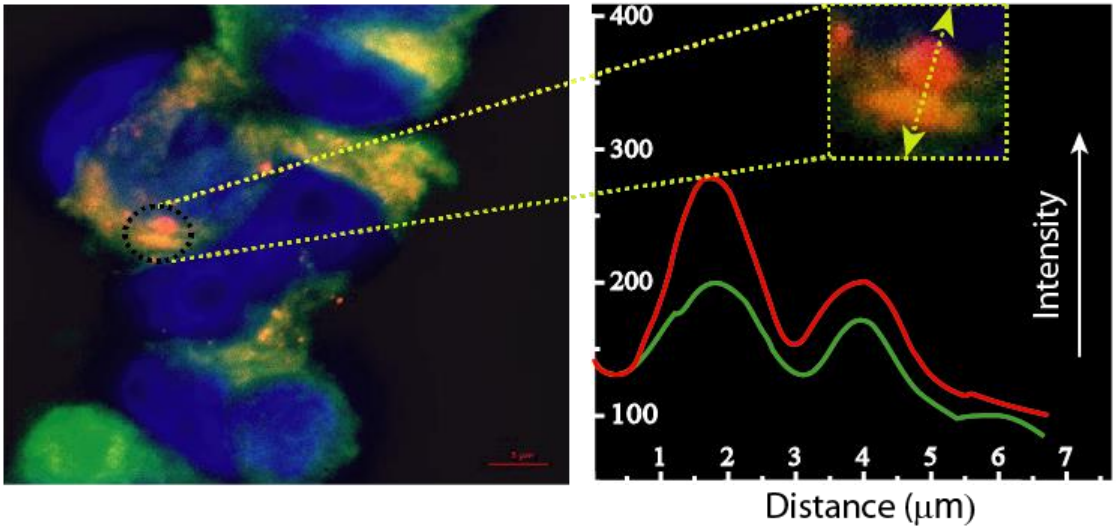

Figure 4.12: Color intensity profile in MCF-7 cells representing the variation of color (both green and red) intensity with distance for a small sub-section of merged image. MCF-7 incubated with RBOE encapsulated 15M6P-GP-ace-PPO micelles show only orange yellowish spherical indicating co-localization of both dyes as is also observed object in the intensity profile.

4.4 Conclusion

Synthesis of pH-responsive M6P-GP block copolymers and theirassembly into micelles to selectively deliver the drugs in the acidic compartment of the cell, i.e. lysosomes was

carried out. an amphiphilic 15M6P-GP-ace-PPO block copolymer was synthesized *via* click chemistry between propargyl end-functionalized M6P-GP polymer and azide end-functionalized acetal-containing PPO. The characterisation of self-assembled micelles was carried out by electron microscopy (TEM, AFM), fluorescence microscopy, and dye encapsulation techniques. It was shown that prepared M6P-GP-based micelles undergo pH-responsive degradation in acidic pH conditions. The micelles were found to display minimal toxicity to cells *in vitro* and showed exceptional selectivity for trafficking into lysosomes in MCF-7 cell line thus demonstrating their potential for drug-delivery applications. It was shown that M6P-GP-based nanocarriers entered inside the lysosomes of mammalian cells by CI-MPR mediated receptor pathway.

4.5 References

1. Kornfeld, S.; *Annu. Rev. Biochem*. **1992**, *61*, 307-330.
2. Alberts, B.; Johnson, A.; Lewis, J.; Raff, M.; Roberts, K.; Walter. P. *Molecular Biology of the Cell, 4th* Garland Science, New York, **2002**. Chapter 13. *ed.*
3. Ghosh, P.; Dahms, M N.; Kornfeld, S. *Nat. Rev. Mol. Cell Biol*. **2003**, *4*, 202-212.
4. Hassan, A. B. *Am. J. Pathol*. **2003**, *162*, 3–6.
5. De Souza, A. T.; Hankins, G. R.; Washington, M. K.; Orton, T. C.; Jirtle, R. L. *Nat. Genet.* **1995**, *11*, 447–449.
6. O'gorman, B. D.; Weiss, J.; Hettiaratchi, A.; Firth, M. S.; Scott, D. C. *Endocrinology*, **2002**, *143*, 4287-4294.
7. Gary-Bobo, M.; Nirdé, P.; Jeanjean, A.; Morère, A.; Garcia, M. *Curr. Med. Chem.* **2007**, *14*, 2945-2953.
8. Vaillant, O.; Cheikh, E K.; Warther, D.; Brevet, D.; Maynadier, M.; Bouffard, E.; Salgues, F.; Jeanjean, A.; Puche, P.; Mazerolles, C.; Maillard, P.; Mongin, O.; Blanchard-Desce, M.; Raehm, L.; Rebillard, X.; Durand, O. J.; Gary-Bobo, M.; MorÀre, A.; Garcia, M. *Angew. Chem.* **2015**, *54*, 5952-5956.
9. Petersen, N. H. T. *Cancer Cell.* **2013,** *24*, 379–393.
10. Desnick, J. R.; Schuchman, H. E. *Nat. Genet.* **2002**, *3*, 954-966.
11. Futerman, H. A.; Meer, van G. *Nat. Rev. Mol. Cell Bio.* **2014**, *5*, 554-565.
12. Hancock, M. K.; Haskins, D. J.; Sun, G.; Dahms, N. M. *J. Biol. Chem.* **2002**, 277, 11255 – 11264.
13. Olson, J. L.; Orsi, R.; Alculumbre, G. S.; Peterson, C. F.; Stigliano, D. I.; Parodi, J. A.; D'Alessio, C.; Dahms, M. N. *J. Biol. Chem.* **2013**, *288*, 16460-16475.
14. Roberts, D. L.; Weix, D. J.; Dahms, N. M.; Kim, J. J. P. *Cell* **1998**, 93, 639 – 648.
15. Olson, L. J.; Zhang, J.; Dahms, N. M.; Kim, J. J. P. *J. Biol. Chem.* **2002**, 277, 10156 – 10161.
16. Byrd, J. C.; Park, J. H.; Schaffer, B. S.; Garmroudi, F.; MacDoald, R. G. *J. Biol. Chem*. **2000**, 275, 18647 – 18656.
17. Tong, P. Y.; Gregory, W.; Kornfeld, S. *J. Biol. Chem*. **1989**, 264, 7962 – 7969.

18. York, J. S.; Arneson, S. L.; Gregory, T. W.; Dahms, M. N.; Kornfeld, S. *J. Biol. Chem.* **1999**, *274*, 1164-1171.
19. Olson, J. L.; Zhang, J.; Dahms, M. N.; Kim, P. Ja J. *J. Biol. Chem.* **2002**, *277*, 10156-10161.
20. Hoogendoorn, S.; Puijvelde, van M. H. G.; Kuiper, J.; Marel, van der A. G.; Overkleeft, S. H. *Angew. Chem.*, **2014**, *53*, 10975-10978.
21. Srinivas, O.; Radhika, S.; Bandaru, M. N.; Nadimpalli, K. S.; Jayaraman, N. *Org. Bio mol. Chem.*, **2005**, *3*, 4252-4257.
22. Agarwal, V.; Toshniwal, P.; Smith, E. N.; Smith, M. N.; Li, B.; Clemons, D. T.; Byrne, T. L.; Kakulas, F.; Wood, M. F.; Fear, M.; Corry B.; Iyer, S. K. *Chem. Commun.*, **2016**, *52*, 327-330.
23. Vidil, C.; More`re, A.; Garcia, M.; Barragan, V.; Hamdaoui, B.; Rochefort, H.; Montero, L.J. *Eur. J. Org. Chem.* **1999**, 447-450.
24. Barragan, V.; Menger, M. F.; Caran, L. K.; Vidil, C.; Morère, A.; Montero, L. J. *Chem. Commun.* **2001**, 85-86.
25. Das, S.; Parekh, N.; Mondal, B.; Sen Gupta, S. *ACS Macro Lett.* **2016**, *5*, 809-813.
26. Pati, D.; Kalva, N.; Das, S.; Kumaraswamy, G.; Sen Gupta, S.; Ambade. A. V. *J. Am. Chem. Soc*. **2012**, *134*, 7796−7802.
27. Huang, J.; Bonduelle, C.; Thévenot, J.; Lecommandoux, S.; Heise, A. *J. Am. Chem. Soc.* **2012**, *134*, 119–122.
28. Kramer, J. R.; Rodriguez, A. R.; Choe, U.J.; Kamei, D. T.; Deming, T. J. *Soft Matter* **2013**, *9*, 3389–3395.
29. Das, S.; Sharma, D. K.; Chakrabarty, S.; Chowdhury, A.; Sen Gupta, S. *Langmuir* **2015**, *31*, 3402–3412.
30. Pati, D.; Das, S.; Patil, N. G.; Parekh, N.; Anjum, D. H.; Dhaware, V.; Ambade, A. V.; Sen Gupta, S. *Biomacromolecules*, **2016**, *17*, 466–475.
31. Satoh, K.; Poelma, J. E.; Campos, L. M.; Stahl B.; Hawker. C. J. *Polym. Chem*., **2012**, *3*, 1890-1898.
32. Pandey, B.; Mahato, J.; Cotta, K. B.; Das, S.; Sharma, D. K.; Sen Gupta, S.; Chowdhury, A. *ACS Omega*, **2016**, *1*, 600-612.
33. Meldal, M.; Tornøe, C. W. *Chem. Rev.*, **2008**, *108*, 2952-3015.
34. Kolbe, H. C.; Finn, M. G.; Sharpless, K. B.; *Angew. Chem. Int. Ed.*, **2001**, *40*, 2004-2021.
35. Lu, H.; Wang, J.; Bai, Y. G.; Lang, J. W.; Liu, S. Y.; Lin, Y.; Cheng, J. *Nat. Commun.* **2011**, *2*, 206-215.
36. Mai, Y.; Eisenberg, A. *Chem. Soc. Rev*. **2012,** *41*, 5969−5985.
37. Antonietti, M.; Förster, S. *Adv. Mater*. **2003**, *15*, 1323−1333.
38. Ouanezar, M.; Guyomarc'h, F.; Bouchoux, A. *Langmuir*, **2012**, *28*, 4915-4919.
39. Liu, H.; Li, C.; Liu, H.; Liu, S. *Langmuir*, **2009**, 25, 4724–4734.
40. Shen, Y.; Zhan, Y.; Tang, J.; Xu, P.; Johnson, P. A.; Radosz, M.; Van Kirk, E. A.; Murdoch, W. J. *AIChE J*. **2008,** *54*, 2979–2989.
41. Zhao, Z.; Huang, H. D. T.; Yin, Z. Y.; Chi, X. Q.; Wang X. M.; Gao, J. H. *J. Mater. Chem.* **2012,** *22*, 15717–15725.
42. Wang, H.; Xu, F.; Wang, Y.; Liu, X.; Jin, Q.; Ji, J. *Polym. Chem.* **2013**, *4*, 3012–3019.

43. Zhang, C. Y.; Yang, Y. Q.; Huang, T. X.; Zhao, B.; Guo, X. D.; Wang J. F.; Zhang, L. J. *Biomaterials.* **2012,** *33,* 6273–6283.

44. Murthy, N.; Xu, M.; Schuck, S.; Kunisawa, J.; Shastri, N.; Frechet, J. M. J. *Proc. Natl. Acad. Sci.* 2003, *100,* 4995-5000.

45. Kwon, Y. J.; Standley, S. M.; Goh, S. L.; Frechet, J. M. J. *J. Contr. Rel.* **2005**, *105*, 199-212.

46. Bulmus, V.; Chan, Y.; Nguyen, Q.; Tran, H. L. *Macromol. Bioscience.* **2007**, *7*, 446.

47. Zhang, L.; Bernard, J.; Davis, T. P.; Barner-Kowollik, C.; Stenzel, M. H. *Macromol. Rapid Commun*. **2008,** *29*, 123-129.

CHAPTER 5

Silk-Mesoporous Silica based Hybrid Macroporous Scaffolds using Ice-Templating Method: Mechanical, Release and Biological Studies

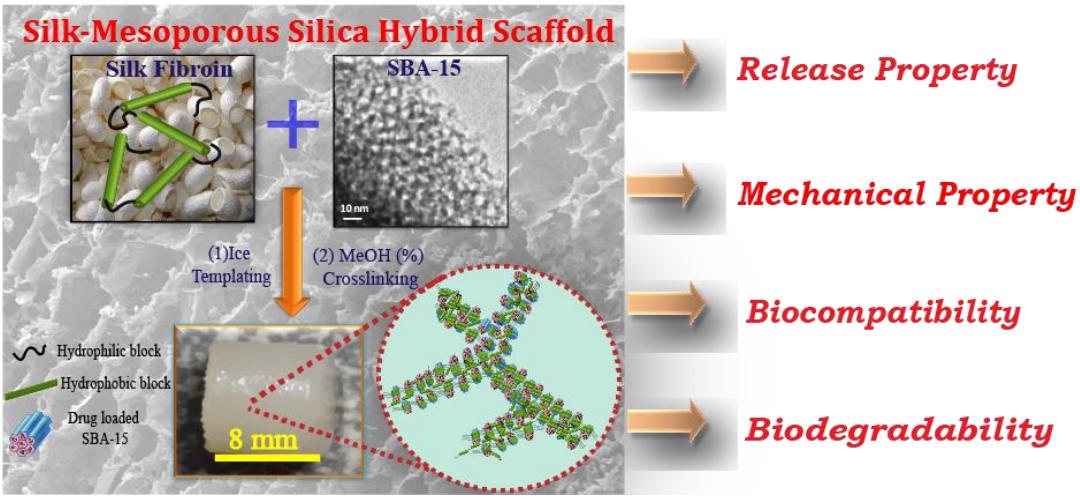

This chapter has been adopted from the corresponding paper, mentioned below;

Pandey, B. *et al.* manuscript is under revision (ACS Applied Biomaterials **2018**).

5.1 Introduction

3D-scaffolds, which mimic the extra cellular matrix (ECM), play a significant role in tissue regeneration by allowing regenerated tissues to assume their function as the scaffold degrades.[1-3] From the early 1990's, enormous progress has been acheived for designing and engineering 3D scaffolds and this has led to the development of a promising class of biomaterials for tissue repair and regeneration.[4-6] Among 3D-scaffolds, drug releasing scaffolds are clinically desired since they allow spatiotemporal release of the drug over a sufficient period of time, which in turn enables control over drug availability and also minimizes the toxic and side effects of the released drug.

For synthesis of 3D scaffolds, both natural and synthetic polymeric materials have been used.[7,8] Silk fibroin (SF), a natural fibrous protein from the *Bombyx mori* silk worm has been extensively investigated as a potential 3D-scaffold for tissue engineering.[9,10] A large part of the silk fibroin protein contains hydrophobic domains, mainly consisting of Gly-Ala-Gly-Ala-Gly-Ser repeating units,[11,12] which leads to the formation of both intra- and intermolecular β-sheet structures[13] which are responsible for the high mechanical strength, insolubility, and thermal stability of silk-based materials. This versatility of the silk fibroin coupled with the excellent mechanical strength, tunable porosity, swelling property, high oxygen and water vapour permeability, biocompatibility, biodegradability, and non-immunogenicity renders them as very interesting and ideal candidates for biomedical applications such as tissue engineering and drug delivery.[14–18,9] Various reports have demonstrated the use of silk fibroin-based scaffolds for drug delivery and tissue engineering.[19-21] Although SF-based scaffolds provide excellent ECM characteristics for various cell types including chondrocytes, fibroblasts, and mesenchymal stem cells,[22-25] their usage as 3D-scaffolds which allow prolonged and sustained release of biomolecules and/or drugs have been limited.[26,27]

For tunable and sustained drug release, ordered mesoporous silica particles have shown great promise.[28] Their large surface, tunable pore size and availability of free silanol groups for interactions /functionalization for the adsorption of biomolecules have led to wide range of applications in sustained drug delivery, cell targeting, biosensing and bioimaging.[29] In fact mesoporous silica particles can be tuned for controlled release of drugs which can range from minutes to several days and can also be effected by various stimuli such as pH, temperature and light.[30] Hence the fabrication of composite biomaterials made from silk fibroin and mesoporous silica particles will combine the

inherent properties of both and could be used as 3D scaffolds that would facilitate tunable sustained release of drugs. Although silk-silica materials have been explored as scaffolds for cell growth, the work has been limited to 2D films or silk-coated bioactive glasses, which are not suitable for soft-tissue engineering.[31,32]

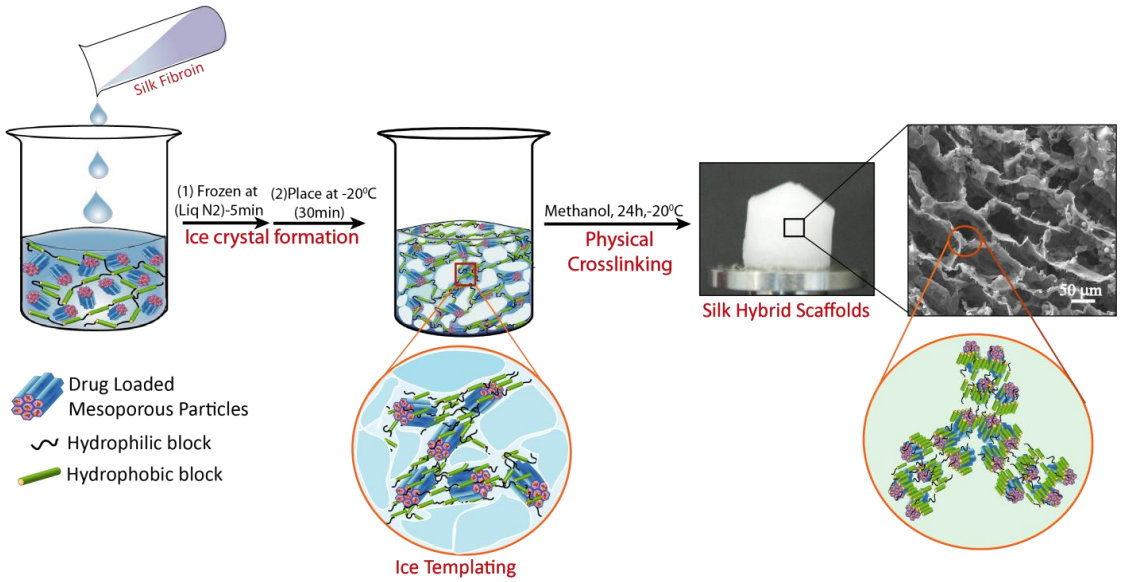

Figure 5.1: Preparation of macroporous silk-mesoporous silica hybrid scaffolds using "ice templating method" and physical crosslinking described in this chapter.

This chapter describes the first example of a macroporous hybrid scaffolds prepared by embedding high percentage (~75%) of sub-micrometer sized mesoporous silica particles (SBA-15) within the silk matrix using ice templating strategy and physical cross-linking of silk fibroin (Figure 5.1). Hybrid scaffolds obtained by combination of silk fibroin as organic and high amount of mesoporous silica particles as inorganic component are soft in nature, biocompatible and biodegradable. They are also macroporous with an average pore size of ~60 µm, which makes them suitable for mammalian cell culture. In addition, the use of mesoporous silica particles in the 3D matrix allows easy incorporation of small and macro molecules inside the scaffold which can be released over an extended period of time during the tissue regeneration process. In this work, two model molecules (FITC-BSA as macromolecule and calcein as small molecule) were encapsulated in the hybrid scaffolds via mesoporous silica particles. Further, their release behavior was studied and also compared with two individual systems (scaffolds made from 100% silk and from bare mesoporous silica particles). Mechanical properties of these composite scaffolds are also investigated which demonstrate that the mechanical property of the composites can be tuned by changing the percentage of cross-linking in silk matrix. Their mechanical response lies in different region of the soft tissue stiffness which makes it possible for it to

be used in soft tissue engineering application. Finally, the cell proliferation and cytotoxicity studies of these hybrid scaffolds were performed using mouse fibroblast L929 cells to indicate that these scaffolds are suitable for tissue engineering applications.

5.2 Experimental Section

5.2.1 General

Tetraethyl orthosilicate (99%), hexadecyltrimethylammonium bromide (99%), lithium bromide, Pluronic 123 (Mav:5800), trimethyl benzene, Albumin, Fluorescein isothiocyanate conjugate from bovine (FITC-BSA), Protease XIV were obtained from Sigma-Aldrich. Cocoons from *Bombyx mori* silkworm were obtained from Central Sericultural Research and Training Institute, Mysore. Distilled deionized water (DI, resistivity18.2 MΩ·cm) from Millipore was used to fabricate scaffolds. All other chemicals used were obtained from Merck, India. The (3-(4,5-Dimethylthiazol-2-yl)-2,5-diphenyltetrazolium bromide (MTT) reagent and calcein were procured from Invitrogen, India. L929 fibroblast cells were purchased from NCCS, Pune, Maharashtra, India. Cells were maintained in Dulbecco modified eagle medium (DMEM:Gibco) with 10% FBS (fetal bovine serum). Aqueous silk fibroin solution was prepared by following the previously published procedure.[33] TEM samples of SBA-15 particles were prepared by dispersing solid particles in isopropanol through sonication and placing the resulting suspension on a carbon-coated copper grid (400 mesh size) and allowing to dry in air. Nitrogen adsorption and desorption studies were carried out using Quantachrome instrument. Samples were preheated at 100°C for 18 hours in the vacuum line. Multi-point BET surface area was calculated from adsorption isotherm from P/P_0:0.1-0.3 and pore size distributions were calculated from adsorption isotherm using the BJH method. Epi fluorescence microscopic images were taken with Carl Zeiss system equipped with a 10x objective. Thermogravimetric analysis (TGA) of the mesoporous silica particles (SBA-15) and the SH-75-1 scaffolds were carried out using a TA Instrument SDT Q600 analyzer between 100 and 1000°C in air (flow 25 mL min^{-1}) at a heating rate of 2°C min^{-1}. All samples were dried under vacuum at 60°C overnight prior to TGA runs.

5.2.2 Synthesis of spherical SBA-15 (Santa Barbara Amorphous-15 Particles)

SBA-15 mesoporous particles were prepared by following the procedure reported by Zhao et al.[46] with small modifications using trimethyl benzene (TMB) as swelling agent. In a

typical batch process, 3 g of non-ionic triblock copolymer P123 (Pluronic 123 [(EO)20(PO)70(EO)20) Mav: 5800] as a structure-directing agent was taken in a polypropylene beaker and 60 mL distilled deionised water was added to it. The mixture was allowed to stir by using an overhead stirrer (with teflon blades) for one hour to dissolve completely. To this solution, 60 mL of 1.5 M HCl were added dropwise, and the reaction mixture was allowed to stir for another one hour at 35 °C. To this solution, a mixture of CTAB (0.6 g) and TMB (0.517g) in 25 mL of de-ionized water and 20 mL absolute ethanol were added. The resulting surfactant solution was stirred vigorously at 35 °C for 15 minutes. To this warm mixture, tetraethylorthosilicate (TEOS, 18 g, 86.4 mmol, 10 mL) as silica source was added dropwise with vigorous stirring at 35 °C for 1 h. The resulting mixture was transferred into an airtight metallic reactor lined with teflon and subjected to hydrothermal synthesis at 75 °C for 10 h and then aging at 125 °C for 48 h. After this, it was allowed to cool at room temperature. The mixture was then filtered and was washed multiple times with water until the pH of the water became neutral. The white solid was allowed to dry in air, and then crushed using a mortar and pestle. The surfactant template was removed by refluxing with ethanol for 16 h each time. The sample was cooled to and preserved under argon atmosphere for further use. Yield: 4.7 g.

5.2.3 Encapsulation of small molecule and macromolecule in SBA-15 particles

5.2.3.1 Encapsulation of calcein inside SBA-15 particles

Hydrophilic dye calcein was used as model molecule to study the *in vitro* release behaviour from SH-75-1 hybrid scaffold. For calcein loading, SBA-15 particles (120 mg) were sonicated in 5mL PBS buffer solution (pH=7.4) followed by the addition of (2.5mg) for 1 h and further left for overnight stirring at room temperature. Then, Calcein loaded SBA-15 particles was collected by centrifugation, washed thoroughly with deionised water (5 times) to remove physiosorbed matter, and dried at 50 °C. All the washings were collected. The amount of calcein encapsulated was calculated from the difference in the initial concentration of calcein and that of the reaction medium combined with the all washings using UV-Vis spectrophotometry. The encapsulation efficiency (EE %) and loading capacity of calcein in SBA-15 particles is ~26% and ~5.4 mg/gm of SBA-15 particles. The EE% and loading capacity (mg/g) were calculated using equations shown below.

$$EE\% = \frac{\text{Amount Encapsulated Calcein}}{\text{Total amount of feed Calcein}} \text{x } 100$$

$$\text{Loading Capacity}\left(\frac{\text{mg}}{\text{g}}\right) = \frac{\text{Amount of Encapsulated Calcein (mg)}}{\text{Total amount of SBA 15 particles(g)}}$$

5.2.3.2 Encapsulation of macromolecules (FITC-BSA) inside SBA-15 particles

For protein loading, SBA-15 particles (120 mg) were sonicated in 5mL of phosphate buffer (50mM, pH 4.7) followed by the addition of FITC-BSA (10 mg). The FITC-BSA and SBA-15 mixture was stirred at room temperature (22°C) for 24 h and then centrifuged. After loading, the samples were washed with deionized water and lyophilized. An amount of FITC-BSA encapsulated onto SBA-15 was determined by absorbance at wavelength 488 nm (FITC-BSA λ_{Ex} = 488 nm, λ_{Em} = 518 nm) of the initial solution of FITC-BSA to that of the reaction medium combined with the subsequent washings using UV-Vis spectrophotometry. The encapsulation efficiency (EE %) and loading capacity of FITC-BSA in SBA-15 particles is ~47% and ~39 mg/g of SBA-15 particles. The EE% and loading capacity (mg/g) were calculated by following same procedure as shown for calcein encapsulation.

5.2.4 Preparation of Silk-SBA-15 hybrid scaffolds (~75% Inorganic content)

Aqueous derived silk-SBA-15 hybrid scaffolds were prepared by ice templating method[34]. It was typically performed by dispersing 30 mg of micron sized SBA-15 particles in 100 µL DI water by sonication for 15min in a plastic container (mould). The particle concentration in the overall composite was ≈10 wt % of the volume of water. Then 200µL of silk fibroin solution (5 wt %) was added to this aqueous dispersion and mixed gently. The dispersion was immediately frozen in liquid nitrogen and then immediately placed in a freezer maintained at −20°C. After 30 min, 300µL of 1% methanol solution (cold) was added into the frozen condition and maintained the temperature of -20 °C for another 24 h. After 24 h, the frozen gel was removed from the freezer and allowed to thaw at RT. The thawed scaffold was then washed several times with water to remove excess methanol. This scaffold is termed as a SH-75-1scaffold where '75' indicates (w/v) percentage of (SBA-15) and '1' indicates percentage of methanol used for cross-linking. Model molecule loaded (calcein as a small molecule and FITC-bovine serum albumin as macromolecule) SH-75-1 scaffolds were also prepared for release studies by following the similar procedure used for SH-75 scaffolds.

5.2.5 Preparation of scaffolds of different organic-inorganic content

5.2.5.1 Preparation of hybrid scaffolds containing 75% inorganic content (SH-75) with different concentration of methanol

To a dispersion of 30 mg of micron sized mesoporous silica particles in 100µl of water, 10 mg (200 µl of stock solution) of silk fibroin (350 kDa) was added and mixed well. The particle concentration in the overall composite is ≈10 wt % of the volume of water. After 30 min, 300 µL of 1%, 20%, 40%, 60%, 80%, 100% methanol solution (cold) was added sequentially in frozen condition and place all the samples in a freezer maintained at a temperature of -20 °C for another 24 h. After 24 h, the frozen gel was removed from the freezer and allowed to thaw at RT. The prepared scaffolds were washed several times with water to remove the excess methanol. The hybrid scaffolds with different methanol percent is termed as SH-75-1, SH-75-20, SH-75-40, SH-75-60, SH-75-80, SH-75-100. Silk hybrid scaffolds prepared without methanol crosslinking (lyophilized) is termed as SH-75-0 scaffolds.

5.2.5.2 Preparation of hybrid scaffolds containing 60% inorganic content (SH-60-1)

To a dispersion of 15 mg of SBA-15 particles in 100 µl of water, 10 mg (200 µl of stock solution) of silk fibroin (350 kDa) was added and mixed well. The particle concentration in the overall composite is ≈5 wt % of the volume of water. After 30 min, 300 µL of 1% methanol solution (cold) was added in frozen condition and the container was placed in a freezer maintained at a temperature of -20 °C for another 24 h. After 24 h, the frozen gel was removed from the freezer and allowed to thaw at room temperature . The prepared scaffolds were washed several times with water to remove the excess methanol. The hybrid scaffolds prepared by 60% of inorganic content and crosslinked with 1% methanol are termed as SH-60-1 scaffolds.

5.2.5.3 Preparation of hybrid scaffolds containing 90% inorganic content (SH-90-1)

To a dispersion of 60mg of SBA-15 particles in 100µl of water, 7mg (200µl) of silk fibroin (350 kDa) was added and mixed well. The particle concentration in the overall composite is ≈20 wt % of the volume of water. After 30 min, 300µL of 1% methanol solution (cold) was added in frozen condition and place the container in a freezer maintained at a temperature of −20 °C for another 24 h. After 24 h, the frozen gel was removed from the freezer and allowed to thaw at room temperature. The prepared scaffolds were washed several times with water to remove the excess methanol. The hybrid scaffolds prepared by 90% of inorganic content and crosslinked with 1% methanol are termed as SH-90-1 scaffolds.

5.2.5.4 Control scaffolds

No self-standing monolith is formed when pure silk is ice templated until lyophilisation process and it is termed as SF-100-0 scaffolds (without methanol crystallisation). No self-standing scaffold was formed on thawing the aqueous silk fibroin solution as the same concentration was ice-templated and crystallised with 1% methanol. After lyophilisation, the scaffold is termed as (SF-100-1).

5.2.6 Scanning electron microscopy analysis

SEM samples for SBA-15 particles were prepared by dispersing solid particles in isopropanol through sonication and placing the resulting suspension on a silicon wafer and allowed to dry in air. Surface morphology and pore size of silk-hybrid scaffolds were analyzed using SEM. The pore size was calculated by using ImageJ 1.40 software by selecting an average of 25 random pores. For every group, a total of 3 samples (n = 3) were analyzed.

5.2.7 Mechanical studies

Mechanical properties of the scaffolds were measured using TA-ARES G2 instrument, a strain-controlled rheometer equipped with a normal force transducer. A cylindrical sample was obtained by slicing middle portion (diameter ~7 mm; height ~5 mm) from the centimeter sized SH-75-1 scaffold and was used for mechanical study. The previously established protocol was followed to measure mechanical response.[34] All experiments were repeated several times to confirm their reproducibility.

5.2.8 Fourier transform infrared spectroscopy studies

FTIR analysis of silk hybrid scaffolds were performed with Perkin-Elmer FT-IR spectrum GX instrument equipped with an attenuated total reflection (ATR). For each measurement, 64 scans were taken with a resolution of 4 cm^{-1}. Infrared spectra covering the amide I region (1595–1705 cm^{-1}) was selected to identify silk secondary structures.

5.2.9 Procedure for estimation of porosity and swelling property

5.2.9.1 Porosity

A wet cylindrical scaffold (SH-75-1) of known radius, r, and height, h, was taken and the volume calculated as $V_S = \pi r^2 h$. The wet weight of the scaffold was determined as W_S. The scaffold was then dried completely in a vacuum oven and then weighed to determine the scaffold weight, (W_D). The volume of water present in the wet scaffold was then

determined as $V_w = (W_S - W_D)/\rho$, where ρ is the density of water (= 10^3 $kg.m^{-3}$). The porosity of the scaffold was estimated as V_w/V_s.

5.2.9.2 Water uptake capacity

The water uptake capacity of SH-75-1 scaffolds (7 mm diameter and 5 mm height) was carried out in phosphate buffer saline (PBS; pH 7.4) at room temperature (27 ^oC) till the scaffold reached its equilibrium. The water absorption capacity (at regular time intervals) was calculated using the following equation:

$$W_U = [(W_S - W_D)/W_E] \times 100$$

where, W_U is the water uptake capacity of the porous scaffold, W_S is the swollen weight of the scaffold at different time intervals, W_D is the dry weight of the scaffold, and W_E is the wet weight of scaffold at swelling equilibrium.

5.2.10 Loading and in vitro release behavior of small molecules and macromolecules

5.2.10.1 Loading and in vitro release of small molecule (calcein)

To study the release behavior of small molecules from the silk hybrid system, calcein dye was used as a model system. Calcein loaded SH-75-1 scaffold was prepared following the same protocol as described in the previous section (5.2.4). Calcein loaded pure silk scaffolds (control) without SBA-15 particles were prepared by direct loading of calcein (0.5 wt %) in silk fibroin solution (200 µl), and subsequently frozen in liquid nitrogen and cross-linked with 1% aqueous methanol solution. Control scaffolds are lyophilized and used as such for release studies.

In vitro release study of calcein from SH-75-1 scaffolds was carried out in phosphate buffer saline (pH 7.4) at 37 ^oC. The scaffold was immersed in 5 mL of 100 mM PBS solution containing 0.05% sodium azide to inhibit any microbial growth. The whole system was then subsequently kept in a mechanical shaker incubator with rotation rate of 50 rpm at 37^oC. The study was conducted under sealed conditions to ensure no evaporation-mediated loss of PBS. At predefined time points, aliquots were taken out for measurement and replenished with the same volume of fresh PBS solution to maintain the steady state condition. Control experiments of calcein release were conducted with bare SBA-15 particles and SH-100-1 scaffolds to compare the calcein release from SH-75-1 scaffolds. The amount of calcein release was analyzed using fluorescence measurement of the supernatant at a wavelength of 515 nm. These values were compared to a standard curve prepared using known concentrations of calcein (Figure D2). Percentage release

was determined by comparing with the initial loading. A total of 3 samples (n = 3) per group were analyzed. Dark condition was maintained to prevent any photo-quenching upon exposure to light.

5.2.10.2 Loading and in vitro release of macromolecules (FITC-BSA)

FITC labelled Bovine Serum Albumin BSA protein (66 kDa) was used as model biomacromolecule to study release from the silk-SBA-15 hybrid scaffold. FITC-BSA loaded SH-75-1 scaffold was prepared following the same protocol as described in the previous section (5.2.4). Washings were collected for further calculation of the amount of FITC-BSA release. FITC-BSA loaded SF-100-1 scaffolds are prepared by direct loading of FITC-BSA (0.5 wt %) in silk fibroin solution (200 µl), freezing in liquid nitrogen and further cross-linked with 1% aqueous methanol solution. Scaffolds are lyophilized and used as such for release studies.

In vitro release study of model macromolecule from SH-75-1 scaffolds was carried out by following the same procedure used for calcein release. Control experiments of FITC-BSA release was conducted with bare SBA-15 particles and SF-100-1 scaffolds to compare the FITC-BSA release with SH-75-1 scaffolds. The release of FITC-BSA was analyzed through fluorescence measurement of the supernatant at a wavelength of 490 nm. These values were compared to a standard curve prepared using known concentrations of FITC-BSA (Figure D3). Percentage release was determined by comparing with the initial loading. All experiments were performed in triplicate.

5.2.11 Enzymatic degradation studies

In vitro enzymatic degradation study of SH-75-1 scaffolds was done by immersing each weighed scaffold in a 2 mL solution of Protease XIV, which was kept in a glass container and placed at 37 °C incubator. Freshly prepared protease solution of 2 U mL^{-1} activity in PBS (pH 7.4) with 0.05% sodium azide was used to inhibit microbial growth. Similar combinations of SH-75-1 scaffolds without enzymes were used as a control. After every 72 h, enzymatic solution was replaced with freshly prepared protease solution. For dry weight measurement, the enzymatic solution was removed and samples were dried in hot air oven (60°C) overnight. The dry weight was measured at 0, 3, 7, 10, 14, and 21 days, and the percentage degradation of SH-75-1 scaffolds was determined by using the formula:

$$\% \text{ degradation} = [(Wi - Wt)/Wi] \times 100$$

Where W_i is the initial dry weight of SH-75-1 scaffold and Wt is the final weight after 0, 3, 7, 10, 14, and 21 days of enzymatic incubation.

5.2.12 In vitro cell viability studies: Live/Dead assay

L929 cells were seeded on SH-75-1 scaffold in a 96 well flat bottomed non-adherent plate at a density of $2e^4$ cells/scaffold in 10 µL of DMEM containing 10% FBS. The plate was incubated at 37 ºC with 5% CO_2 for 10 minutes that allows the cells to settle on the scaffold followed by the addtion of 200 µL of DMEM with 10% FBS and further incubated up to 7 days. On the 7^{th} day, cells were stained with live/dead staining solution that comprises of 10 µg/mL propidium iodide (PI) and 10 µg/mL acridine orange (AO) (Stock solution were prepared in PBS) in 1 mL of DMEM containing 10% FBS. Cells were incubated at room temperature for 10 minutes. Later, cells were washed two times with PBS and epi-fluorescence images were captured by Axio Observer Z1 Carl Zeiss microscope.

5.2.13 In vitro cell proliferation studies

5.2.13.1 MTT assay

L929 cells were seeded on SH-75-1 scaffold in a 96 well flat bottomed non-adherent plate at a density of $2e^4$ cells/scaffold in 10 µL of DMEM containing 10% FBS. The plate was incubated at 37 ºC with 5% CO_2 for 10 minutes that allows the cells to settle on the scaffold followed by the addtion of 200 µL of DMEM with 10% FBS and further incubated. During incubation, on the 1^{st}, 3^{rd}, 5^{th} and 7^{th} day, the media was replaced with filter sterilized MTT reagent (0.45 mg/mL) prepared in DMEM containing 10% FBS and incubated for 4 h at 37 ºC with 5% CO_2. After incubation, MTT was removed from the wells and 200 µL of DMSO per well was added to dissolve insoluble formazan crystals followed by incubation at 37 ºC with 5% CO_2 for 5–10 minutes. The absorbance was measured at 550 nm using a microtitre plate reader (Multiskan EX, Thermo Scientific). Each absorbance was taken to be the mean of triplicate measurements.

5.2.13.2 DAPI staining assay

L929 cells were seeded on SH-75-1 scaffold in a 96 well flat bottomed non-adherent plate at a density of $2e^4$ cells/scaffold in 10 µL of DMEM containing 10% FBS. The plate was incubated at 37 ºC with 5% CO_2 for 10 minutes that allows the cells to settle on the scaffold followed by the addtion of 200 µL of DMEM with 10% FBS. During incubation, on the 1^{st}, 3^{rd}, 5^{th} and 7^{th} day, cells were washed three times with PBS followed by

fixation with 4% paraformaldehyde for 15 minutes at room temperature. Nucleus of the cell was counter stained by incubating with DAPI (600 nM) for 5 minutes at room temperature and washed with PBS. Epi-fluorescence images were captured by Axio Observer Z1 Carl Zeiss microscope.

5.2.13.3 In vitro cell morphology study by actin cytoskeleton staining

L929 cells were seeded on SH-75-1scaffold in a 96 well flat bottomed non-adherent plate at a density of $2e^4$ cells/scaffold in 10 µL of DMEM containing 10% FBS. The plate was incubated at 37 ºC with 5% CO_2 for 10 minutes that allows the cells to settle on the scaffold followed by the addtion of 200 µL of DMEM with 10% FBS further incubated up to 7 days. On the 7^{th} day, actin cytoskeleton of L929 was stained by using mentioned protocol: SH-75-1 scaffold with cells was washed two times with PBS followed by the cell fixation with 4% paraformaldehyde for 15 minutes at room temperature. The cells were later washed two times with PBS. Cells were permeabilized with the addition of 0.1% Triton X-100 (Sigma-Aldrich) for 5 minutes. The cells were washed again two times with PBS and incubated with 5% BSA for 20 minutes at room temperature. This step was performed to avoid non-specific binding. Actin filaments were stained by incubating 1 : 100 dilution of Alexafluor 488 phalloidin (Thermo Fisher Scientific) prepared in PBS for 30 minutes in the dark at room temperature. Nucleus of the cell was counter stained by incubating with DAPI (600 nM) for 5 minutes at room temperature and washed with PBS. Epi-fluorescence images were captured by Axio Observer Z1 Carl Zeiss microscope.

5.3 Results and Discussions

5.3.1 Preparation of silk-mesoporous silica based hybrid scaffolds

For the preparation of silk–mesoporous based hybrid materials, SBA-15 was chosen as mesoporous material as it has appropriate pore size for loading the small molecules and macromolecules. Therefore, SBA-15 particles were prepared and characterised as reported earlier (Figure 5.2).[46] The particles were characterised by electron microscopy techniques (Figure 5.2a: SEM and Figure 5.2b:TEM) and pore size was determined via nitrogen adsorption-desorption studies. An average particle size of 2-3 µm was observed in SEM. Nitrogen adsorption-desorption studies of SBA-15 particles showed type IV isotherm, which is characteristic of mesoporous materials. The BJH pore-size distribution (PSD) analysis showed very narrow PSD. BJH pore size distribution of SBA-15 showed

presence of hierarchical pore structure with an average pore size and surface area of ~9 nm and 666 m^2 g^{-1}, respectively (Figure 5.2c).

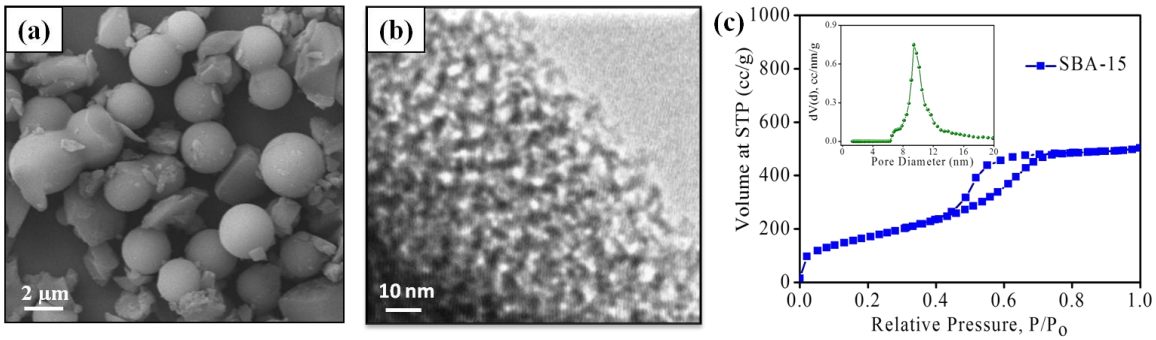

Figure 5.2: (a) SEM image of SBA-15 particles (b) TEM images of synthesized SBA-15 particles (c) Nitrogen adsorption-desorption isotherm of SBA-15 particles.

Further the preparation of silk fibroin-based hybrid macroporous monolith was carried out by ice templating technique,[34,35] using an aqueous dispersion of mesoporous silica particles in silk fibroin solution followed by physical cross-linking (inducing β sheets) with aqueous methanol. Typically, for preparation of SH-75-1 hybrid scaffolds, an aqueous dispersion of mesoporous silica particles (sub micrometer: SBA-15, having final particle concentration ϕ = 10% w/v) was mixed with silk fibroin solution (~5 w/v) and the whole mixture was allowed to freeze. During the process of ice templating, the ice crystals locally concentrated the mesoporous particles and the silk fibroin at the grain boundaries. Ice-crystal here acted as the porogen. The silk fibroin in this hybrid particle-protein network was physically cross-linked via slow diffusion of methanol in the frozen state (*viz*., at −20°C) over about one day. Physical cross-linking of the silk protein entrapping the mesoporous particles in its fibrous matrix and in frozen state helps to recover the monolithic sample by a simple thawing process at room temperature and reduces the cost of expensive freeze drying. The as prepared hybrid scaffold is termed as SH-75-1 (Figure 5.3). Methanol is well known to induce β sheet structure (silk crystallization) through increased hydrogen bonding *via* dehydration of hydrated hydrophobic domains in silk I structure and increased interchain cross-linking.[14] This process helps to stabilize the porous scaffolds with high particle loading in the composite scaffolds.

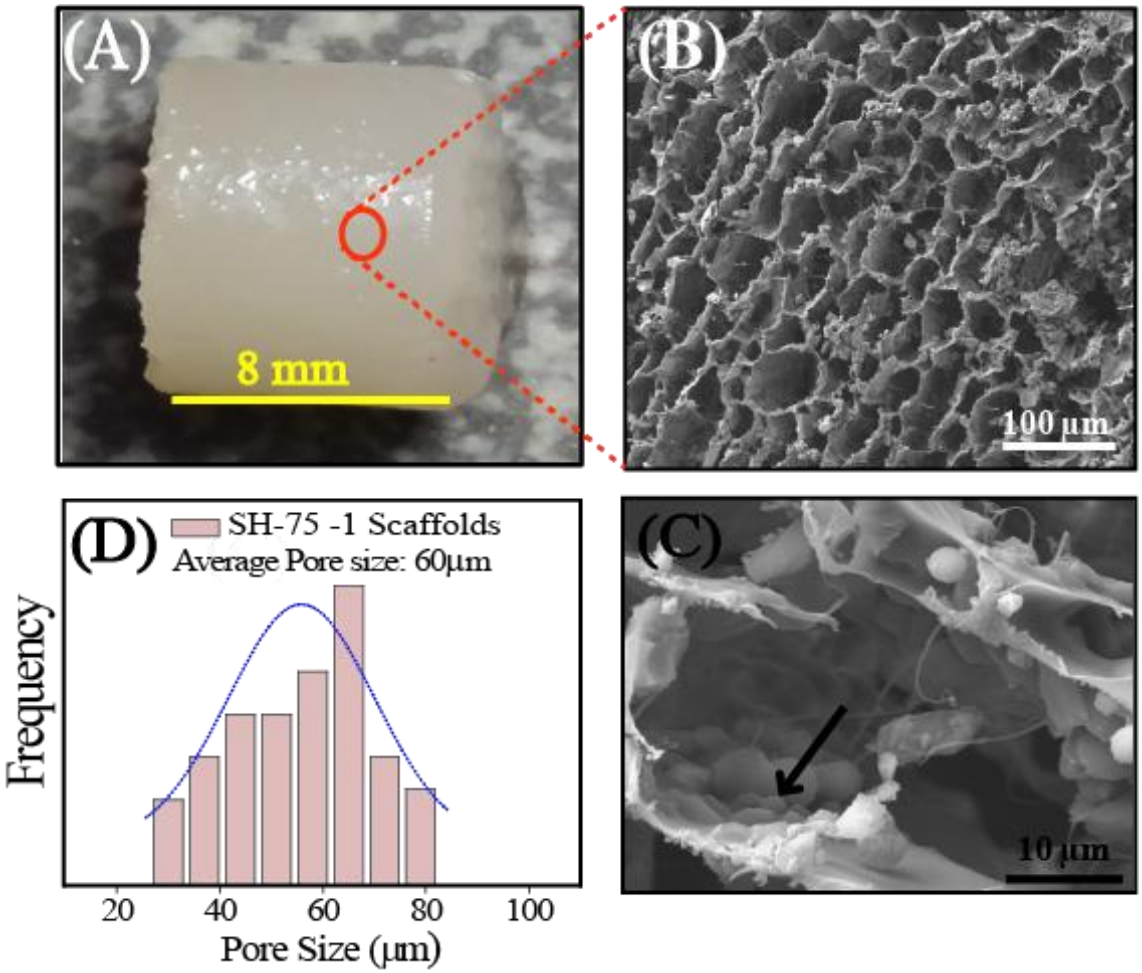

Figure 5.3: Morphological characteristics of SH-75-1 scaffold (a) Photograph of large sized SH-75-1 hybrid scaffold prepared using silk fibroin and micron size mesoporous SBA-15 particles using ice templating method (b) Scanning electron micrographs of hybrid SH-75-1 scaffold (c) SEM Image of SH-75-1 scaffold at high magnification (black arrow showing SBA-15 particles are embedding within the pore wall) (d) Pore size distribution of SH-75-1 scaffold shows an average pore size range of 30–80 μm.

Various factors that affect the cross-linking have been described previously.[14,42] These includes the concentration of protein required for cross-linking, the concentration of the cross-linker, temperature and time needed for the scaffold formation. However, the cross-linking process also depends on the local concentration of cross-linking groups in the silk fibroin (hydrophobic domains) and cross-linker to induce crosslinking. Interactions between silk fibroin and silica particles can be explained by their physiochemical properties *viz*. isoelectric point (pI), charge density, hydrophilicity, and hydrophobicity among others.[36] As pI value of silk is 3.9, the silk fibroin solution is negatively charged at neutral pH[36] along with bare silica particles which are also negatively charged at neutral pH (pI=2-3)[28]. Since both the species bear negative charges (more negative charges in silica particles as compare to silk) at neutral pH, the interactions between them after

templating porous silica particle within silk matrix would be not favorable. However, as silk fibroin comprises of both hydrophobic (>60%) and hydrophilic peptide sequences, a predominent hydrogen bonding interaction between polar groups on silica and protein moieties are possible.[37] Subsequently, silk fibroin coat on the SBA-15 particles are forced to cross-link via the formation of β sheet which stabilizes the whole system leading to the formation of self-standing 3D scaffolds.

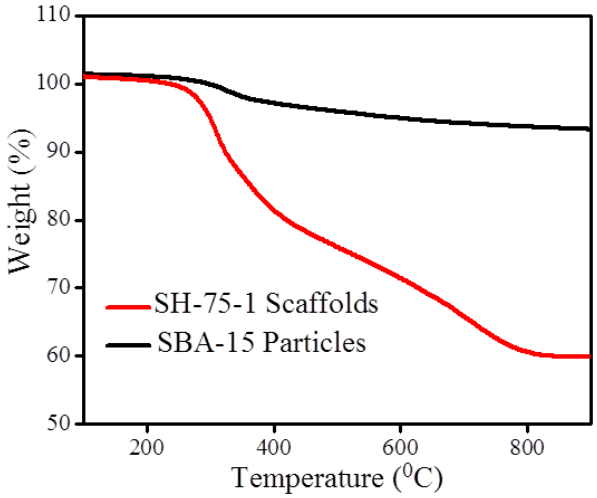

Figure 5.4: TGA analysis of SBA-15 particles (black line) as a control (b) TGA of SH-75-1 scaffold (red line) prepared using the micron sized SBA-15 particles and silk using ice templating method.

5.3.2 Morphology of silk-mesoporous silica based hybrid scaffolds

The morphological architecture of hybrid scaffold fabricated from silk fibroin and SBA-15 particles with different inorganic content was determined by SEM analysis (Figure 5.3 and Figure 5.6). SEM images of the SH-75-1 scaffold reveal a sponge-like morphology with randomly oriented interconnected pore architecture, with a pore size larger than 20μm rendering it suitable for tissue engineering. Moreover, these pores are connected through pore walls that comprised of cross-linked silk-coated SBA-15 particle with an average wall thickness of ~10µm. The pore size is narrowly distributed between 30-80 μm, with an average pore size of 60μm (Figure 5.3c). At higher magnification, the coating of mesoporous particles with a layer of crystallized silk fibroin in the pore wall can be observed (Figure 5.3b). TGA analysis of SH-75-1 scaffolds confirmed that the organic content was ~25% by weight (Figure 5.4). The organic content in the scaffold was obtained as the difference between the weight loss for the hybrid scaffold and that for only SBA-15 particles. However, when the SBA-15 concentration was increased up to 90% (SH-90-1 scaffold), the SEM image revealed that the majority of the pores were

either blocked or small pores with some aggregated patches of silk and SBA-15 particles were present (Figure 5.6b). On the other hand, decreasing the inorganic content (SBA-15) up to 60% afforded a scaffold with pores that were mostly elongated (columnar like structure) and the size ranged from 30- 150 μm (Figure 5.6a). Such drastic changes on the scaffold morphology can be attributed to change in concentration of the overall solid constituent which alters the solution concentration and hence affect the ice crystal growth during the freezing process. Therefore, the hybrid scaffold containing 75% of silica (SH-75-1) was chosen for further biological studies since it had the correct pore size and interconnectivity required for tissue engineering applications. When silk fibroin solution without mesoporous particle was ice templated and cross-linked with by 1% aqueous methanol, only a viscous material was obtained on freeze thawing as discussed in Section 5.2.1. SEM image of lyophilized silk scaffolds (SF-100-1) reveals a very small pore size within the range of ~20µm (Figure 5.6c).

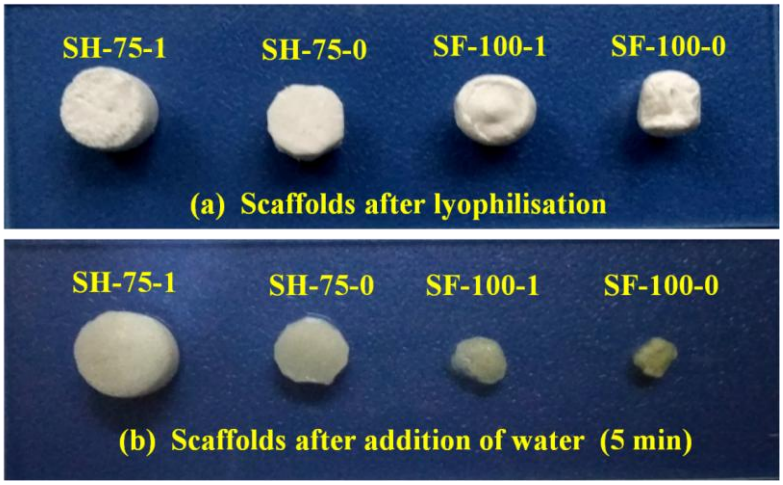

Figure 5.5: (a) Photographs of prepared scaffolds (SH-75-1, SH-75-0, SF-100-1, SF-100-0) after lyophilisation and (b) Photographs of scaffolds (SH-75-1, SH-75-0, SF-100-1, SF-100-0) after addition of water (5 min). Image (a) and (b) shows the comparison of all the scaffolds before and after addition of water.

For the silk-silica hybrid system, the property of the material produced depends upon the relative proportion of both the species as well as the optimized environmental conditions employed for their fabrication. When no methanol treatment was employed with the ice templated dispersion only a viscous material was obtained upon thawing (SH-75-0 scaffolds). For scaffolds that were attempted with 100% SF (SF-100-0 and SF-100-1; no silica content), no self-standing monolith was formed until the viscous material is lyophilized (Figure 5.5). Upon lyophilization of 100% SF scaffold, no macropores can be seen from SEM (Figure 5.6c). Nevertheless, the scaffold completely collapsed when

dipped in water (Figure 5.5). Therefore, for the preparation self-standing hybrid scaffold, the presence of both silk-silica microstructure as well as methanol cross-linker is critical.

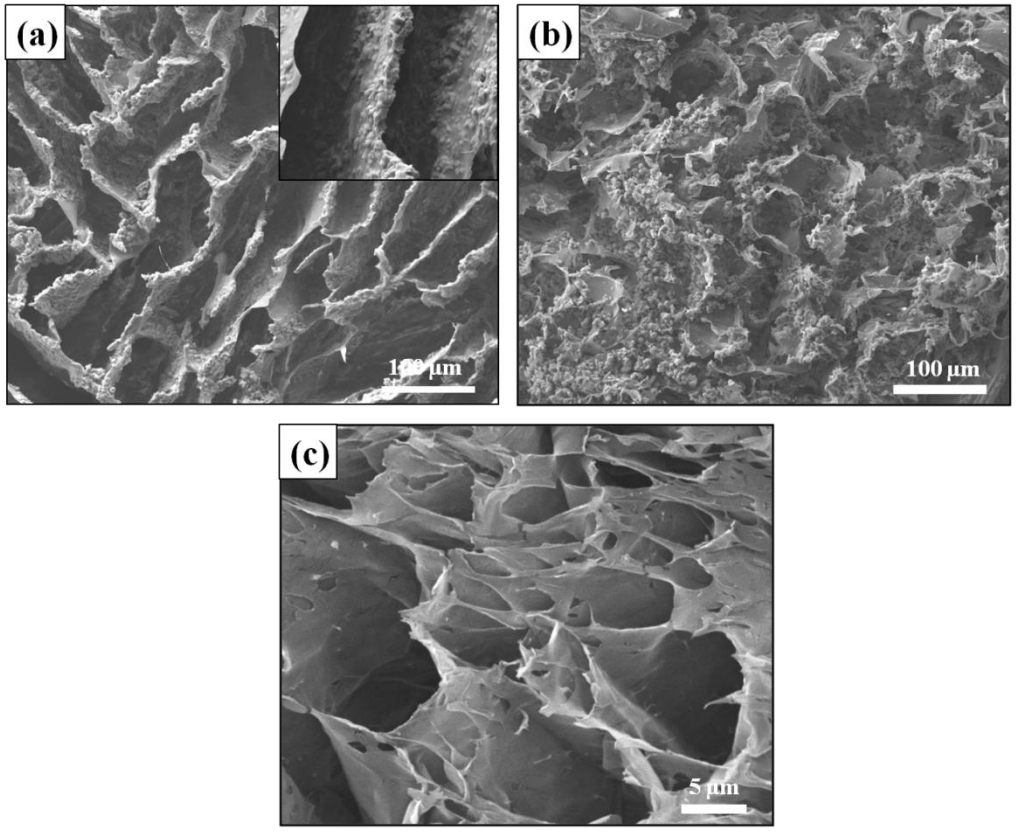

Figure 5.6: SEM images of scaffolds (a) SH-60-1 scaffold (inset: magnified section showing pore wall of SH-60-1 scaffold) (b) SH-90-1 scaffolds (c) Pure silk scaffolds (SF-100-1) after lyophilisation.

Due to the macroporous architecture and amphiphilic nature of the SH-75-1scaffolds, water can easily enter the pores to cause an effective swelling of the hybrid system. To analyze the water absorption capacity and porosity behavior of hybrid scaffolds, they were allowed to swell up to the fully hydrated in phosphate buffer saline (pH 7.4). SH-75-1 scaffolds with ~80% porosity were obtained, and porosity can be varied by changing particle concentration (Tables 5.1 and 5.2). The observed water absorption capacity of the SH-75-1 scaffolds was ~73% (Figure 5.7).

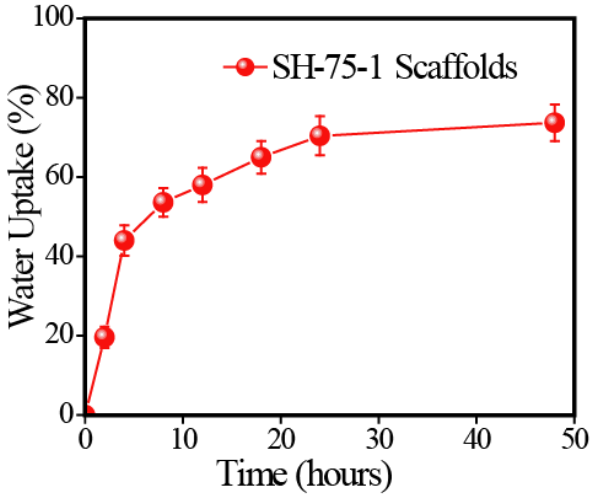

Figure 5.7: Plot for water absorption capacity of SH-75-1 scaffolds.

Table: 5.1 Prepared SH-75-1 scaffolds with varying inorganic-organic content.

Scaffolds Types	SBA-15 (%) (Inorganic content)[a]	Silk (Organic content)[b] (%)	Methanol (%)	Young's Modulus (KPa)	Porosity (%)
SH-60-1	60%	40%	1	27± 0.9 kPa	~89
SH-75-1	75%	25%	1	37± 0.6 kPa	~80
SH-90-1	90%	10%	1	56± 1.3 kPa	~54
SF-100-1	0	100	1	-	-
SH-75-0	75	25	0	-	-
SF-100-0	0	100	0	-	-

[a]weight percent of inorganic content (supporting information: Methods D), [b]weight percent of silk fibroin (experimental section). [c]Aqueous methanol (vol%) is used for crosslinking.

5.3.3 Mechanical properties

Typically, in tissue regeneration process, 3D scaffolds provide structural support and protection to the growing cells and avoid failure against applied internal and external forces under physiological condition. [1,3,39a] Hence the mechanical properties of the hybrid scaffolds were investigated in their fully hydrated state to mimic the *in vivo* physiological condition. Here, we attempted the synthesis of SH-75-1 scaffolds with tunable stiffness by increasing the degree of cross-linking in the silk molecular structure. The degree of cross-linking was tuned by varying the methanol treatment from 1% - 100%. A linear increase

in the modulus from 37 ± 0.6 kPa to 181 ± 5.9 kPa was observed with variation in methanol concentration (Figure 5.8a and Table 5.3). This 5-fold increase in Young's modulus and corresponding mechanical strength from scaffold A to scaffold F in Figure 5.8a comes from the increase in the degree of cross-linking in silk fibroin matrix since methanol is known to induce beta sheets via hydrogen bonding (physical cross-linking) in silk fibroin.[14] Similar measurements on SH-90-1 and SH-60-1 scaffolds also showed that Young's modulus can be tuned with increasing inorganic content (Figure D1). The mechanical properties arise from the cross-linked gel like structure of the silk[42] and the moduli of the scaffold is a measure of its stiffness. Generally, for tissue engineering applications mechanical response of scaffold should closely match the tissue being used for cell growth in an environment that represents their natural state.[38] Typically, the modulus of soft tissues ranges from <1kPa (brain tissue) up to ~600 kPa (cartilage tissue), it indicates a strong correlation between mechanical property of the scaffolds and soft tissue response.[39] Therefore, it would be highly advantageous to develop scaffolds (implants) with different mechanical properties that can adapt itself to the intrinsic properties of soft tissues. For example, the SH-75 scaffolds with the modulus within the range of 20-100 kPa can be considered as representative for tendon tissues and nascent or collagenous bone.[39,40] Beside this, these matrices also help in structural support of growing cells which depends on their stiffness.[41,39a]

Table 5.2. Properties of SH-75-1 hybrid scaffolds with varying methanol content.

	Characteristics of SH-75-1 Silk hybrid Scaffolds	
(1)	Porosity (%)	~80%
(2)	Average pore diameter range (μm)	30-80 (μm)
(3)	Water uptake (%)	~73%
(4)	Swelling equilibrium (hrs)	24
(5)	Young's Modulus (KPa)	37 ± 0.6 KPa
(6)	Degree of degradation (%) (in four weeks)	~90%

Table 5.3. Represents SH-75 silk hybrid scaffolds with varying methanol content.

SH-75 scaffolds	SH-75-0	SH-75-1	SH-75-20	SH-75-40	SH-75-60	SH-75-80	SH-75-100
Methanol (%)	0	1	20	40	60	80	100
Young's Modulus (KPa)	-	37±0.58	88±0.9	102±1.1	142±1.8	170±1.9	192±5.9

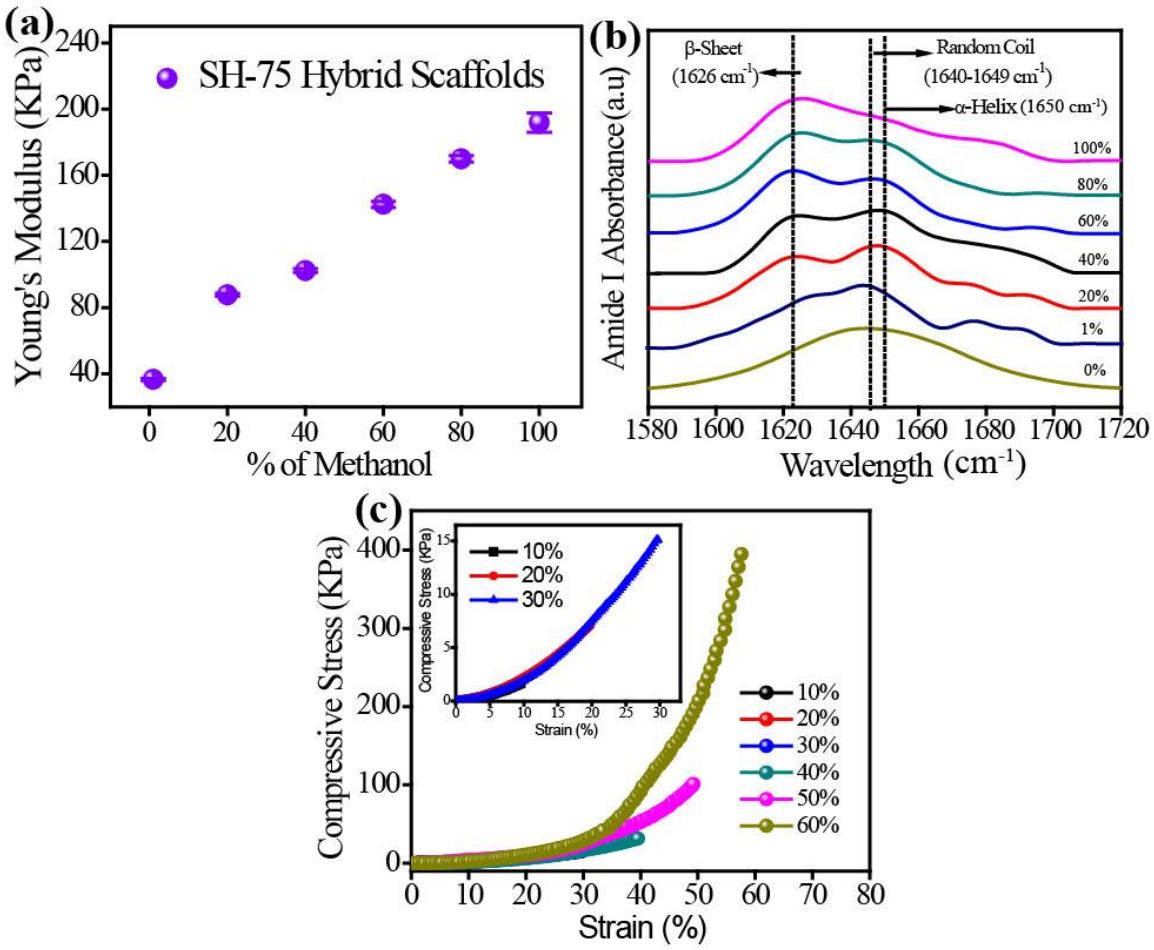

Figure 5.8: (a) Effect of methanol on Young's modulus of SH-75 scaffolds (b) FTIR Spectra of SH-75 scaffolds (c) compression stress-strain curve of SH-75 scaffolds at different strain value viz. from 10 to 60 %.

In SH-75-1 scaffolds, the pore wall comprises of both mesoporous particles (~75% inorganic) and silk fibroin. For a constant silk to particle ratio, the rigidity of wall can be tuned by degree of cross-linking. Since pore walls mainly contribute to showing resistance against compressive strain, modulus of the hybrid scaffold is determined solely

by cross-linking density. Remarkably, modulus of all the hybrid scaffolds prepared by varying methanol concentration lies in the distinct region of the soft tissue stiffness and thereby revealing the ability to produce the scaffolds for a range of tissue engineering application.

5.3.4. Analysis of secondary structure transition

The secondary structural transition in SH-75-1 scaffolds induced by methanol treatment was determined by Fourier transform infrared attenuated total reflection spectra (FTIR-ATR) analysis (Figure 5.8b). It is well known that the regenerated silk fibroin forms water-insoluble structures on exposure to organic solvents or by physical shear.[11-13] When silk fibroin solution comes in exposure to methanol, it induces the formation of β-sheets (crystallinity) in high percentage which leads to the formation of water insoluble structures. The introduction of methanol to silk fibroin solution causes dehydration of initial hydrophobic domains (silk I structures), which results in an induction of interchain cross-linking and finally forms the β-sheets.[14,42] The FTIR spectra of pure silk fibroin exhibit absorption bands at 1230 cm^{-1} (C−N stretching: amide III), 1540 cm^{-1} (N−H bending: amide II), 1650 cm^{-1} (carbonyl stretching: amide I), they are characteristic bands in the random coil conformation of the silk. Generally, after methanol treatment, the additional peaks at 1270 cm^{-1}, 1520 cm^{-1} and 1630 cm^{-1} were observed, which are characteristic of β-sheets, and indicates that methanol treatment leads to the induction of β-sheets.[42] Herein, for silk hybrid scaffolds, the amide I (1600-1700 cm^{-1}) region was selected for monitoring the formation of β-sheet (Figure 5.8b). In SH-75-0 scaffolds, no change in the amide I region was observed as no methanol is used for crosslinking which induce the β-sheet. Whereas in the SH-75-1 scaffolds with 24 h methanol treatment, a peak at 1626 cm^{-1} starts appearing in the amide I region which is indicative of β-sheet formation. Upon increasing the methanol percentage from 1% to 100% in SH-75 scaffolds, the characteristic peak of β-sheet (1626 cm^{-1}) starts increasing,while the peaks corresponding to the random coil (1640-1649 cm^{-1}) and α-helix (1650 cm^{-1}) decreases concurrently (Figure 5.8b). The results indicated that, by increasing methanol concentration gradually, β-sheet content in the SH-75 scaffolds also increases which induces more crystallinity. The result also correlates with mechanical behavior of all SH-75 scaffolds with varying methanol concentration where Young's modulus increases with increasing methanol content.

5.3.5. In vitro release of model molecules

A reliable and controllable release of drugs/biomolecules along with retainment of structural integrity in 3D scaffolds in physiological condition is important for tissue engineering applications. Release of model molecules depends on several factors including size and nature of the model molecule (hydrophilicity or hydrophobicity), interaction of molecules with surrounding silk matrix, degree of cross-linking in silk, pore size distribution in 3D scaffolds, pH and temperature of surrounding medium. Therefore, the release behavior of small molecules and biological macromolecules from fabricated silk hybrid 3D construct was studied. Here, the silk hybrid composites basically comprise of two components i.e. inorganic part as mesoporous particles (SBA-15 particles) and organic part as silk fibroin. Mesoporous silica materials as an inorganic solid were chosen to form the silk-based hybrid composite as they are attractive hosts for encapsulation of small molecule and biological macromolecules in high amount, depending upon their well-ordered and controlled pore (size), and large pore volume.[28,29] In this study, calcein was chosen as a small model molecule and FITC labeled BSAprotein was used as a model biomacromolecule for the release study.

5.3.5.1 Release study for calcein

A comparative study of 30 days release of calcein with SH-75-1 hybrid scaffolds revealed an initial fast release (~47%) during the first 3-4 days followed by a sustained release over several days until it reached an equilibrium state (~67% overall release; Figure 5.9a). This release kinetics is different from that observed with either bare SBA-15 particles or SF-100-1. In both these materials an initial burst release of 80% for SBA-15 and 90% for SF-100-1 scaffold was observed (Figure 5.9a and Figure D4b). Such a bimodal release profile can be understood based on the varied interactions of calcein with the SH-75-1 hybrid scaffold. Synthesis of calcein loaded SH-75-1 scaffolds involve first encapsulation of calcein inside the pores of mesoporous SBA-15 followed by coating and cross-linking with silk fibroin to form the hybrid scaffolds. So in hybrid scaffolds the release behaviour of calcein is affected by the dual barrier effect- (i) interaction between the carboxylate groups in calcein and the silanol groups inside the mesopores, and (ii) interaction with silk fibroin inside the macropores. In addition, pore entrance of the mesoporous SBA-15 is likely to be partially blocked by the silk fibroin and the extent of this blockage is likely to affect the release behavior.

This result clearly confirms the role played by the hybrid scaffold in controlling the release rate of small model molecules. This type of slow release system can be useful for

particular tissue engineering as well as tissue repair purposes, where the drug release rates can match the tissue growth and material degradation.

5.3.5.2 Release study for FITC-BSA

Controlled release of larger biomolecules was also investigated since biomolecules such as growth factor controls the adhesion and proliferation of cells. As a model system, the release of the protein BSA from SH-75-1 hybrid scaffolds was investigated for a period of 30 days. BSA is a large protein (MW = 69 KDa) with hydrodynamic radius 4.5nm and the size if compatible with the pore size of the SBA-15. Similar to calcein loaded SH-75-1 scaffold, FITC-labelled BSA was loaded in SH-75-1 scaffold and the amount of BSA released was followed by fluorescence measurement of the conjugated FITC. To ensure whether the conformational stability of the protein was preserved after release from the SH-75-1 hybrid scaffolds, circular dichroism measurement of the released protein was performed (Figure 5.9c). The fluorescein-labelled BSA initially showed faster release in 3-4 days and subsequently showed a prolonged release with a course of time to finally reach an equilibrium state. This release profile of FITC-BSA differs from either bare SBA-15 particles or scaffolds made with 100% SF where a much higher burst release was observed (Figure 5.9b). This FITC-BSA release kinetics is different from that observed with either bare SBA-15 particles or SF-100-1scaffolds. In both these materials an initial fast release of 62% for SBA-15 and 70% for SF-100-1scaffold was observed (Figure 5.9b and Figure D4a). The adsorption behaviour and percentage loading of protein in mesoporous silica particles directly affect the release behaviour and is well explained by Kawi and co-workers.[43] They have shown that the different rates in the whole release process can be explained by interactions between incorporated FITC-BSA molecules with mesoporous silica particles. These interactions are basically in the form of hydrophilic (free OH groups in the mesopores), electrostatic (charged amino groups in the BSA proteins at pH 7.4) or hydrophobic (beta sheets as a major component in silk matrix). As was observed with the release of calcein from SH-75-1 scaffolds, the diffusion of BSA is also influenced by the dual barrier effect. Hence, the initial fast release in bare particles can be attributed to following reasons: (a) Small amount of BSA adsorbed on the outer surface de-adsorbed easily from the silica surface (b) some loosely bound BSA inside the silica pores could be easily released in beginning.

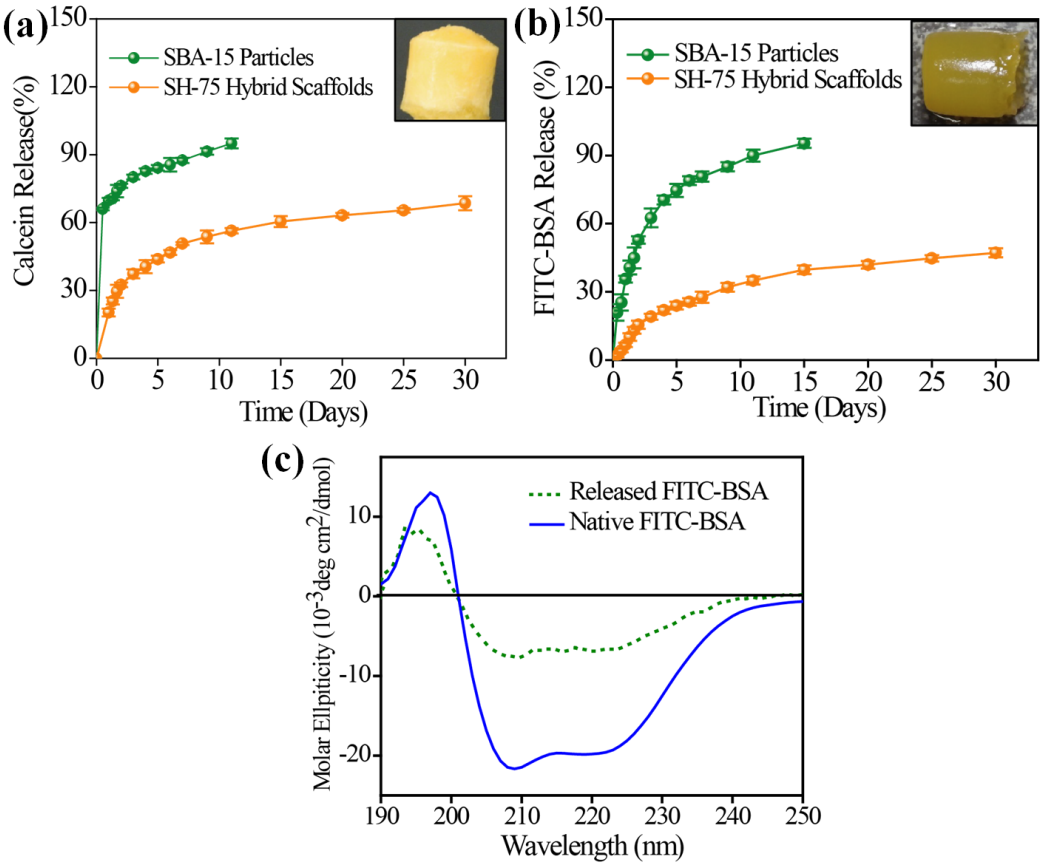

Figure 5.9: (a) Release profile of calcein (small molecule) from SH-75-1 scaffolds and bare SBA-15 particles (b) Release profile of FITC-BSA (macromolecule) from SH-75-1scaffolds and bare SBA-15 particles (c) Circular Dichroism spectrum of FITC-BSA after and before release from SH-75-1scaffolds.

At pH 7.4, silica as well as BSA has net negative charge as isoelectric point of BSA is 4.9 and for silica is 2-3. Therefore, at this pH BSA molecule starts detaching from the pore walls and start diffusing. Also, BSA is highly soluble in water; both electrostatic as well as hydrophilic interaction plays a role in diffusing out from mesopores. After coming out from the mesopores, FITC-BSA also faces some interaction with the crystallized silk fibroin. In comparison to the bare SBA-15 particles or 100% SF scaffolds (without particles), the release of FITC-BSA from silk hybrid system is slow as it is controlled by the dual barrier effect, that is the model molecules are only adhered to silk matrix (in case of pure silk scaffolds) or encapsulated in silica (in case of bare mesoporous particles) as compared to model molecules loaded in mesopores of particles covered in the hybrid constructs. These results clearly reveal the important role played by the 3D scaffold in controlling the release rate of large model molecules. This type of slow release system can be used as an implantable system for the treatment of long-term disease, where therapeutic drugs/proteins/enzymes are expected to be released for more than a year.

5.3.6 In vitro enzyme degradation

The degradation behavior of biomaterials is an important feature regarding functioning *in vivo* (release of cargo) and renovating new tissue structure over time. Bio-inspired natural polymers like silk undergo effective enzymatic degradation under physiological conditions into soluble components (amino acids), thereby making it suitable as biodegradable scaffolds for tissue engineering application. Control over the rate of degradation is another important feature for designing functional tissue, as the rate of scaffold degradation should match the rate of tissue growth. The extent of degradation depends on various factors like structure and morphology of polymers, processing conditions; biological conditions, mechanical strength, and location of implant.[44] To determine the enzyme degradability of hybrid scaffold, the scaffolds were incubated in the presence of protease XIV, a model enzyme with broad specificity and degradation measured by the loss of soluble mass known as the degree of degradation (~DD%) (Figure 5.10a). Degradation results over a 21 day period shows that the presence of the protease enzyme results in facilitated scaffold degradation (DD% = ~90) compared to the buffer alone (PBS) due to the enzymatic recognition of the silk polypeptide structure. The degradation process also depends on the conformational access of enzyme with the respective inter and intra polypeptide chains in the hybrid structure. During degradation process, enzyme starts degrading from the surface to inner side of the hybrid structure, and weight loss of the scaffolds occurs with time. Due to this there is no change in the shape of the samples until the 10^{th} day of the degradation process (Figure 5.10c) whereas SEM image of SH-75-1 hybrid scaffolds at 14^{th} day of this enzyme degradation study shows that silk fibroin matrix degrades and silica particles are left behind (Figure 5.10b). From these results it can be concluded that enzyme degrades the silk matrix (through the pore wall) from the surface of silk fibroin coated particles and the overall structural morphology of scaffolds remains unaltered in initial 10 days of degradation. This property of retaining the structure of hybrid scaffold during the degradation process is an important property for possible tissue engineering applications.

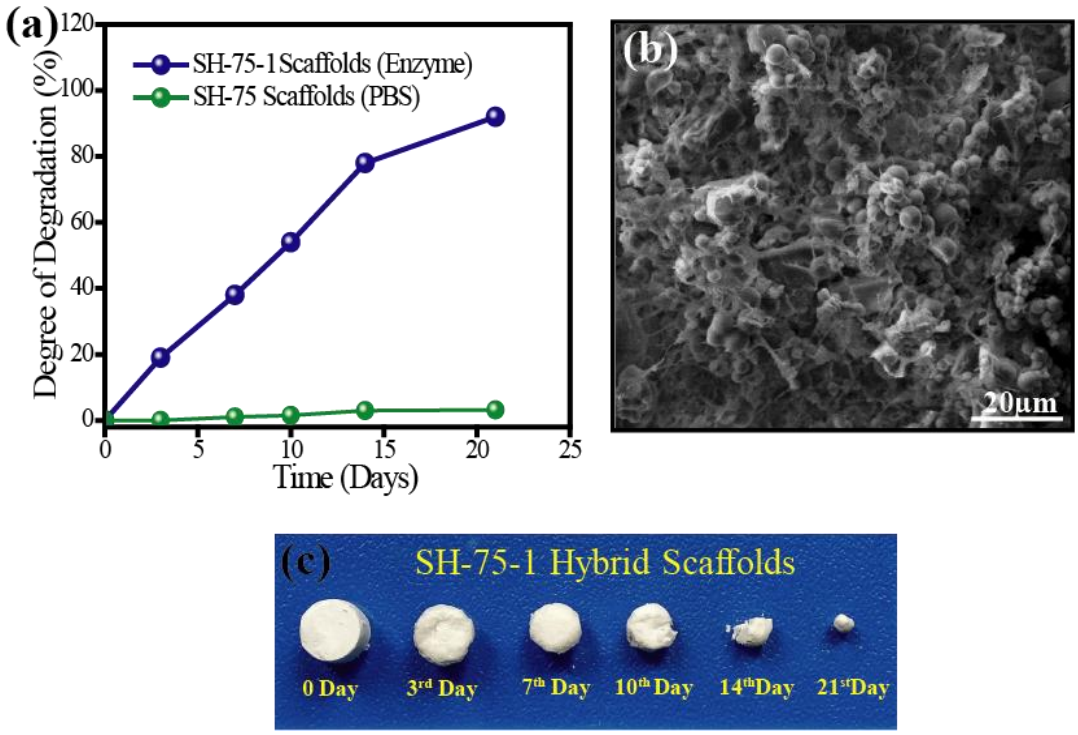

Figure 5.10: (a) Degree of degradation of hybrid scaffolds in the presence of an enzyme (protease XIV, 200µg/mL) and in the presence of PBS only (control) during 21 days incubation at 37 °C. (b) SEM image of SH-75-1 scaffolds at 14th day of enzyme degradation. (c) Photographs of SH-75-1 scaffolds degraded with time.

5.3.7 In vitro cell viability and cell proliferation

Since the developed SH-75-1 scaffold showed high porosity (~80% porosity with average pre size ~60µm), mechanical strength comparable to soft tissues and biodegradability, their efficacy as a scaffold towards *in-vitro* mammalian cell culture study was evaluated using the mouse fibroblast cell line L929. Potential of of the developed material towards biological application depends on its non-cytotoxic behavior and hence the evaluation of biocompatibility of SH-75-1 scaffold was performed by using Live/Dead assay using AO and PI stains. Increased number of viable cells (green fluorescence) as compared to non-viable cells (red fluorescence) on 7th day of cell seeding in Figure 5.11b (Figure D5) showed non-cytotoxicity and biocompatibility of developed SH-75-1 scaffolds.[45]

Cell proliferations were evaluated by performing MTT test and DAPI staining. MTT data in Figure 5.11a shows that as the day progresses from day one to seven the number of viable cells on the SH-75-1 scaffold increases.[45] The cell proliferations were further confirmed by cell nucleus staining with DAPI and the same trend was observed in Figure 5.12. Therefore, data obtained from live/dead assay, MTT assay and DAPI staining showed optimum biocompatibility and excellent cell proliferation on SH-75-1 scaffolds.

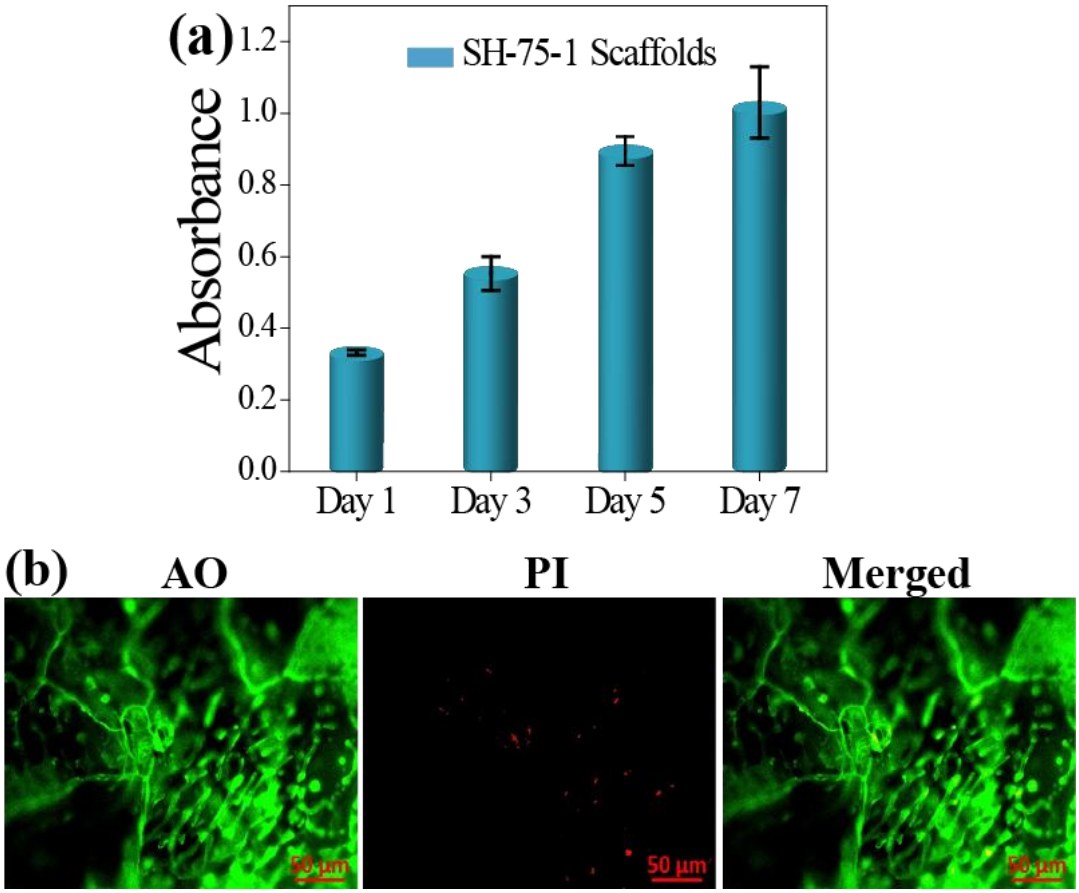

Figure 5.11: (a) Cell proliferation assay (MTT assay) of L929 cells cultured on SH-75-1 scaffolds (b) Epifluorescence Microscopic Images of Live /Dead assay performed on SH-75-1 scaffolds at 7th day. Scale bar is 50 µm.

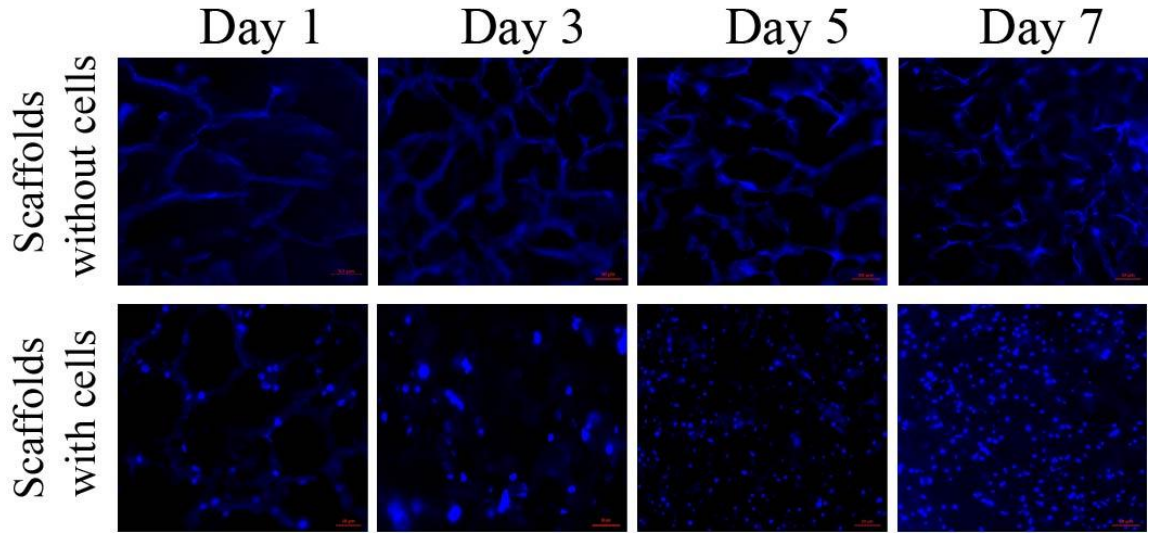

Figure 5.12: Epifluorescence Microscopic Images of cell proliferation assay of L929 cells cultured and stained with DAPI on SH-75-1 scaffolds. Scale bar is 50 µm.

The cellular morphology was evaluated by F-actin cytoskeleton staining with alexafluor 488 phalloidin. Figure 5.13 show epi-fluorescence images of F-actin cytoskeleton of L929 grown on SH-75-1 on 7th day of cell seeding. Elongated cell morphology with increased number of cells further provides support for the potential biological application of SH-75-1 scaffolds. All these data indicated that the scaffold SH-75-1 was non-toxic and could support the growth of mouse fibroblast cells inside them.

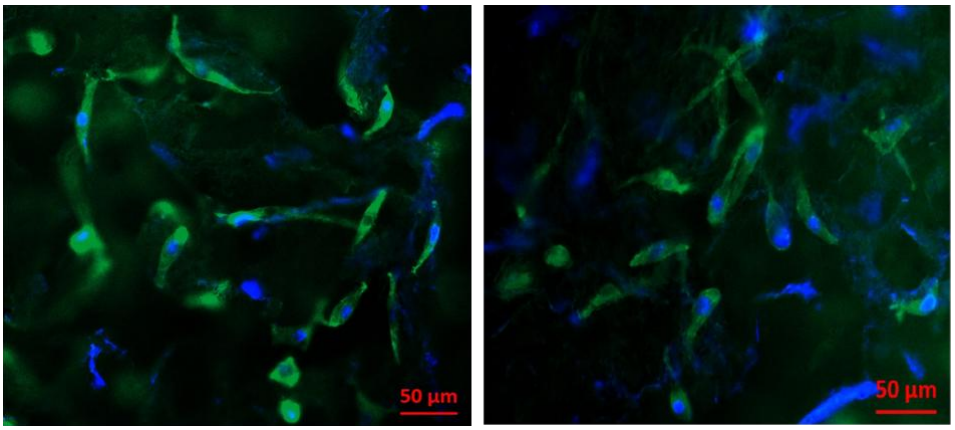

Figure 5.13. Epifluorescence images of L929 actin cytoskeleton stained by Alexa Fluor 488 Phalloidin at the end of 7th day cell growth on SH-75-1 scaffold. Scale bar is 50 µm.

5.4 Conclusions

In conclusion, the preparation of self-standing macroporous scaffold of mesoporous silk-silica composite was demonstrated by using ice templating strategy. The scaffolds were prepared by freezing an aqueous dispersion of mesoporous silica particles (inorganic colloid), silk fibroin (organic crosslinkable polymer) and methanol (cross-linker) and by allowing the polymer to cross-link around the particles in the frozen state. This protocol resulted in scaffolds with tunable mechanical response that contains large amount of mesoporous silica particles (~75% by weight). These macroporous scaffolds have very high porosity (~80%) with ~60 µm average pore size. The average pore size of the scaffold, the mechanical properties and the ability to vary the mechanical strength of the hybrid scaffolds can be exploited to match a distinct range of soft tissue engineering applications. Scaffolds that contain small and macromolecule loaded mesoporous silica particles were also prepared to evaluate their efficacy for therapeutic delivery during tissue regeneration and repair process. The release behaviour of encapsulated molecules like calcein and BSA is largely influenced by their interaction with the mesoporous silica and the silk fibroin. The hybrid scaffold is also shown to be enzymatically degradable.

Further, preliminary biological studies was done on the ice-templated hybrid silk scaffolds to check their biocompatibility and the results indicates that silk hybrid composites are promising candidate in therapeutically relevant repair and regeneration of soft tissues.

5.5 References

1. Kim, T. G.; Shi, H.; Lim, D. W. *Adv. Funct. Mater.* **2012**, *22*, 2446–2468.
2. Tsang, L. V.; Bhatia, S.N. *Adv. Drug Delivery Rev.* **2004**, *56*, 1635– 1647.
3. O'Brien, F. J. *Mater. Today.* **2011**, *14*, 88-95.
4. Langer, R.; Vacanti, J. P. *Science.* **1993**, *260*, 920-926.
5. Shoichet, M. S. *Macromolecules* **2010**, *43*, 581-591.
6. Shoichet, M. S.; Owen, S. C. *J. Biomed. Mater. Res. Part A.* **2010,** *94A*, 1321.
7. Stratton, S.; Shelke, N. B.; Hoshino, K.; Rudraiah, S.; Kumbar, S. G. *Bioactive Materials*. **2016,** *1*, 93-108.
8. Yoon D. M., Fisher J. P. (**2009**). Springer, Boston, MA.
9. Vepari, C.; Kaplan, D. L. *Prog. Polym. Sci.* **2007**, *32*, 991–1007.
10. Mandal, B. B.; Kundu, S. C. *Macromol. Biosci.* **2008**, *8*, 807−818.
11. Zhou, C. Z.; Confalonieri, F.; Jacquet, M.; Perasso, R.; Li, Z. G.; Janin, J. *Proteins.* **2001**, *44*, 119−122.
12. Ha, W. S.; Gracz, H. S.; Tonelli, A. E.; Hudson, S. M. *Biomacromolecules.* **2005**, *6*, 2563−2569.
13. Heslot, H. *Biochimie.* **1998**, *80*, 19−31.
14. Nazarov, R.; Jin, H.; Kaplan, D. L. *Biomacromolecules* **2004**, *5*, 718−726.
15. Kim, U. J.; Park, J.; Kim, H. J.; Wada, M.; Kaplan, D. L. *Biomaterials* **2005**, *26*, 2775−2785.
16. Hofmann, S.; Foo, C. T.; Rossetti, F.; Textor, M.; Novakovic, G. V.; Kaplan, D. L.; Merkle, H. P.; Meinel, L. *J. Controlled. Release* **2006**, *111*, 219−227.
17. Numata, K.; Kaplan, D. L. *Adv. Drug. Delivery. Rev.* **2010**, *62*, 1497−1508.
18. Rockwood, D. N.; Preda, R. C.; Yücel, T.; Wang, X.; Lovett, M. L.; Kaplan, D. L. *Nat. Protoc.* **2011**, *6*, 1612−1631.
19. Wang, Y.; Kim, H. J.; Novakovic, G. V.; Kaplan, D. L. *Biomaterials.* **2006**, *27*, 6064−6082.
20. Mauney, J. R.; Nguyen, T.; Gillen, K.; Kirker-Head, C.; Gimble,J. M.; Kaplan, D. L. *Biomaterials* **2007**, *28*, 5280−5290.
21. Zhang, X.; Wang, X.; Keshav, V.; Wang, X.; Johanas, J. T.; Leisk,G. G.; Kaplan, D. L. *Biomaterials* **2009**, *30*, 3213−3223.
22. Yamamoto, K.; Tomita, N.; Fukuda, Y.; Suzuki, S.; Igarashi, N.; Suguro, T. *Biomaterials* **2007**, *28*, 1838−1846.
23. Murphy, A. R.; John, P., St.; Kaplan, D. L. *Biomaterials*. **2008**, *29*, 2829−2838.
24. Mandal, B. B.; Kundu, S. C. *Biomaterials*. **2009**, *30*, 2956−2965.
25. Wang, Y.; Blasioli, D. J.; Kim, H. J.; Kim, H. S.; Kaplan, D. L. *Biomaterials.* **2006**, *27*, 4434−4442.
26. Wongpanit, P.; Ueda, H.; Tabata, Y.; Rujiravanit, R. *J Biomater Sci Polym Ed*. ***2010***, *21*, *1403–1419.*
27. Karageorgiou, V.; Tomkins, M.; Fajardo, R.; Meinel, L.; Snyder, B.; Wade, K.; Chen, J.; Vunjak-Novakovic, G.; Kaplan, D. L. *J. Biomed. Mater. Res A.* **2006,** *78(2)*, 324-334.

28. Vallet-Regi, M., Balas, F., Arcos, D. L. *Angew. Chem. Int. Ed.* **2007**, *46*, 7548 – 7558.
29. (a) Rosenholm, J.; Sahlgren, C.; Linden, M. *J. Mater. Chem*. **2010**, *20*, 2707–2713. (b) Vivero-Escoto, J.L.; Slowing, I.I.; Trewyn, B.G.; Lin, V.S.-Y. *Small*. **2010**, *6*, 1952–1967 (c) Rosenholm, J.; Sahlgren, C.; Linden, M. *Nanoscale*, **2010**, *2*, 1870–1883.
30. Zhu, J.; Niu, Y.; Li, Y.; Gong, Y.; Shi, H.; Huo, Q.; Liu, Y.; Xu, Q. *J. Mater. Chem. B*, **2017**, *5*, 1339-1352.
31. Wu, C.; Zhang, Y.; Zhu, Y.; Friis, T.; Xiao, Y. *Biomaterials.* **2010**, *31*, 3429–3438.
32. Mieszawska, A.J.; Fourligas, N.; Georgakoudi, I.; Ouhib, N.; Belton, D.J.; Perry, C.C.; Kaplan, D..L. *Biomaterials*. **2010**, *31*, 8902–8910.
33. Nisal, A.; Kalelkar, C; Bellare, J.; Lele, A. *Rheol. Acta*, **2013**, *52*, 833–84.
34. Rajamanickam, R.; Kumari, S.; Kumar, D.; Ghosh, S.; Kim, J. C.; Tae, G.; Gupta, S. S.; Kumaraswamy, G. *Chem. Mater*. **2014**, *26*, 5161−5168.
35. (a) Zhang, H.; Hussain, I.; Brust, M.; Butler, M. F.; Rannard, S. P.; Cooper, A. I. *Nat. Mater***. 2005**, *4*, 787 (b) Deville, S.; Saiz, E.; Nalla, R. K.; Tomsia, A. P. *Science*. **2006**, *311*, 515. (c) Munch, E.; Launey, M. E.; Alsem, D. H.; Saiz, E.; Tomsia, A. P.; Ritchie, R. O. *Science*. **2008**, *322*, 1516.
36. Belton, D. J.; Mieszawska, A.J.; Currie1, H.A.; Kaplan, D. L.; Perry, C.C. *Langmuir*. **2012**, *28 (9)*, 4373–4381.
37. Shchepelina, O; Drachuk, I.; Gupta, M.K.; Lin, J.; Tsukruk, V.V. *Adv. Mater.* **2011**, *23*, 4655–4660.
38. Liu, J.; Zheng, H.; Poh, P. S. P.; Machens, H.-G.; Schilling, A. F. *Int. J. Mol. Sci.* **2015**, *16 (7)*, 15997−16016.
39. (a) Discher, D. E.; Janmey, P.; Wang, Y. L. *Science*. **2005**, *310*, 1139−1143. (b) Wang, B. H.; Campbell, G. *Spine* **2009**, 34 (25), 2745−2753. (c) Huang, G.; Wang, L.; Wang, S.; Han, Y.; Wu, J.; Zhang, Q.; Xu, F.; Lu, T. J. *Biofabrication.* **2012**, *4 (4)*, 042001. (d) Shirbin, S.J.; Karimi, F.; Chan, N.J.; Heath, D.E.; Qiao, G.G. *Biomacromolecules.* **2016**, *17 (9)*, 2981-2991.
40. Discher, D.E.; Mooney, D.J.; Zandstra, P.W. *Science*. **2009**, *324*, 1673-1677.
41. Engler, A.J.; Sen, S.; Sweeney, H.L.; Discher, D.E. *Cell.* **2006**, *126*, 677-689.
42. (a) Li, M.; Lu, S.; Wu, Z.; Yan, H.; Mo, J.; Wang, L. *J. Appl. Polym. Sci.* **2001**, *79*, 2185-2191.(b) Li, M.; Lu, S.; Wu, Z.; Yan, H.; Mo, J.; Wang, L.; Zhang, C.; Yan, H.; Huang, D.; Ye, H. *J. Appl. Polym. Sci.* **2001**, *79*, 2192-2199. (c) Nam, J.; Park, Y. H. *J. Appl. Polym. Sci.* **2001**, *81*, 3008-30021.
43. Song, S.-W.; Hidajat, K.; Kawi, S. *Langmuir* **2005**, *21*, 9568-9575.
44. Numata, K.; Cebe, P.; Kaplan, D.L. *Biomaterials*, **2010**, *31*, 2926–2933.
45. Parekh, N.; Hushye, C.; Warunkar, S.; Sen Gupta, S.; Nisal, A. *RSC Adv.*, **2017**, ***7***, 26551-26558.
46. Zhao, D.; Feng, J.; Huo, Q.; Melosh, N.; Fredrickson, G. H.; Chmelka, B. F.; Stucky, G. D. *Science* **1998**, *279*, 548-552.

CHAPTER 6

Summary and Future Directions

6.1 Summary

This thesis includes the brief discussion towards potential applicability of synthetic functional polypeptides as they can mimic natural polypeptides (proteins) after the formation of self-assembled structures and further involved in the biomolecular recognition process. A thorough study of the formation of functional amphiphilic polypeptides consisting of synthesis and modification, self-assembly into different nanostructures, their characterization and encapsulation property along with the cellular internalization behaviour was carried out. Further, the stimuli-responsive behaviour of the synthesized responsive polypeptides-based morphologies for their application in controlled and targeted drug delivery was studied. In the area of hybrid biomaterials, the fabrication of silk and mesoporous silica-based 3D scaffolds for the tissue engineering application along with drug delivery property was studied. The current chapter presents the summary and conclusions of the work described in previous chapters and future directions based on this work.

Chapter 1 presents an overview of the functional role played by post-translational modification (PTM) process, i.e. glycosylation and phosphorylation in a living organism. It involves detailed description of the role played by various glycoproteins and phosphoglycoproteins in functional proteomics depending on their chemical structure and mechanism of action. A detailed discussion of the functional polypeptides, which contain stimuli-responsive groups that play an essential role in biomedical applications, was exemplified. Influenced by different types of actions performed by these native proteins to maintain the biological system, extensive literature on properties of synthetic functional polypeptides, their self-assembly and exploration of their suitable biological applications was also provided.

Chapter 2 elaborates the synthesis of a newly designed class of glycopolypeptide-based polymersomes (PICsomes) from the self-assembly of two oppositely charged polypeptides, which also contain carbohydrates as a bioactive group, called as GP-PICsomes. A key role played by the secondary conformation of functional polypeptides in the self–assembly process to form an ordered and regular morphology was demonstrated. Further, the individual polymersomes (GP-PICsome) were visualised to show the effective probing of the colocalization of encapsulated dyes. It is described for the first time how biomolecular recognition process can be visualised with the help of micron size

GP-PICsomes. The bioactivity of glycopolypeptide-based self-assembled PIC structures was retained after the self-assembly.

Chapter 3 discusses the preparation of glycopolypeptide-based stimuli-responsive interface crosslinked (ICL) micelles from amphiphilic block copolymer $(PCL_{50})_2$-*b*-Pr-gly_6-*b*-GP_{40} for programmed and targeted drug delivery. For this purpose, miktoarm star copolymer was synthesized by ROP of two conventional NCA's (DL-propargyl glycine NCA and α-*galacto*-*O*-lys NCA) sequentially by amine-terminated branched hydrophobic polycaprolactone $(PCL_{50})_2$-NH_2. Free alkyne groups of the middle block at core-shell interface of the UCL micelles were crosslinked by using bis-(azidoethyl) disulfide (BADS) as redox-responsive crosslinker *via* click chemistry to form interface crosslinked (ICL) micelles. Further, the synergistic effect of dual stimulus (redox and enzyme) on the drug release behaviour from ICL micelles was studied by using doxorubicin (DOX) as a model drug. Furthermore, the UCL and ICL micelles are made suitable towards biological application as potential drug carriers with low cytotoxicity and the ability to target specific cancer cells and release the drugs in a time-dependent manner.

Chapter 4 describes the successful preparation of pH-responsive M6P-GP based micellar nanostructures to selectively deliver the drugs in the acidic compartment of cell i.e. lysosomes. An amphiphilic 15M6P-GP-ace-PPO block copolymer was synthesized using click chemistry, which exhibits acetal as a pH-responsive group at the junction of two blocks. The M6P-GP labelled block copolymer was self-assembled into the micellar structure and shown to undergo pH-responsive release in acidic condition. The micelles were found to display minimal toxicity to cells *in vitro* and showed exceptional selectivity for trafficking into lysosomes in MCF-7 cell line. It was demonstrated that M6P-GPs labeled nanocarriers enter into the lysosomes of mammalian cells through the CI-MPR receptor pathway.

Chapter 5 describes the successful synthesis of hybrid biomaterials by using silk fibroin as natural biopolymer and mesoporous silica (SBA-15) as inorganic drug delivery agent. Silk-mesoporous silica 3D scaffolds were fabricated by using ice templating strategy and physical crosslinking *via* methanol in silk fibroin. The use of mesoporous silica particles in the 3D matrix allows easy incorporation of small and macromolecules inside the scaffold, which can be released over an extended period of time during the tissue regeneration process. Two model molecules (FITC-BSA as macromolecule and calcein as

a small molecule) were incorporated in the hybrid scaffolds via mesoporous silica particles and, their release behaviour was studied. By tuning the amount of silk fibroin, mesoporous silica and methanol, the mechanical properties of the hybrid scaffolds were modulated and the scaffold exhibited stiffness in the range of soft tissue (~200 KPa). Further, biological studies were performed on the ice-templated silk-hybrid scaffolds that suggest their excellent biocompatibility and indicate that silk-hybrid composites can be promising candidates in therapeutically relevant repair and regeneration of soft tissues.

6.2 Future Directions

Based on the results of research presented in this thesis, here some future aspects of this work have been proposed, which are summarized below.

6.2.1 Understanding biophysical phenomenon

Different types of fluorescent probes have been used in the biology to image the anatomical features as they can behave as contrasting agents in cellular environment.[1-3] Therefore, they help in the understanding of internal biological processes. Typical fluorescence-based experiment studies were involved in the use of fluorescent sensors for performing intensity/excited state lifetime assays of fluorescent probes.[4-6] Further, unlike solution the cellular environments exhibit heterogeneous nature regarding viscosity, polarity, and other physical parameters. Therefore, in most of the cases, this measurement is perturbed by the undesired interaction of nascent florescent probes with other biological components or metabolites in body fluid.[3,4] Therefore, it is more advantageous to use these fluorogenic agents after encapsulating inside polymeric nano-carriers. These nanocarriers help in understanding and designing of new sensing technique, which involves a high resolution to distinguish the signals evolved from different and specific cellular organelles.[7,8] Das et al. showed that it is possible to visualize individual, spatially segregated nanosized (<100 nm) polymersomes with high contrast by using spatially and spectrally resolved fluorescence imaging (SRFM).[9] An effective probing of dye colocalization and energy-transfer of the dyes within the individual polymersomes was investigated which show the extent of dual-dye encapsulation at single polymersome level. In chapter 2 also, dye colocalization within individual GP-PICsomes was shown to confirm the vesicle formation by using total internal reflection fluorescence microscopy (TIRFM). Biomolecular recognition process was also studied to understand internal biological interaction processes using bioactive GP-PICsome as a suitable model.[10]

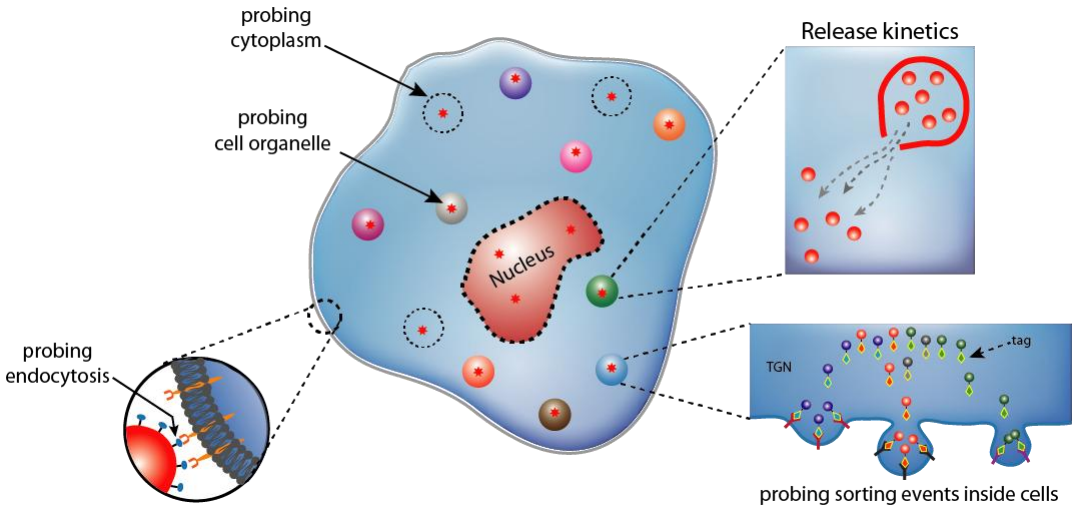

Figure 6.1: Illustration of different biophysical phenomena at the subcellular level.

It is believed that SRFM and TIRFM techniques, would help to get quantitative information on the distribution of fluorescent probes and thus sensing of the cellular environment within individual cells and organs can also be studied. This process would help us to understand various bio-physical phenomena that occur with the nanomaterials either on the surface of the cell membrane or inside the cell. Figure 6.1 represents the different biophysical events that can be examined at subcellular level, such as, (a) interaction between cell surface receptor proteins and ligand incorporated on nanoparticle surface leading to receptor-mediated endocytosis; (b) release kinetics of loaded molecules from nanomaterials inside the cell (c) live microscopy of fluorescently labeled M6P-GP can reveal about the sorting event at the Trans Golgi Network (TGN) for lysosomal delivery. Therefore, these types of techniques would help to understand internal biological phenomena and further can be applied to treat various diseases in the biomedical field.

6.2.2 Glycopolypeptide-based smart biomaterials

For past several decades, huge amount of research has been done towards the synthesis of stimuli-responsive polymers because of their promising applications in different fields starting from self-healing materials, gene or drug nano-carriers, imaging and diagnostics, adaptive coatings, etc.[11-14] As discussed in chapter 1, stimuli-responsive polymers can exist in several forms such as self-assembled aggregates, solution assemblies, gels, bulk solids, films. These polymers undergo reversible or irreversible changes in physical properties in response to various stimuli such as temperature, pH, analyte of interest (ions, bioactive molecules, etc.), light irradiation, ionic strength, electric and magnetic fields, mechanical forces, either individual or a combination of several of them. Therefore, in the designing of stimuli-responsive polymers several factors such as controlling the chain

topologies, location of responsive moieties and functional linkages between the building blocks play a crucial role and thus various molecular architectures have been extensively investigated.

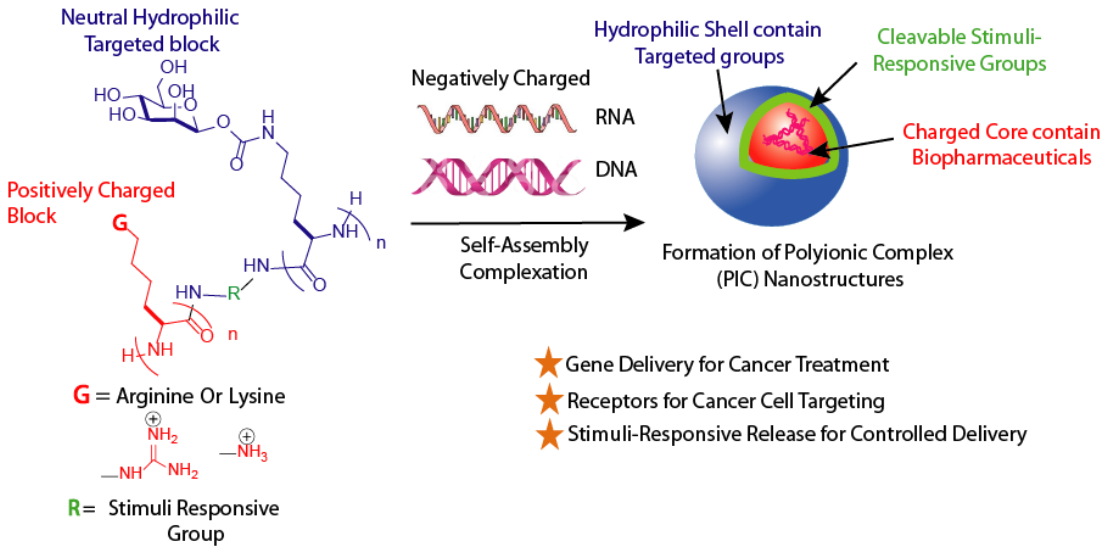

Scheme 6.2: Synthetic strategy proposed for glycopolypeptide based PIC structures for gene delivery in cancer treatment.

Glycopolypeptides-based nanoassemblies can also be made to exhibit the stimuli-responsive behaviour in response to several stimuli. For example, Chapter 2 discusses the self-assembly of charged polypeptides conjugated with glycopolypeptides (GP) that forms the GP-based polyionic complex PIC structures. PIC structures itself show a response to different pH, based on the type of charged polymers and are mainly studied towards the delivery of charged biomolecules such as a gene (plasmid DNA, siRNA, oligo DNA, and proteins).[15] Extending this strategy herein, a scheme is proposed in which GP's can be used for gene therapy after conjugation with PIC structures (Figure 6.2). Polylysines and polyarginine-based biodegradable cationic blocks can be used to form the PIC complex with genetic materials due to the presence of high amount of positive charge. Gene therapy is not only applicable to treat the genetically-related disorders but they can also be applied to cancer treatment.[16] Therefore, along with the specific tumor targeting capability of glycopolypeptides, a particular gene can be transferred to the cancer cells by using GP-PIC based structures, which block the genetic division of cancer cell and inhibits its growth. Other stimuli-responsive groups can also be incorporated in these GP-based charged PIC nanoassemblies to demonstrate the controlled and tunable gene delivery along with the cell targeted ability.

Beside all other responsive stimuli, glycopolypeptides (GP's) based structures can also be used to build sugar-responsive system, which can be helpful in the treatment of diseases like diabetes. It is well known that boronic acids and their substituted compounds can bind to 1,2 and 1,3 diols, which can be responsive against external stimuli such as diols (saccharides and nucleotide), pH, ionic strength.[17-19]

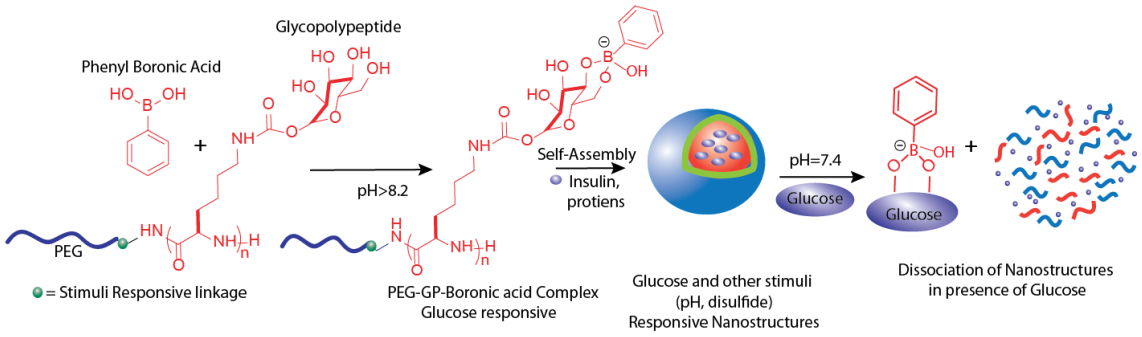

Figure 6.3: Proposed scheme for sugar-responsive hydrophilic glycopolypeptide-boronic acid based self-assembled structures for insulin delivery in diabetic treatment.

Several reports demonstrated that synthetic polymer bearing diols could bind to boronic acid and thus can be used for sugar-responsive (insulin) delivery or sensing.[17] Boronic acids bind to diols containing compounds with high affinity due to reversible ester bond formation.[18] After addition of 1,2 and 1,3 diols, the cyclic boronate ester formed from anionic boronate species are stable whereas ester formed from neutral boronic acid are hydrolytically labile.[19] As GP's also exhibit diols attached to the main peptide backbone, they can form the boronate ester with the boronic acids. These glycopolypeptide-based boronate esters are pH and sugar-responsive therefore their self-assembled structures can be used for insulin delivery or glucose sensing for diabetic patients. Using this idea herein, a scheme is proposed (Figure 6.3) where glycopolypeptide can also be a substitute for insulin delivery.

Various reports are available wherein, the formation of polysaccharide-based responsive gels is reported, since diols of the polysaccharide can also be crosslinked using borax as a crosslinker in slightly alkaline medium.[20] Based on this methodology, responsive glycopolypeptide-based gels can also be prepared by using borax as a crosslinker. Due to the presence of diols in the side chain of polypeptide backbone of GP's, they can be crosslinked with the borax (Figure 6.4). These gels could be responsive to pH and thus can be easily applicable in biomedical application.

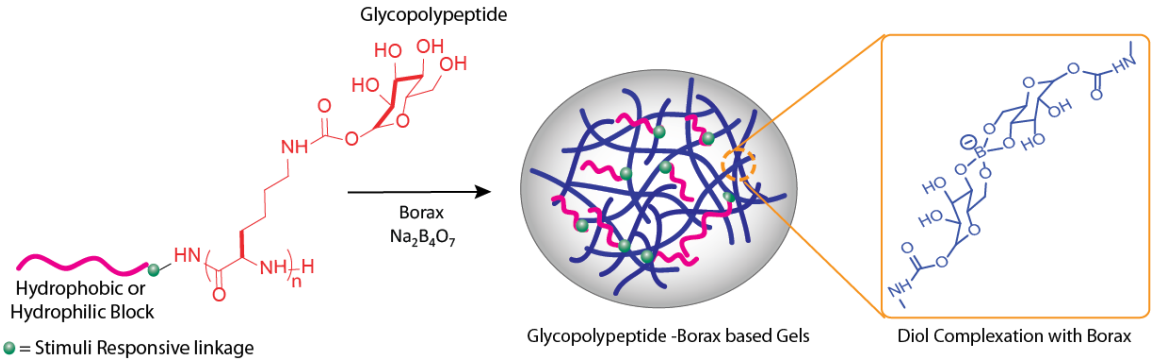

Figure 6.4: Fabrication of glycopolypeptide-borax based gels.

Further, in Chapter 4, the drug delivery in lysosomes for cancer treatment via amphiphilic mannose-6-phosphate based nanostructures has been discussed. Besides this, mannose-6-phosphate-based polymer can also be explored for the treatment of other diseases such as lysosomal-related disorders (LSD)[21,22] As lysosome contains 40 different types of hydrolytic enzymes which are involved in the hydrolysis of macromolecules inside the cell and transferr the fragments to another part of cells for the recycling process[23], they are responsible for cleaning the garbage of the cell. If one of the hydrolytic enzymes is defective, then massive amount of molecules accumulates within the cell causing cell death. This type of defectiveness of enzymes leads to lysosomal-related disorders, which can destroy healthy cells. Therefore, there is a need to design such kind of carriers that can deliver the enzymes to lysosomes for their proper functioning. It has been reported that mannose-6-phosphate glycopolypeptides (M6P-GP) can selectively target the lysosomes.[24]

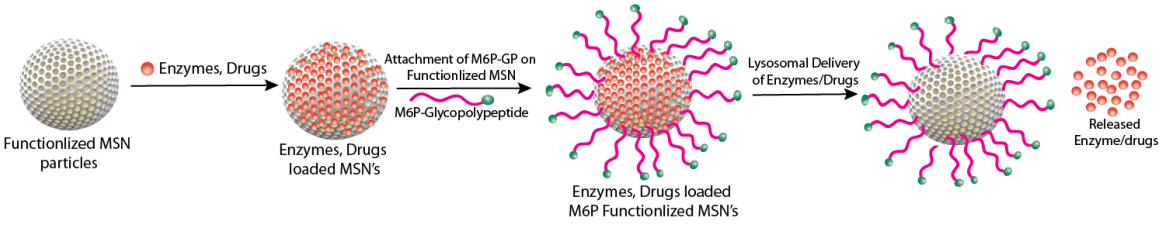

Figure 6.5: Schematic illustration of enzyme/drug-loaded M6P-GP functionalized MSN nanocarrier synthesis.

Thus, M6P-GP-based nanocarriers can be designed by using mesoporous silica nanoparticle (MSN) as template for loading enzymes /drugs, which can be selectively transferred to the lysosomes (Figure 6.5).

6.3 References

(1) Johnson, I. *Histochem. J.* **1998**, *30*, 123–140.

(2) Terai, T.; Nagano, T. *Curr. Opin. Chem. Biol.* **2008**, *12*, 515–521.

(3) Ueno, T.; Nagano, T. *Nat. Methods.* **2011**, *8*, 642–645.

(4) Basabe-Desmonts, L.; Reinhoudt, D. N.; Crego-Calama, M. *Chem. Soc. Rev.* **2007**, *36*, 993–1017.

(5) Kulkarni, S. J. *2011 Int. Conf. Biosci. Biochem. Bioinforma.* **2011**, *5*, 443–446.

(6) Long, F.; Zhu, A.; Shi, H.; Wang, H.; Liu, J. *Sci. Rep.* **2013**, *3*, 2308.

(7) Guo, Z.; Kim, G.-H.; Yoon, J.; Shin, I. *Nat. Protoc.* **2014**, *9*, 1245–1254.

(8) Isailovic, D.; Xu, Y.; Copus, T.; Saraswat, S.; Nauli, S. M. *Appl. Spectrosc.* **2011**, *65*, 575–583.

(9) Das, S.; Sharma, D. K.; Chakrabarty, S.; Chowdhury, A.; Gupta S. S. *Langmuir* **2015**, *31*, 3402−3412.

(10) Pandey, B.; Mahato, J.; Cotta, K. B.; Das, S.; Sharma, D. K.; Gupta S. S.; Chowdhury, A. *ACS Omega*, **2016**, *1*, 600-612.

(11) Hu, J. M.; Liu, S. Y. *Macromolecules*, **2010**, *43*, 8315–8330

(12) Li, C. H.; Hu, J. M.; Liu, S. Y. *Soft Matter*, **2012**, *8*, 7096–7102.

(13) Langer, R.; Tirrell, D. A.; *Nature*, **2004**, *428*, 487–492.

(14) Xu, H.; Wang, C.; Wang, C. L.; Zoval, J.; Madou, M. *Biosens. Bioelectron.*, **2006**, *21*, 2094–2099.

(15) Lee, Y.; Kataoka, k.; *Soft Matter*, **2009**, *5*, 3810–3817.

(16) Dizaj, S.M.; Jafari, S.; Khosroushahi, A.Y. *Nanoscale Res. Lett*. **2014**, *9*, 252–261.

(17) Vancoillie, G.; Hoogenboom, R. *Sensors* **2016**, *16*, 1736-1754.

(18) Wang, B.; Ma, R.; Liu, G.; Li, Y.; Liu, X.; An, Y.; Shi, L. *Langmuir* **2009**, *25*, 12522-12528.

(19) Matsumoto, A.; Ikeda, S.; Harada, A.; Kataoka, K. *Biomacromolecules* **2003**, *4*, 1410-1416.

(20) Balakrishnan, B.; Jayakrishnan, A. *Biomaterials* **2005**, *26*, 3941–3951.

(21) Desnick, J. R.; Schuchman, H. E. *Nat. Rev. Genet*. **2002**, *3*, 954−966.

(22) Futerman, H. A.; van Meer, G. *Nat. Rev. Mol. Cell Biol.* **2004**, *5*, 554−565.

(23) Ghosh, P.; Dahms, M N.; Kornfeld, S. *Nat. Rev. Mol. Cell Biol.* **2003**, *4*, 202-212.

(24) Das, S.; Parekh, N.; Mondal, B.; and Gupta, S. S. *ACS Macro Lett.*, **2016**, *5*, 809–813.

Appendix

Appendix A (Chapter 2)

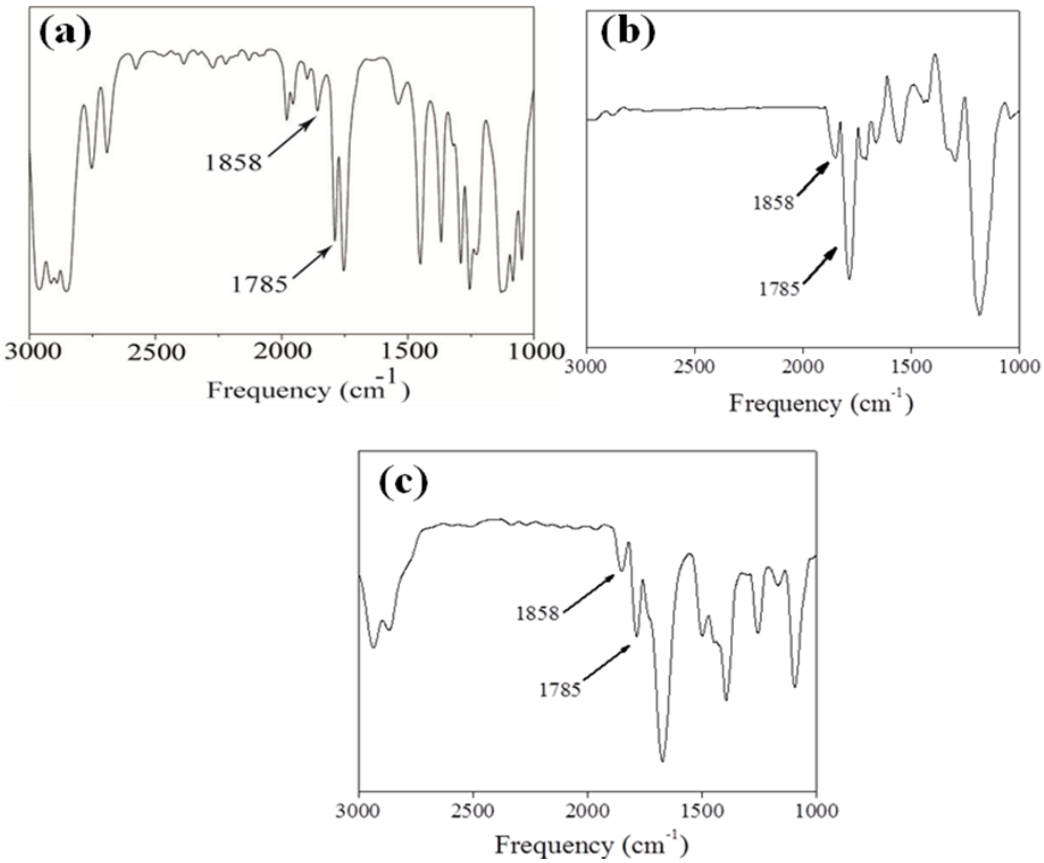

Figure A1. FTIR Spectra of (a) per-*O*-acetylated-D-glucose-*L*-lysine NCA (b) N-ε-Trifluoroacetyl-*L*-lysine NCA (c) γ-Benzyl-*L*-glutamate NCA: two unsymmetrical anhydride stretching of NCA ring at 1858 and 1785 cm^{-1} are characteristics of NCA formation.

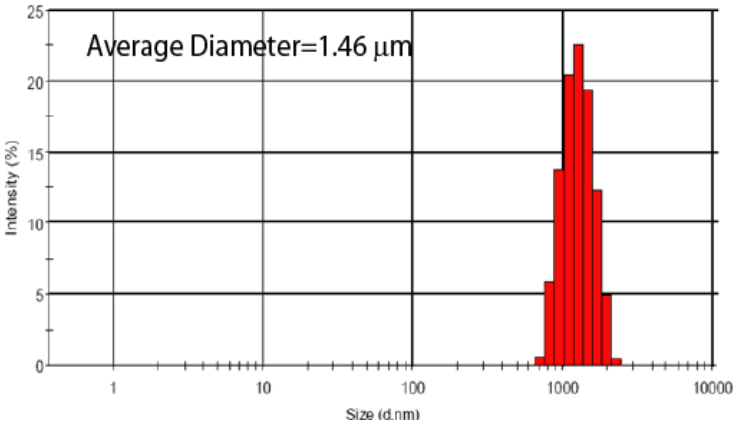

Figure A2: DLS measurement of GP-PICsomes formed by the self assembly of block aniomer (PEG_{2k}-PLG_{100}) and block catiomer (GP_{20}-PLL_{100}) in 50 mM phosphate buffer (pH 7.4).

Average diameter of GP-PICsomes (µm) with respect to time (days)						
NaCl Concentration	**I**	**II**	**III**	**IV**	**V**	**VI**
Without NaCl	1.5	1.46	1.43	1.43	1.40	1.36
75 mM	1.39	1.32	1.09	0.8	0.74	0.68
150 mM	0.56	0.34	-	-	-	-

Figure A3: Changes in the size of GP-PICsomes with increasing salt concentration.

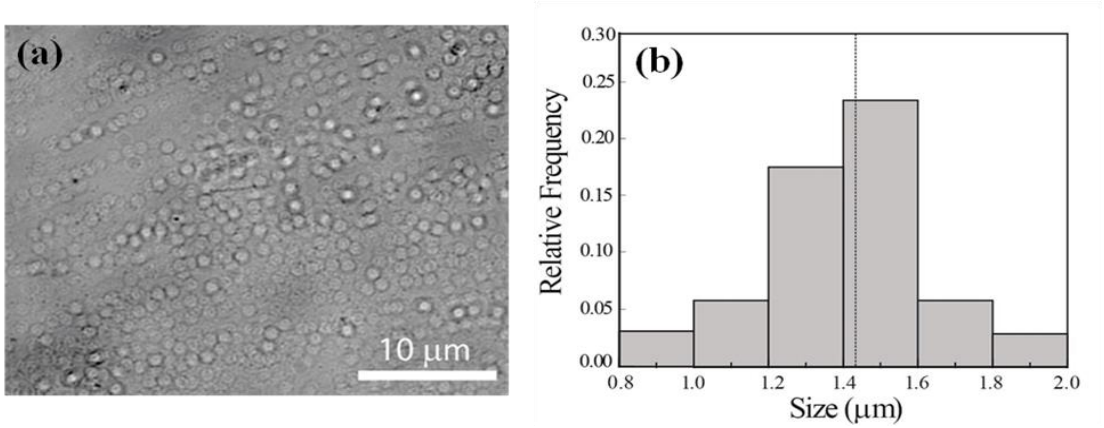

Figure A4: Optical microscopic Image and corresponding size distribution figure of GP-PICsomes (Average Diameter=1.43µm).

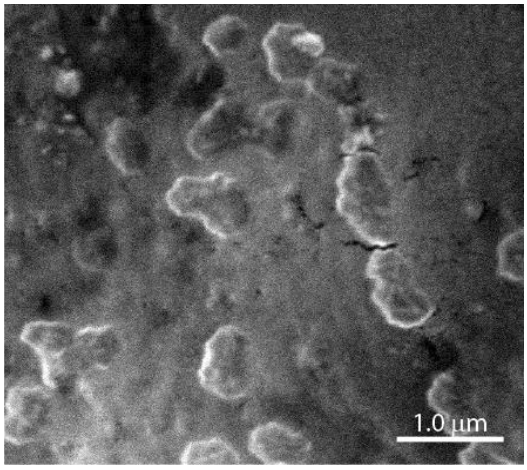

Figure A5: SEM image of aggregates formed by the self-assembly of homoaniomer (Hx-PLG_{100}) and block catiomer (GP_{20}-PLL_{100}) in 50 mM phosphate buffer (pH 7.4).

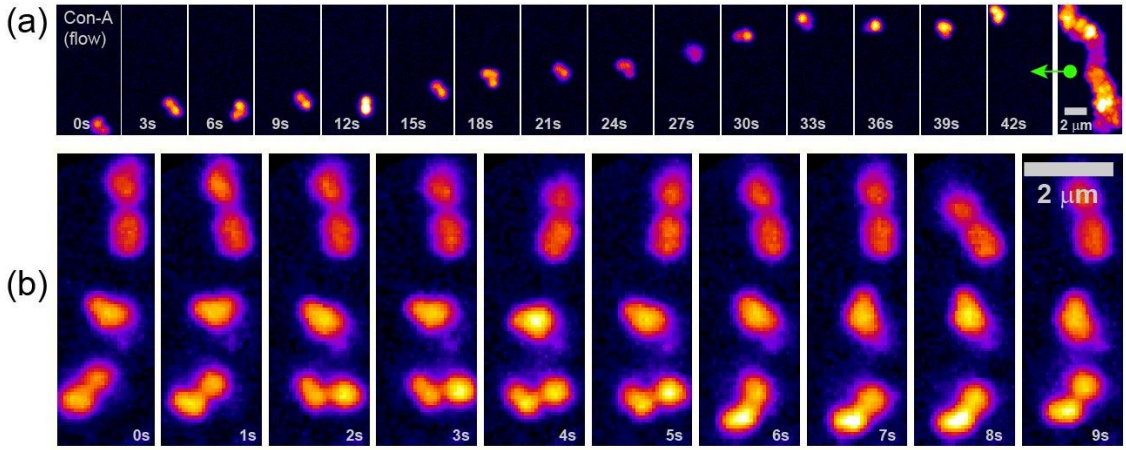

Figure A6: Fluorescence microscopy of GP-PICsomes (a) Dynamics of a small RhB-GP-PICsome aggregate in the presence of buffer containing 0.5mg/ml Con-A (weak unidirectional flow) represented by fifteen single-frame sequential snapshots along with its Maximum Projection image (right panel) of the same area. (b) Hindered motion of surface bound (partially anchored) RhB-GP-PICsome aggregates over a time span of 9s.

Figure A7: Captions for the Movies:

Figure A7 Movie 1: Wide field movie of a single RhB-GP-PICsome diffusing randomly in buffer solution. The movie is played at 10 fps although it was acquired at ~3.3 fps and the area shown is identical to that in Figure 2.12a (top panel).
https://pubs.acs.org/doi/suppl/10.1021/acsomega.6b00142/suppl_file/ao6b00142_si_002.avi

Figure A7 Movie 2: Random motion of another single Rh labelled GP-PICsome in buffer solution. The movie is played at 10 fps although it was acquired at 3.3 fps and the area shown is identical to that in Figure 2.12a (bottom panel).

https://pubs.acs.org/doi/suppl/10.1021/acsomega.6b00142/suppl_file/ao6b00142_si_003.avi

Figure A7 Movie 3: Movie of RhB-GP-PICsome in presence of Con-A, showing a small cluster undergoing tumbling motion in buffer solution. The movie is played at 10 fps although it was acquired at ~3.3 fps and the area shown is identical to that in Figure 2.12b.

https://pubs.acs.org/doi/suppl/10.1021/acsomega.6b00142/suppl_file/ao6b00142_si_004.avi

Figure A7 Movie 4: Small RhB-GP-PICsome aggregate in presence of unidirectional buffer flow. The movie is played at 10 fps although it was acquired at ~3.3 fps and the area shown is identical to that in Figure 2.12c.

https://pubs.acs.org/doi/suppl/10.1021/acsomega.6b00142/suppl_file/ao6b00142_si_005.avi

Figure A7 Movie 5: The dynamics of a larger RhB-GP-PICsome aggregate in the presence of a buffer flow. The movie is played at 10 fps although it was acquired at ~3.3 fps and the area shown is identical to that in Figure 2.12d.

https://pubs.acs.org/doi/suppl/10.1021/acsomega.6b00142/suppl_file/ao6b00142_si_006.avi

Figure A7 Movie 6: Movie of RhB-GP-PICsome aggregate-clusters while changing the Z focus during movie collection. The movie is played at 10 fps although it was acquired at ~6.6 fps and the area shown is a section of the time averaged image Figure 2.10f, from frame 30 to 50. The movie shown here is a 17.5 micron X 17.5 micron area of the main movie with co-ordinates (24.50, 4.9). A small section was selected as the entire movie had a very large size.

https://pubs.acs.org/doi/suppl/10.1021/acsomega.6b00142/suppl_file/ao6b00142_si_007.avi

Figure A7 Movie 7: Deaggregation of a RhB GP-PICsome aggregate upon addition of excess mannose. The movie is played at 10 fps although it was acquired at ~3.3 fps and the area shown is identical to that in Figure 2.13a.

https://pubs.acs.org/doi/suppl/10.1021/acsomega.6b00142/suppl_file/ao6b00142_si_008.avi

Figure A7 Movie 8: Dynamics of a RhB-GP-PICsome aggregate-clusters incubated with excess galactose depicting its swivel motion by intermittent buffer flow. The movie is played at 10 fps although it was acquired at ~3.3 fps and the area shown is identical to that in Figure 2.13b (right panel).

https://pubs.acs.org/doi/suppl/10.1021/acsomega.6b00142/suppl_file/ao6b00142_si_009.avi

^{1}H NMR, ^{13}C and DEPT Spectra of the compounds

(* peak in NMR indicates residual solvents peak)

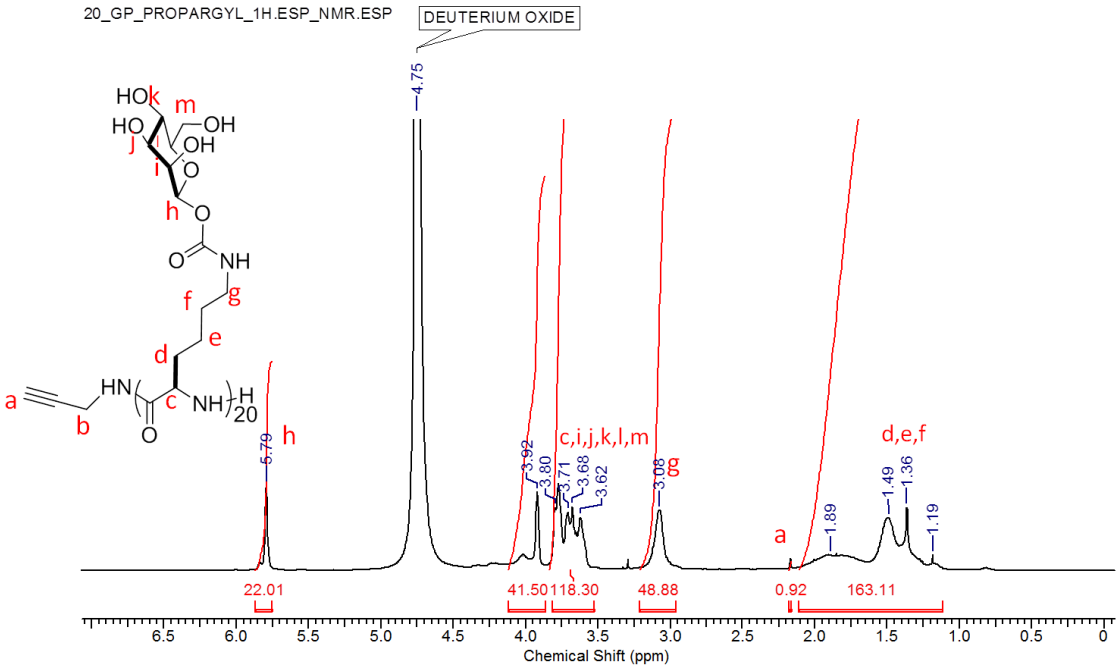

Figure A8: ^{1}H NMR ($CDCl_3$, 400 MHz) Spectrum of Pr-GP_{20} **(1d)**

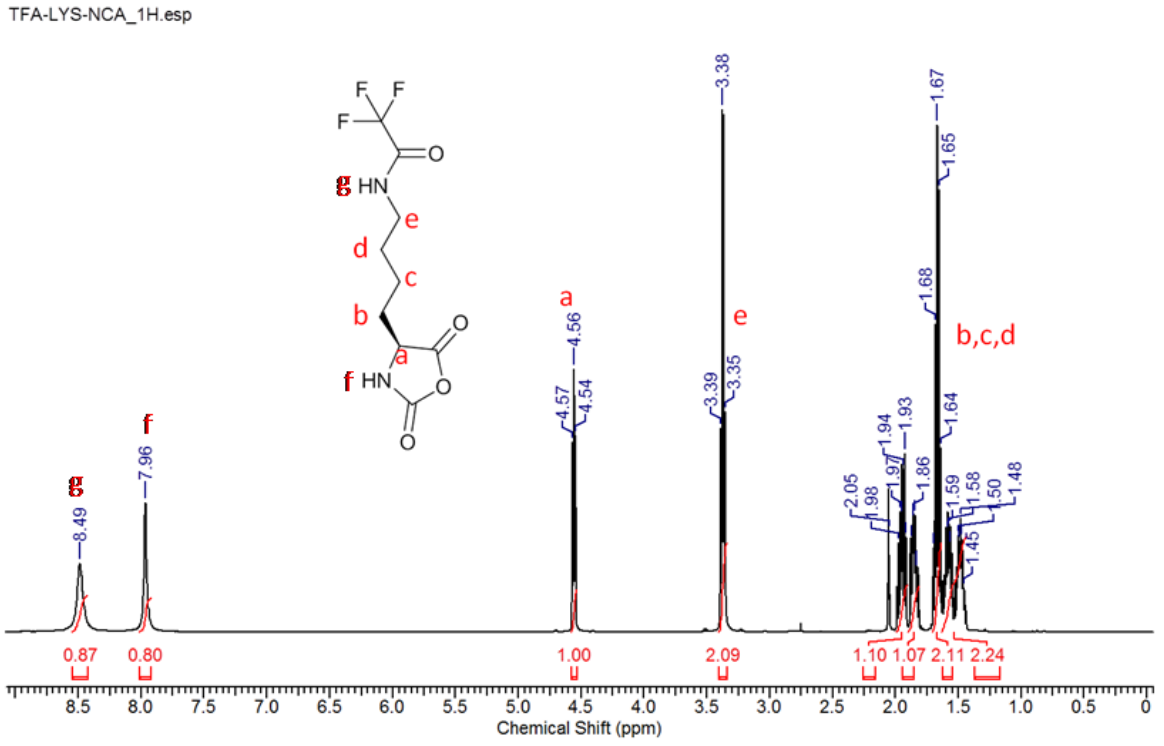

Figure A9: ^{1}H NMR ($CDCl_3$, 500.13 MHz) Spectrum of TFA-Lys-NCA **(2b)**

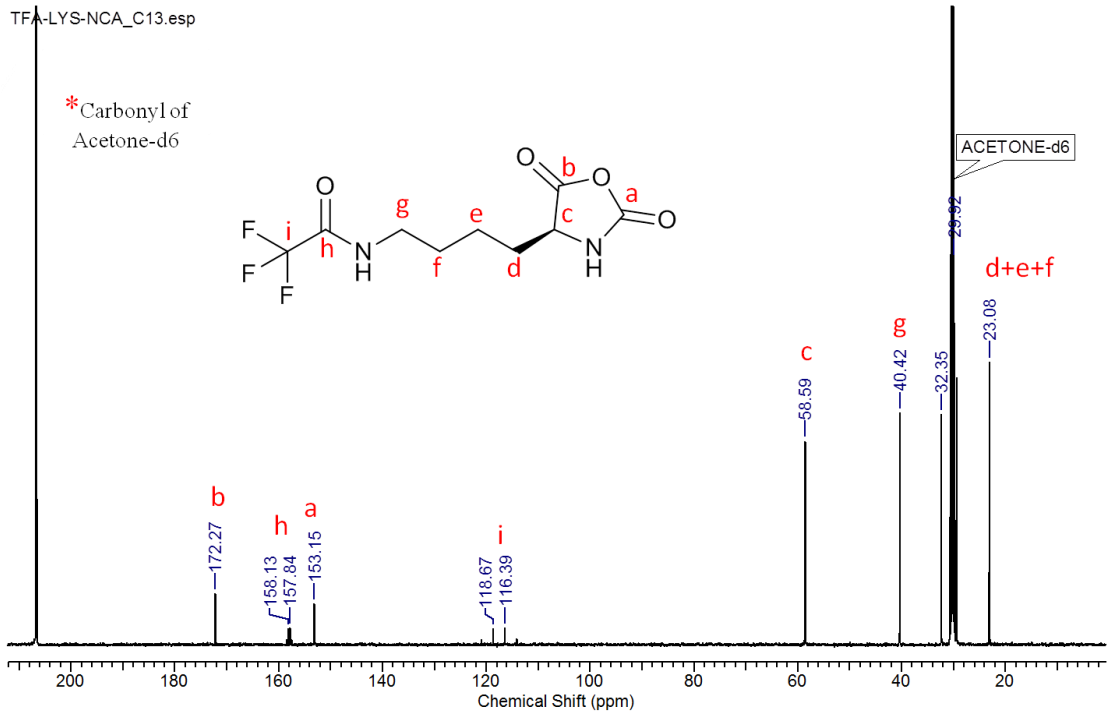

Figure A10: C^{13}NMR ($CDCl_3$, 125.76 MHz) Spectrum of TFA-Lys-NCA **(2b)**

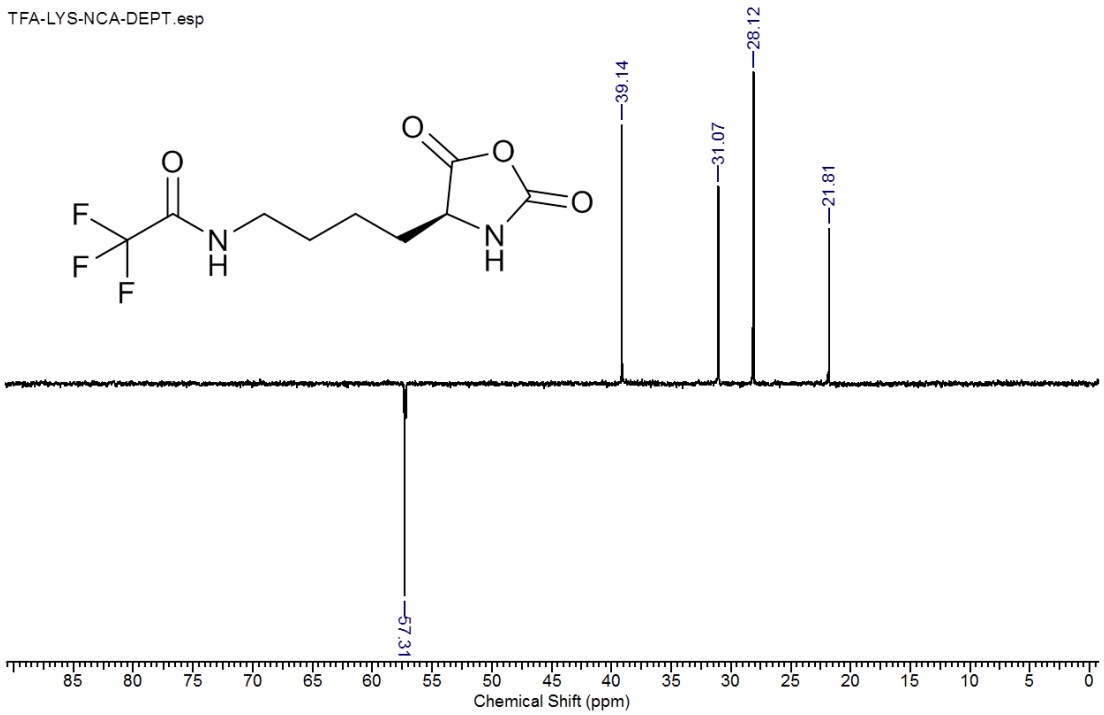

Figure A11: DEPT NMR ($CDCl_3$, 125.76 MHz) TFA-Lys-NCA **(2b)**

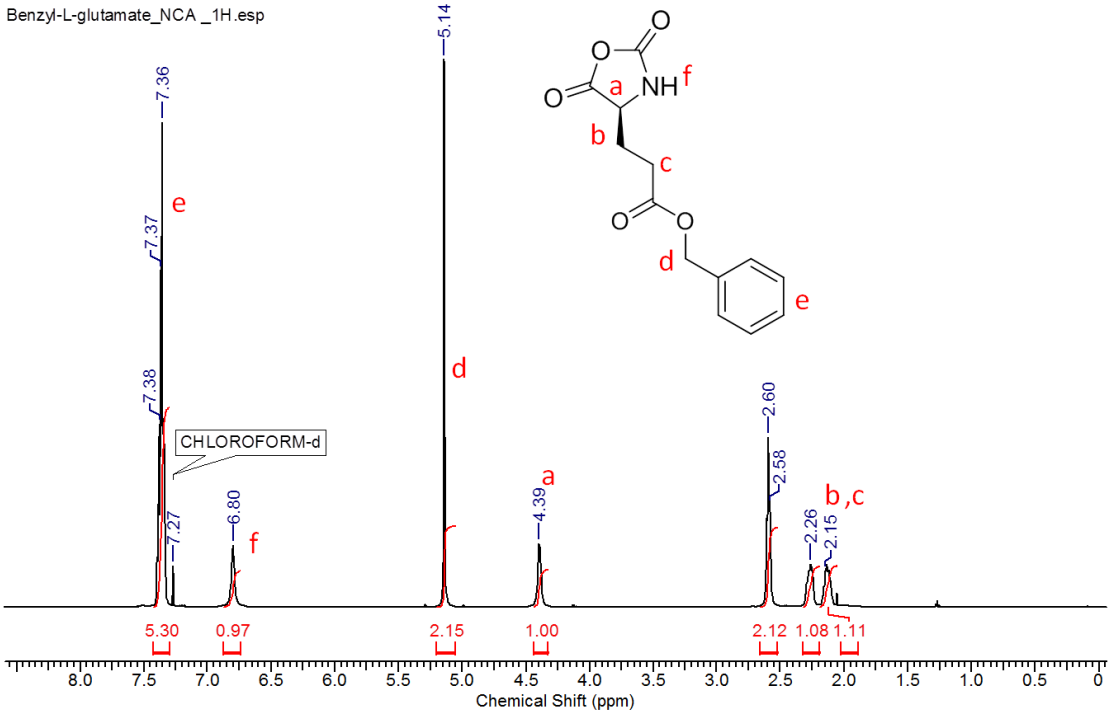

Figure A12: ^{1}H NMR ($CDCl_3$, 500.13 MHz) Spectrum of Bn-Glu-NCA **(3a)**

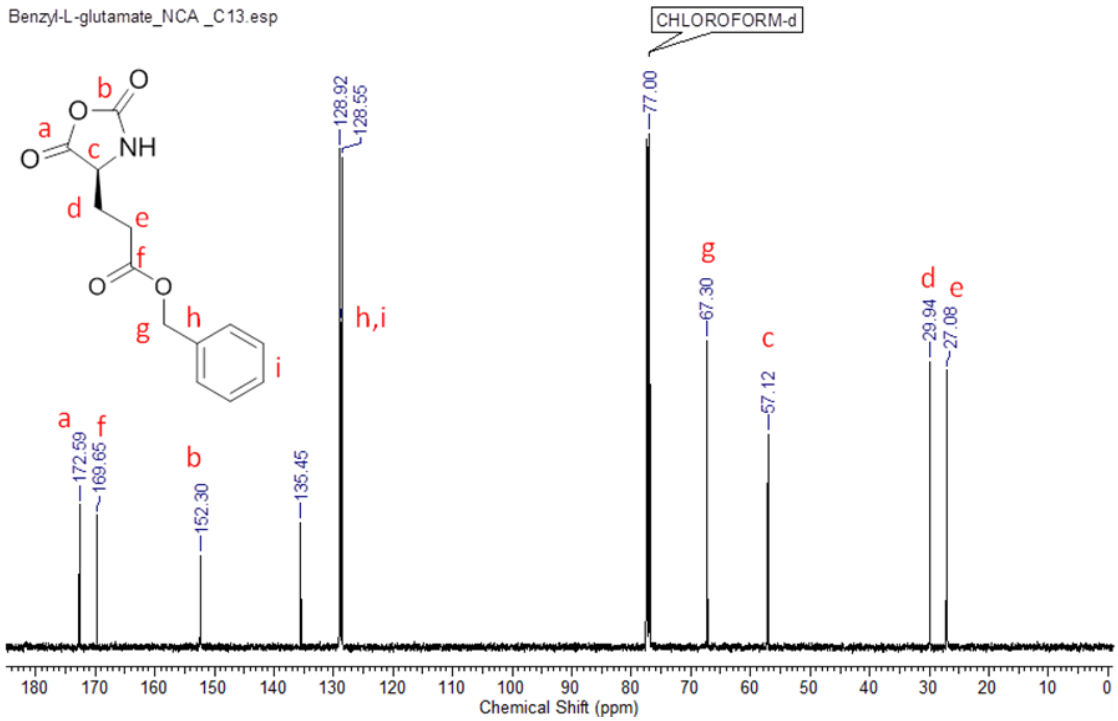

Figure A13: C^{13}NMR ($CDCl_3$, 125.76 MHz) Spectrum of Bn-Glu-NCA **(3a)**

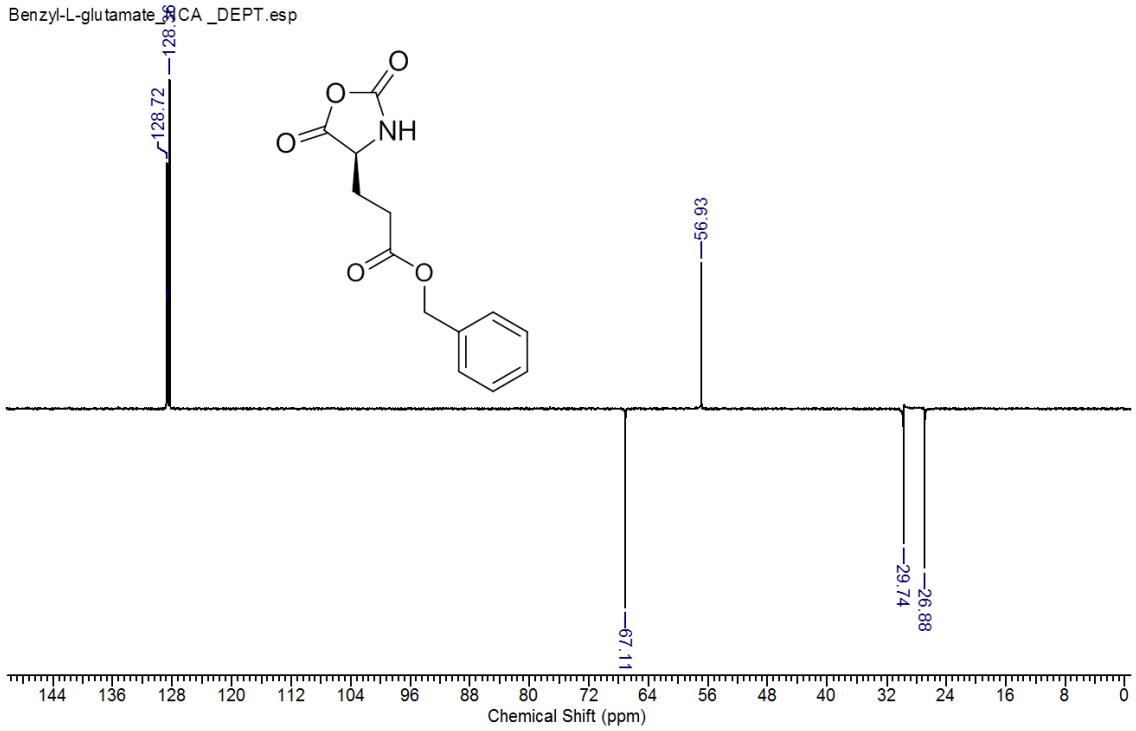

Figure A14: DEPT NMR ($CDCl_3$, 125.76 MHz) Bn-Glu-NCA **(3a)**

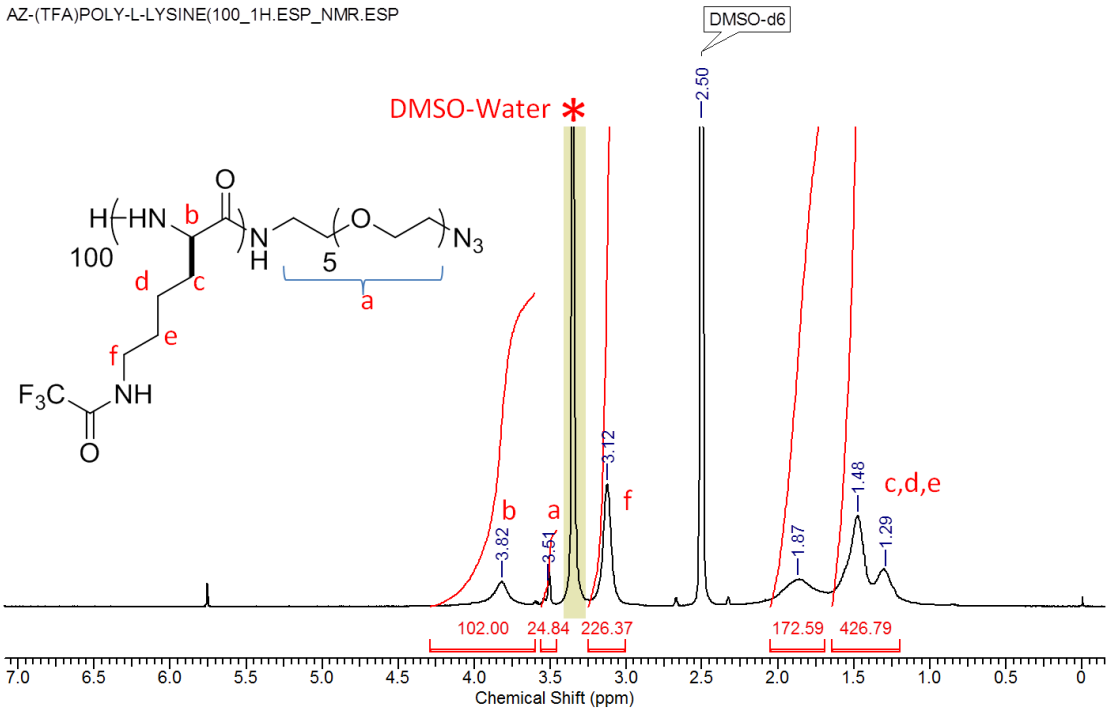

Figure A15: ^1H NMR ($CDCl_3$, 400 MHz) Spectrum of N_3-PLL(TFA)$_{100}$ **(2c)**

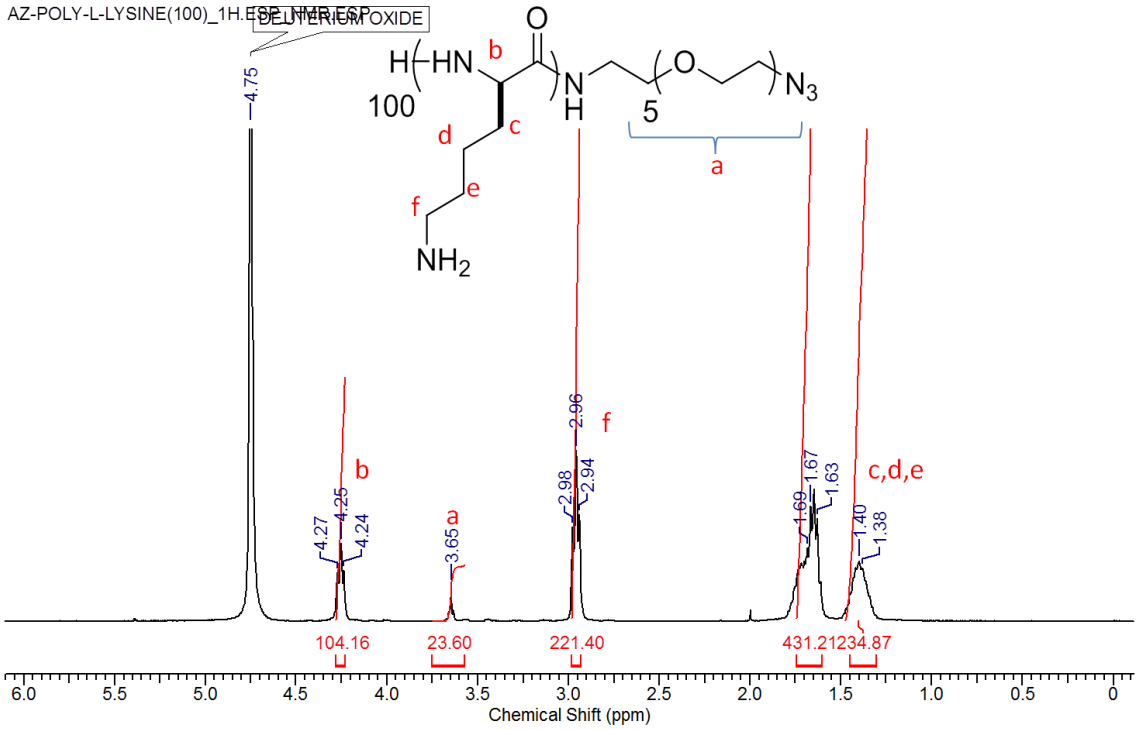

Figure A16: ^{1}H NMR ($CDCl_3$, 400 MHz) Spectrum of N_3-PLL_{100} **(2d)**

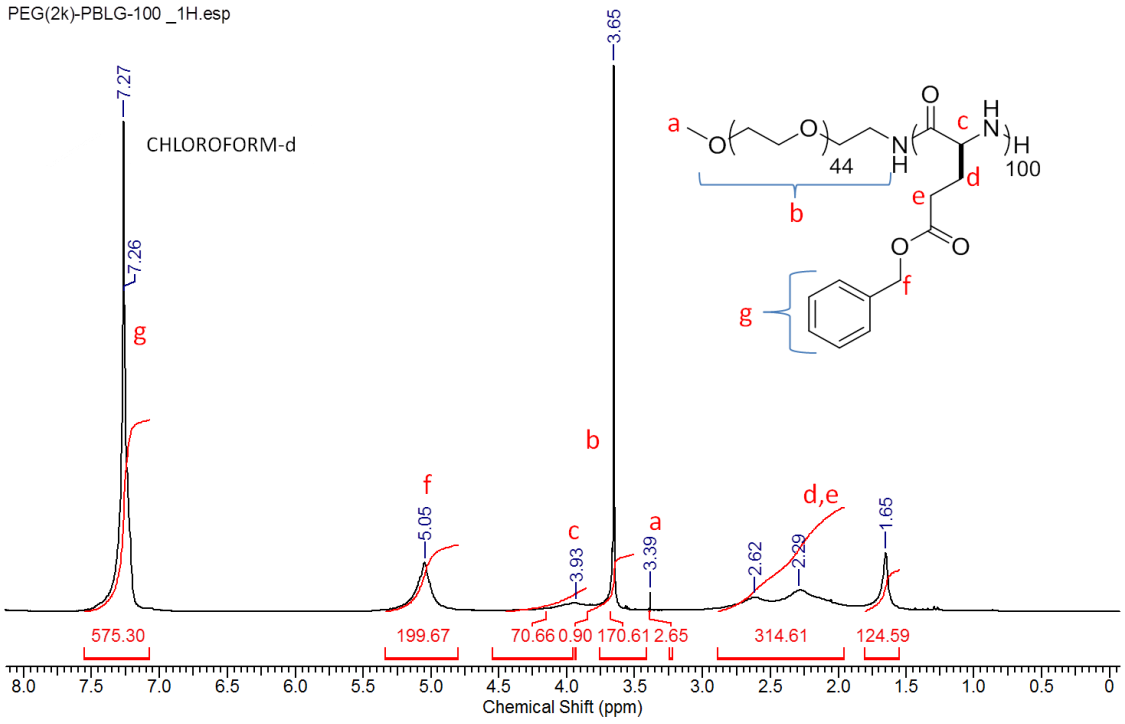

Figure A17: ^{1}H NMR ($CDCl_3$, 400 MHz) Spectrum of PEG_{2k}-$PBLG_{100}$ **(3b)**

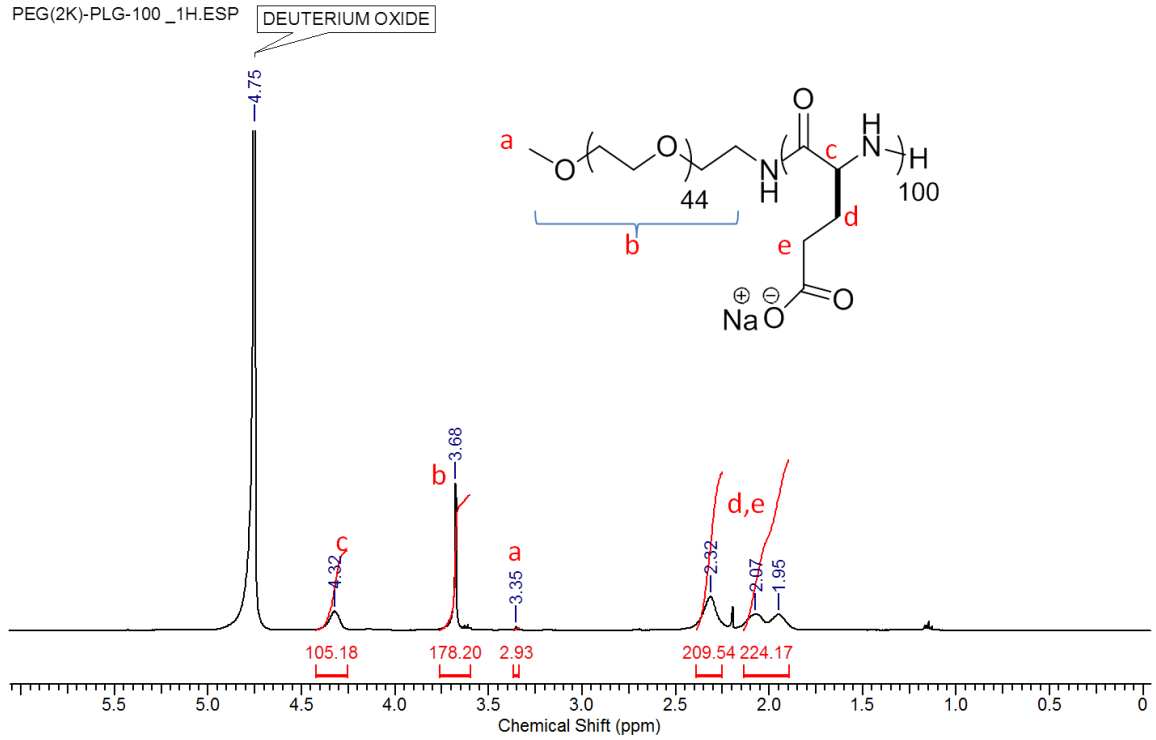

Figure A18: ^{1}HNMR spectrum of the synthesized PEG_{2k}-PLG_{100} **(3c)** block copolymer (aniomer).

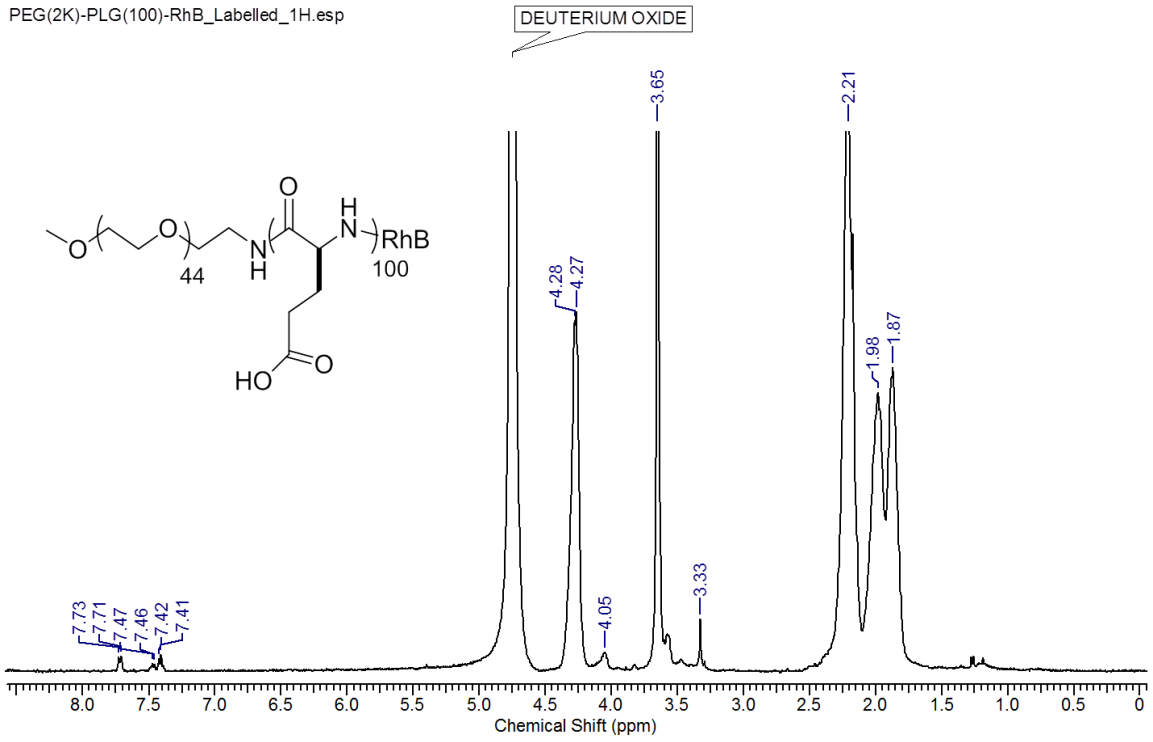

Figure A19: ^{1}H NMR ($CDCl_3$, 400 MHz) Spectrum of RhB-PEG_{2k}-$PBLG_{100}$ **(3d)**

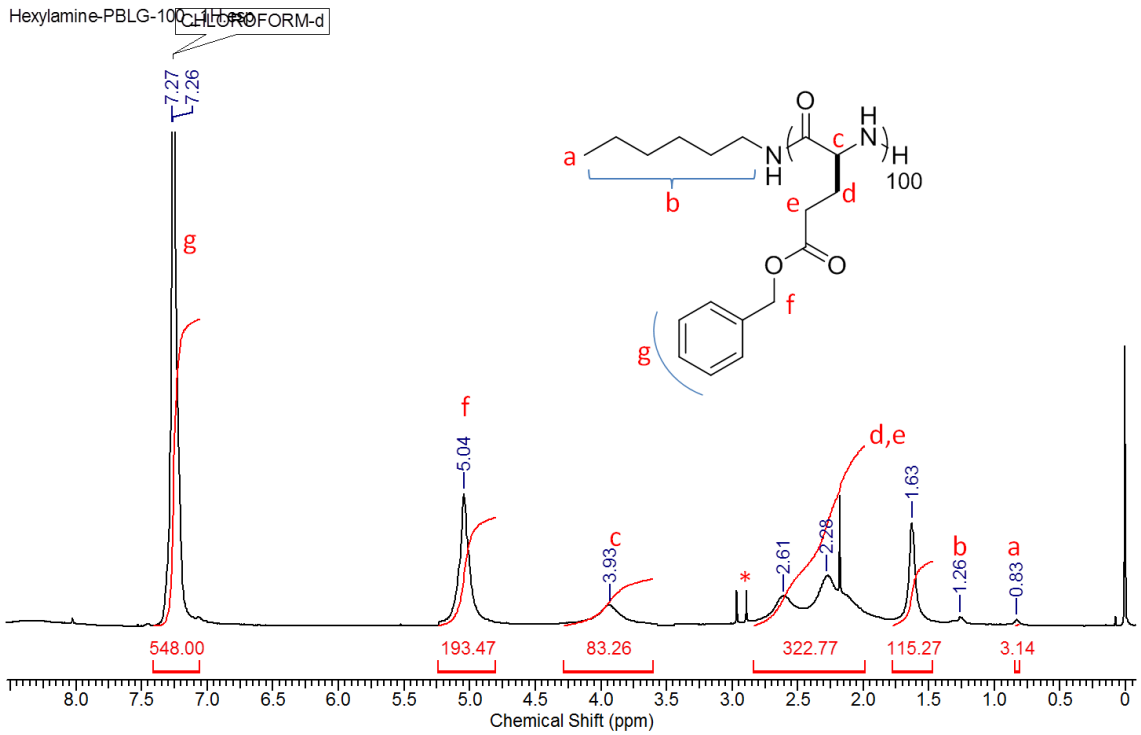

Figure A20: ^{1}H NMR ($CDCl_3$, 400 MHz) Spectrum of Hx-$PBLG_{100}$ **(5a)**

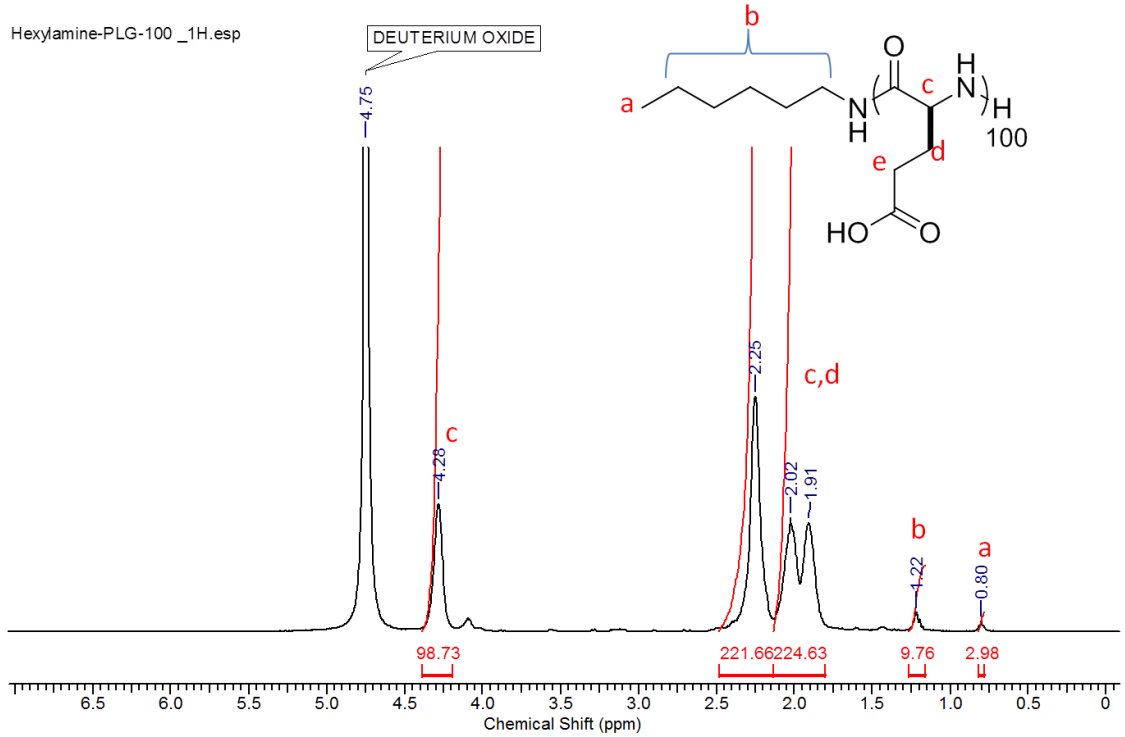

Figure A21: ^{1}H NMR ($CDCl_3$, 400 MHz) Spectrum of Hx-PLG_{100} **(5b)**

Appendix B (Chapter 3)

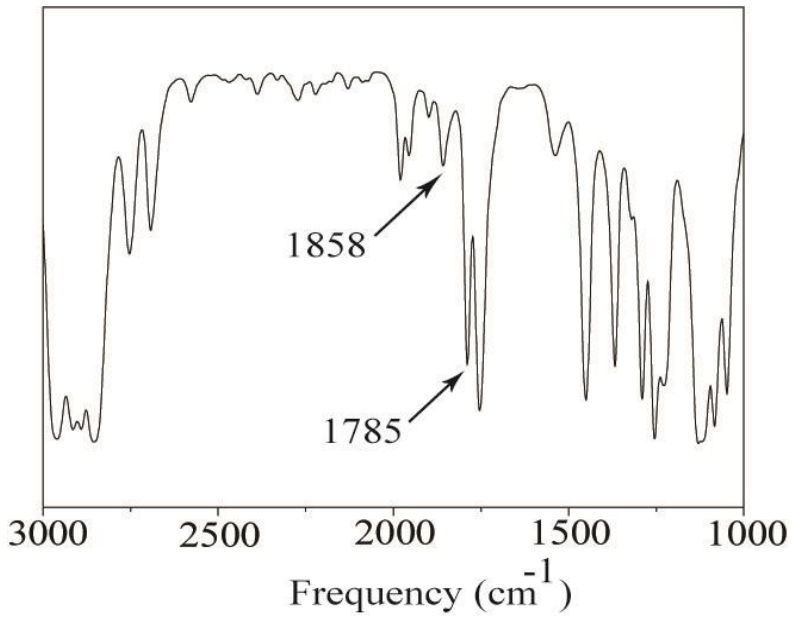

Figure B1: FT-IR Spectra of per-*O*-acetylated-D-galactose-L-lysine NCA shows two unsymmetrical infrared stretching at 1858 and 1785 cm^{-1}.

^{1}H NMR, ^{13}C and DEPT Spectra of the compounds

(* peak in NMR indicates residual solvents peak)

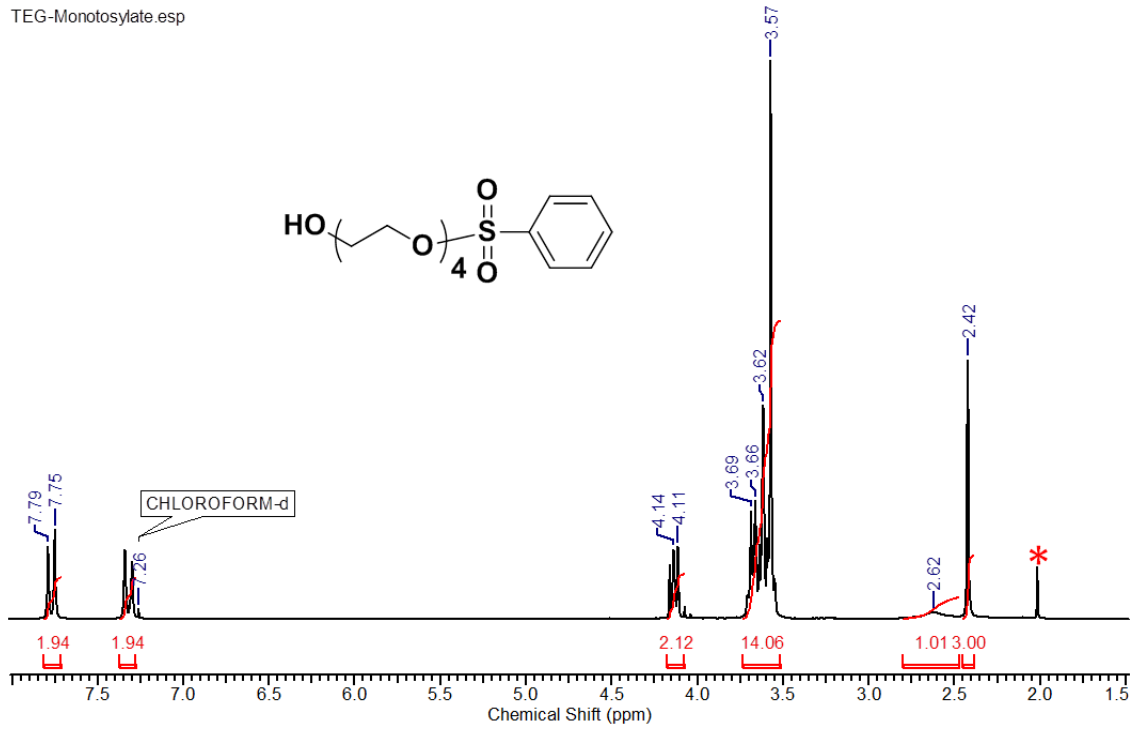

Figure B2: ^{1}H NMR ($CDCl_3$**,** 200 MHz) Spectrum of Tetra ethylene glycol monotosylate **(1)**

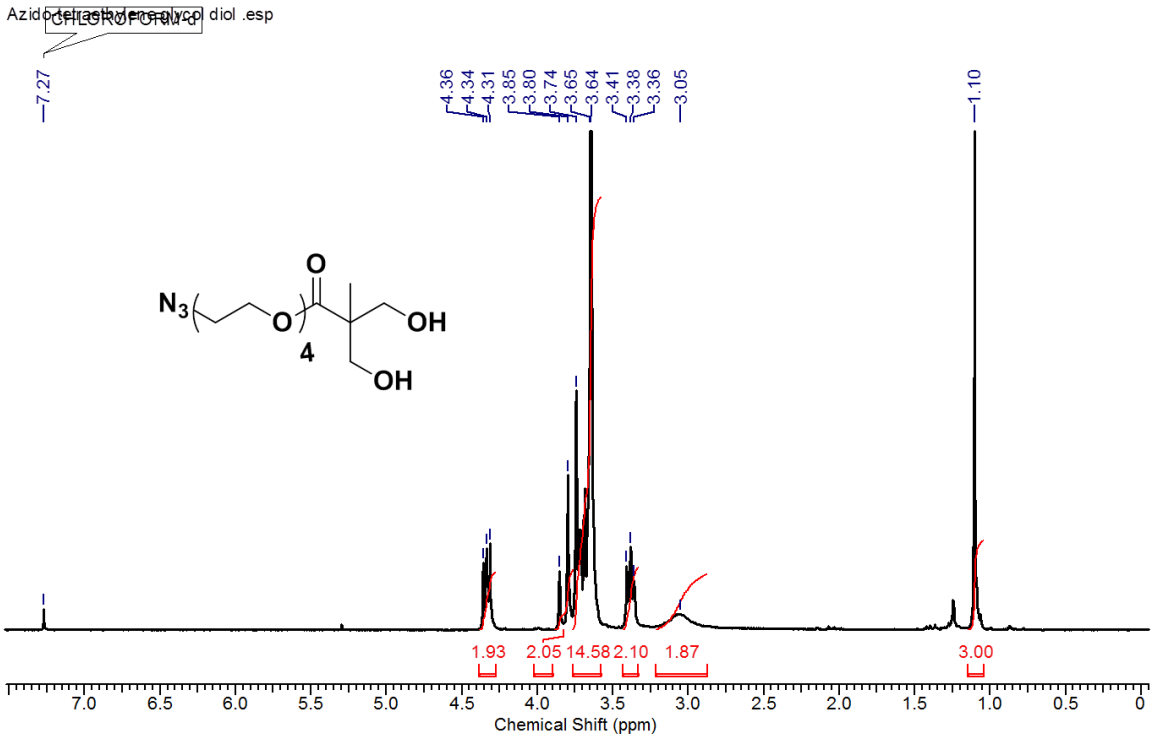

Figure B3: ^{1}H NMR ($CDCl_3$**,** 200 MHz) Spectrum of Azido-tetraethylene glycol diol **(3)**

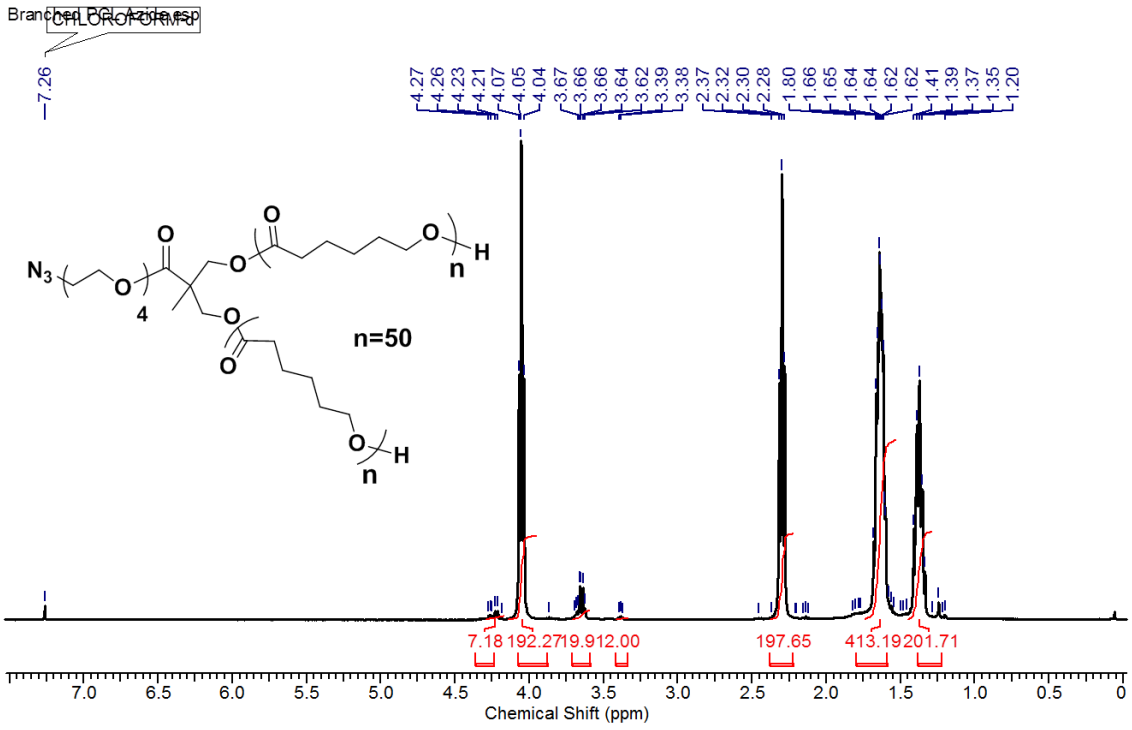

Figure B4: ^{1}H NMR ($CDCl_3$, 400 MHz) Spectrum of $(PCL_{50})_2$-N_3 **(4)**

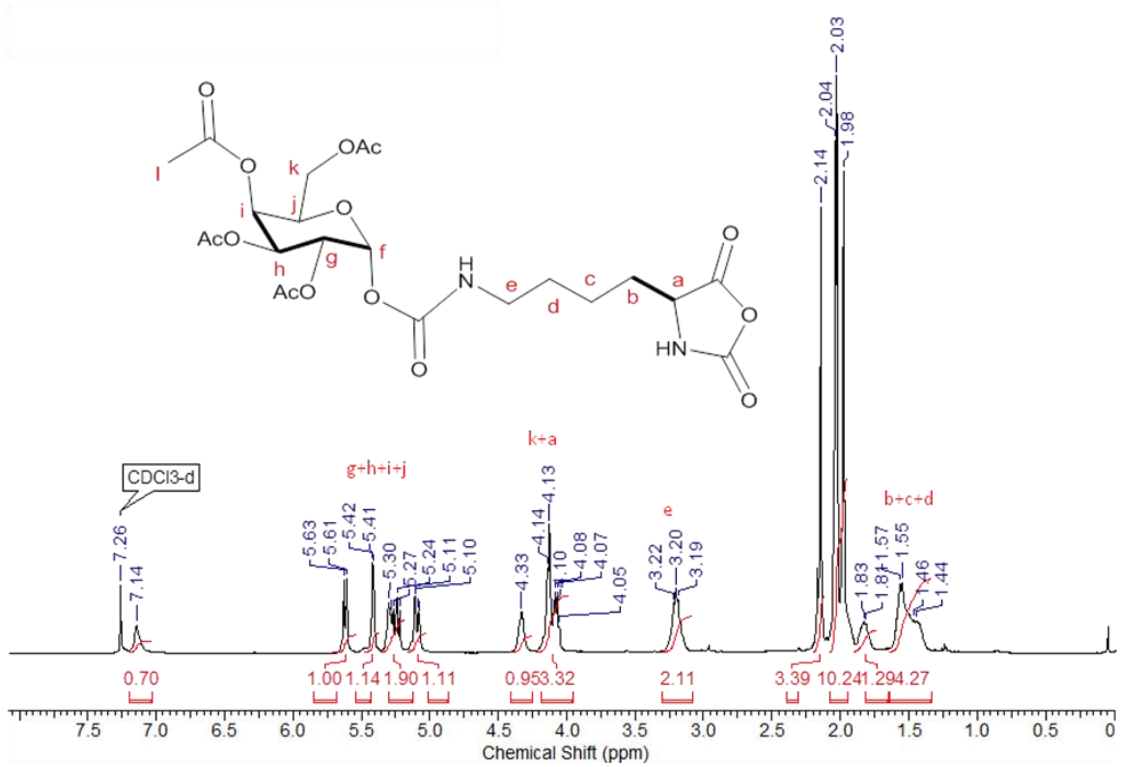

Figure B5: ^{1}H NMR ($CDCl_3$**,** 400 MHz) Spectrum of *galacto*-glyco NCA **(6)**

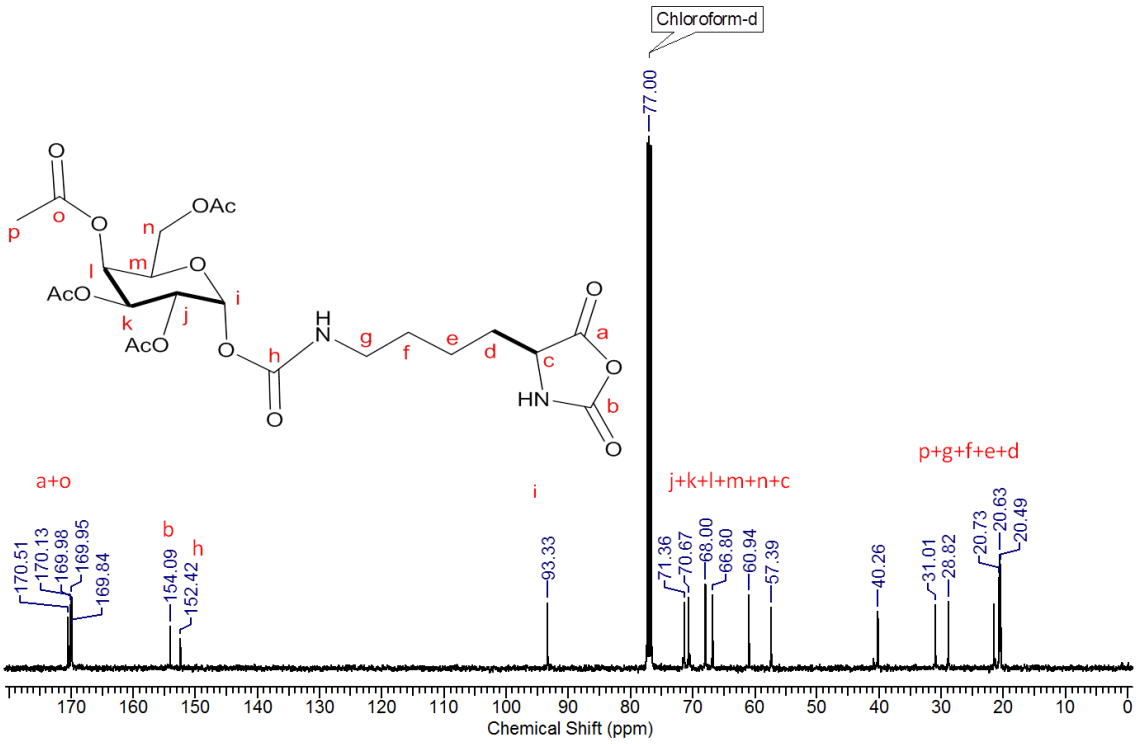

Figure B6: ^{13}C NMR ($CDCl_3$**,** 100 MHz) Spectrum of *galacto*-glyco NCA **(6)**

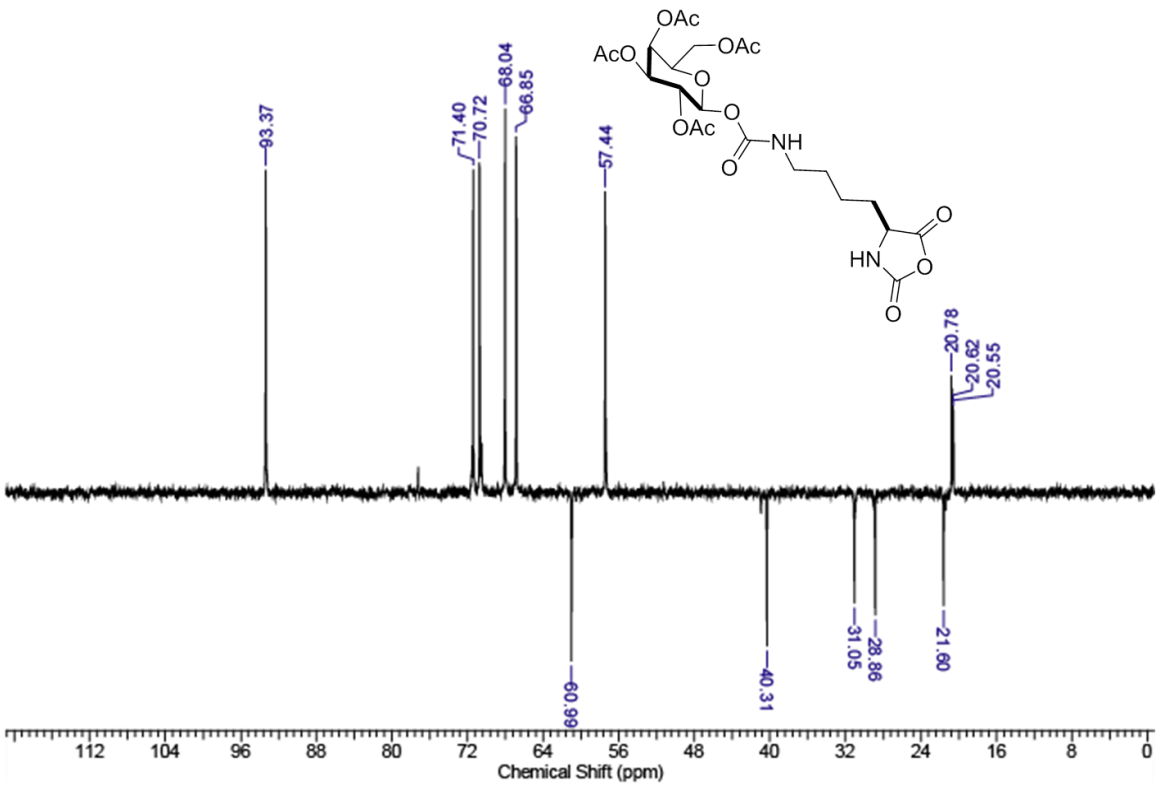

Figure B7: DEPT NMR ($CDCl_3$, 100 MHz) Spectrum of *galacto*-glyco NCA **(6)**

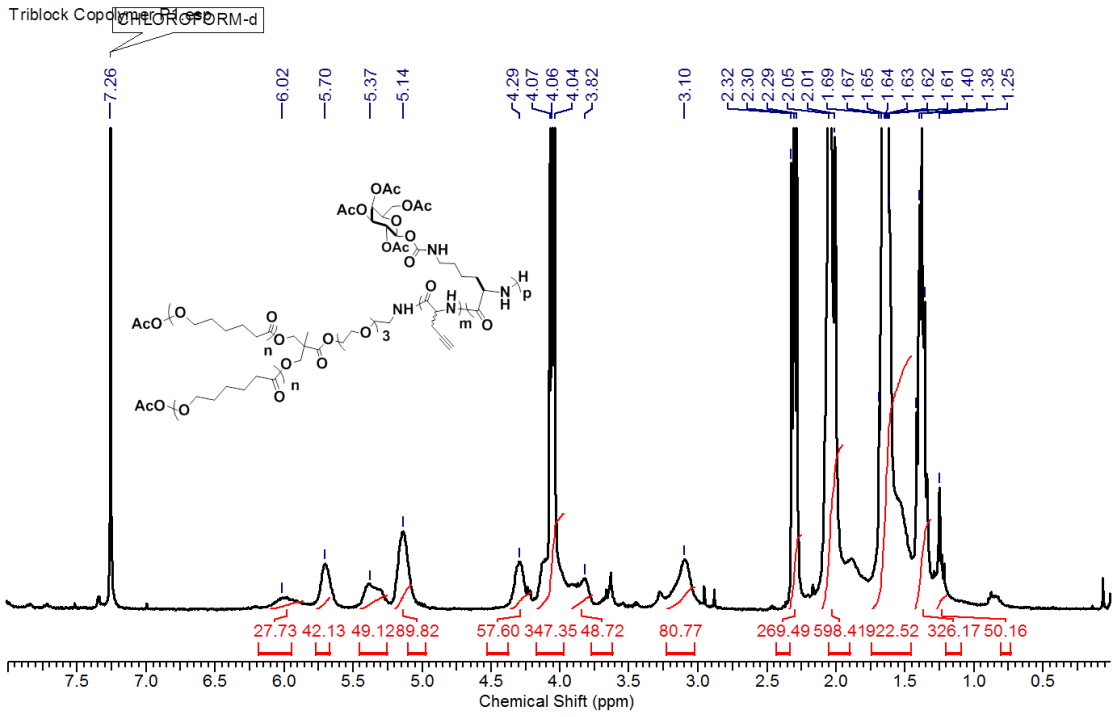

Figure B8 : ^1H NMR ($CDCl_3$, 400 MHz) Spectrum of $(PCL_{50})_2$-b-Pr-gly_6-b-$AcGP_{40}$

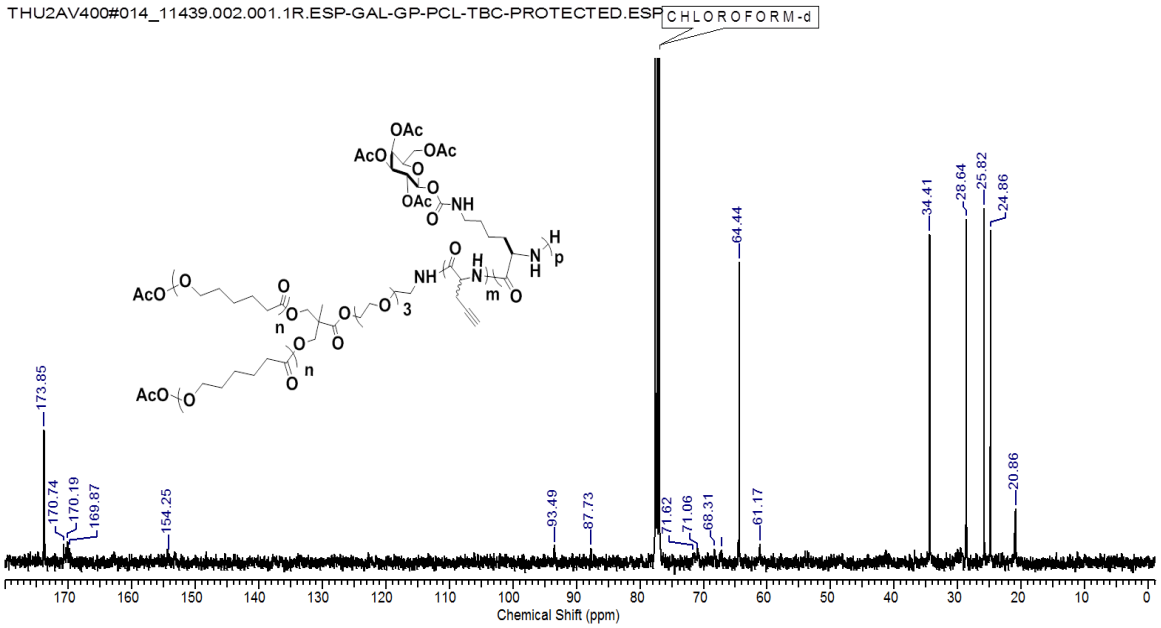

Figure B9: ^{13} C NMR ($CDCl_3$, 100 MHz) Spectrum of $(PCL_{50})_2$-b-Pr-gly_6-b-$AcGP_{40}$

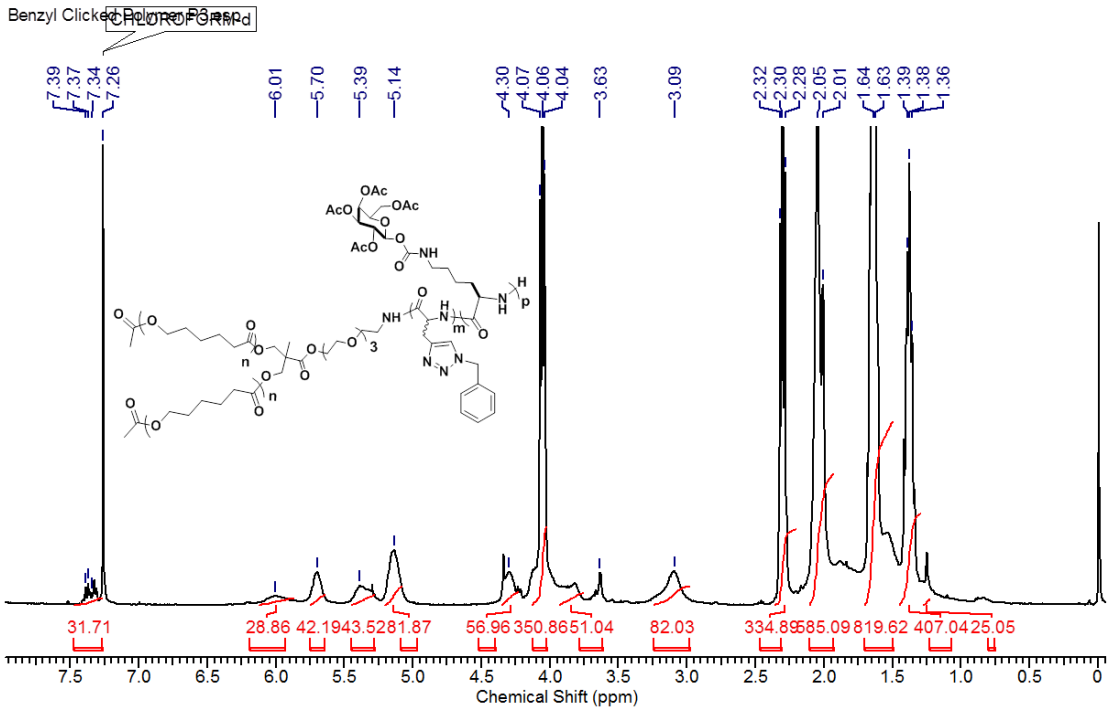

Figure B10: ^{1}H NMR ($CDCl_3$, 400 MHz) Spectrum of benzyl clicked $(PCL_{50})_2$-b-Pr-gly_6-b-$AcGP_{40}$

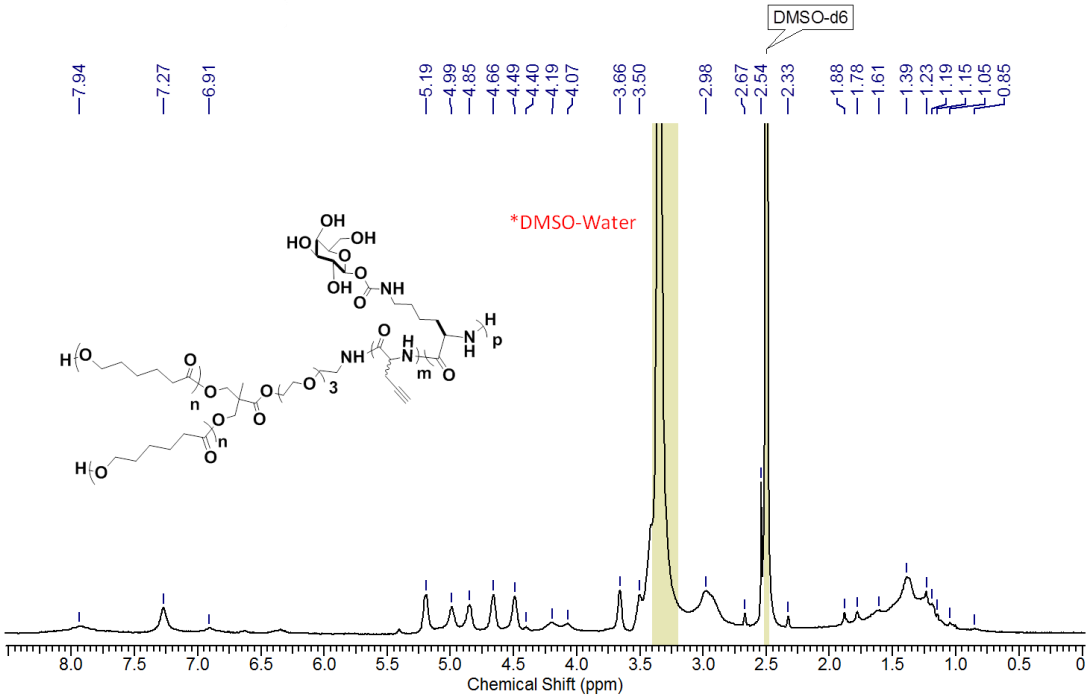

Figure B11: ^{1}H NMR ($CDCl_3$, 400 MHz) Spectrum of Deprotected block copolymer **(P2)**

Appendix C (Chapter 4)

^{1}H NMR, and ^{31}P Spectra of the compounds

(* peak in NMR indicates residual solvents peak)

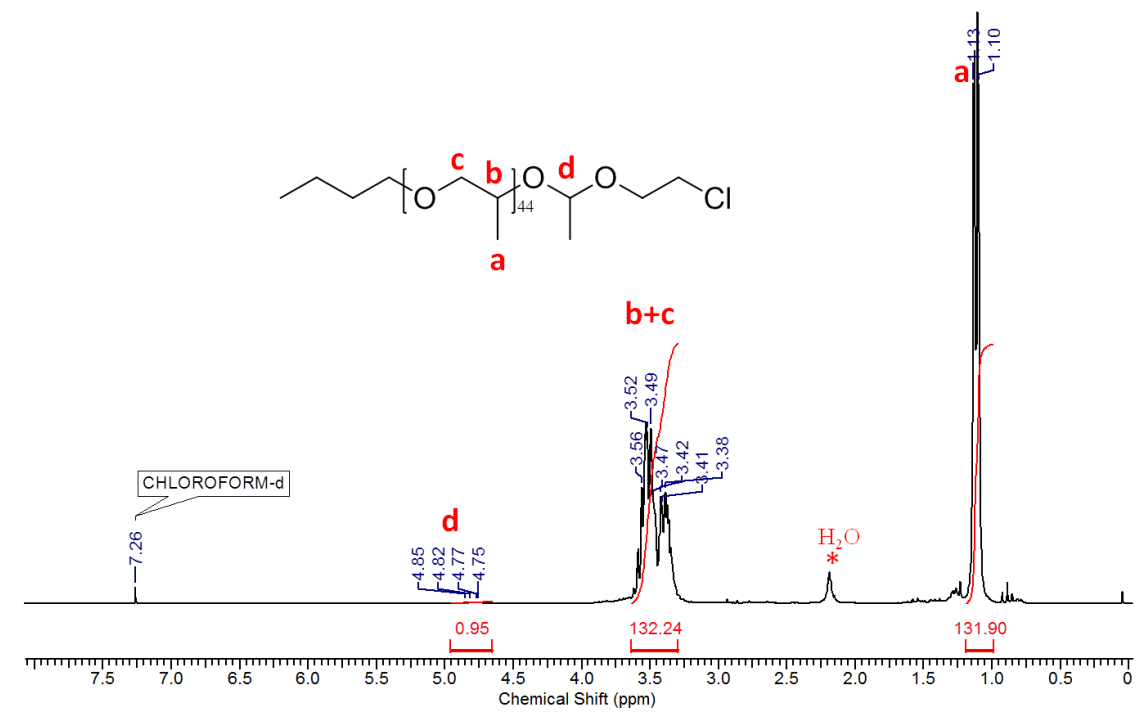

Figure C1: ^{1}H NMR ($CDCl_3$**,** 400 MHz) Spectrum of PPO−Ace-Cl **(1)**

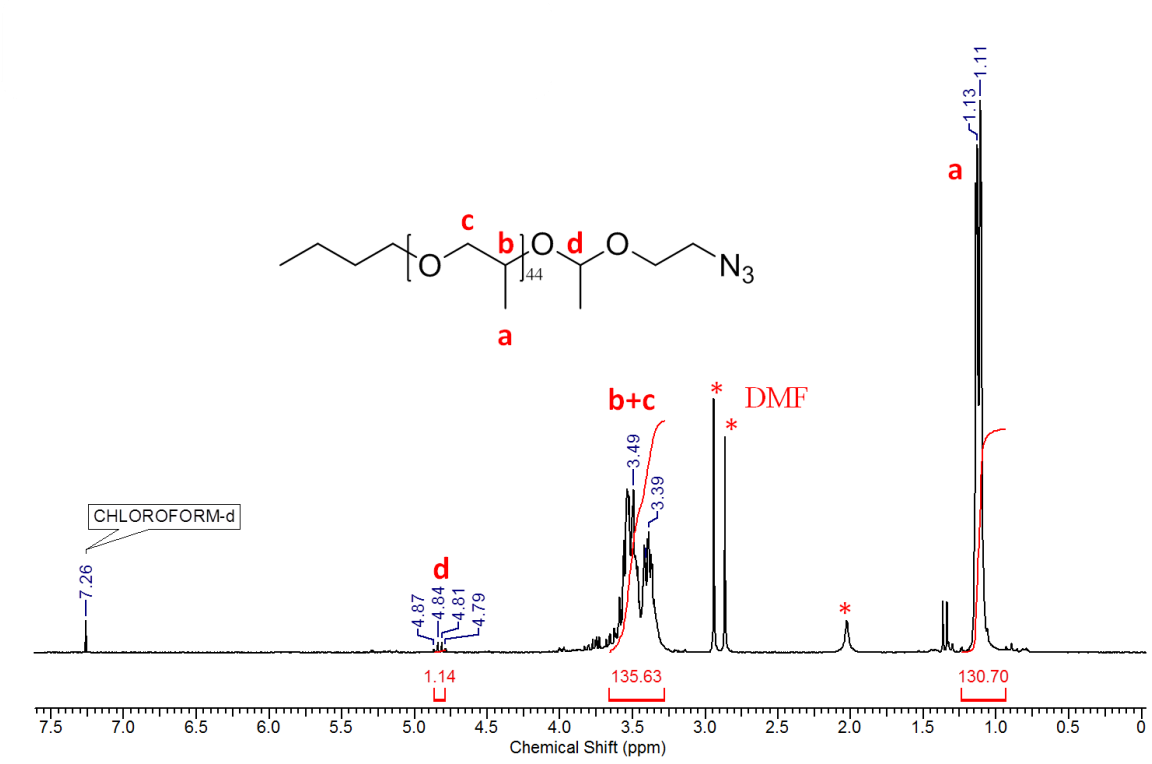

Figure C2: ^{1}H NMR ($CDCl_3$**,** 400 MHz) Spectrum of PPO−Ace-N_3 **(2)**

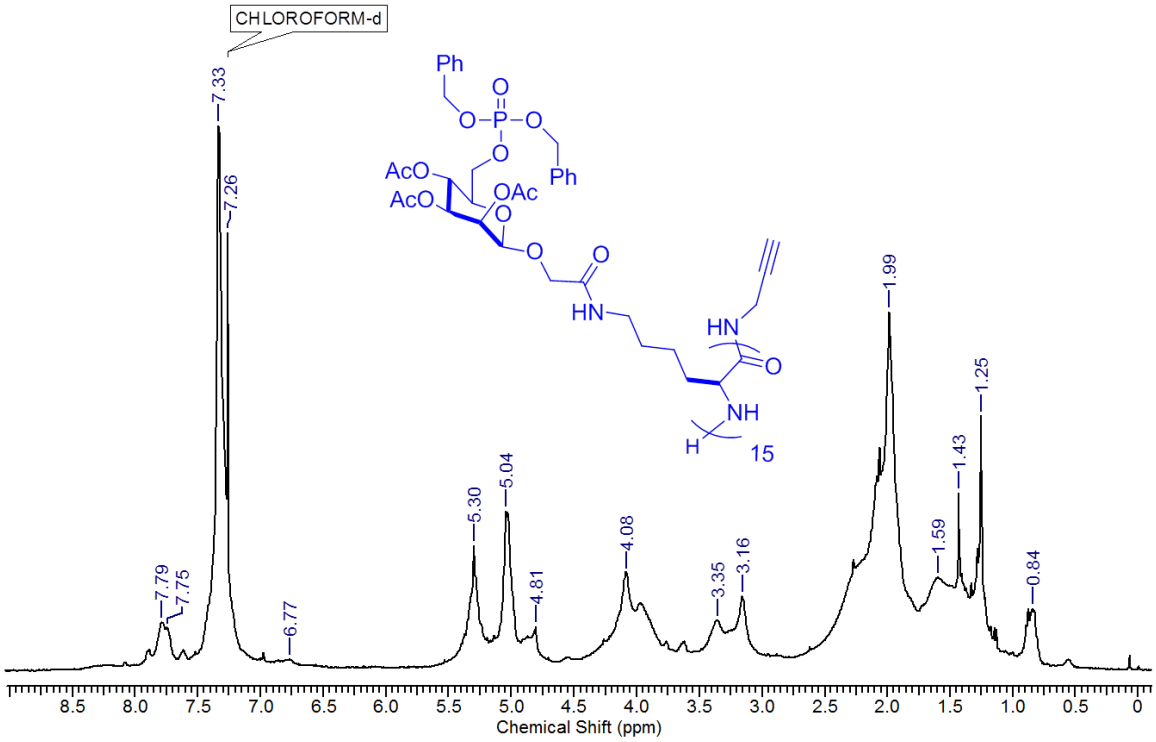

Figure C3: ^{1}H NMR ($CDCl_3$**,** 400 MHz) Spectrum of Pr-15M6P-GP **(3)**

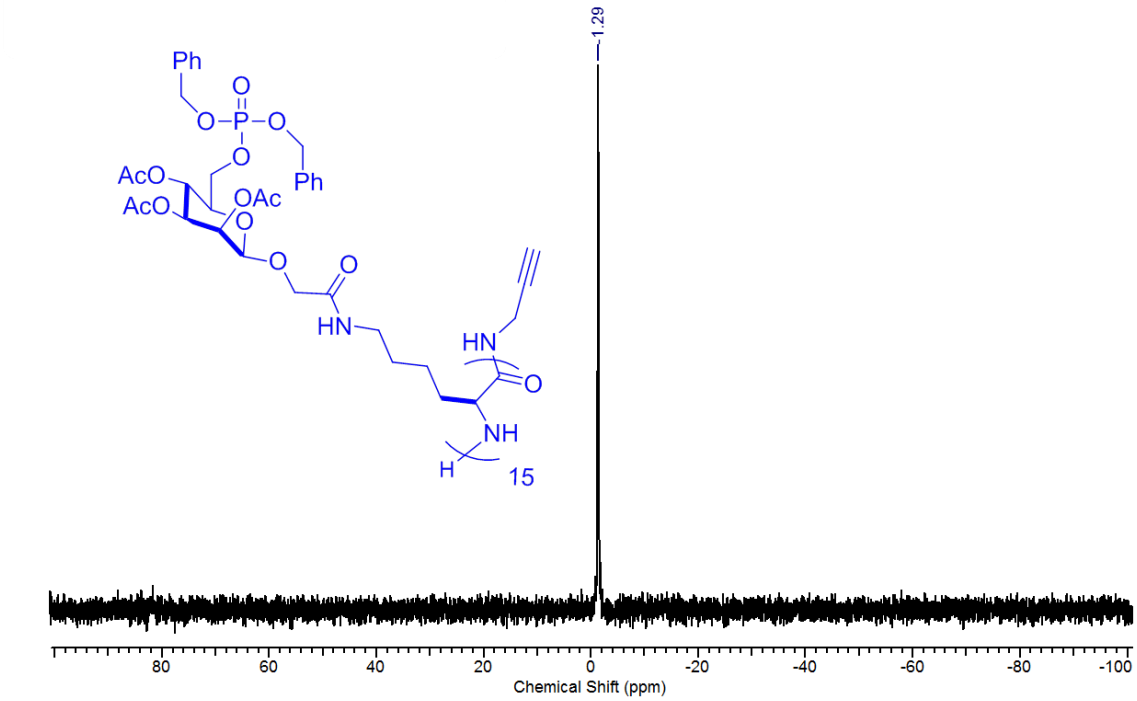

Figure C4: ^{31}P NMR ($CDCl_3$, 202.46 MHz) Spectrum of Pr-15M6P-GP **(3)**

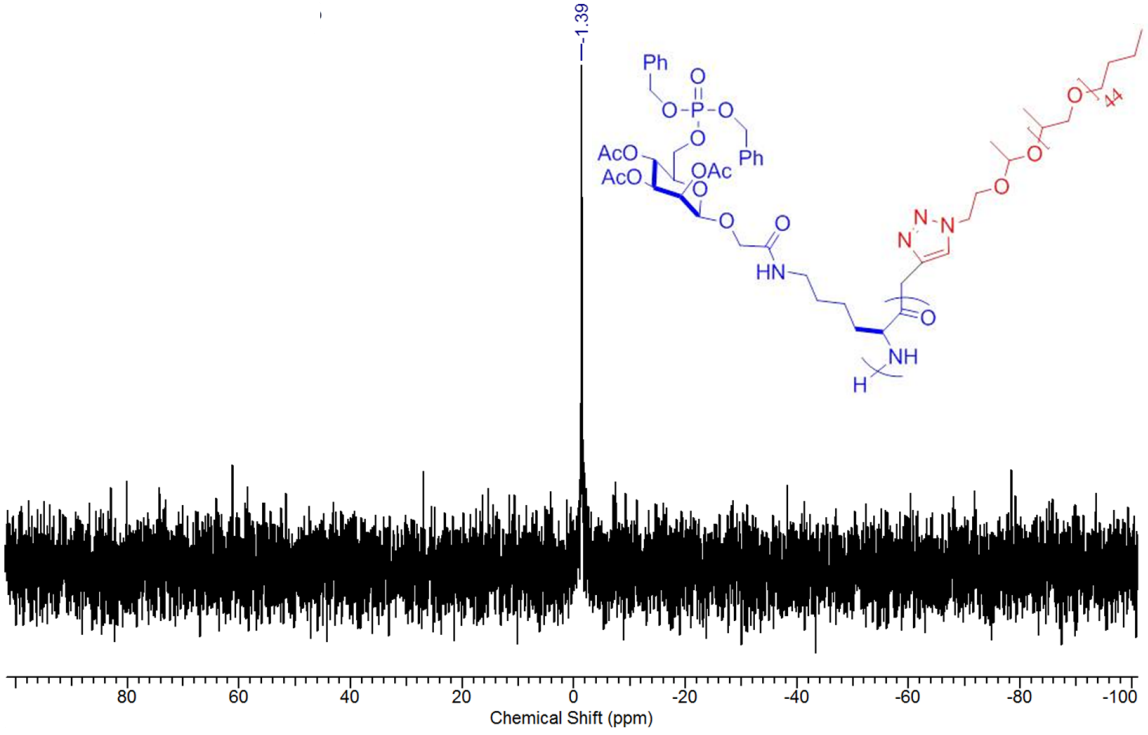

Figure C5: ^{31}P NMR ($CDCl_3$, 202.46 MHz) Spectrum of 15M6P-GP-ace-PPO polymer **(4)**

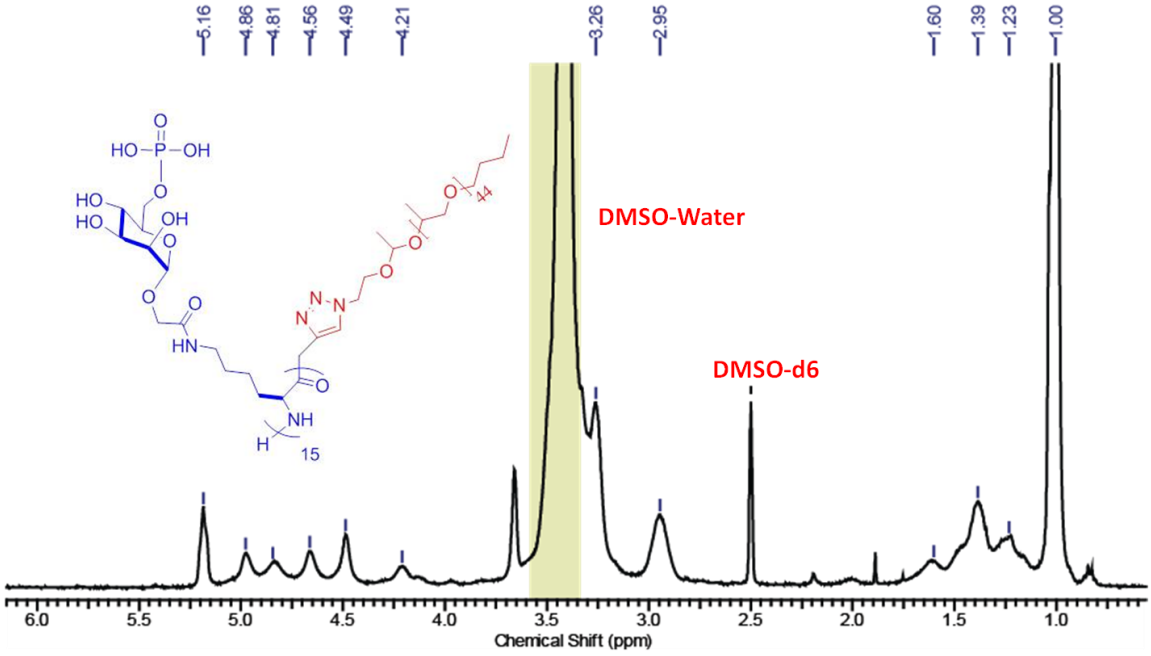

Figure C6: ^{1}H NMR (DMSO-d6, 400 MHz) Spectrum of 15M6P-GP-ace-PPO **(5)**

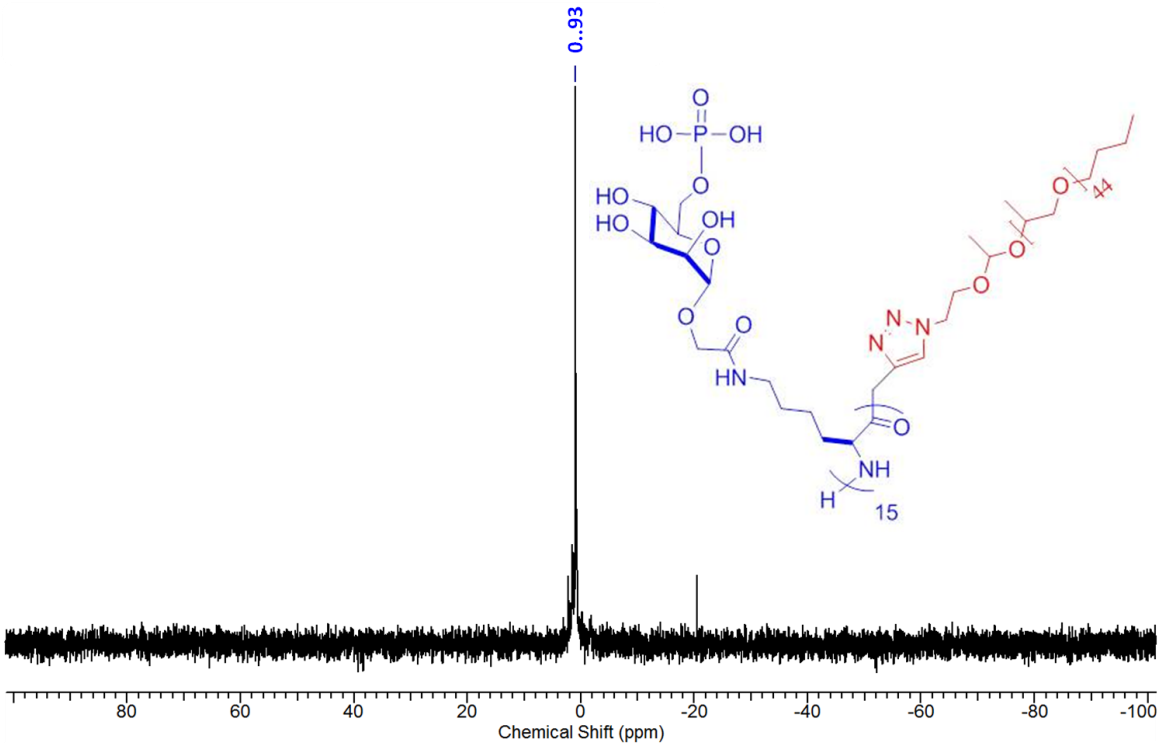

Figure C7: ^{31}P NMR (DMSO-d6, 202.46 MHz) Spectrum of deprotected 15M6P-GP-ace-PPO polymer **(5)**

Appendix D (Chapter 5)

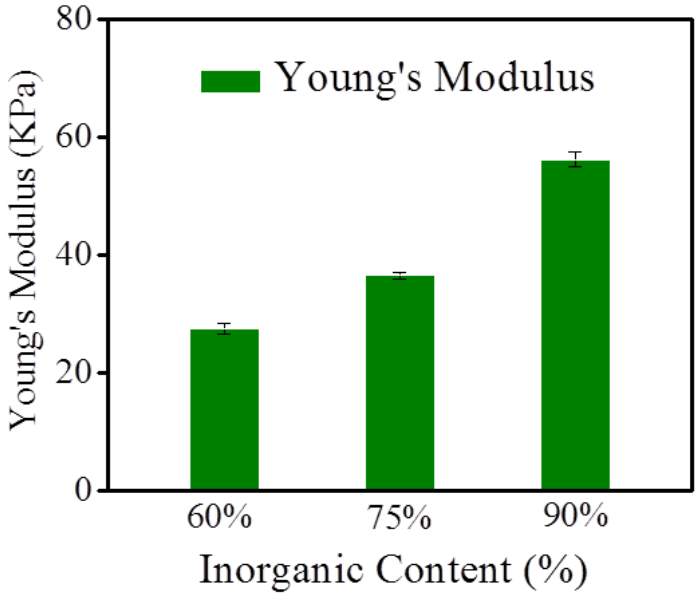

Figure D1: (a) Young's Modulus of silk hybrid scaffolds by varying the particle concentration (viz. from 60 to 90 %,).

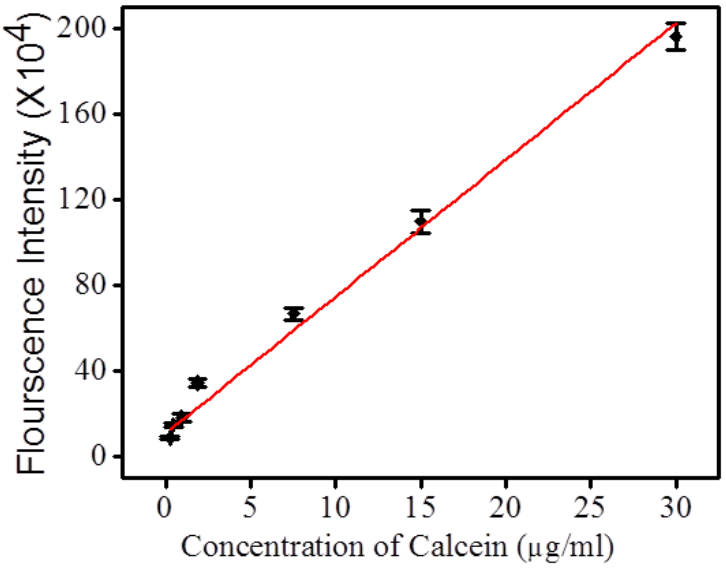

Figure D2: Calibration curve for calcein in 100 mM, pH 7.4 PBS.

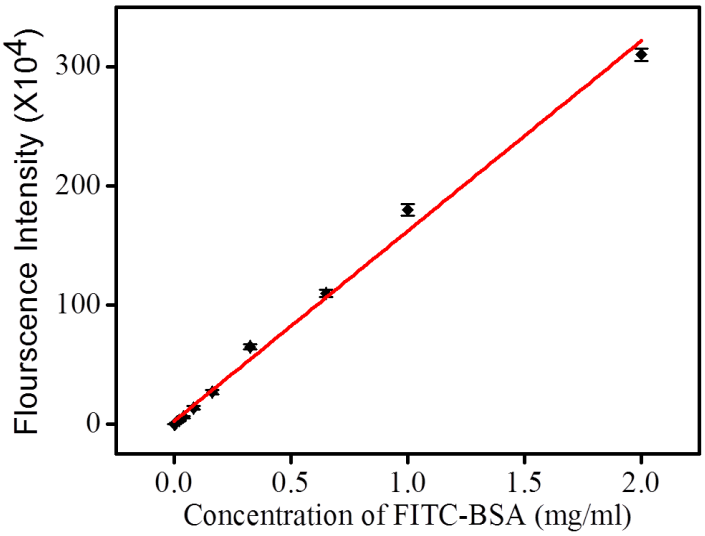

Figure D3: Calibration curve for FITC-BSA in 100 mM, pH 7.4 PBS.

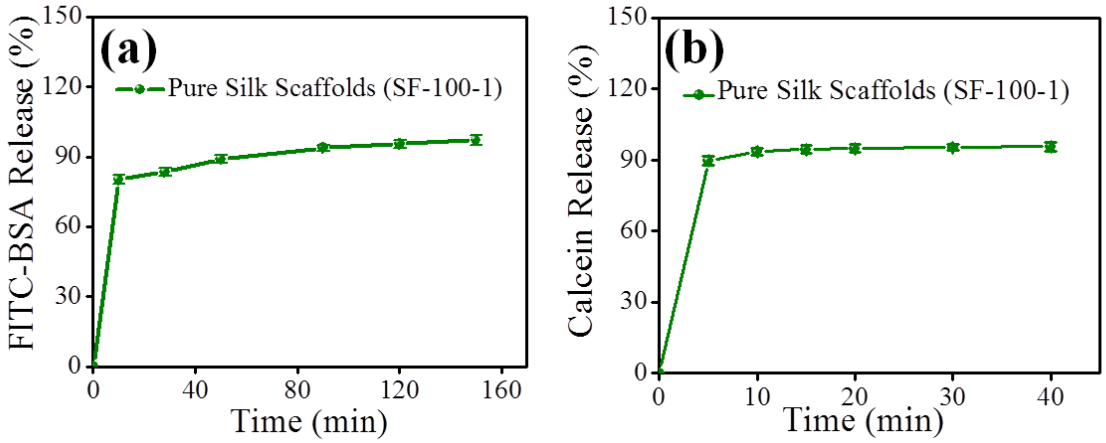

Figure D4: (a) Release profile of FITC-BSA from lyophilized pure silk scaffolds (SF-100-1) (b) Release profile of calcein from lyophilized pure silk scaffolds (SF-100-1).

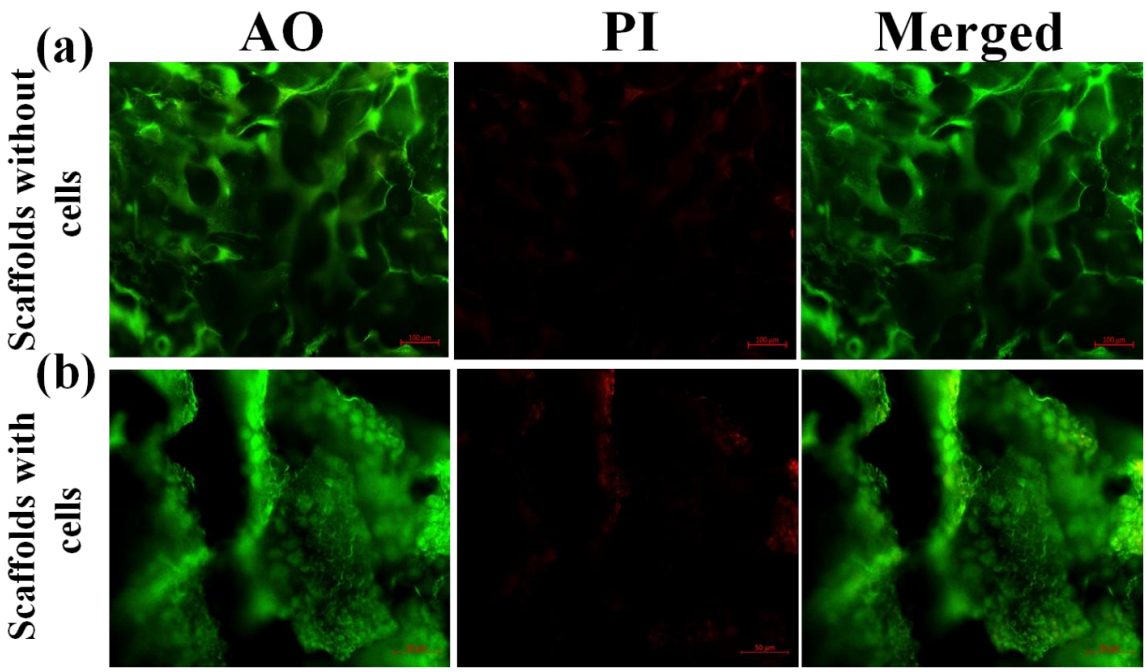

Figure D5: Epifluorescence Microscopic Images of Live-Dead assay images of SH-75-1 scaffolds at 7th day (a) scaffolds without cells as a control (scale bar:100 µm) (b) scaffolds with cells indicate the cell proliferation in groups in some region of scaffolds (Scale bar: 50 µm).

List of Publications

1. Glycopolypeptide grafted Bioactive Polyionic Complex Vesicles (PICsomes) and their Specific Polyvalent Interactions. **Bhawana Pandey**, Jaladhar Mahato, Karishma Berta Cotta, Soumen Das, Dharmendra K. Sharma, Arindam Chowdhury and Sayam Sen Gupta*.
   ACS Omega, **2016**, *1* (4), pp 600–612, **DOI:** 10.1021/acsomega.6b00142

2. Silk-Mesoporous silica based Hybrid Macroporous Scaffolds using Ice-Templating Method: Mechanical, Release and Biological Studies. **Bhawana Pandey**, Soumyajyoti Chatterjee, Nimisha Parekh, Anuya Nisal and Sayam Sen Gupta*.
   ACS Applied Biomaterials (Manuscript under Revision, **2018)**

3. Amphiphilic Glycopolypeptide based Crosslinked Nanocarriers for Dual Stimuli-Responsive Drug Delivery. **Bhawana Pandey**, Ashootosh V Ambade and Sayam Sen Gupta.
   (Manuscript under Preparation, **2018)**

4. pH-Responsive Self-Assembled Nanostructures from Amphiphilic Mannose-6-Phosphate Glycopolypeptides for Lysosomal Targeted Drug Delivery. **Bhawana Pandey**, Basudeb Mondal, Nimisha Parekh, Soumen Das, Sayam Sen Gupta.
   (Manuscript under Preparation, **2018)**

Erratum

About the Author

Bhawana Pandey, Daughter of Mrs. Vijay Laxmi Pandey and Mr. Suresh Chand Pandey was born in Bharatpur, Rajasthan. She received her secondary education from Indian Public Senior Secondary School, Jaipur. She completed her B.Sc. from University Maharani College, Rajasthan University in 2010. After the completion of her B.Sc. she joined Department of Chemistry, University of Rajasthan to pursue her M.Sc under Rajasthan University. She was awarded CSIR research fellowship for 2013-2018. She joined CSIR-NCL, Pune to pursue her Ph.D. degree in January 2013 under the joint supervision of Dr. Sayam Sen Gupta and Dr. Ashootosh V. Ambade.

Council of Scientific and Industrial Research

National Chemical Laboratory